# Understanding the aqueous history of Gale crater, Mars as recorded by B and Li in Ca-sulfate veins

Debarati Das

Department of Earth & Planetary Sciences
McGill University
Montreal, Quebec, Canada

September 2022

A thesis submitted to McGill University in partial fulfilment of the requirements of the degree of Doctor of Philosophy

## Abstract

Gale crater is a ~155 km wide crater predominantly consisting of sedimentary rocks including evaporites, that are interpreted to have formed in fluvio-lacustrine conditions over multiple aqueous events. The diagenetically precipitated Ca-sulfate veins in Gale crater contain boron, and their clay-rich sedimentary host rocks contain lithium. B and Li are highly water soluble and fluid pH sensitive elements that are frequently incorporated in evaporites or adsorbed to clay minerals in terrestrial evaporative settings during the last stages of brine evolution. In the case of Gale crater, the Ca-sulfate veins are interpreted to have formed from secondary diagenetic fluid events where primary evaporites, including primary borates, were remobilized to form B-containing secondary Ca-sulfate veins, whereas clay-rich sedimentary rocks are interpreted to contain Li due to adsorption of Li on clay minerals. In terrestrial settings, borate formation is dependent on acidic fluid conditions followed by drying whereas adsorption of Li and B on clay minerals is dependent on alkaline fluid conditions. In this study, we use Curiosity rover data analysis, thermochemical modeling and terrestrial analog samples analyses to determine the distribution of B and Li in phases identified in both Gale crater and the terrestrial analogs to establish relative fluid pH and seasonal environmental conditions that led to the formation of B and Li containing secondary Ca-sulfate veins in Gale crater. We analyzed Ca-sulfate veins in Gale crater to determine the B and Li concentrations and trends between the abundance of these elements. We also modify a widely accepted Martian fluid composition to include B and Li in order to thermochemically model seasonal cycles in Gale crater. Following this we analyzed terrestrial analog samples from Southern California region to ground truth the observations made in Gale crater and the results of the Gale-relevant model.

Through the investigation of Ca-sulfates in Gale crater, we find that B and Li abundances in the veins are inversely proportional to each other. Through geochemical modeling of a Gale-relevant system, we find that formation of primary borates and Ca-sulfates require multiple wet-dry cycles. Through the study of terrestrial analog samples from Southern California, we find that B enrichment is linked to presence of evaporitic minerals while Li and B enrichment is linked to presence of clay minerals in the samples. Based on these findings, we establish that the relationship between B and Li in Ca-sulfate veins of Gale crater is representative of sequential precipitation over multiple wet dry-cycles with varying pH conditions that consisted of both alkaline and acidic fluid events. We suggest that B enrichment took place in Gale crater fluids during relatively acidic pH fluid conditions followed by periods of drying to precipitate primary borates and Ca-sulfates, while Li and B were adsorbed onto clay minerals in the sedimentary rocks in other fluid events with relatively alkaline pH condition. We also infer that the B and Li enrichment in secondary Ca-sulfate veins likely formed due to remobilization of primary borates followed by reprecipitation as microcrystals within the Ca-sulfate vein and remobilization of B and Li containing clay minerals in Ca-sulfate veins walls in secondary diagenetic events. Through this work we establish that fluid pH and seasonal conditions that are optimal for origin of life and habitability of terrestrial microbial communities were likely present in the early aqueous history of Gale crater.

## Résumé

Le cratère Gale est un cratère d'environ 155 km de diamètre composé principalement de roches sédimentaires avec des observations fréquentes d'évaporites à l'aide du rover Curiosity, qui sont interprétées comme s'étant formées dans des conditions fluvio-lacustres au cours de plusieurs événements aqueux. Les veines évaporitiques de sulfate de Ca dans le cratère Gale contiennent du bore et les roches sédimentaires riches en argile contiennent du lithium. Le B et le Li sont des éléments hautement solubles dans l'eau et sensibles au pH qui sont fréquemment mis en déposés dans les évaporites ou adsorbés sur les minéraux argileux dans un climat d'évaporation au cours des dernières étapes de l'évolution de la saumure en milieu terrestre. Dans le cas du cratère Gale, les veines de sulfate de Ca sont interprétées comme résultantes d'événements fluides diagénétiques secondaires où les évaporites primaires, y compris les borates primaires, ont été remobilisées pour former des veines secondaires de sulfate de Ca contenant du B sur plusieurs événements aqueux, tandis que les roches sédimentaires riches en argile sont interprétées comme contenant du Li en raison de l'adsorption de Li sur les minéraux argileux. En milieu terrestre, la formation de borate dépend de la présence de fluides acides (qui permettent la saturation des ions borate dans le fluide) suivies de périodes de séchage (qui permettent la précipitation des borates) tandis que l'adsorption de Li et B sur les minéraux argileux dépend de la présence de fluide alcalin. Dans un environnement où les évaporites et les roches sédimentaires riches en argile sont présentes dans un mélange physique, la distribution de B et de Li entre les phases évaporitiques et les roches sédimentaires contenant de l'argile permet d'estimer le pH du fluide, le degré d'évaporation et la détermination de la présence de pH variables du fluide sur plusieurs cycles humides-secs. Sur Terre, il a été déduit que la présence de cycles humides-secs joue un rôle important dans l'origine de la vie, tandis que les conditions de pH aqueux variant de légèrement

acides à légèrement alcalines jouent un rôle crucial dans la stabilité du matériel génétique dans les organismes microbiens terrestres. Par conséquent, les estimations du pH des fluides et les contraintes sur les cycles saisonniers sont importantes pour déterminer la gamme et l'étendue des environnements habitables sur Mars. Dans cette étude, nous utilisons l'analyse des données du rover Curiosity, des techniques de modélisation thermochimique et l'analyse d'échantillons analogues terrestres pour déterminer la distribution de B et de Li dans les phases identifiées à la fois dans le cratère Gale et dans une zone terrestre similaire à Gale afin d'établir le pH relatif des fluides et les conditions environnementales saisonnières nécessaires pour former des veines secondaires de sulfate de Ca contenant du B et du Li dans le cratère Gale par analogie terrestre. Nous établissons que la relation entre le B et le Li dans les veines de sulfate de Ca du cratère Gale est représentative de précipitations séquentielles sur plusieurs cycles secs-humides avec des conditions de pH variables qui consistent en des événements fluides alcalins et acides. Nous proposons que l'enrichissement en B a eu lieu dans les fluides du cratère Gale pendant des conditions de pH relativement acide suivi de périodes de séchage pour précipiter les borates primaires et les sulfates de Ca (avec une exigence minimale de 250 cycles humides-secs) tandis que le Li et le B furent adsorbés sur les minéraux argileux dans les roches sédimentaires lors d'autres événements fluides avec un pH relativement alcalin. Nous inférons également que l'enrichissement en B et en Li dans les veines secondaires de sulfate de Ca s'est probablement formé en raison de la remobilisation des borates primaires suivie d'une reprécipitation sous forme de microcristaux dans les veines de sulfate de Ca et de la remobilisation des minéraux argileux contenant du B et du Li dans les parois des veines de sulfate de Ca lors d’événements diagénétiques secondaires. Grâce à ce travail, nous établissons que le pH du fluide et les conditions saisonnières optimales pour l'origine de la vie et l'habitabilité des communautés microbiennes terrestres étaient probablement présents dans les débuts de l'histoire aqueuse du cratère Gale.

## Acknowledgements

I would like to thank my supervisors Dr. Kim Berlo and Dr. Richard Leveille for their guidance and supervision that made completing this thesis possible. I would also like thank my collaborators Dr. Patrick Gasda, Dr. Susanne Schwenzer, Dr. Stuart Turner, Dr. Nina Lanza, and Dr. Laura Crossey for their mentorship and help with this project. I would not be the scientist I am today without you all.

I would like to the team who assisted with the analytical parts of the project and field work at McGill University, Los Alamos National Laboratory, and University of New Mexico, and the EPS McGill administrative team. Thank you to Anna Jung, Isabelle Richer, Brigitte Dionne, Roberta Beal, Eric Peterson, Matthew Nellessen, Kelsey Lamothe, Angela Di Ninno, Anne Kosowski and Kristy Thorton. I would also like to thank Dr. Galen Halverson for providing useful suggestions as my PhD progress committee member. I would also like to thank Dr. Russell Steele, Dr. Yajing Liu, Dr. Eric Galbraith, Dr. John Stix, Dr. Jeffrey McKenzie, and Dr. Christie Rowe for their support throughout my PhD journey. I am grateful for the financial support I received for this project from Natural Sciences and Engineering Research Council of Canada, McGill University, Canadian Space Agency, Los Alamos National Laboratory and National Geographic. The completion of this project would not have been possible without the resources I received.

I would also like to thank my fellow Earth and Planetary Sciences graduate students for their support and friendship, particularly Haylea Nisbet, Kyle Henderson, Becky Paisley, and Florentine Zwillich for all the geochemistry and writing discussions. Finally, I'd like to thank my parents, Tapasi Das and Dr. Subrata Das, and my partner, Alexandre de Verteuil, for their unwavering support and for always cheering me on through this journey.

# Table of Contents

Abstract………………………………………………………………………………… 2

Résumé……………………………………………………………………………… ….4

Acknowledgements…………………………………………………………………… ..7

Table of contents…………………………………………………………………… …...8

List of Figures……………………………………………………………………… ..13

List of Tables………………………………………………………………………… …16

Contribution to original knowledge……………………………………………………..18

Contribution of Authors…………………………………………………………………19

**Introduction………………………………………………………………………………..21**

1. Context and motivation……………………………………………………………….21
2. Thesis rationale………………………………………………………………………..25
3. References……………………………………………………………………………..27

**Chapter One………………………………………………………………………………..34**

Abstract……………………………………………………………………………………….35

1. Introduction……………………………………………………………………………..35
2. Geologic context………………………………………………………………………...38
    2.1. Mount Sharp Group-Murray Formation……………………………………………39
3. Geochemistry of boron and lithium……………………………………………….......42
    3.1. Common borates and their formation conditions…………………………….......42

3.2. Substitution and adsorption of boron……………………………………………….…43

3.3. Substitution and adsorption of lithium…………………………………………….…..44

3.4. Terrestrial examples of B- and Li-rich brines………………………………….……45

4. Methodology……………………………………………………………………….……..46

4.1. Data collection and processing………………………………………….….……....46

4.2. Subtraction of bedrock component from Ca-sulfate veins…………………….………..48

5. Results…………………………………………………………………………….……….49

5.1. Morphology of sulfate veins……………………………………………….………50

5.2. Stratigraphic detections of boron and lithium in veins……………………….………55

6. Discussion………………………………………………………………………….………61

6.1. Relationship of boron and lithium in calcium-sulfate veins…………………….………61

6.2. Possible timing and mechanism of boron and lithium emplacement…………………64

6.2.1. Murray sections below VRR……………………………………………...64

6.2.2. VRR…………………………………………………………………….65

6.3. Possible alternative models……………………………………………….........69

7. Conclusion…………………………………………………………………………69

8. Supporting information……………………………………………………………..72

S1 Common borates and their formation……………………………………………72

S2 Subtraction of bedrock contribution from Ca-sulfate vein compositions………….77

S3 Boron detection in Ca-sulfate veins of Gale crater………………………………82

S4 Possible borate phases in Ca-sulfate veins …………………………………………85

9. References……………………………………………………………………...88

**Link to Chapter Two……………………………………………………………………113**

References……………………………………………………………………………115

**Chapter Two…………………...……………………………………………………117**

Abstract……………………………………………………………………………………117

1. Introduction………………………………………………………………………………118
2. Geologic context of Gale crater…………………………………………………………122
3. Hypothesis and objective……………………………………………………………...124
4. Methodology……………………………………………………………………………..126
   - 4.1. Assumptions……………………………………………………………………...126
   - 4.2. Thermochemical modeling tool…………………………………………………..129
   - 4.3. Thermochemical database update and testing……………………………………130
   - 4.4. Establishing a Gale relevant scenario to model an evaporative environment…………131
     - 4.4.1. Global Mars relevant fluid: Modified Gale Portage Water……………………132
     - 4.4.2. Gale relevant host rock: Modified average Hartmann's Valley………………..136
     - 4.4.3. Establishing a local Gale relevant fluid: Titrating modified GPW with modified Hartmann's Valley rock composition……………………………………………..137
     - 4.4.4. Setting evaporation and dissolution cycles……………………………………..140
       - 4.4.4.1. Evaporation…………………………………………………………..141
       - 4.4.4.2. Dilution……………………………………………………………….142
5. Results……………………………………………………………………………………144
   - 5.1. Cycling……………………………………………………………………………144
   - 5.2. Extrapolation……………………………………………………………………...147
   - 5.3. Comparing the simulated mineral assemblage to terrestrial and Martian observations…………………………………………………………………………150

6. Discussions……………………………………………………………………………156

6.1. Constraining time for simulated wet-dry cycles using terrestrial analogs……………..156

6.2. Estimating time constraint for Gale crater……………………………………………..158

7. Conclusions……………………………………………………………………………163

8. References……………………………………………………………………………..164

**Link to Chapter Three………………………………………………………………...184**

References……………………………………………………………………186

**Chapter Three…………………………………………………………………………188**

Abstract…………………………………………………………………………………188

1. Introduction……………………………………………………………………………189

2. Geologic context of Gale crater………………………………………………………192

2.1. Fluvio-lacustrine deposits of Gale crater……………………………………………192

2.2. Evaporites in Gale crater……………………………………………………………196

2.3. B and Li in Gale crater………………………………………………………………197

3. Terrestrial analog study sites…………………..…………………………………...199

4. Hypotheses and objective…………...……………………………………………...200

5. Methods………………………………………………………………………………..201

5.1. Terrestrial analog sample collection…………………………………………………...201

5.2. Sample analysis and data processing………………………………………………..…206

5.2.1. X-Ray Diffraction…………………………………………………………207

5.2.2. Laser Induced Breakdown Spectroscopy (LIBS)………………………………208

6. Results…………………………………………………………………………………210

6.1. Sample characterization (major oxide compositions; crystalline and amorphous fractions; B and Li abundances) ……………………………………………………210
6.1.1. Borate containing samples……………………………………………………...214
6.1.2. Ca-sulfate containing samples…………………………………………………216
6.1.3. Samples with no predominant borates or Ca-sulfates…………………………..218
6.2. Determining elemental distribution in the samples using Principal Component Analysis…………………………………………………………………………………..222
6.3. Comparison of terrestrial and Gale crater observations………………………………225
6.3.1. Comparing physical mixing trends between terrestrial samples and Gale crater………………………………………………………………………………225
6.3.2. Comparing phases between terrestrial samples and Gale crater………………..228
7. Discussion…………………………………………………………………………………..230
7.1. B and Li distribution in phases of multimineralic analog samples……………………230
7.2. B and Li distribution in phases determined using Principal Component Analysis……235
7.3. Comparing terrestrial analog samples and Gale crater rocks…………………………237
7.4. Implications for Gale crater………………………………………………………………240
8. Conclusions………………………………………………………………………………244
9. References…………………………………………………………………………………..245

**Final conclusions……………………………………………………………………………264**

1. Major findings………………………………………………………………………………264
2. Conclusions and implications………………………………………………………………266
3. Topics for further research…………………………………………………………………….268
4. References…………………………………………………………………………………..269

# List of Figures

## Chapter One

**Figure 1**. Overview of Curiosity's Gale Crater sampling area and summary of boron detections in the Vera Rubin ridge area…………………………………………………………………..36

**Figure 2.** Morphologies of light-toned materials where boron has been observed in VRR….…51

**Figure 3.** Vein textures observed by Remote Micro Imager……………………………………53

**Figure 4.** Veins containing dark features………………………………………………………..54

**Figure 5.** Plot showing the corrected Li concentration of the high-Ca veins against elevation, compared with the Li concentration of the surrounding bedrock……………………………..…58

**Figure 6.** Histogram showing the distribution of Ca-rich veins in Gale Crater throughout Curiosity's traverse (sols 0—2311), frequency of Ca-rich veins with boron, and comparison of Li concentration of veins with relative frequency of boron detections in veins……………………59

**Figure 7.** Average corrected Li concentration of the veins with B detection frequency and average B peak areas with 2σ standard error bars……………………………………………….60

**Figure S1.** Flow chart showing common borate phases on Earth and their formation conditions (cation availability, temperature, pressure, and pH conditions)………………………………….74

**Figure S2.1** Plot showing a positive correlation between wt% $SiO_2$ and Li concentration of the veins ($R^2$ value 0.415) indicating contribution of bedrock in the veins…………………………80

**Figure S2.2** Comparing corrected Li concentration values of the veins with the bedrock Li concentrations………………………………………………………………………………………80

## Chapter Two

**Figure 1.** Illustration of the hypothesized sequence of events occurring in Gale crater and tested in the thermochemical model……………………………………………………………………..125

**Figure 2.** A plot indicating the relative abundances of minerals formed in varying water: rock ratio during the titration of a local Gale lake fluid and Hartmann's Valley rock………………140

**Figure 3.** Resultant minerals after evaporating the fluid down to 10 moles $H_2O$……………...142

**Figure 4.** Resultant minerals after mixing early brine with ground water……………………..144

**Figure 5.** Step-like and gradual increase in concentration of $Li^+$ with increasing number of cycles……………………………………………………………………………………………147

**Figure 6.** Resultant minerals obtained after evaporating the extrapolated fluid composition that has undergone 250 wet-dry cycles…………………………………………………………...149

**Figure 7.** Number of moles/kg of $Mg^{2+}$ for a corresponding amount of $SO_4^{2-}$ to start precipitating Mg-sulfate using the Gale relevant fluid at 1 bar pressure and 25°C…………………………..154

**Figure 8.** Number of moles/kg of $Na^+$ for a corresponding amount of $Cl^-$ to start precipitating halite using the Gale relevant fluid at 1 bar pressure and 25°C………………………………...155

**Figure 9.** Average wet-dry cycling times for three types of terrestrial closed lakes…………...157

**Figure 10.** Gale stratigraphic record with minimum annual cycles estimated for forming Ca-sulfates and borates based on water levels inferred using observed sedimentological facies….160

## Chapter Three

**Figure 1.** Stratigraphic column (left) and rover path indicating topographic features, lithologic formations, members and units…………………………………………………………………194

**Figure 2.** a) Sampling areas in Furnace Creek, Ryan, Searles Lake, and Rio Tinto borate mine indicated in b) Geologic map of Furnace Creek, CA, indicating the geologic units and sampling sites in the Gower Gulch area……………………………………………………………..204

**Figure 3.** Representative field context images for borates (a), Sulfate (b), halite (c), clay-rich sedimentary rocks (d), basalt (e), and ash (f) collected from borate mine, Searles Lake and Gower Gulch…………………………………………………………………………………205

**Figure 4.** Close-up images of the samples including borates(a), Ca-sulfate(b), halite (c), clay-rich sedimentary rocks (d), basalt (e), and ash (f) collected from borate mine, Searles Lake and Gower Gulch…………………………………………………………………………………205

**Figure 5.** Relative crystalline and amorphous proportions in twenty-one samples determined using XRD and full-pattern analysis techniques. Corresponding B and Li concentrations shown in top panels……………………………………………………………………………….…214

**Figure 6.** Lithium concentration in seven borate-containing samples plotted with abundances of phases identified using XRD…………………………………………………………...216

**Figure 7.** B (a) and Li (b) concentration in eight Ca-sulfate-containing samples plotted with abundances of phases identified using XRD and a trendline to indicate the relationship between amorphous phase abundance and B and Li abundance………………………………………218

**Figure 8.** B (a) and Li (b) concentration in the six samples that do not predominantly contain borates or Ca-sulfates plotted with abundances of phases identified using XRD and a trendline to indicate the relationship between amorphous phase abundance and B and Li abundance…….220

**Figure 9.** a) Principal components PC 1 (62% of variance) and PC 2 (13% of variance) for terrestrial analog samples, b) loadings plot for PC1with Al, Fe, Li, Mg, Na and Si positive and Ca negative c) loadings plot for PC2 with the elements Mg, Al, Ca, and Li positive and B and Na negative…………………………………………………………………………………224

**Figure 10.** Ternary diagram indicating molar proportions of $Al_2O_3$, ($CaO$+$Na_2O$+$K_2O$), and ($FeO_T$+$MgO$) for terrestrial samples collected for this work, reference pure igneous and clay mineral data, and reference Gale crater nontronite data plotted in mole percent………………228

# List of Tables

## Chapter One

**Table S1.** Major borates, formulas, deposit types, locations, and structural subdivisions………75

**Table S2.1.** Ideal Ca-sulfate composition calculated by averaging the compositions of three high-Ca targets with 0 wt% $SiO_2$, $TiO_2$, and $Al_2O_3$…………………………………………...81

**Table S2.2.** Analysis of the error propagation for different cases of CaO content and Li vein and bedrock content……………………………………………………………………………..81

**Table S3.1.** Targets that show presence of boron in them in the Murray formation in Gale crater.........................................................................................................................83

**Table S3.2.** Number of calcium sulfate veins and observed boron in various stratigraphic units of Gale Crater……………………………………………………………………………….84

## Chapter Two

**Table 1.** Fluid composition from Searles Lake (Felmy and Weare, 1986) used for testing the updated CHIM-XPT database………………………………………………………………..131

**Table 2.** Fluid composition of Gale Portage Water and modification made using Icelandic natural lakes and groundwater. Composition of fluid are indicated in molar concentration (moles/kg of water or rock)………………………………………………………………..135

**Table 3**. Average bedrock composition of the Hartmann's Valley target area modified with S, Li, and B concentrations measure in Nakhlite meteorites……………………………………….137

**Table 4.** Molar concentration (M) of fluid composition used in each step of the four cycles simulating a Gale relevant wet-dry scenario……………………………………………………145

**Table 5.** Extrapolated fluid composition for cycles 5-250. Fluid composition in molar concentration (moles/kg)…………………………………………………………………..…148

**Table 6.** Minerals formed throughout the modeled steps (titration, evaporation, and fluid-mixing) with corresponding molar concentration (moles/kg) of $Li^+$ ions in the fluid…………………..149

**Table 7.** Comparison of minerals resulting from this work to minerals reported in Death Valley and minerals observed or reported plausible in Gale crater………………………………… …152

## Chapter Three

**Table 1.** Major oxide composition with B and Li concentrations for the twenty-two samples collected from southern California………………………………………………………..210

**Table 2.** Crystalline and amorphous phase quantifications for twenty-one samples estimated using XRD and quantifications done using full-pattern analysis with corresponding B and Li concentrations measured using PGNAA and Fus-LAICPMS techniques respectively……...…212

**Table 3.** Major oxides measured using the LANL ChemCam unit………………………….....225

**Table 4.** Comparison of phases identified in the samples from Southern California to minerals observed or reported plausible in Gale crater and to minerals formed as a result of thermochemical modeling of a Gale-relevant scenario………………………………………...229

## Contribution to original knowledge

I confirm that this thesis presents original research and the results of my own work, unless otherwise referenced and acknowledged in this thesis. This thesis contributes to the original knowledge of water-soluble elements found in association with evaporites in Gale crater, Mars and expands the existing study to include the elements boron and lithium. Chapter one summarizes the first investigation of B and Li trends associated with calcium sulfate veins in Gale crater observed using the Curiosity rover in-situ analytical techniques. Through this work we also model the possible environmental conditions that could have led to the enrichment of B and Li in Ca-sulfate veins starting from a Gale-relevant fluid. The results summarized in Chapter 2 provide the first theoretical geochemical and temporal constraints for late-stage aqueous activity in Gale crater. Through the results summarized in Chapter 3 we also establish the nature of the mineralogical phases that act as reservoirs for B and Li associated with Ca-sulfates in a Gale-like terrestrial environment and provide ground truthing for the hypothesis made in Chapter one and the thermochemical modeling results summarized in Chapter 2. This work is the first estimate for possible reservoirs of B and Li associated with Ca-sulfates in Gale crater based on terrestrial observations. Overall, these three chapters enhance our understanding of late-stage aqueous activities in Gale crater at a higher temporal resolution and enable broad prediction of minerals to be expected along the traverses of the two rovers currently investigating crater lake beds on Mars based on comparison with terrestrial analogs and theoretical modeling results.

## Contribution of authors

This manuscript is composed of three central chapters. Chapter one was published in the Journal of Geophysical Research: Planets (Volume 125, Issue 8) on June 18, 2020. I am the main author of this chapter along with twelve of my co-authors: my supervisors: Dr. Kim Berlo and Dr. Richard Leveille; my collaborators from Los Alamos National Laboratory: Dr. Patrick Gasda, and Dr. Roger Wiens; and my collaborators from the Mars Science Laboratory Team: Dr. Jens Frydenvang, Dr. Nicolas Mangold, Dr., Dr. Rachel Kronyak, Dr. Olivier Forni, Dr. Agnes Cousin, Dr. Sylvestre Maurice, Dr. Olivier Gasnault. Dr. Gasda acquired the ChemCam data and developed the data processing methodology used in Chapter 1 and I carried out the processing, analysis, and interpretations for data used for this work. The other co-authors on this chapter provided guidance with the manuscript preparation.

Chapter 2 is in preparation for submission in a future issue of Journal of Geophysical Research: Planets. I am the lead author on this chapter with co-authors: my supervisors: Dr. Kim Berlo and Dr. Richard Leveille; my collaborators from The Open University: Dr. Stuart Turner and Dr. Susanne Schwenzer; my collaborators from Los Alamos National Laboratory: Dr. Patrick Gasda, and Dr. Nina Lanza; my collaborators from University of Oregon: Dr. Mark Reed and Dr. Jim Palandri; and my collaborator from University of New Mexico: Dr. Laura Crossey. I designed modeling workflow in collaboration with Dr. Susanne Schwenzer, Dr. Stuart Turner, Dr. Patrick Gasda, Dr. Kim Berlo, and Dr. Richard Leveille and carried out all the modeling steps described in this work. Dr. Stuart Turner updated the modeling database to include thermochemical parameter of three borates that were previously not included. Dr. Mark Reed and Dr. Jim Palandri developed the modeling software used for this work and provided guidance for optimizing the usage of the modeling software for this work. I carried out the processing, analysis, and interpretations for data used for this work. All co-authors on this work provided guidance for the manuscript preparation for this chapter.

Chapter 3 is in preparation for submission in a future issue of Journal of Geophysical Research: Planets. I am the lead author on this chapter with co-authors: my supervisors: Dr. Kim Berlo and Dr. Richard Leveille; my collaborators from Los Alamos National Laboratory: Dr. Patrick Gasda, Roberta Beal, Adriana Reyes-Newell, Dr. Ann Ollila, Dr. Samuel Clegg, Dr. Nina Lanza; and my collaborator from University of New Mexico: Matthew Nellessen, Eric Peterson, and Dr. Laura Crossey. I collected field samples from Southern California with Dr. Patrick Gasda and with the assistance of Kelsey Lamothe. I processed the collected field samples and sent them to Los Alamos National Laboratory, University of New Mexico, and Activation Laboratories for geochemical analysis. At Los Alamos National Laboratory and University of New Mexico, Roberta Beal, Adriana Reyes Newell, Matthew Nellessen, and Eric Peterson provided data using the ChemCam engineering unit and X-Ray diffraction instrument under the guidance of Dr. Patrick Gasda, Dr. Samuel Clegg, Dr. Ann Ollila, Dr. Nina Lanza, and Dr. Laura Crossey. I performed data processing and analysis for this work. All co-authors on this work provided guidance for the manuscript preparation for this chapter. All three chapters were written by me with feedback for each chapter provided by the respective co-authors.

# Introduction

## 1 Context and motivation

Gale crater is a ~155 km wide crater with a central sedimentary mound (Aeolis Mons, informally known as "Mt. Sharp") located between the Southern Highlands and Northern Lowlands division in the northwestern part of the Aeolis quadrangle (Milliken et al., 2010; Grotzinger and Milliken, 2012; Fraeman et al., 2016). Gale crater shows evidence of fluvio-lacustrine conditions represented by sedimentary rocks (Milliken et al., 2010; Grotzinger et al., 2014; 2015; Banham et al., 2018; Stack et al., 2019; Edgar et al., 2020, Vasavada et al., 2014; 2022) that are being investigated by the NASA Curiosity rover since August 2012.

Based on the rocks and minerals analyzed using the Curiosity rover, Gale crater is interpreted to have hosted an ancient habitable lake (Grotzinger et al., 2014; Hurowitz et al., 2017; Rampe et al., 2020; Turner et al., 2020; Rivera-Hernández et al., 2020; Bristow et al., 2018; Rapin et al., 2019). Gale crater also shows the presence of evaporites such as Ca-sulfates, halite, and minor amounts of carbonate that are interpreted to have formed as a result of multiple generations of fluid activity consisting of various fluid compositions, pH and evaporative states (Nachon et al., 2017; Thomas et al.,2019; Gasda et al., 2017; 2022, Rapin et al, 2019; 2021; Sutter et al., 2017). In this work, evaporites are referred to as either primary or secondary. In terrestrial settings, freshly precipitated evaporites which have not undergone any burial, replacement, dehydration, or dissolution are referred to as "primary" (Warren, 2000, 2006). With time and processes such as burial, dehydration, dissolution and remobilization, remixing with new fluids, and re-precipitation, evaporites can experience multiple degrees of diagenesis which is reflected in their mineralogy and textures. Evaporites that have undergone any diagenetic processes are referred to as "secondary".

The Ca-sulfates, halite and carbonates observed in Gale crater are interpreted to be predominantly representative of secondary diagenetic processes which consisted of multiple generations of dissolution and reprecipitation of primary evaporites into rock fractures and as cements (Thomas et al., 2019; Nachon et al., 2017; Kah et al., 2018; Schwenzer et al., 2016; Gasda et al., 2017; Dietrich et al., 2022; Rapin et al., 2021; Sutter et al. 2017). Data collected using the instruments onboard the Curiosity rover in Gale crater also show a mixing between the evaporites and surrounding sedimentary rocks (L'Haridon et al., 2018; Gasda et al., 2022). This mixing is inferred to be due to either the presence of secondary evaporitic cements within the sedimentary rocks or simultaneous sampling of evaporite veins and sedimentary bedrock at the same time during Curiosity rover analytical techniques (Gasda et al., 2022).

The secondary Ca-sulfate veins show the presence of water soluble and mobile element B (Gasda et al., 2017) and sedimentary rocks show the presence of Li (Frydenvang et al., 2020). Enrichment of B secondary in Ca-sulfate veins of Gale crater is interpreted to have been caused by remobilization of primary borates and re-precipitation in close association with Ca-sulfates over multiple periods of aqueous activity in areas that also show evidence of elevated evaporation (Gasda et al., 2017). This interpretation is based on the common coexistence of Ca-sulfate and borates in terrestrial dry lake environments that have experienced multiple wet-dry cycles (Lowenstein et al., 1999; Swihart et al., 2014) as aggregates of extremely fine crystals consisting of micron sized crystals of borates and Ca-sulfates (as shown in micrographs described by Hunt, 1996). However, In Gale crater, no crystalline borates have been observed as of this work and the measurement of B is limited to low Fe-targets due to spectral interferences of Fe from high Fe-sedimentary rocks with spectral signal of B (Gasda et al., 2017). The presence of Li in rocks of Gale carter is attributed to either adsorption of Li onto clay minerals in the sedimentary rocks or the incorporation of Li within phyllosilicate or potassic alumina-rich silicate minerals (Payre et al., 2017). However, in Gale crater, the presence of Li is predominantly associated with adsorption on to clay minerals and Li abundance in the sedimentary rocks is used as a proxy for clay mineral content (Frydenvang et al., 2020).

In terrestrial settings, evaporite precipitation and adsorption to clay minerals are both pH sensitive processes that also depend on extent of fluid evaporation. Adsorption of B and Li on clay minerals require a high pH aqueous condition (pH 9-11) (Rohman et al., 2020; Li and Liu, 2020; Karahan 2006; Nellessen et al., 2019) while emplacement of boron in borates and in close association to other evaporites such as Ca-sulfate and halite requires relatively high concentration of borate ions in a relatively acidic fluid (pH 3-5) followed by a dry period that enables the precipitation of the evaporites (Kistler and Helvaci, 1994; Birsoy and Ozbas, 2012; Felmy and Weare, 1986; Li et al., 1996; Bixler and Sawyer, 1957). As borate formation and B and Li adsorption are pH sensitive processes that require two different sets of pH conditions, in an environment, where both evaporites and clay minerals are present, the distribution of B and Li between evaporites and clay minerals can indicate the changing fluid pH and evaporative conditions.

Three different types of evaporites have been observed in Gale crater (Ca-sulfate, halite, and carbonates) with the inferred presence of borates in close association with Ca-sulfates based on the enrichment of B in the secondary sulfate veins of Gale crater. In an evaporative environment, different evaporites precipitate from a parent fluid in a sequence based on the relative solubilities and the concentration of ions present in the fluid (Dalton, 2016). When a brine evaporates, the relative concentration of solutes gradually increases during evaporation and the least soluble evaporitic phase precipitates first while the most soluble phase tends to remain in solution or precipitates last (Aquilano et al., 2016; Getenet et al., 2022). In terrestrial dry lake systems, the saturation point for an evaporitic phase in a fluid is dependent on geologic processes that cause selective enrichment of soluble elements through aqueous weathering of rocks over seasonal cycles (Eugster and Maglione, 1979; Nesbitt and Young, 1982; Nesbitt and Wilson, 1992). As the formation of evaporitic assemblages are dependent on seasonal cycles, the relationship between different types of evaporites in an assemblage can be reflective of the regional seasonal cycle and the relative timescale of the cycles (Lowenstein et al., 1999; Li et al, 1996). Hence in a scenario where the fluid composition is known or can be estimated for a region, an observed assemblage consisting of various evaporites provides an opportunity for the estimation of temporal constraints on seasonal cycles and geochemical constraints on fluid evolution through the seasonal cycles.

As described above, the relationship between water-soluble elements in evaporites is reflective of the extent of evaporation, the distribution of water-soluble elements between evaporites and sedimentary rocks are reflective of aqueous pH condition and extent of evaporation. In this work, we study evaporites and their surrounding sedimentary rocks in Gale crater and in terrestrial analog settings in order to estimate fluid and environmental conditions and during primary evaporite formation in Gale crater. We do this by expanding the study of water-soluble elements in secondary Ca-sulfate veins in Gale crater to include B to Li while expanding the topographical area of investigation of B. We use the relationship between B and Li in secondary Ca-sulfate veins measured using the Curiosity rover to present a hypothesis regarding the formation conditions of primary evaporites in Gale crater (Chapter 1). Based on the evaporites observed and estimated in Gale crater, we use thermochemical modeling techniques to propose a seasonal cycling requirement with temporal and early Gale lake fluid composition estimates to form primary evaporites in Gale crater (Chapter 2). We also ground truth the observations made in Gale crater and thermochemical modeling results by comparing the observed and estimated phases and mixing trends in Gale crater to phases and mixing trends in samples collected from a terrestrial analog area in Southern California (Chapter 3).

## 2 Thesis rationale

On Earth, lacustrine environments support a wide range of biotic communities. Aqueous pH and fluid composition along with seasonal variations play a crucial role in the habitability of the microbial organisms that reside in these environments (Dartnell, 2011; Shock and Holland, 2007; Hud and Fialho.,2019; Becker et al., 2016; 2019; Marsh, 2022). Extremely acidic environments denature proteins and hydrolyze cellular components while extremely alkaline environments limit hydrogen availability for crucial bioenergetic processes and therefore both highly acidic and alkaline conditions are hazardous to the majority of terrestrial organisms (Dartnell, 2011). Deoxyribonucleic acid (DNA) and ribonucleic acid (RNA) which are biological molecules that contain genetic information, are reported to be most structurally stable between slightly acidic (~5) to neutral pH with tolerance up to alkaline pH (~8; Roberts and Crothers, 1992; Küpfer, P.A. and Leumann, 2007; Jarvinen et al., 1991). The majority of terrestrial organisms can survive within moderately acidic to alkaline conditions showing optimal habitability conditions at neutral pH (Shock and Holland, 2007).

The presence of wet-dry cycles has also been inferred to play an important role in the origin of life on Earth (Hud and Fialho.,2019; Becker et al., 2019; Marsh, 2022). Repeated wet and dry conditions in the same location over seasonal cycles are interpreted to have provided the environments necessary to complete formation of the nitrogenous bases that form the structure of key building blocks of life i.e., DNA and RNA (Becker et al., 2016; 2019).

Hence, estimates of fluid pH and constraints on seasonal cycles are important for determining the range and extent of habitable environments on Mars. The study of B and Li in phases that can help us determine an estimate on Gale crater fluid pH and evaporative state, provide a higher resolution of understanding of habitability potential during the various stages of Gale crater's aqueous history.

Prior to this study, the investigation of B in Ca-sulfate veins in Gale crater was limited to only one peer-reviewed article (Gasda et al., 2017) which reports data up to the first ~1500 sols and suggests that borates act as reservoirs of B in Ca-sulfate veins. In this work, we expand the investigation of water-soluble elements associated with Ca-sulfate veins in Gale crater from just B to both B and Li covering a larger geographic area compared to previous the previous work by Gasda et al., 2017.

We also do not have a baseline geochemical constraint on the aqueous fluids that could have emplaced primary borates and Ca-sulfates in close association or a temporal constraint on the geochemical processes responsible for this juxtaposition. Through this work, we establish a constraint for the minimum time and fluid composition required to form primary borates and Ca-sulfates in Gale crater using thermochemical modeling techniques.

As described in the previous section, the distribution of B and Li between evaporites and sedimentary rocks in Gale crater can enable estimation of fluid pH and evaporative states possible in Gale crater's early aqueous history, however the in-situ investigation of B in Gale crater using the Curiosity rover is limited to low-Fe Ca-sulfate targets (i.e., Ca-sulfate veins) due to spectral interferences of Fe from high Fe-sedimentary rocks with spectral signal of B (Gasda et al., 2017). Hence, we investigate the distribution of B and Li in mixed samples (evaporites and sedimentary rocks) from a terrestrial analog area in southern California where a similar environment as that which is inferred for Gale crater is reported, without the limitation to low-Fe targets. We apply our findings from terrestrial analog samples to infer fluid pH and evaporative extent in Gale crater and suggest possible reservoirs for both B and Li associated with Ca-sulfates in Gale crater.

This work was undertaken with the aim of better understanding of (1) the relationship between B and Li in secondary Ca-sulfate veins in Gale crater using Curiosity rover data to estimate the possible early conditions in Gale crater that formed primary evaporites, (2) the relative time constraint for the formation of primary borates in close association with Ca-sulfates for a Gale-relevant scenario using thermochemical modeling techniques, and (3) the possible reservoirs of B and Li in Gale crater and fluid pH conditions in Gale carter's early aqueous history based on terrestrial analog samples from Southern California.

## 3 References

Aquilano, D., Otálora, F., Pastero, L. and García-Ruiz, J.M., 2016. Three study cases of growth morphology in minerals: Halite, calcite and gypsum. *Progress in Crystal Growth and Characterization of Materials*, *62*(2), pp.227-251.

Banham, S. G., Gupta, S., Rubin, D. M., Watkins, J. A., Sumner, D. Y., Edgett, K. S., et al. (2018). Ancient Martian aeolian processes and palaeomorphology reconstructed from the Stimson formation on the lower slope of Aeolis Mons, Gale crater, Mars. Sedimentology, 65(4), 993–1042.

Becker, S., Thoma, I., Deutsch, A., Gehrke, T., Mayer, P., Zipse, H., et al. (2016). A high-yielding, strictly regioselective prebiotic purine nucleoside formation pathway. *Science*, *352*(6287), 833-836. https://doi.org/10.1126/science.aad2808

Becker, S., Feldmann, J., Wiedemann, S., Okamura, H., Schneider, C., Iwan, K., et al. (2019). Unified prebiotically plausible synthesis of pyrimidine and purine RNA ribonucleotides. *Science*, *366*(6461), 76-82.

Birsoy, R. and Özbaş, Ü., 2012. Activity diagrams of borates: implications on common deposits. *Carbonates and Evaporites*, *27*(1), pp.71-85.

Bixler, G.H. and Sawyer, D.L., 1957. Boron Chemicals from Searles Lake Brines. *Industrial & Engineering Chemistry*, *49*(3), pp.322-333.

Bristow, T.F., Rampe, E.B., Achilles, C.N., Blake, D.F., Chipera, S.J., Craig, P., Crisp, J.A., Des Marais, D.J., Downs, R.T., Gellert, R. and Grotzinger, J.P., 2018. Clay mineral diversity and abundance in sedimentary rocks of Gale crater, Mars. *Science advances*, *4*(6), p.eaar3330.

Dalton, G. R., Lee, A. Y., & Young, S. L. (2016). IUPAC/NIST Solubility Database (No. IUPAC/NIST Solubility Database).

Dietrich, W., Bryk, A., Banham, S., Rubin, D., Thompson, L., Caravaca, G. and Williams, R., 2022, March. Climate and Diagenetic Implications of Possible Soft Sediment Deformation of the Basal Aeolian Stimson Sediments in Gale Crater. In *53rd Lunar and Planetary Science Conference*.

Edgar, L. A., Fedo, C. M., Gupta, S., Banham, S. G., Fraeman, A. A., Grotzinger, J. P., et al. (2020). A Lacustrine Paleoenvironment Recorded at Vera Rubin Ridge, Gale Crater: Overview of the Sedimentology and Stratigraphy Observed by the Mars Science Laboratory Curiosity Rover. Journal of Geophysical Research: Planets, 125(3). https://doi.org/10.1029/2019JE006307

Eugster, H.P. and Maglione, G., 1979. Brines and evaporites of the Lake Chad basin, Africa. *Geochimica et Cosmochimica Acta*, *43*(7), pp.973-981.

Felmy, A.R. and Weare, J.H., 1986. The prediction of borate mineral equilibria in natural waters: Application to Searles Lake, California. *Geochimica et Cosmochimica Acta*, *50*(12), pp.2771-2783.

Fraeman, A. A., Ehlmann, B. L., Arvidson, R. E., Edwards, C. S., Grotzinger, J. P., Milliken, R. E., et al. (2016). The stratigraphy and evolution of lower Mount Sharp from spectral, morphological, and thermophysical orbital data sets: Stratigraphy and Evolution of Mount Sharp. Journal of Geophysical Research: Planets, 121(9), 1713–1736.

Frydenvang, J., Mangold, N., Wiens, R. C., Fraeman, A. A., Edgar, L. A., Fedo, C., et al. (2020). The chemostratigraphy of the Murray formation and role of diagenesis at Vera Rubin ridge in Gale crater, Mars, as observed by the ChemCam instrument. Journal of Geophysical Research: Planets.

Gasda, P. J., Haldeman, E. B., Wiens, R. C., Rapin, W., Bristow, T. F., Bridges, J. C., et al. (2017). In situ detection of boron by ChemCam on Mars. Geophysical Research Letters, 44(17), 8739-8748. 795

Getenet, M., García-Ruiz, J.M., Otálora, F., Emmerling, F., Al-Sabbagh, D. and Verdugo-Escamilla, C., 2022. A Comprehensive Methodology for Monitoring Evaporitic Mineral Precipitation and Hydrochemical Evolution of Saline Lakes: The Case of Lake Magadi Soda Brine (East African Rift Valley, Kenya). *Crystal growth & design*, *22*(4), pp.2307-2317.

Grotzinger, J. P., and Milliken, R. E. (2012). The sedimentary rock record of Mars: Distribution, origins, and global stratigraphy. Sedimentary Geology of Mars, 102, 1-48.

Grotzinger, J. P., Sumner, D. Y., Kah, L. C., Stack, K., Gupta, S., Edgar, L., et al. (2014). A habitable fluvio-lacustrine environment at Yellowknife Bay, Gale Crater, Mars. Science, 343(6169), 1242777.

Hud, N.V. and Fialho, D.M., 2019. RNA nucleosides built in one prebiotic pot. *Science*, *366*(6461), pp.32-33.

Hurowitz, J. A. et al. (2017). Redox stratification of an ancient lake in Gale crater, Mars. Science, 356(6341), eaah6849.

Kah, L. C., Stack, K. M., Eigenbrode, J. L., Yingst, R. A., & Edgett, K. S. (2018). Syndepositional precipitation of calcium sulfate in Gale Crater, Mars. Terra Nova, 30(6), 431-439.

Karahan, S., Yurdakoç, M., Seki, Y. and Yurdakoç, K., 2006. Removal of boron from aqueous solution by clays and modified clays. *Journal of Colloid and Interface Science*, *293*(1), pp.36-42.

Kistler, R.B. and Helvaci, C., 1994. Boron and borates. *Industrial minerals and rocks*, *6*, pp.171-186.

Li, W. and Liu, X.M., 2020. Experimental investigation of lithium isotope fractionation during kaolinite adsorption: Implications for chemical weathering. *Geochimica et cosmochimica acta*, *284*, pp.156-172.

Li, J., Lowenstein, T.K., Brown, C.B., Ku, T.L. and Luo, S., 1996. A 100-ka record of water tables and paleoclimates from salt cores, Death Valley, California. *Palaeogeography, Palaeoclimatology, Palaeoecology*, *123*(1-4), pp.179-203.

Lowenstein, Tim K., Jianren Li, Christopher Brown, Sheila M. Roberts, Teh-Lung Ku, Shangde Luo, and Wenbo Yang. "200 ky paleoclimate record from Death Valley salt core." *Geology* 27, no. 1 (1999): 3-6.

Milliken, R. E., J. P. Grotzinger, and B. J. Thomson. "Paleoclimate of Mars as captured by the stratigraphic record in Gale Crater." *Geophysical Research Letters* 37, no. 4 (2010).

Nachon, M., Mangold, N., Forni, O., Kah, L. C., Cousin, A., Wiens, R. C., et al. (2017). Chemistry of diagenetic features analyzed by ChemCam at Pahrump Hills, Gale crater, Mars. Icarus, 281, 121-136. https://doi.org/10.1016/j.icarus.2016.08.026

Nellessen, M.A., Crossey, L., Peterson, E., Gasda, P.J., Lanza, N., Yeager, C., Parsons, B., Labouriau, A., Wiens, R.C., Clegg, S. and Das, D., 2019, July. Boron Adsorption in Clay Minerals: Implications for Martian Groundwater Chemistry and Prebiotic Processes. In *Ninth International Conference on Mars* (Vol. 2089, p. 6353).

Nesbitt, H. W., and R. E. Wilson. "Recent chemical weathering of basalts." *American Journal of science* 292, no. 10 (1992): 740-777.

Nesbitt, H.W., Young, G.M., 1982. Early Proterozoic climates and plate motions inferred from major element chemistry of lutites. Nature 299, 715–717.

Payré, V., Fabre, C., Cousin, A., Sautter, V., Wiens, R. C., Forni, O., et al. (2017). Alkali trace elements in Gale crater, Mars, with ChemCam: Calibration update and geological implications: Alkali Trace Elements with Chemcam. *Journal of Geophysical Research: Planets*, *122*(3), 650–679.

Rampe, E.B., Bristow, T.F., Morris, R.V., Morrison, S.M., Achilles, C.N., Ming, D.W., Vaniman, D.T., Blake, D.F., Tu, V.M., Chipera, S.J. and Yen, A.S., 2020. Mineralogy of Vera Rubin ridge from the Mars science laboratory CheMin instrument. *Journal of Geophysical Research: Planets*, *125*(9), p.e2019JE006306.

Rapin, W., Ehlmann, B.L., Dromart, G., Schieber, J., Thomas, N.H., Fischer, W.W., Fox, V.K., Stein, N.T., Nachon, M., Clark, B.C. and Kah, L.C., 2019. An interval of high salinity in ancient Gale crater lake on Mars. *Nature Geoscience*, *12*(11), pp.889-895.

Rapin, W., Dromart, G., Rubin, D., Deit, L.L., Mangold, N., Edgar, L.A., Gasnault, O., Herkenhoff, K., Le Mouélic, S., Anderson, R.B. and Maurice, S., 2021. Alternating wet and dry depositional environments recorded in the stratigraphy of Mount Sharp at Gale crater, Mars. *Geology*, *49*(7), pp.842-846.

Rivera-Hernández, F., Sumner, D.Y., Mangold, N., Banham, S.G., Edgett, K.S., Fedo, C.M., Gupta, S., Gwizd, S., Heydari, E., Maurice, S. and Nachon, M., 2020. Grain size variations in the Murray formation: Stratigraphic evidence for changing depositional environments in Gale crater, Mars. *Journal of Geophysical Research: Planets*, *125*(2), p.e2019JE006230.

Rohmah, M., Lalasari, L.H., Natasha, N.C., Sulistiyono, E., Firdiyono, F. and Soedarsono, J.W., 2020. Adsorption Behavior of Alkali Metal (Na+, Li+, and K+) from Bledug Kuwu brine by Resin Adsorbent for Purification: pH and Flow Rate Parameter. *Orient. J. Chem*, *36*(2), pp.273-279.

Schwenzer, S. P., Bridges J. C.,Wiens R. C., Pamela G. Conrad, S. P. Kelley, R. Leveille, Nicolas Mangold et al. "Fluids during diagenesis and sulfate vein formation in sediments at Gale crater, Mars." *Meteoritics & Planetary Science* 51, no. 11 (2016): 2175-2202.

Stack, K. M., Grotzinger, J. P., Lamb, M. P., Gupta, S., Rubin, D. M., Kah, L. C., et al. (2019). Evidence for plunging river plume deposits in the Pahrump Hills member of the Murray formation, Gale crater, Mars. Sedimentology, 66(5), 1768–1802.

Sutter, Brad, Amy C. Mcadam, Paul R. Mahaffy, Doug W. Ming, Ken S. Edgett, Elizabeth B. Rampe, Jennifer L. Eigenbrode et al. "Evolved gas analyses of sedimentary rocks and eolian sediment in Gale Crater, Mars: Results of the Curiosity rover's sample analysis at Mars instrument from Yellowknife Bay to the Namib Dune." *Journal of Geophysical Research: Planets* 122, no. 12 (2017): 2574-2609.

Swihart, George H., Steven B. Carpenter, Yun Xiao, Eddie H. McBay, David H. Smith, and Yingkai Xiao. "A Boron Isotope Study of the Furnace Creek, California, Borate District." *Economic Geology* 109, no. 3 (2014): 567-580.

Thomas, N. H., Ehlmann, B. L., Meslin, P. -Y., Rapin, W., Anderson, D. E., Rivera-Hernández, F., et al. (2019). Mars Science Laboratory Observations of Chloride Salts in Gale Crater, Mars. Geophysical Research Letters, 46(19), 10754–10763.

Vasavada, A. R., Grotzinger, J. P., Arvidson, R. E., Calef, F. J., Crisp, J. A., Gupta, S., et al. (2014). Overview of the Mars Science Laboratory mission: Bradbury landing to Yellowknife Bay and beyond. Journal of Geophysical Research: Planets, 119(6), 1134-1161.

Vasavada, A. R. (2022). Mission Overview and Scientific Contributions from the Mars Science Laboratory Curiosity Rover After Eight Years of Surface Operations. *Space Science Reviews*, *218*(3), 14.

# Chapter One

## Boron and Lithium in Calcium Sulfate Veins: Tracking Precipitation of Diagenetic Materials in Vera Rubin Ridge, Gale Crater

D. Das[1], P. J. Gasda[2], R. C. Wiens[2], K. Berlo[1], R. J. Leveille[1], J. Frydenvang[3], N. Mangold[4], R. E. Kronyak[5], S. P. Schwenzer[6], Olivier Forni[7], Agnes Cousin[7], S. Maurice[7], O. Gasnault[7]

[1]Department of Earth and Planetary Sciences, McGill University, Quebec, Canada H3A 0E8.

[2]Los Alamos National Laboratory, Los Alamos, NM, USA 87545.

[3]University of Copenhagen, Copenhagen, Denmark.

[4]Laboratoire de Planétologie et Géodynamique, UMR6112 CNRS, Université de Nantes, Université Angers, Nantes, France.

[5]Department of Earth and Planetary Sciences, University of Tennessee, Knoxville, TN USA.

[6]AstrobiologyOU, School of Environment, Earth and Ecosystem Sciences, The Open University, Milton Keynes, United Kingdom

[7]Institut de Recherche en Astrophysique et Planétologie, Université de Toulouse, CNRS, CNES, Toulouse, France.

Published in Journal of Geophysical Research : Planets, June, 2020

DOI: https://doi.org/10.1029/2019JE006301

## Abstract

The NASA *Curiosity* rover's ChemCam instrument suite has detected boron in calcium-sulfate-filled fractures throughout the sedimentary strata of Gale crater including Vera Rubin ridge (VRR). The presence of elevated B concentration provides insights into Martian subsurface aqueous processes. In this study we extend the dataset of B in Ca-sulfate veins across Gale crater, comparing the detection frequency and relative abundances with Li. We report 33 new detections of B within veins analyzed between sols 1548 and 2311 where detections increase in Pettegrove Point and Jura members, which form VRR. The presence of B and Li in the Ca-sulfate veins is possibly due to dissolution of pre-existing B in clays of the bedrock by acids or neutral water and redistribution of the elements into the veins. Elevated frequency of B detection in veins of Gale crater correlate with presence of dehydration features such as desiccation cracks, altered clay minerals and detections of evaporites such as Mg-sulfates, chloride salts in the host rocks. The increased observations of B also coincide with decreased Li concentration in the veins (average Li concentration of veins drops by ~15 ppm). Boron and Li have varying solubilities and Li does not form salts as readily upon dehydration as B, causing it to remain in the solution. So, the weak negative correlation between B and Li may reflect the crystallization sequence during dehydration on Vera Rubin ridge.

## 1 Introduction

Boron is a light, soluble element that is found on Earth as borates in evaporite deposits and in clay-bearing sediments. The high solubility of B (as $B(OH)_3$ in acid and $B(OH)_4^-$ in alkaline water) makes it a good tool for understanding surface and sub-surface aqueous processes (Hunt, 1966; Lerman, 1966; Couch and Grim, 1968; Tanner, 2002; Helvaci and Ortí, 2004; Grew, 2017; Helvaci and Palmer, 2017). Characterization of borate phases enables the reconstruction of fluid temperature, salinity, and pH conditions in sedimentary systems (Frederickson and Reynolds, 1960; Lerman, 1966; Harder, 1970; Perry, 1972; Keren and Mezuman, 1981; Miranda-gasca *et al.*, 1998; Helvaci and Ortí, 2004).

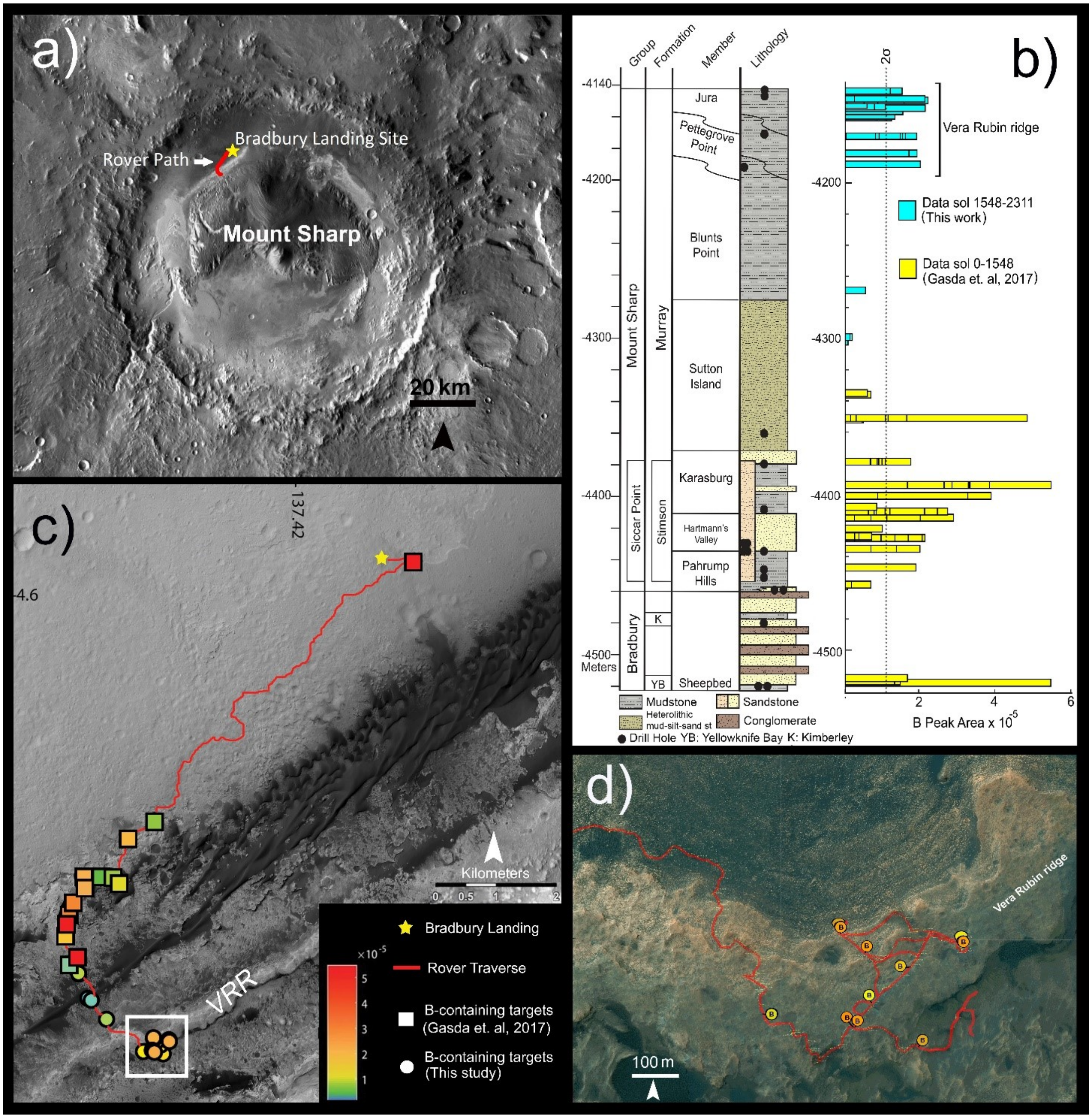

**Figure 1.** Overview of Curiosity's Gale Crater sampling area and summary of boron detections in the Vera Rubin ridge area. **a)** Gale Crater with red line indicating Curiosity's traverse from

Bradbury Landing site to the rover position on Sol 2052. **b)** Gale Crater stratigraphic column with normalized peak area for each boron detection plotted as bars versus elevation. **c)** The rover traverse map showing boron detection locations. Colors on the filled squares and circles represent the normalized boron peak area according to the color bar. **d)** MRO HiRISE image of Vera Rubin ridge indicating the boron detection locations with the same color scheme as shown in Figure 1C.

Borates can stabilize ribose, the simple sugar that forms the backbone of ribonucleic acid (RNA) (Kim *et al.*, 2011; Furukawa *et al.*, 2013; Furukawa and Kakegawa, 2017). Without borate ions, ribose decomposes in water within a geologically short time (ribose half-life is 300 days at 25°C and pH 7.0) (Larralde *et al.*, 1995). Although there are numerous hypotheses proposed for the origin of life (Ruiz-mirazo *et al.*, 2013), the most recent work on prebiotic chemical syntheses of RNA nucleotides proposes wet-dry cycles in the presence of salts like borates, nitrites, and carbonates, where boric acid is a reagent that assists in the reaction (Powner *et al.*, 2009; Becker *et al.*, 2016, 2019; Hud and Fialho, 2019). The NASA Curiosity rover detected B in 43 locations along its traverse in Gale crater (Gasda *et al.*, 2017). These observations, along with the recent discovery of organic molecules on Mars (Ming *et al.*, 2014; Eigenbrode *et al.*, 2018) and ribose in chondrites (Furukawa *et al.*, 2019) provide a basis for the possibility of prebiotic chemical reactions involving borates having occurred on Mars.

The Mars boron observations were made using the ChemCam instrument suite while targeting Ca-sulfate filled fractures or “veins”. Boron has been primarily detected in veins hosted in phyllosilicate-rich lacustrine Yellowknife Bay and Murray formation mudstones. The B enrichment likely occurred during a sequence of events that include initial deposition of B in evaporite layers in stratigraphically higher units, followed by later groundwater dissolution of the evaporites, transportation to underlying layers, and co-precipitation of borates in fractures along with Ca-sulfate (Gasda *et al.*, 2017). Concentrations of 154–166 ppm B have also been detected in clays within Martian meteorites (Stephenson *et al.*, 2013). While remote detection of borates is possible (e.g, Cloutis *et al.*, 2016), the authors are not aware of borate detections made by orbital remote sensing instruments or by other in situ Curiosity instruments such as CheMin. Evaporite elements including Cl, Na, and, S are detected on Mars using ground-based observations (Baird *et al*., 1976) (evaporite minerals including sulfates and chlorides detected from orbit :e.g., Glotch *et al.*, 2010; Ehlmann *et al.*, 2016), co-enrichments of Na and Cl observed with ground-based observations (Thomas *et al*., 2018, 2019; Rapin *et al*., 2019) and evaporite minerals including gypsum, anhydrite, bassanite, and chloride salts detected by CheMin (Vaniman *et al*., 2018; Morris *et al*., 2019; Thomas *et al.*, 2018, 2019). Based on the detection of these evaporites, we infer the possible presence of borate evaporites on Mars.

## 2 Geologic context

Gale crater is a ~155 km diameter impact crater with a central mound (Aeolis Mons, informally known as "Mt. Sharp") (Figure 1A), located in the northwestern part of the Aeolis quadrangle (Grotzinger and Milliken, 2012). In 2012, NASA's Mars Science Laboratory (MSL) *Curiosity* rover landed on Aeolis Palus. The rover has traversed ~22 km from the Bradbury Rise landing site, across outcrops of fluvio-lacustrine deposits (Grotzinger *et al.*, 2014, 2015; Vasavada *et al.*, 2014) and local eolian deposits (Banham *et al.*, 2018). The geology of Gale crater points to an ancient environment with a long duration water body that would have been habitable (Grotzinger *et al.*, 2015). A stratigraphic column depicting the sedimentary facies encountered is shown in Figure 1B. The first facies, belonging to the Bradbury group, is a fluvio-deltaic deposit exposed along the crater floor, interfingered with the Mount Sharp group (Grotzinger *et al.*, 2015). The deposits of this group include mudstones, sandstones, and conglomerates; low levels of chemical weathering suggesting a relatively cold climate and minimal water-rock interaction (McLennan *et al.*, 2014). The Mount Sharp group consists of the Murray formation, which is largely lacustrine in origin and shows more significant indications of chemical weathering (Mangold *et al.*, 2019). The Mount Sharp group also present features that are interpreted as lake margin and evaporitic environments (Kah *et al.,* 2018; Stein *et al.,* 2018; Rapin *et al.,* 2019). The Siccar Point group unconformably overlies the Murray formation of the Mount Sharp Group, and is interpreted as a younger deposit of basaltic eolian sandstone (Banham *et al.*, 2018; Siebach *et al.*, 2019).

## 2.1 Mount Sharp Group—Murray Formation

The Murray formation (Figure 1B) is currently divided into seven members (Fedo *et al.*, 2018; Siebach *et al.*, 2019), representing a series of lake deposits that experienced episodic drying. New members could be defined as the rover continues to move up-section from VRR. The Pahrump Hills member is interpreted to represent deposition by density-controlled river plumes in a freshwater lake (Stack *et al.*, 2018; Siebach *et al.*, 2019; Sun *et al.*, 2019) and shows the dominant presence of thinly laminated mudstones. The Hartmann's Valley member is interpreted to have formed in a fluvial environment based on the presence of meter-scale trough cross-bedding with steep foresets (Fedo *et al.*, 2018; Gwizd *et al.*, 2018; Siebach *et al.*, 2019). The Karasburg member is interpreted as lake deposits with some interbedded lake-margin facies (Siebach *et al.*, 2019). The Sutton Island member is made of heterolithic mudstone-sandstone (Fedo *et al.*, 2017; Siebach *et al.*, 2019). The Blunts Point member formed as low-energy suspension from fallout in a lacustrine environment (Siebach *et al.*, 2019). Episodic lake drying and desiccation caused by fluctuating lake levels are interpreted in Hartmann's Valley through the Sutton Island members based on altered clay minerals found in drill samples (Bristow *et al.*, 2018). Halite is identified in these members based on correlation between Na and Cl observations in the Quela drill target in the Karasburg member (Achilles *et al*., 2018; Thomas *et al.*, 2019). The Sutton Island member also shows the presence of dark-toned concretions and desiccation cracks indicative of wet-dry cycles associated with transient low lake levels (Sun *et al.*, 2018; Stein *et al.*, 2018; Haber *et al.*, 2019; Siebach *et al.*, 2019).

The Pettegrove Point and Jura members comprise Vera Rubin ridge (VRR; Fig. 1A), a nearly 250 m wide linear topographic feature that runs parallel to the northern foothill of the crater's peak, Mount Sharp, for nearly seven kilometers (Fraeman *et al.*, 2013, 2018). VRR was originally identified based on enhanced detections of hematite by the Compact Reconnaissance Imaging Spectrometer for Mars (CRISM) on the Mars Reconnaissance Orbiter (Fraeman *et al.*, 2013). The stratigraphic members of VRR, Pettegrove Point and Jura, are compositionally similar to lower Murray formation strata. However, VRR is erosionally more resistant compared to the underlying Murray members, resulting in the ridge formation (Edgar *et al.*, 2018; Fedo *et al.*, 2018; Fraeman *et al.*, 2018; Heydari *et al.*, 2018; Rivera-Hernández *et al.*, 2019; Siebach *et al.*, 2019). The boundary between the two members is not observed as a clear hiatus, leading to the interpretation that the morphological differences between the two members are likely due to secondary (diagenetic) processes.

VRR bedrock typically varies from bright to pale red or purple in color. These color differences may correspond to grain size (Johnson *et al.*, 2019). In situ images from the rover have shown that the topmost member of VRR (Jura), exhibits distinct color gradients. Decameter-scale gray patches are interspersed among the red bedrock, suggesting a possible redox relationship between these color units (Horgan *et al.*, 2019). The bulk chemical composition of VRR mudstones falls within the compositional range of Murray formation rocks, although there are variations in in situ geochemistry (Frydenvang *et al.*, 2019 and Thompson *et al.*, 2019). VRR rocks show an overall decrease in Chemical Index of Alteration (CIA; defined as the molar ratio of $Al_2O_3$ and the sum of $Al_2O_3$, CaO, $Na_2O$, and $K_2O$; Nesbitt and Young, 1982), strong decrease in Li content, an increase in MnO content near the contact between the Pettegrove Point and Jura members (Frydenvang *et al.*, 2019), and broadly elevated $Na_2O$ concentrations compared to the underlying Murray formation (Thompson et al., 2019). Diagenetic iron-rich features, including concretions and nodules, are also reported in VRR (L'Haridon et al., 2019; David *et al.*, 2019).

***Veins in the Murray Formation.*** Light- and dark-toned veins are observed across all members of the Murray formation and are found in complex associations with other diagenetic features (Gasda *et al.*, 2017; Nachon *et al.*, 2017; Fedo *et al.*, 2018; L'Haridon *et al.*, 2018; Stein *et al.*, 2018; Kronyak *et al.*, 2019; Siebach *et al.,* 2019; Sun *et al.*, 2019). Pahrump Hills shows the presence of light- and dark-toned veins throughout the stratigraphy (Nachon *et al.*, 2017; Kronyak *et al.*, 2019). The dark-toned veins enriched in Ca show the presence of fluorine and are interpreted as fluorite veins (Forni *et al.*, 2017, 2019; Nachon *et al.*, 2017). The light-toned veins are enriched in Ca and sulfur, and are interpreted as Ca-sulfate veins (Nachon *et al.*, 2017). Boron has been detected exclusively in light-toned Ca-rich veins and patches (Gasda *et al.,* 2017). Light-toned veins in Hartmann's Valley are encountered preferentially along vertical fractures within host rocks, frequently displaying central gaps within the veins and fibrous textures (L'Haridon *et al.*, 2018), but also displaying a concentration of Fe-rich and Mg-rich light-toned veins (L'Haridon *et al.*, 2018). The Karasburg member also shows the presence of light-toned Ca-rich veins (Gasda *et al.*, 2017) whereas the Sutton Island and Blunts Point members show the presence of abundant horizontal and sub-horizontal Ca-sulfate veins that are crosscutting finely laminated mudstone and are dispersed within concretionary bodies (Sun *et al.*, 2019; Rapin *et al.*, 2019).

## 3 Geochemistry of boron and lithium

### 3.1 Common borates and their formation conditions

B has a high affinity for oxygen and forms covalent boron-oxygen bonds in borates. On Earth, there are over 230 borate minerals present in the upper crust that originate by igneous, sedimentary, and metamorphic processes (Grew *et al.*, 2011; Grew, 2017). The type of borate formed is dictated by the amount of dissolved B in the solution and conditions including pH and temperature of the solution, degree of evaporation, the cations available in the fluid, and depth of burial of the borate formed (Christ *et al.*, 1967; Birsoy and Özbaş, 2012). Here we focus on evaporitic borate deposits as they are the most relevant to Gale crater.

Common evaporitic borate minerals include colemanite ($Ca_2B_6O_{11}\cdot 5H_2O$), borax ($Na_2O.2B_2O_3.10H_2O$), kernite ($Na_2O.2B_2O_3.4H_2O$), ulexite ($Na_2O.2CaO.5B_2O_3.16H_2O$), probertite ($Na_2O.2CaO.5B_2O_3.16H_2O$), and hydroboracite ($CaMgB_6O_8(OH)_6\cdot 3H_2O$). Figure S1 shows a flowchart indicating formation conditions of common borates, constructed based on thermodynamic stability diagrams and chemical compositions (Christ *et al.*, 1967; Birsoy and Özbaş, 2012). It shows the chemical compositions, major cation category, deposit types, formation locations, and structural subdivisions of the common borates found on Earth (Christ *et al.*,1967; Birsoy and Özbaş, 2012). Boron may also be present as ions in inclusion fluids within host crystals. Possible fluid inclusion phases associated with borates and boric acid are discussed in section S4 in the supporting material. Although high contents of B and Li are commonly associated with hydrothermal activity on Earth (Seyfried *et al.,* 1984), these elements can also be liberated from relatively low temperature weathering of typically felsic igneous rocks (Risacher and Fritz., 2009).

### 3.2 Substitution and adsorption of boron

In addition to forming borates, B is also commonly found adsorbed to clay minerals (Hingston, 1964; Keren *et al*., 1981; Keren and Mezuman, 1981; Keren and O'connor, 1982; Palmer *et al.*, 1987; Williams *et al.*, 2001) and amorphous materials (Biggar and Fireman, 1960; Bingham *et al*., 1971; Evans and Sparks, 2008; Abu-Sharar *et al.*, 2014; Goldberg, 1997; Goldberg *et al*., 1993; 2008). Borate ions can also substitute for other ions within minerals such as mica and illite (Stubican and Roy, 1962; Hingston, 1964, Couch and Grim, 1968), calcite, aragonite (Kitano *et al.,* 1978; Hemming *et al.*, 1995; Mavromatis *et al.*, 2015), and ettringite (a minor Ca-Al-Si sulfate solid solution hydrated evaporite mineral; Csetenyi and Glasser, 1993; Seryotkin *et al.*, 2018).

Under relatively low-temperature conditions, $B(OH)^-_4$ anions are adsorbed onto the frayed edges (where Si—O and Al—O bonds have broken leaving positively charged sites: Couch and Grim, 1968) and between the silica layers of clay minerals (Stubican and Roy, 1962; Couch and Grim, 1968). This adsorption is rapid and followed by a slower diffusion of B into the clay structure (Couch and Grim, 1968). Above 60°C, B atoms can substitute for aluminum (Stubican and Roy, 1962) in clay mineral lattices (Stubican and Roy, 1962; Hingston, 1964). At the temperature range of 60-120°C, smectites begin to collapse into illite, which allows boron-aluminum substitution in the clay lattice (Burst, 1957; Eberl and Hower, 1976; You *et al.*, 1996; Williams *et al*., 2001). The uptake of B within clay crystal structures depends on concentration, salinity of the solution, temperature, and interaction duration (Couch and Grim, 1968). Experiments show that B adsorption in clays and amorphous materials (and therefore the availability of B for incorporation into the mineral lattice) occur only in alkaline conditions (Keren *et al.*, 1981), at low temperatures (<120°C: Palmer *et al.*, 1987; Goldberg *et al.*, 1993; You *et al.*, 1996) and relatively high salinity (Lerman, 1966; Couch and Grim, 1968; Harder, 1970; Abu-Sharar *et al.*, 2014). Therefore, the two ways B can go into solution from clay and amorphous materials are: 1) in high-water rock ratio conditions where the adsorbed B on clay mineral surfaces can be dissolved by neutral to acidic fluids and 2) in acidic conditions where B is released from the clay lattice on dissolution of the clay itself.

### 3.3 Substitution and adsorption of lithium

Li is more soluble than B in water; Li does not form salts as readily upon dehydration (although Li carbonates [zabuyelite: Miangping *et al.*, 2000] and Li silicates [jadarite: Stanley *et al.*, 2007] are reported associated with evaporites in playas in China and Serbia) and remains in the brine as dehydration continues (Hamzaoui *et al.*, 2003). Overall, Li is a conservative element that stays in solution and does not form salts easily (Risacher and Fritz*.,* 2009). However, lithium is also commonly found adsorbed to or incorporated within the structure of terrestrial clay minerals (Greene-Kelly, 1955; Vine, *et al.*, 1980). The clays that adsorb Li on their surface and incorporate Li into their structures can be a notable source of Li (Vine and Dooley*,* 1980; Greene-Kelly, 1955). Similar to the behavior of B, high water-rock ratio can dissolve Li adsorbed on clay minerals due to the high solubility of Li and dissolution of clays in acids can quickly remove the Li from the clay structure (Dalton *et al.*, 2016; Huang and Keller, 1971; Hall, 1977; Simon and Anderson, 1990). Although Li is not a universal proxy for clay content on Mars, it can indicate a relative change in the amount of clays in Gale crater (Forni, *et al.*, 2015; Frydenvang *et al.*, 2019).

### 3.4 Terrestrial examples of B- and Li-rich brines

Although boron and lithium are predominantly associated with geothermal inputs on Earth (Li *et al*., 2019; Seyfried *et al.,* 1984), terrestrial brines can provide insight into B and Li systematics on Mars as the separation of the two elements in salt-forming environments appears to be common. In case of Gale crater, it is possible that the major water body and the groundwater was influenced by a hydrothermal system (or multiple systems) as large impacts produce long-lasting sources of heat below the surface, so Gale lake may have experienced early stage of hydrothermal activities (Schwenzer *et al.,* 2012). Systems with multiple sources of B and Li in a dry lake environment can act as an analog for better understanding the geochemistry of Gale crater.

Saline lake deposits on the Andean Plateaus show presence of B- and Li-bearing brines in internally drained, evaporative basins (Steinmetz, 2017). The brine composition is associated with local residual brines, solutions from weathered rocks, and parental lithology in addition to geothermal input (Steinmetz, 2017). However, the predominant sources of B in this case are reported to be inflow from residual brine and weathering of local rocks; in contrast, Li is associated with geothermal sources (Steinmetz, 2017). The evolutionary pathway of the evaporating water composition, in this case study, is interpreted to be determined by the extent of evaporation and the relative quantities of initial precipitated mineral phases such as calcite and sulfates (Steinmetz, 2017). Borates, sulfates and Li- and B-containing brines are reported in this region (Steinmetz, 2017). The brines contain up to 450 ppm of B and 125 ppm of Li (Steinmetz, 2017). Li-micas are also observed in this area; however, it is also stated these Li-micas are relatively rare findings in playa lake environments (Steinmetz, 2017).

The hyper-arid basins of Salar de Atacama in Chile also show the presence of Li- and B-rich brines in which the Li and B are determined to be sourced predominantly from varied locations of recharge corresponding to surrounding sub-watershed regions with possible geothermal inputs (Munk *et al.,* 2018). Mineral precipitation and brine evolution in this case study is also determined to be dependent on the composition of the source rocks, extent of brine mixing and evaporation (Munk *et al.,* 2018). Brines of Salar de Uyuni in the Southwest of the Bolivian Altiplano are also rich in Li and B (Haferburg *et al.,* 2017). These brines are slightly acidic to near-neutral pH with Li and B concentrations of up to 2000 and 1400 ppm (Haferburg *et al.,* 2017). The source of B and Li in this case is also attributed to leaching of ancient evaporite from the catchment area during the evolution of the basin (Risacher and Fritz, 1991) which acts as a good analog for one of the possible enrichment methods of B and Li into evaporite veins of Gale crater as discussed in this study in Section 6.

## 4 Methodology

### 4.1 Data collection and processing

The ChemCam instrument suite onboard the *Curiosity* rover consists of a laser induced breakdown spectroscopy (LIBS) instrument and remote micro-imager (RMI). The LIBS instrument provides atomic emission spectra of targets (up to seven meters standoff distance) by focusing a pulsed 1067 nm laser, with a 350–550 µm diameter spot size, creating a plasma from the ablated surface (Maurice *et al.*, 2012; Wiens *et al.*, 2012). Together with color images from the Mastcam imaging suite (Malin *et al.*, 2010) and Mars Hand Lens Imager (MAHLI; Edgett *et al.*, 2012), the RMI allows for visual identification of features and the geologic context for each observed point (Le Mouélic *et al.*, 2015). Sampling frequency is dependent on the rover's resources and its topographic accessibility to the sampling area. Although efforts are made to collect bedrock and diagenetic features, including veins, at each rover location, compared to sampling performed for chemostratigraphic studies on Earth, rover sample sets are less systematic. The Martian data interpretations are therefore subject to some sampling bias.

ChemCam data are acquired by lasing the area under investigation in either a linear or gridded array with a typical spacing of 1–2 mrad that spans approximately 15 mrad (Wiens *et al.*, 2015). Each ChemCam analysis point is typically hit by 30 laser pulses and average chemical compositions are calculated after discarding the data from the first five spectra due to the pervasive dust coating on the rocks (Wiens *et al.*, 2013; Clegg *et al.*, 2017). Major element concentrations of Ca sulfate veins and surrounding rocks are determined using multivariate analytical methods including partial least squares for the ChemCam spectra (Wiens *et al.*, 2013; Clegg *et al.*, 2017). Sulfur is not typically quantified by the ChemCam team, as its emission lines are weak in the spectral range covered by this instrument. Because of this, Ca-sulfates are identified by the presence of strong enrichments of Ca (e.g., > 20 wt. % CaO) along with the identification of a S peak. The calibration for B is described by Gasda *et al.,* (2017) with a limit of detection (LOD) of ~100 ppm. The calibration for Li is provided using a univariate model with an LOD of 5 ppm and root mean square error (RMSE) of 5 ppm (Payré *et al.*, 2017). The data used for plotting the Li concentrations can be found in the PDS Geosciences Node Data and Services repository (https://pds-geosciences.wustl.edu/missions/msl/chemcam.htm) and the corrected Li concentrations can be found in a Zenodo data repository (Das, 2020: http://doi.org/10.5281/zenodo.3877377). For boron, the presence of iron can limit detection. The majority of ChemCam targets contain >18 wt.% $FeO_T$ (Gasda *et al.*, 2017; Mangold *et al.,* 2017). ChemCam data shows unresolved neutral atomic B emission lines at 249.75 and 249.84 nm. An Fe II line interferes with the B feature at 249.96 nm (Sansonetti and Martin, 2005; Gasda *et al.,* 2017). Hence, B can only be detected in low-Fe targets, and so far, only in Ca-sulfate veins. New targets for this study were selected based on low Fe content of the target ($FeO_T$ < 13 wt%), reasonable total emission of the ChemCam spectra (>5 x $10^{13}$ photons), and targets within four meters. The B peak area (labeled on Figure 1B) is corrected for the expected peak area ±2σ uncertainty of the very weak Ca III emission line at 249.84 nm as determined by method blanks (described in supporting information document by Gasda *et al.*, 2017). The detection of B is determined by fitting the B and iron peaks in the feature and identifying targets with non-zero B peak areas after the calcium III correction. In Gasda *et al.* (2017), most of the targets have >3σ certainty of B detection.

### 4.2 Subtraction of bedrock component from Ca-sulfate veins

The LIBS laser often hits an area consisting of both bedrock and Ca-sulfate (Nachon *et al.*, 2014), resulting in a mixed composition (Figure S2.1). To understand the trends in soluble elements of the veins, the contribution of the bedrock must be removed from these mixed observations. The ratio between $SiO_2$ in the bedrock and veins is used to determine the percentage of bedrock contribution in these observations. For each vein or partial vein target, nearest bedrock targets are identified. The composition of a maximized number of nearest available bedrock targets are averaged to determine an average bedrock composition. The average bedrock composition for all the major oxides and Li is multiplied by the vein-observation-to-bedrock $SiO_2$ ratio and is then subtracted from the vein observation. The bedrock-subtracted vein compositions are then renormalized to an average oxide sum of an ‘ideal’ Ca-sulfate target to obtain the corrected oxide and Li values. This method has not been applied for B, as B cannot be measured in the bedrock due to the high $FeO_T$ content of the bedrock. The ideal Ca-sulfate targets are compositionally close to anhydrite (Table S2.1), and are chosen based on the lack of $SiO_2$, $Al_2O_3$ and $TiO_2$, as these elements are typically the least soluble in vein-forming fluids and therefore should not be present in pure Ca-sulfate veins. If the true composition of the veins is gypsum or bassanite (presence of bassanite veins has been confirmed in Gale crater by Rapin *et al.,* 2016 and Vaniman et al., 2018), this renormalization method may impart a small error to the data, increasing the absolute amount of Li detected in the veins by up to 8.5 rel.%, much less than the expected error due to uncertainty (Table S2.2). The relative amount of Li within a vein is expected to remain constant. Error is calculated using linear propagation of uncertainty (section S2) based on the RMSE accuracy of the major oxide model (Clegg *et al.,* 2009). Since a single bedrock point is used for error propagation rather than an average of points, this method is the most conservative method of estimating error. As more bedrock targets are averaged as part of the correction, the error is expected to decrease by the square root of the number of samples used to calculate the mean. More details about the correction method and error propagation can be found in section S2 in supporting information.

## 5 Results

Boron was detected in 21 new vein targets (after detections reported by Gasda *et al.,* 2017) with 33 single-point observations (with a range of one to four B observations per target). Boron concentrations in the 21 vein targets range between ~100-150 ppm, which is comparatively lower than the up to ~300 ppm detections in the lower units described by Gasda *et al.,* (2017). Table S3.1 lists the target names, analysis sol number, ChemCam observation point number, corrected B peak area, vein type, and the host unit names of all B-containing targets. Corrected Li concentration of all vein targets vary between 5 and 65 ppm; these results can be found in the supporting data file named “Corrected-Li-ppm.xlsx”. After correcting for rock content in the vein observations, Ti, Al, Fe, Na, K, Mg, Sr, Ba, and Rb concentrations are below the quantification limit for the targets.

### 5.1 Morphology of sulfate veins

On VRR, B is observed in both thick and thin veins and Ca-sulfate patches that are a few centimeters in width and irregular in shape (patches in some cases appear to be broken or partially exposed veins). Boron is found in veins that are more erosionally resistant than surrounding host rock as well as in veins exposed flush with the bedding plane surface (Figure 2C and D). A few thicker, patchy light-toned targets, possibly representing remnants of eroded veins, also show B presence (Figure 2E). Boron is detected in two different float rock targets (Figure 2F and G): Askival, which is a silicified feldspathic cumulate rock (Bridges *et al.*, 2019) with a Ca-sulfate rim (CaO abundance of 30.8 wt % and clear S emission peaks), and Blair Atholl, which is a Ca-rich (twice targeted with 34.7 and 33.6 wt. % CaO) light-toned float rock. These observations show that B is detected in light-toned veins with no preference for morphology or rock type.

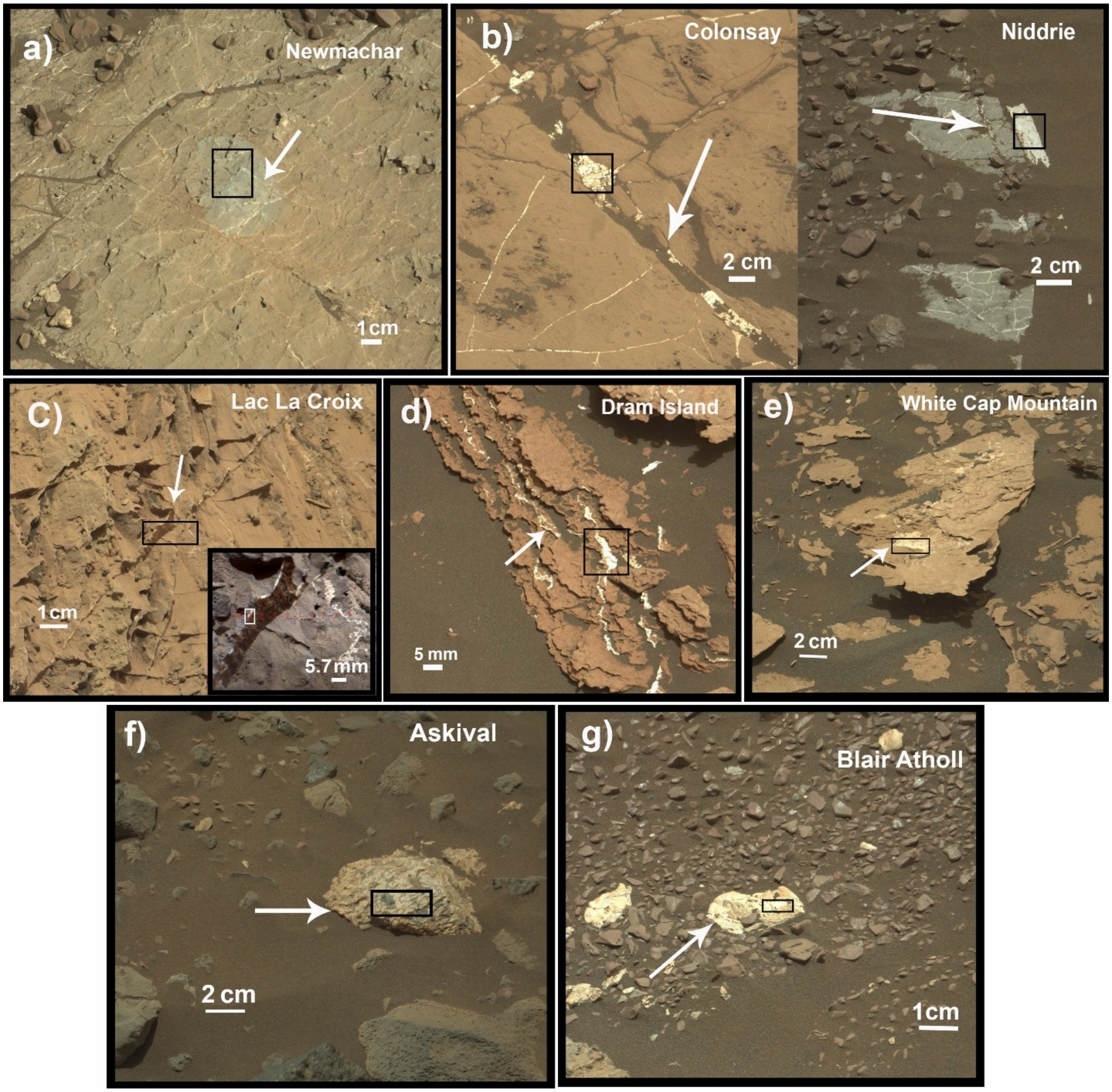

**Figure 2.** Morphologies of light-toned materials where boron has been observed in VRR. **a)** Thin veins cross-cutting each other in target Newmachar shown by white arrow (sol 1965 with B detected in point15). MastCam image ID 1965MR0102770000901670E01. **b)** Truncation of thin veins against thicker veins shown by white arrows in Colonsay (left, sol 2012 with B detection in point 6, MastCam image ID: 2012MR0105980000902590C00) and Niddrie (right, sol 2250 with

B detection in point 4 and 5 MastCam image ID: 2250MR0120360010106377C00). **c)** Erosionally resistant veins in Lac La Croix shown by white arrow (sol 2048 with B detection in point 9). MastCam image ID: 2048MR0108370000903354C00. **d)** Veins running across bedding planes in Dram Island shown by white arrow (sol 1641 with B detection in point 5). MastCam image ID: 1641MR0105920000903652C00. **e)** Patchy white toned material observed in target White Cap Mountain shown by white arrow (sol 1707 with B detection in point 5). MastCam image ID: 1707MR0089010000803320E01. **f)** Askival, a silicified feldspathic float rock shown by white arrow (sol 2015 with B detection in point 2). MastCam image ID: 2016MR0106360160902714C00. **g)** Blair Atholl, a Ca-rich light-toned float rock shown by white arrow (sol 2235 with B detection in point 2, 3, 4, and 5). MastCam image ID: 2235MR0118800000106144C00.

Figure 2B shows two sets of textural relationships where, based on the cross-cutting relationship, the veins hosting B appear to have formed in different fracturing events from surrounding veins. The target Colonsay in Figure 2B (left) shows that the vein hosting B is cross-cut by another vein in the top-left corner. The thinner veins on the bottom left truncate against the thicker, boron-containing vein. Although the exact sequence of vein formation is unknown, the cross-cutting vein on the top left corner likely formed after the one in the middle. In case of the target Niddrie, (Figure 2B right) a similar observation is made where the thinner veins in the left side truncate abruptly against the thicker vein. This occurrence may suggest that different fracture and fluid flow generations brought in fluids with varying composition and may add to the explanation of detecting B in only some spots, however, the absence of B detection does not indicate complete absence of B due to the ~100 ppm detection limit of boron. The cross-cutting features seen from the surface only provide a limited picture of the three-dimensional relationship of the veins under the surface.

Vein textures and crystal habits (Figure 3) can shed light on potential formation mechanisms and crystal growth histories. Tooth-like textures with a central discontinuity can be observed in the vein in Figure 3A and a fibrous habit of the white infill material can be observed in Figure 3B. Similar textures observed in veins in lower stratigraphic units have been interpreted to have formed by a repetitive fracture filling process called crack sealing (Hilgers and Urai, 2002; Kronyak *et al.*, 2019). In the targets Long Porcupine (Figure 4A) and Milton Ness (Figure 4B), light-toned veins contain variably sized dark-toned features within their matrix. For target Long Porcupine, two veins intersect each other orthogonally. Both veins have been analyzed, but only one vein shows the presence of B. A similar textural setting is observed in Figure 4B where the target shows multiple veins with varying morphologies. The B-containing vein (middle) shows the presence of small dark features (similar to features observed by L'Haridon *et al.*, 2019).

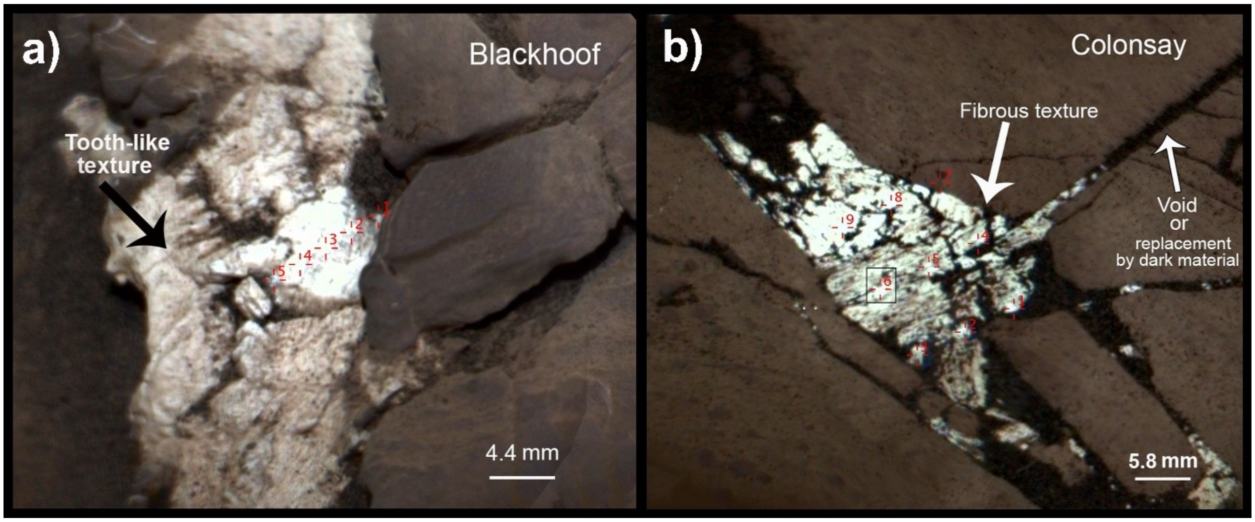

**Figure 3.** Vein textures observed by Remote Micro Imager. **a)** Tooth-like texture in target Blackhoof (sol 2045). Points 3 and 4 show presence of boron. MastCam image ID:

2045MR0108220020903332C00. (**b)** Fibrous texture visible within vein (sol 2012). Boron was detected in point 6. Darker material observed in sections of the thick and orthogonal thin veins may be a void formed by erosion of the vein or replacement by dark-toned features. MastCam image ID: 2012MR0105980000902590C00.

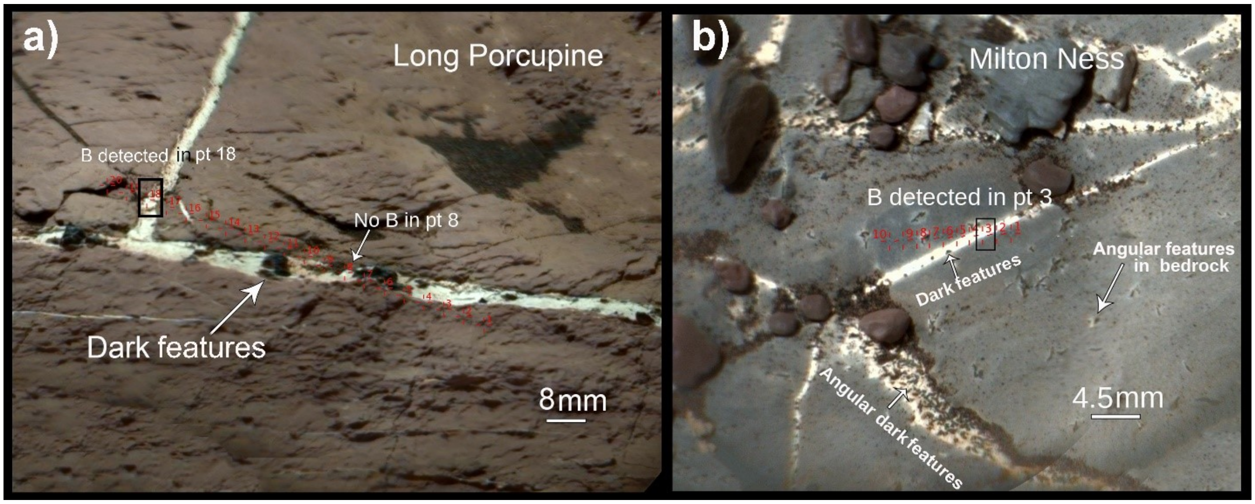

**Figure 4.** Veins containing dark features. **a)** Light toned veins in Long Porcupine (sol 1552) show an orthogonal intersection with dark-toned features in one side. MastCam image ID: 1552MR0079700000800082E01. **b)** Light-toned veins in Milton Ness (sol 2218) showing different densities and morphologies of dark-toned features. Angular features are also observed in the host bedrock of the veins. MastCam image ID: 2218MR0117520000105898C00.

The intersecting vein in the bottom left area also shows dark features but these are angular in shape and significantly higher in numbers. Angular features are also observed in the surrounding bedrock. However, the lack of B observation is not an indicator of the element’s absence; it may be present at a concentration just below the limit of detection.

### 5.2 Stratigraphic detections of boron and lithium in veins

Figure 5 shows bedrock-corrected Li concentrations of the Ca-sulfate veins (pink) compared to nearby bedrock (black). All errors described in this section, unless otherwise stated, are 2σ standard error. The corrected Li values in the veins below the contact between the Blunts Point and Pettegrove Point members (Li peak 1 between -4231m to -4221m in Figure 5) have an average of 21 ± 5 ppm. Values below the contact between Pettegrove Point and Jura members (Li peak 2 between -4191m to -4181m in Figure 5) have an average of 21 ± 5 ppm). Both locations have a significantly higher average of Li abundance than the average corrected Li abundance of all the veins in Gale crater (12 ± 2 ppm). Lithium has a significantly lower abundance in the veins of Jura member (with an average of 8 ± 2 ppm) compared to the veins in the peak Li locations in Pettegrove Point and Blunts Point, and slightly lower than the average Li concentration of all Gale veins (11 ± 2 ppm). The concentration of Li is relatively lower in the Jura bedrock with an average of 8 ± 1 ppm compared to the average Li concentration of all bedrock targets (average of 13.2 ± 0.3 ppm). The distribution of corrected Li values in the veins for each stratigraphic unit is statistically different from the distribution of the measured Li values of the surrounding bedrock (see section S2 in supplemental information for detailed discussion of error).

The stratigraphic units where ChemCam detected veins (>20 wt% CaO; <13 wt% $FeO_T$) and the frequency of B detections within vein targets is shown in Figure 6 and Table S3.2. Figure 1 shows B detections throughout the traverse beginning in Yellowknife Bay formation, but no detections in the remaining Bradbury group or lower Murray formation. B detections increase through the Pahrump Hills (7 detections), Hartmann's Valley (11 detections), and Karasburg (27 detections) members and decrease in the Sutton Island member (13 detections). Although veins were often targeted in the Blunts Point member, the B detection frequency decreases drastically (one target in this unit was below the 2σ threshold for detection). B detection frequency increases in the upper Pettegrove Point (11 detections) and Jura (16 detections) members. The detections appear to be concentrated toward higher elevations in VRR in the Jura member (between -4171 to -4142 m). The increased detections in Pettegrove Point and Jura members contrast in the detection frequency between the Blunts Point member and both VRR members.

Figure 6 also shows a comparison between B detection frequency and average corrected Li concentration of the veins. This plot shows high Li concentration of the veins is only observed at units with low B detection frequency across the rover's traverse. This potential link between Li concentration of the veins and relative B peak area is further illustrated in Figure 7. Figure 7A shows the B observation frequency every 10 m elevation and possibly has a weak inverse relationship with the corrected Li concentration of the veins. Figure 7B shows a similarly weak inverse relationship between relative B peak areas averaged over every 10 m elevation and the average corrected Li concentration of the veins. A curve defined by power law ($f(x) = Ax^B$) is fitted through both scatter plots and illustrates the potential relationship (e.g., that of a phase change, whereas one element leaves solution through crystallization, and the other is concentrated in the brine) between the two elements. The $R^2$ values suggests the relationship between B and Li weakly follows the power law. These fitted curves are only for illustrative purpose as they are constructed using only non-zero data. Hence, the power law relationship shown in Figure 7 does not fully describe the system. The 2σ Spearman's correlation coefficient between B observation frequency and average Li concentration of veins per 10 m is -0.53 and between B average peak area and Li concentration of veins per 10 m is -0.48. These values indicate a weak negative correlation between B observation and average Li concentration of veins and between B average peak area and Li concentration of veins per 10 m. In summary, the relationship between Li and B is weak in the limited dataset and a power law relationship only partially describe the system; chemical modeling of all the trace elements is likely required to build a full picture of the groundwater system in VRR.

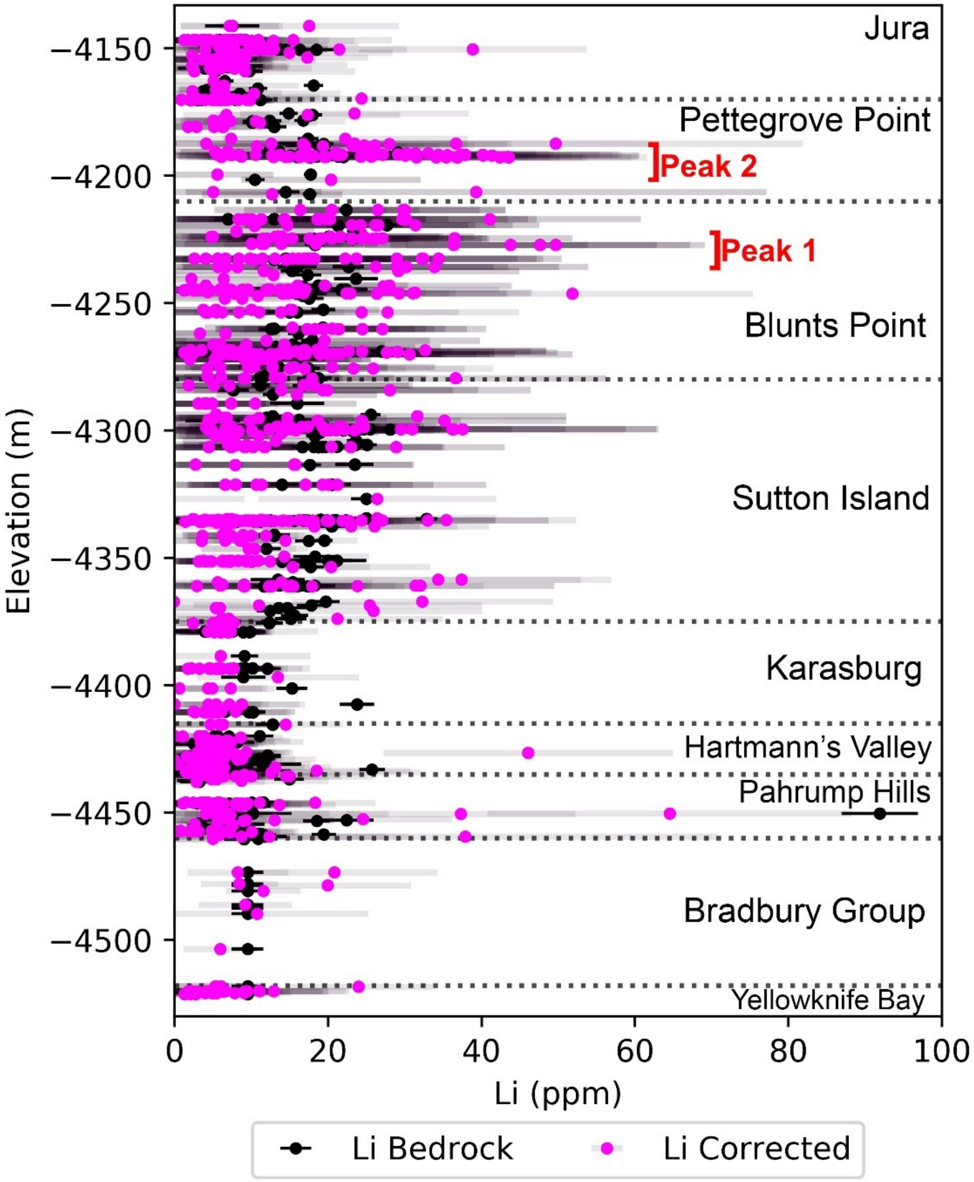

**Figure 5.** Plot showing the corrected Li concentration of the high-Ca veins against elevation, compared with the Li concentration of the surrounding bedrock. Pink filled circles show the corrected Li concentration of the veins. Black filled circles show the Li concentration of the surrounding bedrock. Locations with increased concentration of Li are visible right below the contact between Blunts Point and Pettegrove Point members (Peak 1) and below the contact between Pettegrove Point and Jura members (Peak 2). Errors propagated during the correction

calculations are shown as grey bars. Errors associated with the original vein and bedrock compositions are shown as thin black bars.

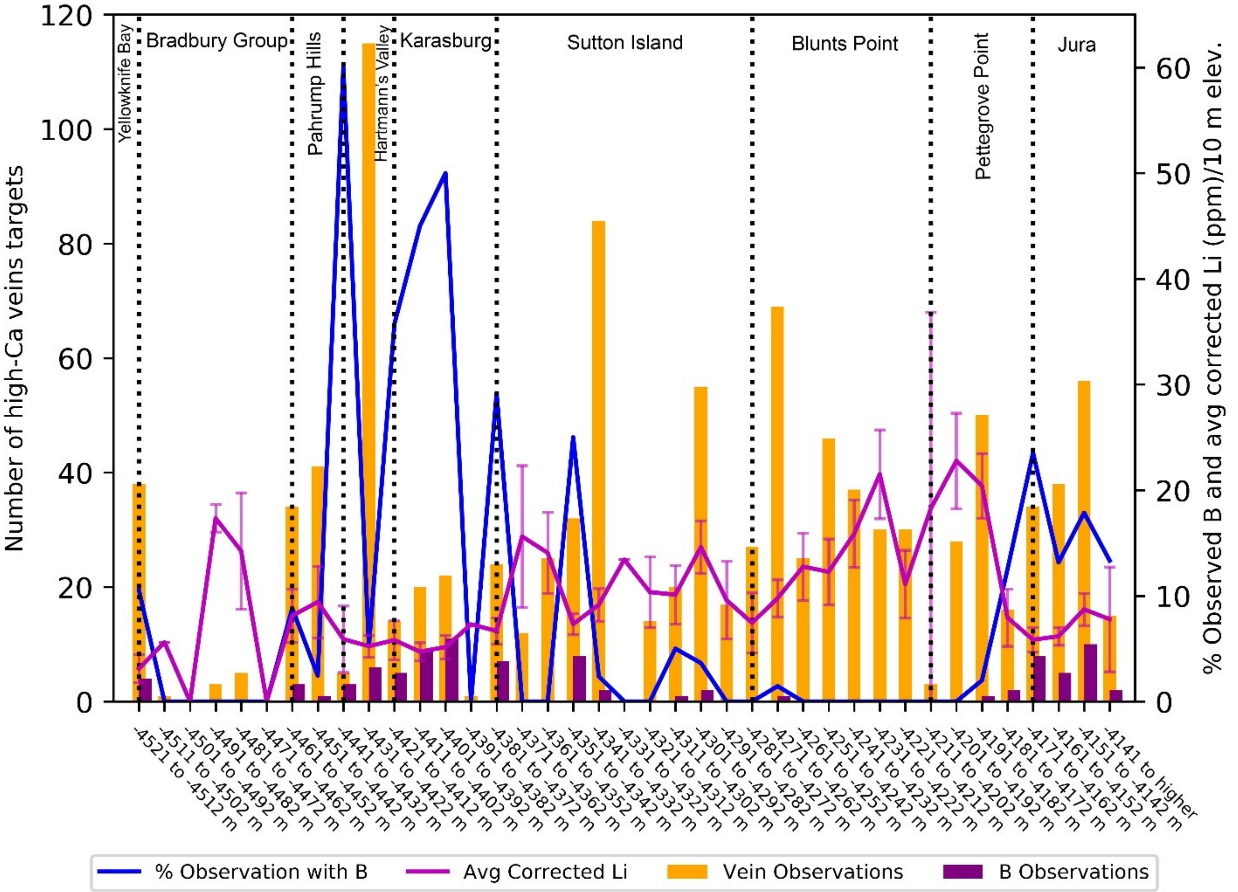

**Figure 6.** Histogram showing the distribution of Ca-rich veins in Gale Crater throughout Curiosity's traverse (sols 0—2311), frequency of Ca-rich veins with boron, and comparison of Li concentration of veins with relative frequency of boron detections in veins. The orange bars show the number of Ca-rich (>20 wt% Ca) targets (left axis) in intervals every 10 m elevation (horizontal axis). The purple bars show the number of Ca-rich veins containing boron. The blue line indicates the percentage of veins with boron out of all analyzed veins at that elevation (right axis). The average corrected Li concentrations of the veins are plotted as a magenta line (right axis) and 2σ standard errors bars are shown. The vertical dotted lines separate the different

stratigraphic units of Gale Crater. The units shown are the Bradbury group and members of the Murray formation. Yellowknife Bay formation is a part of the Bradbury group, but it is shown separately because of the boron observations made there. Ca-rich veins occurred much less frequently in the rest of the Bradbury group, with no boron observations. Comparison of the pink and blue lines in the plot indicates a negative correlation between the frequency of B detection in the veins and the concentration of Li.

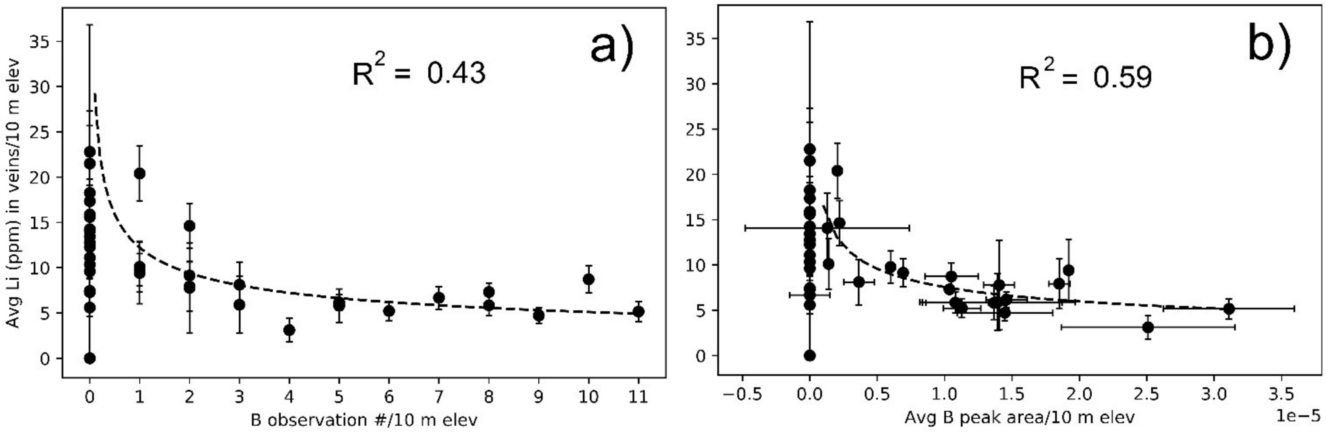

**Figure 7.** Average corrected Li concentration of the veins with B detection frequency and average B peak areas with 2σ standard error bars. a) A weak inverse correlation between B detection frequency every 10 m elevation (x-axis) and the average Li concentration of the veins (y-axis) with an $R^2$ value of 0.43. The Spearman's correlation coefficient between B observations frequency and average Li concentration of veins per 10 m is -0.5. b) A weak inverse correlation, illustrated by the black dashed power law curve based on non-zero data points, between B peak areas averaged over 10 m elevation bins (x-axis: the B peak area average values are of the order of magnitude ~$10^{-5}$ which is shown as 1e-5 on the right end of the x-axis of this plot) and average Li concentration of the veins (y-axis), with an $R^2$ value of 0.59. The Spearman's correlation coefficient between B average peak area and Li concentration of veins

per 10 m is -0.48. For Figure 7B, the average B peak areas shown at zero are below the detection limit. In some cases, where the average peak areas are more than zero, but error bars cannot be seen, the error bars are smaller than the plotted data points.

## 6 Discussion

### 6. 1 Relationship of boron and lithium in calcium-sulfate veins

We see no direct evidence that indicates the exact sequence of events that resulted in B and Li enrichment in veins of VRR. We hypothesize a possible sequence of events in Gale crater based on observations made on Earth and supporting observations made in Gale crater. The sequence of events discussed in the following sections is only one of the possible pathways and at this stage without geochemical models to support them, provide a useful working hypothesis but are speculative at best.

In addition to B, the Ca-sulfate veins show the presence and variation in concentration of another fluid mobile element: Li. The boron-containing Ca-sulfate veins show an increase in Li in Sutton Island, Blunts Point, and lower Pettegrove Point members (Figure 6) but a decrease in veins of upper Pettegrove Point and Jura members. Figures 6 and 7 show that with increase in frequency and relative abundance of B, the abundance of Li in the veins decreases. This relationship could partially be a result of preferential separation of B from Li during precipitation of borates based on the power law fitted to data in Figure 7. In the case of a brine, with increasing dehydration, Li remains in the brine as other salts precipitate out due to the conservative nature of Li (Risacher and Fritz., 2009; Hamzaoui *et al*., 2003). In Gale crater, progressive dehydration of the groundwater would cause B to precipitate as a borate, leaving Li in the brine. The remnant Li-rich brine may have moved down gradient from the borate-bearing veins along VRR (refer to elevations in Figures 6 and 7), producing the observed spatial and stratal separation of the elements.

The Li patterns of the veins across the stratigraphy of Gale crater do not follow the Li concentration patterns of the surrounding bedrock (Figure 5). The average corrected Li concentration in the veins is relatively low in the lower Murray members (Pahrump and Hartmann's Valley) and begins increasing in mid-Murray members (Karasburg, Sutton Island and Blunts Point) with a sharp drop in the Pettegrove Point member (Figure 6). This pattern of Li concentration corresponds to an opposite pattern in the detection frequency of B across the traverse. Members with low Li concentration (Pahrump and Hartmann's Valley in lower Murray; upper Pettegrove Point and Jura in upper Murray) correspond to a higher detection frequency of B in the veins and members with high Li (Murray members: Karasburg, Sutton Island and Blunts Point) correspond to low detection frequency. For example, in the upper elevations of Pettegrove Point (Figure 6) a sharp drop in Li concentration is observed over the same elevation range as a sharp increase in the number of B detections.

This inverse correlation of Li concentration of veins and B detection frequency could possibly reflect a classic progression of evaporation based on relative solubilities of Li and B (Dalton *et al.*, 2016). Li exists in solution commonly as Li ions; however, it can precipitate as Li chloride when the solution reaches saturation with respect to Li. Li chloride is two orders of magnitude more soluble than B in solution as boric acid at 0°C (Dalton *et al.*, 2016).

Terrestrial studies show that Li is adsorbed to clays (Greene-kelly, 1955; Starkey, 1982) and although it is not a universal proxy for clay content, it can be is used as an indicator of relative clay amount across VRR. The lower levels of Li in the bedrock (Frydenvang *et al.*, 2019) suggest reduced clay content in the Jura member. This is confirmed by the relatively low abundances of phyllosilicates detected in VRR bedrock compared to surrounding units by X-ray diffraction with the CheMin instrument (Bristow *et al.*, 2018; Rampe e*t al.*, 2019). As discussed in Section 3.2 and 3.3, B and Li adsorbed to clays can be incorporated into the clay structure as well as adsorbed by on clay surfaces (Frederickson and Reynolds, 1960; Lerman, 1966; Harder, 1970; Perry, 1972; Karahan *et al.*, 2006), although B cannot be detected in the clay-rich bedrock due to its $FeO_T$ content and interference with the B measurements (Gasda *et al.*, 2017). Boron and lithium can only be re-mobilized from clays through two ways: 1) adsorbed B and Li on clay mineral surfaces can be dissolved by neutral to acidic fluids in high water-rock ratio conditions; 2) boron and lithium trapped within clay lattice can be only be released into solution through dissolution of the host clay minerals. Enrichment of B and Li in Ca-sulfate veins after recirculation of fluids may have been a result of varying degrees of both these processes. In Figure 7, we observe only a weak correlation between B and Li, which may suggest that more than one process may have been responsible for the enrichment of B and Li.

Within the host bedrock, Li is reported to follow the morphology of the ridge rather than the elevation and is observed to be elevated in the Sutton Island, plateauing in the upper Sutton Island, decreasing towards Blunts Point, increasing again in the upper Blunts Point and strongly decreasing in the mid-Pettegrove Point to Jura members (Frydenvang *et al.*, 2019). In the Jura member, the Li concentration of both bedrock and veins drops significantly (Figures 6 and 7). However, the drop in Li concentration of the veins and the bedrock are likely caused by different factors. Notably, in terrestrial borate rich evaporites such as salars in the Bolivian and Chilean Andes (Risacher and Fritz, 2009), Li remains in the brine while B-salts precipitate. Thus, the Li concentration of veins might reflect the extent of dehydration of the diagenetic fluids beyond the solubility of Li-salts, while the Li concentration of the bedrock is controlled by the clay content of the bedrock.

## 6.2 Possible timing and mechanism of boron and lithium emplacement

### 6.2.1 Murray sections below VRR

In specific locations of the Murray formation, B is detected in light-toned Ca-sulfate veins. The frequency of B detection does not correlate with the frequency of Ca-sulfate targets analyzed throughout the upper Murray formation, so there is no fixed percentage of B in the veins. As discussed in Gasda *et al.* (2017), it is possible that later groundwater fluids remobilized pre-existing unobserved local B-rich evaporite layers in the immediate vicinity while they were circulating through the cracks in the Murray to form the Ca-sulfate veins and eventually redeposit the dissolved B as isolated borate grains in crevices of the veins located close to the primary evaporites. Based on the observation of truncating veins (Figure 2), fibrous and tooth like textures of vein fillings (or cements) (Figure 3), and veins containing dark features (Figure 4), it may also be interpreted that veins formed in multiple stages. More than one fluid flow event could have occurred, moving fluids through the cracks with varying compositions as (as is interpreted for veins with similar morphologies; Kronyak *et al*., 2019; L'Haridon *et al*., 2019). These events, which may have taken place as stratally isolated events, may have cause differences in fluid conditions between veins and the diversity of lithology through which the veins have formed. These differences may be responsible for the variation of the frequency of B occurrence and its concentration.

Other studies of Ca-sulfate veins and clay minerals in lower Murray members (Pahrump Hills, Hartmann's Valley, and Karasburg) suggest an upper temperature limit of ~60°C (Nachon *et al.*, 2014, 2017; Vaniman *et al*., 2014; Schwenzer *et al.*, 2016; Rapin *et al.*, 2016) which suggests that the extent of burial depth in these members is relatively minimal. With minimal burial depths, the formation of initial borate phases that require higher temperature and pressure for their formation can be ruled out.

Increased frequency of B detection in the lower Murray (members Pahrump Hills, Hartmann's Valley, and Karasburg, and the lowest strata of Sutton Island) may point towards the initial availability of B-rich evaporites in the bedrock. Increased frequency of B detection correlates with the detection of chloride salts (eg. Forni *et al.*, 2017; Thomas *et al*., 2019), Mg sulfates (Rapin *et al.,* 2019), the presence of desiccation cracks (Stein *et al.*, 2018), and altered clay minerals (Bristow *et al.*, 2018). These occurrences suggest elevated evaporation and support the possibility of pre-existing B-rich evaporites in the bedrock. The lack of observation of the B in upper strata of Sutton Island may suggest that the fluids which emplaced the B in veins were short lived relative to the timescales of diffusion and circulation rates of borate in the groundwater. The decrease of B detections upslope into the Sutton Island member may represent the water table level at the time of B emplacement. No evidence for these local B-rich evaporites in the bedrock have been found yet, however it may be possible that these evaporite layers were very thin, resembling a crust (Lowenstein *et al.*, 1985), and may have completely dissolved and been carried away by fluids during the remobilization process. (Borates and associated temperatures are shown in Figure S1; borate phases in Ca-sulfate veins of Gale crater are discussed in section S4.)

### 6.2.2 VRR

Vera Rubin ridge was initially deposited in a lacustrine setting as evidenced by its thin laminations similar to the Blunts Point unit, which later underwent secondary complex sets of diagenetic events (Edgar *et al.*, 2018; Fedo *et al.*, 2018; Fraeman *et al.*, 2018; Heydari *et al.*, 2018; Rivera-Hernández *et al.*, 2019; Siebach *et al.*, 2019). Presence of minerals such as jarosite and akageneite in VRR suggest that the fluids associated with the diagenetic events may have been acidic (Morris, *et al.*, 2019; Rampe, *et al.*, 2019). Our hypothesis, explained below, is that these diagenetic events may have mobilized B and Li out of clays in the VRR host rocks. A later set of groundwater events took place after the lithification and fracturing of VRR bedrock caused formation of Ca-sulfate veins (Nachon *et al.*, 2017; Kronyak *et al.*, 2019; Sun *et al.*, 2019). This fluid flow event may have recirculated previously liberated B and Li from the clay minerals into the Ca-sulfate veins in VRR, and our second hypothesis is that the B and Li became separated from each other during the last stages of calcium sulfate precipitation and groundwater desication. The stages and timing between the initial set of diagentic events that altered VRR and the later fluid flow events that formed the sulfate veins are unknown.

The observations of the sedimentary facies of VRR suggest that, prior to the diagenetic fluid events that altered it, VRR was chemically and mineralogically very similar to other lacustrine Murray sediments (Fedo *et al*., 2018; Siebach *et al*., 2019). Hence, much like the lower Pahrump Hills region, very little B was likely present within the groundwater prior to the diagenetic event that altered VRR. Directly below VRR, the Blunts Point member unit does not show any evidence of a lake margin or evaporitic environment; rather, it shows evidence of a low-energy lacustrine environment. The lack of other evidence such as desiccation cracks, altered clay minerals, or evaporitic materials (e.g., chloride salts: Thomas *et al.*, 2019) is consistent with a lake rather than a lake-margin environment. While Pettegrove Point and Jura also show increased presence of chlorides (Thomas *et al.*, 2019), these observations might be explained by alteration of the bedrock minerals during the diagenetic event, resulting in formation of Cl-rich crystalline akaganeite in upper VRR (Rampe *et al.,* 2019), rather than pre-existing layers of evaporites. Moreover, both members of VRR and the Blunts Point member also show evidence of a low-energy lacustrine environment (Fedo *et al*., 2018; Siebach *et al*., 2019) which makes it difficult to explain the presence of primary boron-rich evaporites. Therefore, we suggest there is not enough evidence for evaporites near Blunts Point or VRR to be the source of the boron. Rather, the evidence points to B likely being sourced from the surrounding rocks during the diagenetic event.

Results from the X-ray diffraction instrument CheMin indicate the presence of gray hematite, ferripyrophyllite, and opal-CT, suggesting that the diagenetic fluids were warm; the presence of minerals jarosite and crystalline akaganeite observed in two drill holes in VRR suggest that the fluids were acidic (Morris, *et al*., 2019; Rampe, *et al*., 2019) at least at one point in time. Note that acidic events also might be later in time than circumneutral diagenesis, based on the age dating of the Mojave2 drill core sample at Pahrump Hills (Martin *et al.,* 2017). The lack of depletion of soluble major elements argues against a strong or prolonged acid interaction (Frydenvang *et al*., 2019), but might indicate an ion-exchange process through contact with a saline fluid (e.g., Nir *et al.,* 1986; Gast *et al.,* 1971). The presence of warm and (at least briefly) acidic conditions on higher elevations of VRR would explain the decrease in clay content, as acids are known to readily dissolve clay minerals (Huang and Keller*,* 1971; Hall, 1977; Simon and Anderson, 1990). The exact timing of the first set of diagenetic events at VRR and the Ca-sulfate vein forming events and the relationship between the two events is unknown, however, it is known that Ca-sulfate vein formation took place after the lithification of the Stimson formation (e.g., Frydenvang *et al.,* 2019). Boron and lithium were possibly deposited in the Ca-sulfate veins during the second set of fluid circulation events and the relative solubilities of the elements defined the sequence of mineral precipitation and evaporite formation in the veins. Calcium sulfate is one order of magnitude lower in solubility than boric acid (sassolite) and sodium tetraborate hexahydrate (borax), and three orders of magnitude lower than solubility of Li chloride at 0°C (Dalton *et al.*, 2016). Calcium sulfate begins to crystallize at fluid temperatures as high as 40°C-60°C and will continue crystallizing at lower temperatures (Hardie, 1967). After extensive crystallization of calcium sulfates, the water-to-rock ratio is expected to decrease, which would cause the resultant fluid to be rich in more soluble elements such as B, Li, and Cl. As the fluid evaporates further, B would crystallize as borate salts, while Li would remain in solution due to its inherent higher solubility even at low temperatures (Dalton *et al.*, 2016). Sodium and chlorine precipitate as chloride salts after borates. The acidic environment in Jura (Morris, *et al.*, 2019; Rampe *et al.*, 2019) may have affected the type of borate that crystallizes out of the diagenetic fluids in Gale crater. On Earth, sassolite, a borate that forms in acidic environments, is reported in dry lakes of Southern California (Allen and Kramer, 1957; Smith *et al.*, 1958). Therefore, it is possible that sassolite may have formed as a secondary borate in acidic conditions on VRR (Figure S1). After the crystallization of borates, the remaining fluid is still expected to contain Li as it does not form salts easily. The remaining Li-rich fluid would have moved down gradient to the underlying stratigraphic units (peaks 1 and 2 labeled in Figure 5) and pooled on top of impermeable layers. This brine is unlikely to move through lower layers due its extremely low water to rock ratio. This sequence of events is one potential explanation for the separation between B and Li after prolonged dehydration of the brine resulting after Ca-sulfate formation. In summary, VRR started out similar to the underlying lacustrine Murray units; however, VRR underwent a diagenetic event altering its mineralogy and chemistry. This diagenetic event possibly liberated both B and Li from clay minerals in VRR. A later fluid flow event may have remobilized the B and Li and deposited them into fractures along with Ca-sulfate. The separation in B and Li would result due to differences in solubilities of the two elements and movement of the brine within VRR.

### 6.3 Possible alternative models

Well crystallized akageneite forms from the hydrolysis of Fe3+ in Cl-bearing solutions under acidic pH (Refait and Genin, 1997; Remazeilles and Refait, 2007; Zhao *et al*., 2012; Peretyazhko *et al*., 2016; 2018). Although the presence of jarosite and crystalline akaganeite indicate an acidic environment, mobilization of iron oxide in VRR could be suggestive of slightly alkaline and reducing fluids (L'Haridon *et al*., 2018; David *et al*., 2019). Because of this, a significant possibility is that different generations of fluids could have had different pH values. Another possibility is that the boron found in the veins in and around VRR was not sourced locally. Boron has been observed over the 22 km of the rover's traverse (Gasda *et al.*, 2017). In that case, acidic ground water need not be invoked to leach the boron out of the phyllosilicates locally. Instead, this step could have occurred elsewhere, although at least mildly acidic fluids would aid in transporting the boron in solution to its precipitation sites within VRR. All of these possibilities are consistent with the extensive diagenetic activity for which there is evidence at VRR. To narrow down the above-mentioned possibilities, studies of terrestrial analogues as well as geochemical modeling for Martian aqueous solutions are required.

## 7 Conclusions

We report 33 new B detections in Ca-sulfate veins between sols 1548 and 2052. An increase of B detections is observed in Pahrump Hills, Hartmann's Valley, and Karasburg and in VRR (upper Pettegrove Point and Jura members). Boron detection frequency and its relative peak area show a weak inverse correlation with corrected Li concentration of the veins. This weak inverse correlation between B and Li is observed across the stratigraphy of Gale crater and may reflect the crystallization sequence from the diagenetic fluid as a result of end-stage dehydration of evaporative brines. Boron detection in the Murray members below VRR may be caused by remobilization of B from pre-existing borate evaporites into the Ca-sulfate rich late-stage veins by groundwater. The presence of pre-existing thin layers of borates is inferred based on evidence of elevated dehydration (e.g, desiccation cracks and chlorides) during emplacement the bedrock. The presence of minerals such as crystalline akageneite and jarosite in VRR indicate that at least one pulse of warm and acidic diagenetic fluid altered the VRR bedrock. We hypothesize that B and Li were drawn out of the bedrock due to dissolution of clay minerals by the diagenetic fluids rather than by remobilization of pre-existing evaporites in VRR. However, another possibility is that these materials originated from a more distant source. The weak inverse relationship of B with Li may result from the different solubilities of the elements, but more work is needed in the form of chemical modeling to fully tease out the relationship between these two elements in the groundwater. B is less soluble than Li and easily crystallizes out of the fluid as borates while Li remains in the fluid. The increase in Li in the late-stage diagenetic features may be a snapshot of the last vestiges of liquid diagenetic fluid flowing through rocks of VRR. This study of B and Li contributes to our understanding of the diagenetic and dehydration history of VRR and how it may have influenced the geochemistry and habitability of Gale crater.

The geochemistry of late-stage diagenetic features of Gale crater suggests that the subsurface environment was likely conducive for key prebiotic chemical reactions. Gale crater has undergone multiple episodes of groundwater activity throughout its history with changing Eh, pH, temperatures, and redox conditions (Nachon et al., 2014; Lanza et al., 2016; Hurowitz et al., 2017; Frydenvang et al., 2019; L'Haridon et al., 2019). This changing diagenetic environment could have, at some point in its history, been suitable for reactions between borates and organic molecules (Eigenbrode et al., 2018; ten Kate, 2018) present in Gale crater. Li and B-rich brines in Andean salars show the presence of diverse microbial communities and indicate that hypersaline brines can be habitable (Haferburg et al., 2017). If borate-organic molecules are detected in Gale crater, they would provide insights on the possibility of life on Mars and origin of life on Earth. Like other elements important for life (e.g., CHNOPS), searching for B on Mars is a high priority for understanding its past aqueous and habitable history.

## 8 Supporting information

The following is a supporting information that includes formation parameters of various borate phases, common borates and their type localities (Section S1), data correction steps for lithium concentration of veins (Section S2), data sets including relative boron abundances indicated by peak areas and detection frequency of boron in calcium sulfate veins (Section S3), and possible borate phases in calcium sulfate veins of Gale crater (Section S4).

### Section S1 Common borates and their formation

The largest economic deposits of borates are found in Turkey, South America, and United States of America, in tectonically-active extensional terrains and associated with continental sediments and volcanic soils (Helvaci, 1977; Kistler and Helvaci, 1994; Tanner, 2002; Birsoy and Osbas, 2012). Major borates found on Earth, their chemical formulas, deposit types, formation locations, and structural subdivisions are reported in Table S1. The number of common borates is relatively small, and they are often found in compositional series, with one or two predominant phases in the deposit. A few common borates occur as thermodynamically metastable phases (e.g., tincalconite or meyerhoffite) (Helvaci, 1977; Kistler and Helvaci, 1994; Tanner, 2002; Birsoy and Osbas, 2012). Some borates (e.g., Inyoite) are thermodynamically stable yet form kinetically slower than others and are not found as commonly (Birsoy and Osbas, 2012). The relative abundance of various types of borates can be represented by the area of their stability field in an equilibrium activity diagram and depends on the availability of cations, pH, temperature and pressure conditions (Birsoy and Osbas, 2012). Geologically, only a few borates are common and ones that are rare can form at very limited thermodynamic conditions. These borates and can be seen to occupy small to no areas in their stability (e.g., tertschite, inderborite, ulexite, akasite, gowerite) (Birsoy and Osbas, 2012). Diagenetic processes are also responsible for the formation of a few structurally complex borate phases such as pandermite, ginorite, ascharite and suanite (Christ *et al*., 1967; Birsoy and Osbas, 2012). These phases form after less complex precursor minerals undergo diagenesis due to burial and increase of temperature (Birsoy and Osbas, 2012). Extent of diagenetic process is also controlled by concentration of cations and B, pH, evaporation rate, pressure and temperature (Birsoy and Osbas, 2012). Figure S1 shows a flowchart indicating formation conditions of common borates and is constructed based on the thermodynamic stability diagrams and chemical compositions (Christ *et al*., 1967; Birsoy and Osbas, 2012).

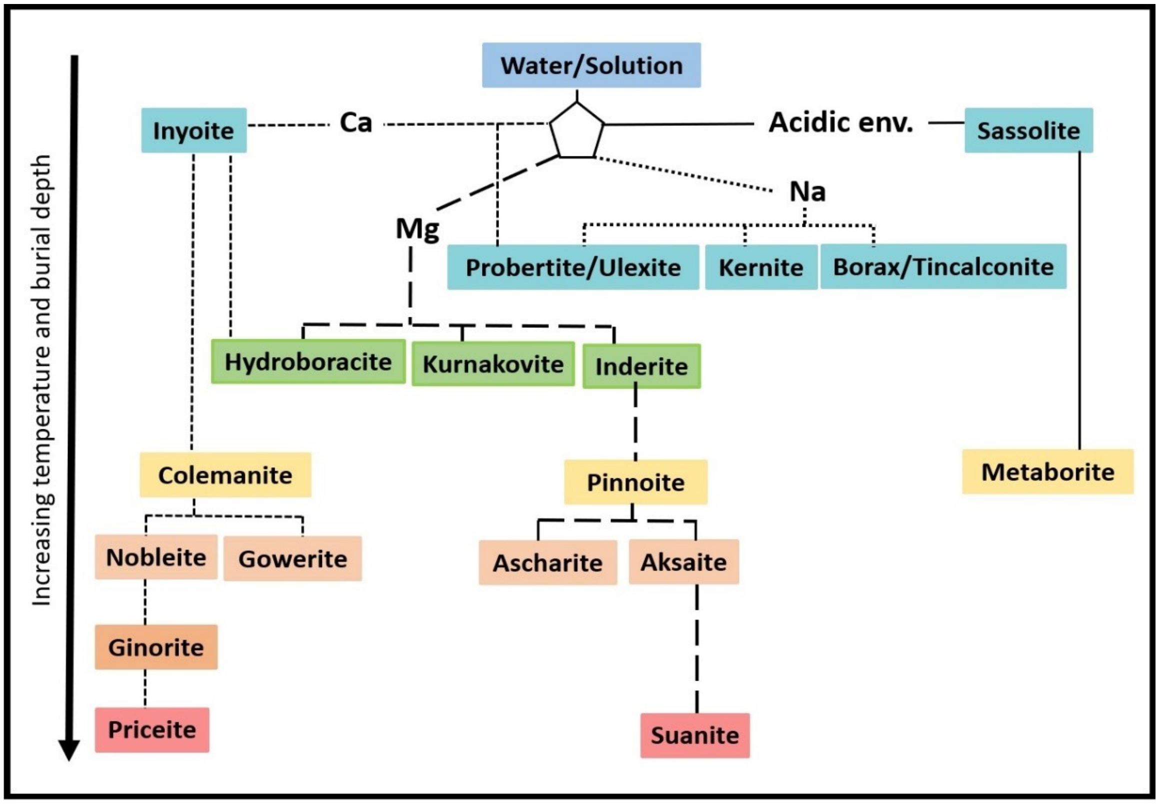

**Figure S1**. Flow chart showing common borate phases on Earth and their formation conditions (cation availability, temperature, pressure, and pH conditions). Based on borate thermodynamic stability diagrams shown by (Christ *et al*., 1967; Birsoy and Osbas, 2012).

**Table S1** Major borates, formulas, deposit types, locations, and structural subdivisions.

| Borate | Formula | Cation | Types of deposits | Example locations | Structural subdivision | Ref |
|---|---|---|---|---|---|---|
| Metaborite | $B_2O_3{\bullet}H_2O$ |  | Playa | Atyrau (Kazakhstan) | Tecto-megaborate | 1 |
| Sassolite | $B_2O_3{\bullet}3H_2O$ |  | Volcanic lagoon | Kramer (USA), Lardarello (Italy) | Isolated-monoborate | 2 |
|  |  |  |  |  |  |  |
| Kernite | $Na_2[B_4O_6(OH)_2]{\bullet}3H_2O$ | Na | Playa surface, lacustrine | Kramer (USA), Loma Blanca (Argentina), Kirka (Turkey) | Ino-borate | 1, 3-9 |
| Tincalconite | $Na_2B_4O_7{\bullet}5H_2O$ |  | Lacustrine | Kramer (USA), Dujiali (Tibet) | Neso-tetraborate | 3-9 |
| Borax | $Na_2[B_4O_5(OH)_4]{\bullet}8H_2O$ |  | Playa surface, Lacustrine | Kramer (USA), Kirka (Turkey), Tincalayu (Argentina), Quinghai (China) | Neso-tetraborate | 1, 3-11 |
|  |  |  |  |  |  |  |
| Priceite | $Ca_2B_5O_7(OH)_5{\bullet}H_2O$ | Ca | Playa lake | Sultancayiri (Turkey) | Unclassified | 3-9 |
| Colemanite | $Ca_2B_6O_{11}{\bullet}5H_2O$ |  | Playa, lacustrine, marine | Kramer (USA), Sijes (Argentina), Kirka, Emet, Bigadic, Kestelek (Turkey) | Ino-triborate | 3-13 |
| Meyerhofferite | $Ca_2(H_3B_3O_7)_2{\bullet}4H_2O$ |  | Playa, lacustrine | Kirka, Emet (Turkey), Kramer (USA) | Neso-triborate | 3-9 |
| Inyoite | $Ca(H_4B_2O_7)(OH){\bullet}4H_2O$ |  | Playa surface, lacustrine | Kirka (Turkey), Kramer (USA), Tincalayu (Argentina), Salinas (Peru) | Neso-triborate | 3-10 |
| Nobleite | $CaB_6O_9(OH)_2{\bullet}3H_2O$ |  | Lacustrine | Sijes (Argentina) | Phyllo-hexaborate | 3-9 |
| Gowerite | $Ca[B_5O_8(OH)][B(OH)_3]{\bullet}3H_2O$ |  | Lacustrine | Sijes (Argentina) | Phyllo-pentaborate | 3-9 |

| | | | | | | |
|---|---|---|---|---|---|---|
| Ginorite | $Ca_2B_{14}O_{20}(OH)_6 \cdot 5H_2O$ | | Playa | Salar de Atacama (Chile) | Phyllo-hexaborate | 3-9 |
| | | | | | | |
| Inderite | $MgB_3O_3(OH)_5 \cdot 5H_2O$ | Mg | Playa surface, lacustrine | Kirka (Turkey), Sijes (Argentina) | Neso-triborate | 3-9 |
| Kurnakovite | $MgB_3O_3(OH)_5 \cdot 5H_2O$ | | Playa surface, lacustrine<br>sulfate | Kirka (Turkey), Loma Blana, Tincalayu (Argentina), Zakang-caka (Tibet) | Neso-triborate | 3-9 |
| Pinnoite | $Mg[B_2O(OH)]$ | | Playa | Zakang caka (Tibet), Qinghai (China) | Neso-diborate | 3-9 |
| Aksaite | $Mg[B_6O_7(OH)_6] \cdot 2H_2O$ | | Buried deposit | Liaoning (China), Atyrau (Kazakhstan) | Neso-hexaborate | 1 |
| Ascharite | $MgBO_2(OH)$ | | Buried deposit | Liaoning (China), Atyrau (Kazakhstan) | Neso-diborate | 3-12 |
| Suanite | $Mg_2[B_2O_5]$ | | Buried deposit | Liaoning (China), Atyrau (Kazakhstan) | Neso-diborate | 3-13 |
| | | | | | | |
| Ulexite,<br>Probertite | $NaCa[B_5O_6(OH)_6] \cdot 5H_2O$ | Ca, Na | Playa surface, playa, lacustrine,<br>sulfate | Kirka (Turkey), Kramer (USA), Sijes, Tincalayu, Loma Blanca (Argentina), Salinas (Peru), Nieer-Co (Tibet) | Neso-pentaborate | 3-13 |
| Hydroboracite | $CaMg[B_3O_4(OH)_3]_2 \cdot 3H_2O$ | Ca, Mg | Playa, lacustrine, marine | Sijes (Argentina), Atyrau (Kazakhstan) | Ino-triborate | 3-13 |

1. Birsoy and Osbas (2012); 2. Kistler and Smith (1983); 3. Meixner (1965); 4. Inan *et al.* (1973); 5. Helvacı *et al.* (1993); 6. Palmer and Helvacı (1995); 7. Helvacı and Orti (1998); 8. Siefke (1991); 9. Kistler and Helvacı (1994); 10. Garrett (1998); 11. Smith (1979); 12. Helvacı and Alaca (1991); 13. Helvacı and Orti (1998).

## Section S2 Subtraction of bedrock contribution from Ca-sulfate vein compositions

Targets that are high in Ca may not be pure Ca-sulfates but a mixture of bedrock and Ca-sulfate. Figure S2.1 shows a plot of Li and $SiO_2$ concentration of all the high Ca-targets (>20 wt % Ca) measured in Gale crater from sol 0-2311. This plot shows that $SiO_2$ content of veins targets in some cases is as high as ~60 wt%. $SiO_2$ forms a positive correlation with the Li concentration of the veins with an $R^2$ value of 0.4. This indicates that the Li concentration of the veins is affected by the bedrock contribution. In order to subtract this contribution, $SiO_2$ of the veins is used as a proxy for calculating the percentage of bedrock concentration in the veins. The $SiO_2$ wt% of the vein is used for calculating the percentage of 'bedrock contribution' in the vein by dividing the vein $SiO_2$ wt% by the $SiO_2$ wt% of the surrounding bedrock and multiplying by 100. i.e:

$$\%\text{ Bedrock contribution in veins} = \frac{\text{SiO2 wt\%vein}}{\text{SiO2 wt\%surrounding bedrock}} \times 100.$$

This percentage is considered to be the 'bedrock contribution' for all elements and the bedrock contribution percentage is subtracted accordingly from each element. After the subtraction, the compositions were scaled up to average oxide sum of an 'ideal' Ca-sulfate composition in order to obtain the corrected oxide and Li values. The ideal Ca-sulfate targets are chosen based on the lack of $SiO_2$, $Al_2O_3$ and $TiO_2$ as these elements are typically insoluble in water under the conditions that likely formed these veins. The compositions of the ideal Ca-sulfate targets are shown in section Table S2.1. Figure S2.2 shows that the correction method is not influenced by the bedrock in a way such that the lithium concentration of the veins shows a similar pattern as that bedrock. The plot shows no correlation between lithium concentration of the veins and the surrounding bedrock ($R^2 = 0.02$) indicating that the lithium concentration of the veins is independent of the bedrock.

Errors on all elements during the correction calculations are calculated based on linear propagation of uncertainty. Errors for rover measurement are reported as RMSEP (Root Mean Square Error of Prediction) which is equivalent to 1σ error. While determining the bedrock percentage contributions and subtraction of the bedrock contribution from each element, the errors are linearly propagated and are still equivalent to 1σ error.

The errors propagated during the correction calculations are shown as grey bars and errors associated with the original vein and bedrock compositions are shown as black bars for Li in Figure 7 in the main paper. We performed an analysis of the error propagation for different cases of CaO content and Li vein and bedrock content. Table S 2.2 shows the results for each case in terms of relative error. For CaO content, we chose veins with 20, 25, 31, and 45 wt% CaO and compared to one nearby bedrock point. For each of these veins, we considered 6 different cases: Li vein >> Li bedrock, Li vein > Li bedrock (high values of Li), Li vein > Li bedrock (low values of Li), Li vein < Li bedrock (high values of Li), Li vein < Li bedrock (low values of Li), Li vein << Li bedrock. When relative error is >100% in Table S 2.2, the value is italicized. Table S 2.2 shows that, for all cases with high CaO wt%, the relative error on the Li is <100%. Generally, as the Li vein: bedrock ratio decreases, error increases. Additionally, as the value of Li decreases, error increases (the error on Li is 5 ppm; Payré *et al*., 2017). In some cases, as CaO < 30 wt%, relative error on the Li increases > 100%. For example, when Li values are low and in the 25 wt% CaO case, the relative error is >100%. For 20 wt% CaO, relative error will be >100% except when the Li in the vein is much higher than the bedrock composition. Therefore, we cannot correct veins with less than 20 wt% CaO, as the error are all expected to be >100%. Note that here we are propagating error based on the estimated accuracy of the major oxide model described in Clegg *et al*., (2017). This is the most conservative method of estimating error for these targets. As more bedrock targets are averaged as part of the correction, the error decreases by the square root of the number of samples used to calculate the mean.

**Comparison of Li distribution using Student's t-test:** The Li distribution in the two peak regions (Peak 1 and 2 in Figure 5) are statistically different compared to the Li distribution of all other veins measured in Gale crater determined using a Student's t-test (t-test values: Peak 1- 6.8, Peak 2- 6.3). The t-test values represent statistical similarity between the distribution of corrected Li veins and bedrock Li concentrations. All t-test values higher than the critical value at a confidence level of 95% indicate that the two distributions are statistically dissimilar. The t-test values for the test between the corrected vein Li and the surrounding bedrock Li concentration for each stratigraphic unit are as follows. Yellowknife Bay- 7.3, Bradbury group- 1.7, Pahrump hills- 3.4, Hartmann's Valley- 12.6, Karasburg- 19.14, Sutton Island- 11.2, Blunts Point- 1.97, Pettegrove Point- 3.4, Jura- 2.6. T-test values for all stratigraphic units except Bradbury group are higher that the critical value (1.96) determined at 95% confidence level. T-test value for Bradbury group is due to low number of veins analyzed in the unit (n = 10) and most likely does not represent statistical similarity between the corrected Li in veins and the Li distribution of the bedrock. The t-test values are lower in higher elevation units Blunts Point, Pettegrove Point and Jura compared to lower elevation units Hartmann's Valley, Karasburg, and Sutton Island.

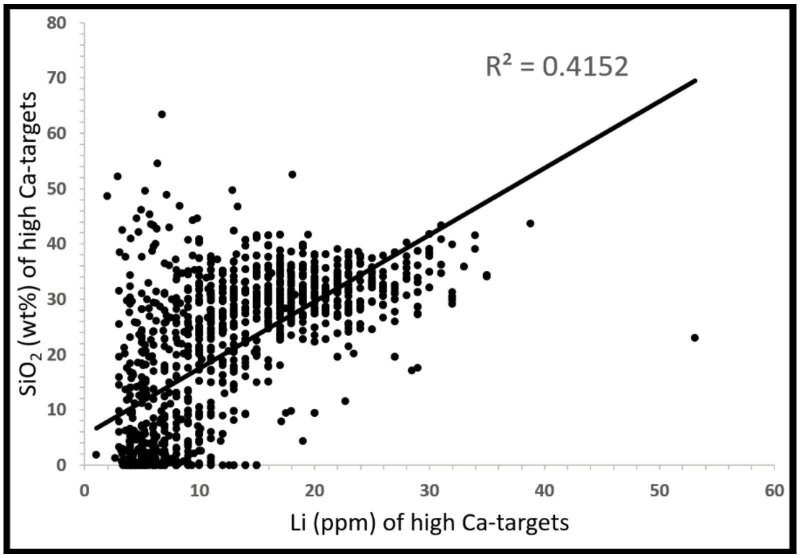

**Figure S2.1** Plot showing a positive correlation between wt% $SiO_2$ and Li concentration of the veins ($R^2$ value 0.415) indicating contribution of bedrock in the veins. The x-axis shows Li concentration of the veins (ppm) and the y-axis shows the wt% $SiO_2$ content of the veins.

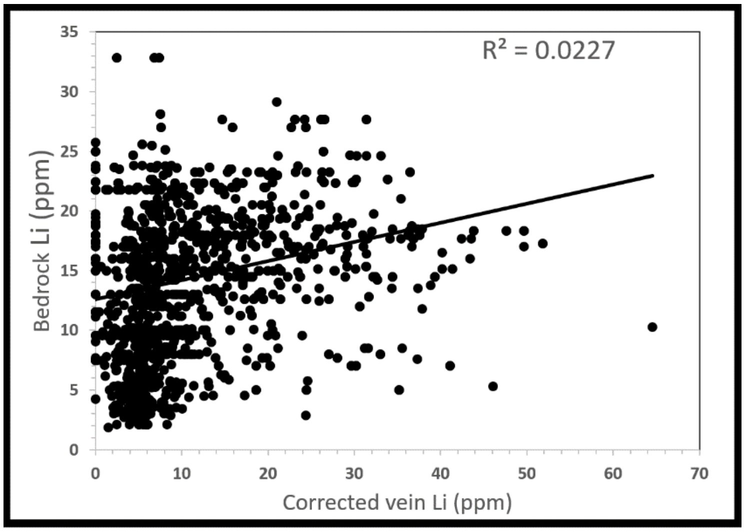

**Figure S2.2.** Comparing corrected Li concentration values of the veins with the bedrock Li concentrations. The x-axis shows corrected Li concentrations of the veins in ppm and the y-axis shows the Li concentration of the bedrock in ppm. There is no correlation between the corrected Li values (seen by the low $R^2$ value of 0.022) of the veins.

**Table S2.1:** Ideal Ca-sulfate composition calculated by averaging the compositions of three high-Ca targets with 0 wt% $SiO_2$, $TiO_2$, and $Al_2O_3$.

| **Target** | Sol | $SiO_2$ wt% | $TiO_2$ wt% | $Al_2O_3$ wt% | $FeO_T$ wt% | MgO wt% | CaO wt% | $Na_2O$ wt% | $K_2O$ wt% | Ba ppm | Li ppm | MnO wt% | Rb ppm | Sr ppm |
|---|---|---|---|---|---|---|---|---|---|---|---|---|---|---|
| Charlottenf-elder | 1360 | 0 | 0 | 0 | 0 | 0.5 | 43.7 | 0.07 | 0 | 2.36 | 4 | 0 | 0 | 107 |
| Biljim | 1749 | 0 | 0 | 0 | 0 | 0.5 | 44 | 0.05 | 0 | 0 | 5 | 0 | 0 | 24 |
| Biljim | 1749 | 0 | 0 | 0 | 0 | 0.5 | 44 | 0.05 | 0 | 0 | 5 | 0 | 0 | 24 |
| Avg | | 0 | 0 | 0 | 0 | 0.5 | 43.9 | 0.056 | 0 | 0.78 | 4.5 | 0 | 0 | 51.7 |

**Table S2.2:** Analysis of the error propagation for different cases of CaO content and Li vein and bedrock content.

| Wt% CaO | Li vein (ppm) | Li bedrock (ppm) | Li vein:bedrock ratio | Relative error (%) |
|---|---|---|---|---|
| 20 | 50 | 15 | 3.33 | 85 |
| 20 | 15 | 14 | 1.07 | 333 |
| 20 | 46 | 45 | 1.02 | 111 |
| 20 | 45 | 46 | 0.98 | 120 |
| 20 | 14 | 15 | 0.93 | 266 |
| 20 | 15 | 50 | 0.3 | 107 |
| 25 | 50 | 15 | 3.33 | 74 |
| 25 | 15 | 14 | 1.07 | 97 |
| 25 | 46 | 45 | 1.02 | 79 |
| 25 | 45 | 46 | 0.98 | 80 |
| 25 | 14 | 15 | 0.93 | 107 |
| 25 | 15 | 50 | 0.3 | 179 |

| | | | | |
|---|---|---|---|---|
| 31 | 50 | 15 | 3.33 | 44 |
| 31 | 15 | 14 | 1.07 | 56 |
| 31 | 46 | 45 | 1.02 | 46 |
| 31 | 45 | 46 | 0.98 | 46 |
| 31 | 14 | 15 | 0.93 | 57 |
| 31 | 15 | 50 | 0.3 | 71 |
| 45 | 50 | 15 | 3.33 | 41 |
| 45 | 15 | 14 | 1.07 | 53 |
| 45 | 46 | 45 | 1.02 | 43 |
| 45 | 45 | 46 | 0.98 | 55 |
| 45 | 14 | 15 | 0.93 | 57 |
| 45 | 15 | 50 | 0.3 | 68 |

## Section S3 Boron detection in Ca-sulfate veins of Gale crater

Although various types of vein filling materials are reported in the Murray formation (Nachon *et al*., 2017; Kronyak *et al*., 2019), for example; light-toned veins, grey raised ridges with varying Mg- and Ca- enrichments, and dark-toned veins), B has been detected exclusively in light-toned Ca-rich veins and patches out of the targets analyzed between sols 1 to 2311. Boron is detected in 21 new vein targets with a total of 33-point observations (with a range of one to four B observations per target). Table S3.1 lists the target names, analysis sol number, ChemCam observation point number, corrected B peak area, vein type and the host unit names of all targets with good peak fits. Table S3.2 shows the number of Ca-rich veins analyzed with ChemCam and the number of B detections made within them for every 10 m elevation range in different stratigraphic units encountered throughout the rover's traverse.

**Table S3.1:** Targets that show presence of boron in them in the Murray formation in Gale crater.

| | Target | Sol | Pt # | Corrected B Peak area | Vein type | Unit |
|---|---|---|---|---|---|---|
| 1 | Peaks Island | 1664 | 2 | 2.51E-06 | Irregular patch | Sutton Island |
| 2 | Peaks Island | 1664 | 4 | 1.90E-06 | Irregular patch | Sutton Island |
| 3 | Long Porcupine | 1552 | 18 | 6.49E-06 | Thin linear (~4mm) | Sutton Island |
| 4 | Dram Island | 1641 | 5 | 1.39E-06 | Patchy thin along beds | Sutton Island |
| 5 | White Cap Mt. | 1707 | 5 | 5.99E-06 | Patchy irregular | Blunts Point |
| 6 | Third White Ash | 1893 | 1 | 8.99E-06 | Thick block (~20mmx2cm) | Grey Jura |
| 7 | Third White Ash | 1893 | 2 | 1.28E-05 | Thick block (~20mmx2cm) | Grey Jura |
| 8 | Newmachar | 1965 | 15 | 2.24E-05 | Thin curvilinear (~1mm) | Grey Jura |
| 9 | Fingals Cave | 1995 | 5 | 1.58E-05 | Irregular blocky patch | Grey Jura |
| 10 | Colonsay | 2012 | 6 | 1.37E-05 | Fibrous thick (~7mm) | Red Jura |
| 11 | Askival | 2015 | 2 | 2.17E-05 | Vein in float rock | Float rock |
| 12 | Blackhoof | 2045 | 3 | 1.96E-05 | Thick curvilinear (~ 9mm) | Pettegrove Pt |
| 13 | Blackhoof | 2045 | 4 | 1.74E-05 | Thick curvilinear (~ 9mm) | Pettegrove Pt |
| 14 | Lac La Croix | 2048 | 9 | 2.04E-05 | Raised thin fin (~2 mm) | Pettegrove Pt |
| 15 | Driesh | 2097 | 4 | 1.51E-05 | Thick curvilinear (~20mm) | Pettegrove Pt |
| 16 | Driesh | 2097 | 6 | 1.65E-05 | Thick curvilinear (~20mm) | Pettegrove Pt |
| 17 | Foinaven | 2130 | 10 | 9.22E-07 | Thick curved (~10 mm) | Pettegrove Pt |
| 18 | Portnahaven | 2146 | 9 | 1.57E-05 | Thick curvilinear (~25mm) | Pettegrove Pt |
| 19 | Portnahaven | 2146 | 10 | 1.94E-05 | Thick curvilinear (~25mm) | Pettegrove Pt |
| 20 | Loch Aline | 2149 | 4 | 6.43E-07 | Thick curvilinear (~15mm) | Pettegrove Pt |
| 21 | Loch Aline | 2149 | 8 | 8.56E-06 | Thick curvilinear (~25mm) | Pettegrove Pt |
| 22 | Laig Bay | 2152 | 5 | 9.54E-06 | Irregular blocky patch | Pettegrove Pt |
| 23 | Milton Ness | 2218 | 3 | 6.36E-06 | Thin linear (~1mm) | Grey Jura |
| 24 | Housay | 2219 | 1 | 1.12E-05 | Dispersed patches | Grey Jura |
| 25 | Housay | 2219 | 4 | 8.35E-06 | Dispersed patches | Grey Jura |
| 26 | Blair Atholl | 2235 | 2 | 5.56E-06 | Light toned float rock | Float rock |
| 27 | Blair Atholl | 2235 | 3 | 1.14E-06 | Light toned float rock | Float rock |
| 28 | Blair Atholl | 2235 | 4 | 9.25E-06 | Light toned float rock | Float rock |

|  |  |  |  |  |  |  |
|---|---|---|---|---|---|---|
| 29 | Blair Atholl | 2235 | 5 | 1.61E-05 | Light toned float rock | Float rock |
| 30 | Niddrie | 2250 | 4 | 2.16E-05 | Thick block (~10 x 30 mm) | Red Jura |
| 31 | Niddrie | 2250 | 5 | 3.05E-06 | Thick block (~10 x 30mm) | Red Jura |
| 32 | Garvock | 2306 | 2 | 1.25E-05 | Angular irregular patch | Red Jura |
| 33 | Garvock | 2306 | 3 | 1.56E-05 | Angular irregular patch | Red Jura |

**Table S3.2** Number of calcium sulfate veins and observed boron in various stratigraphic units of Gale Crater

| Stratigraphic Unit | Interval | Veins # | Total veins # | B obs | Total B obs | % of veins w/B |
|---|---|---|---|---|---|---|
| Yellowknife Bay | - 4521 to - 4512 m | 38 | 38 | 4 | 4 | 11 |
| Bradbury fm | - 4511 to - 4502 m | 1 | 10 | 0 | 0 | 0 |
| Bradbury fm | - 4501 to - 4492 m | 0 |  | 0 |  | 0 |
| Bradbury fm | - 4491 to - 4482 m | 3 |  | 0 |  | 0 |
| Bradbury fm | - 4481 to - 4472 m | 5 |  | 0 |  | 0 |
| Bradbury fm | - 4471 to - 4462 m | 0 |  | 0 |  | 0 |
| Pahrump | - 4461 to - 4452 m | 34 | 79 | 3 | 4 | 9 |
| Pahrump | - 4451 to - 4442 m | 41 |  | 1 |  | 2 |
| Pahrump | - 4441 to - 4432 m | 4 |  | 0 |  | 0 |
| Hartmanns Valley | - 4431 to - 4422 m | 115 | 129 | 6 | 11 | 5 |
| Hartmanns Valley | - 4421 to - 4412 m | 14 |  | 5 |  | 36 |
| Karasburg | - 4411 to - 4402 m | 20 | 67 | 9 | 28 | 45 |
| Karasburg | - 4401 to - 4392 m | 22 |  | 11 |  | 50 |
| Karasburg | - 4391 to - 4382 m | 1 |  | 0 |  | 0 |
| Karasburg | - 4381 to - 4372 m | 24 |  | 7 |  | 29 |
| Sutton Island | - 4375 to - 4362 m | 12 | 259 | 0 | 13 | 0 |
| Sutton Island | - 4361 to - 4352 m | 25 |  | 0 |  | 0 |
| Sutton Island | - 4351 to - 4342 m | 32 |  | 9 |  | 28 |
| Sutton Island | - 4341 to - 4332 m | 84 |  | 1 |  | 1 |
| Sutton Island | - 4331 to - 4322 m | 0 |  | 0 |  | 0 |
| Sutton Island | - 4321 to - 4312 m | 14 |  | 0 |  | 0 |

| | | | | | | |
|---|---|---|---|---|---|---|
| Sutton Island | - 4311 to - 4302 m | 20 | | 1 | | 5 |
| Sutton Island | - 4301 to - 4292 m | 55 | | 2 | | 4 |
| Sutton Island | - 4291 to - 4282 m | 17 | | 0 | | 0 |
| Blunts Point | - 4281 to - 4272 m | 27 | 264 | 0 | 1 | 0 |
| Blunts Point | - 4271 to - 4262 m | 69 | | 1 | | 1 |
| Blunts Point | - 4261 to - 4252 m | 25 | | 0 | | 0 |
| Blunts Point | - 4251 to - 4242 m | 46 | | 0 | | 0 |
| Blunts Point | - 4241 to - 4232 m | 37 | | 0 | | 0 |
| Blunts Point | - 4231 to - 4222 m | 30 | | 0 | | 0 |
| Blunts Point | - 4221 to - 4212 m | 30 | | 0 | | 0 |
| Pettegrove Point | - 4211 to - 4202 m | 3 | 131 | 0 | 11 | 0 |
| Pettegrove Point | - 4201 to - 4192 m | 28 | | 0 | | 0 |
| Pettegrove Point | - 4191 to - 4182 m | 50 | | 1 | | 2 |
| Pettegrove Point | - 4181 to - 4172 m | 16 | | 2 | | 13 |
| Pettegrove Point | - 4171 to - 4162 m | 34 | | 8 | | 17 |
| Jura | - 4161 to - 4152 m | 38 | 109 | 5 | 17 | 13 |
| Jura | - 4151 to - 4142 m | 56 | | 10 | | 18 |
| Jura | - 4141 to higher | 15 | | 2 | | 13 |
| **Total** | | **1086** | | **91** | | |

## Section S4 Possible borate phases in Ca-sulfate veins

Following are the possible boron-containing phases that may have formed in or closely associated to the Ca-sulfate veins in Gale crater and resulted in the boron detection by the rover's ChemCam instrument.

***Fluid inclusion.*** On Earth, the growth of natural minerals from a melt or fluid phase is typically a disequilibrium process which allows surface irregularities to trap aliquots of the growth medium in pockets known as primary fluid inclusions. Later alteration fluids can form additional, secondary fluid inclusions which become trapped by healing of fluid-filled fractures

(Williams and Taylor, 1996; Sirbescu *et al*., 2013). Fluid inclusions of boric acid are reported in evaporites like gypsum (Williams and Taylor, 1996; Tivey *et al*., 1998; Sirbescu *et al.*, 2013) and chlorides (Fan *et al.*, 2015; Thomas *et al.*, 2018) in low-temperature aqueous environments that have formed during crystallization by trapping acid saline water from the reservoir pool. Fluid inclusions are also reported in borates like colemanite from northern Sonora (Mexico), however these fluid inclusions are associated with hydrothermal activity (Miranda-Gasca *et al*., 1998). In case of Ca-sulfate veins of Gale crater, the diagenetic fluids that precipitated the veins may have potentially developed boron-rich fluid pockets while dissolving primary boron-rich evaporites that may have been retained as boron-rich fluid inclusion while the Ca-sulfates precipitated. However, no evidence of fluid inclusions has yet been found using ChemCam and this possibility is purely speculative. Micron-sized fluid inclusions (~ 5-20 µm) are reported within halite crystals found in two chondritic meteorites Monahans and Zag (Zolensky, 2010; Zolensky *et al.*, 2014) and in pyroxene crystals of Martian meteorites (Bodnar, 1999) indicating aqueous interaction and trapped volatiles in primitive astromaterials. Similar sized fluid inclusions are also reported in halites from salt pans of California (Lowenstein *et al.*, 1988). Micron sized fluid inclusions in veins of Gale crater may not be identified at the resolution of RMI or MAHLI. However, larger fluid inclusions (mm - cm scale) have been reported in terrestrial evaporites such as borates, Ca-sulfates and halites (Casas and Lowenstein, 1989; Miranda-Gasca *et al.*, 1998; Benison, 2013; Krüger *et al.*, 2013; Sirbescu *et al.*, 2013) and if fluid inclusions of such sizes were present in Gale crater, they would potentially be detectable by the rover's imaging instruments. In the future, possible fluid inclusions in Martian evaporites may be identified by their uneven, circular or pseudo-crystalline shapes (Goldstein and Samson, 2003) that may contain gas bubble and secondary mineral inclusions (Correns, 2003). It is also possible that the fluid inclusions in the Ca-sulfate veins of Gale crater may have transformed into borate inclusions upon dehydration.

***Borate inclusion.*** The Ca-sulfate veins in Gale crater predominantly consist of bassanite which forms due to dehydration of gypsum in dry conditions (Rapin *et al.*, 2016). There may be a chance of complete evaporation of the fluids that formed the veins, in which case, the boron-rich component of the vein may be a borate inclusion instead of a boron-rich fluid inclusion. In case the ambient fluid condition in the Jura members was acidic, (interpreted based on the presence of minerals like jarosite and crystalline akaganeite (Morris, *et al.*, 2019)) borates such as sassolite may have formed. On Earth, sassolite, a borate that forms in acidic environments, is reported in dry lakes of Southern California in the Kramer borate mine. The sassolite in this mine is inferred to have formed after lithification due to reaction of preexisting borates with sulfuric acid (Allen *et al.*, 1957; Smith *et al.*, 1958). It is possible that borates that form in acidic conditions such as sassolite and metaborite could be present in the Ca-sulfate veins of VRR. In case of more alkaline fluid environments in VRR, (Frydenvang, *et al.*, 2019; Morris, *et al.*, 2019) Ca and Na-borates (that form in alkaline conditions) such as borax, kernite, probertite, and ulexite are possible. Other studies of Ca-sulfate veins and clay minerals in Gale crater suggest an upper limit of ambient temperature to be ~50°C (Nachon *et al.*, 2014, 2017; Vaniman *et al.*, 2014; Schwenzer *et al.*, 2016) which suggests that the extent of burial diagenesis is minimal to none. With minimal burial diagenesis the formation of mature borate phases that require higher temperature and pressure for formation (such as colemanite, gowerite and nobleite as shown in Figure 2) are less likely than borates such as borax, kernite, probertite, and ulexite. Since different pH, salinity levels, pressure, and temperature result in formation of different types of borates, if ChemCam observes a borate mineral in the future, that is large enough to be analyzed using the LIBS instrument, the mineral can provide valuable information regarding the properties of post-depositional paleo-fluids in Gale crater.

## 9 References

Abu-Sharar, T. M., Hani, N. B., & Al-Khader, S. (2014). Boron adsorption–desorption characteristics of irrigated soils in the Jordan Valley. *Geoderma Regional*, *2*, 50-59.

Achilles, C. (2018) *Analyses of Crystalline and X-Ray Amorphous Materials in Gale Crater Rocks and Soils*. https://doi.org/10.1016/j.geodrs.2014.09.007

Allen, R. D., & Kramer, H. (1957). Ginorite and sassolite from Death Valley, California. *American Mineralogist: Journal of Earth and Planetary Materials*, *42*(1-2), 56-61.

Averill, W. A., & Olson, D. L. (1978). A review of extractive processes for lithium from ores and brines. In *Lithium Needs and Resources* (pp. 305-313). Pergamon. https://doi.org/10.1016/B978-0-08-022733-7.50015-0

Banham, S. G., Gupta, S., Rubin, D. M., Watkins, J. A., Sumner, D. Y., Edgett, K. S., et al. (2018). Ancient Martian aeolian processes and palaeomorphology reconstructed from the Stimson formation on the lower slope of Aeolis Mons, Gale crater, Mars. *Sedimentology*, *65*(4), 993-1042. https://doi.org/10.1111/sed.12469

Becker, S., Thoma, I., Deutsch, A., Gehrke, T., Mayer, P., Zipse, H., et al. (2016). A high-yielding, strictly regioselective prebiotic purine nucleoside formation pathway. *Science*, *352*(6287), 833-836. https://doi.org/10.1126/science.aad2808

Becker, S., Feldmann, J., Wiedemann, S., Okamura, H., Schneider, C., Iwan, K., et al. (2019). Unified prebiotically plausible synthesis of pyrimidine and purine RNA ribonucleotides. *Science*, *366*(6461), 76-82. https://doi.org/10.1126/science.aax2747

Benison, K. C. (2013). Acid saline fluid inclusions: examples from modern and Permian extreme lake systems. *Geofluids*, *13*(4), 579-593. https://doi.org/10.1111/gfl.12053

Biggar, J. W., & Fireman, M. (1960). Boron Adsorption and Release by Soils 1. *Soil Science Society of America Journal*, *24*(2), 115-120. https://doi.org/10.2136/sssaj1960.03615995002400020015x

Bingham, F., Page, A. L., Coleman, N. T., & Flach, K. (1971). Boron Adsorption Characteristics of Selected Amorphous Soils from Mexico and Hawaii 1. *Soil Science Society of America Journal*, *35*(4), 546-550. https://doi.org/10.2136/sssaj1971.03615995003500040021x

Birsoy, R., & Özbaş, Ü. (2012). Activity diagrams of borates: implications on common deposits. *Carbonates and Evaporites*, *27*(1), 71-85. https://doi.org/10.1007/s13146-012-0085-6

Blasdale, W. C., & Slansky, C. M. (1939). The solubility curves of boric acid and the borates of sodium. *Journal of the American Chemical Society*, *61*(4), 917-920. https://doi.org/10.1021/ja01873a043

Bodnar, R. J. (1999). *Fluid Inclusions in ALH84001 and Other Martian Meteorites: Evidence for Volatiles on Mars.* Abstract number 1222. Presented at the 30th Lunar and Planetary Science Conference, Houston, TX.

Bridges, J. C., Cousin, A., Sautter, V., Rapin, W., Schwenzer, S. P., Bedford, C., et al. (2019). *Askival: A Silicified Feldspathic Cumulate Sample in Gale Crater.* Abstract number 2345. Presented at the 50th Lunar and Planetary Science Conference, Houston, TX.

Bristow, T. F., Rampe, E. B., Achilles, C. N., Blake, D. F., Chipera, S. J., Craig, P., et al. (2018).

Clay mineral diversity and abundance in sedimentary rocks of Gale crater, Mars. *Science Advances*, *4*(6), eaar3330. https://doi.org/10.1126/sciadv.aar3330

Burst, J. F. (1957). Postdiagenetic clay mineral environmental relationships in the Gulf Coast Eocene. *Clays and Clay Minerals*, *6*(1), 327-341. https://doi.org/10.1346/CCMN.1957.0060124

Casas, E., & Lowenstein, T. K. (1989). Diagenesis of saline pan halite; comparison of petrographic features of modern, Quaternary and Permian halites. *Journal of Sedimentary Research*, *59*(5), 724-739. https://doi.org/10.1306/212F905C-2B24-11D7-8648000102C1865D

Christ, C. L., Truesdell, A. H., & Erd, R. C. (1967). Borate mineral assemblages in the system Na2O- CaO-MgO-B2O3-H2O. *Geochimica et Cosmochimica Acta*, *31*(3), 313-337. https://doi.org/10.1016/0016-7037(67)90045-2

Clegg, S. M., Sklute, E., Dyar, M. D., Barefield, J. E., & Wiens, R. C. (2009). Multivariate analysis of remote laser-induced breakdown spectroscopy spectra using partial least squares, principal component analysis, and related techniques. *Spectrochimica Acta Part B: Atomic Spectroscopy*, *64*(1), 79-88. https://doi.org/10.1016/j.sab.2008.10.045

Clegg, S. M., Wiens, R. C., Anderson, R., Forni, O., Frydenvang, J., Lasue, J., et al. (2017). Recalibration of the Mars Science Laboratory ChemCam instrument with an expanded geochemical database. *Spectrochimica Acta Part B: Atomic Spectroscopy*, *129*, 64-85. https://doi.org/10.1016/j.sab.2016.12.003.

Cloutis, E., Berg, B., Mann, P., & Applin, D. (2016). Reflectance spectroscopy of low atomic weight and Na-rich minerals: Borates, hydroxides, nitrates, nitrites, and peroxides. *Icarus*, *264*, 20-36. https://doi.org/10.1016/j.icarus.2015.08.026.

Correns, C. W. (2003). Fluid inclusions with gas bubbles as geothermometers. *International Journal of Earth Sciences*, *91*(0), s123–s133. https://doi.org/10.1007/s00531-002-0273-z

Couch, E. L., & Grim, R. E. (1968). Boron fixation by illites. *Clays and Clay Minerals*, *16*(3), 249-256. https://doi.org/10.1346/CCMN.1968.0160307

Csetenyi, L. J., & Glasser, F. P. (1992). Borate substituted ettringites. *MRS Online Proceedings Library Archive*, *294*. https://doi.org/10.1557/PROC-294-273

Dalton, G. R., Lee, A. Y., & Young, S. L. (2016). *IUPAC/NIST Solubility Database* (No. IUPAC/NIST Solubility Database).

Das, D. (2020). ChemCam data and corrected Li data [Data set]. Zenodo. http://doi.org/10.5281/zenodo.3877377

David, G., Cousin, A., Forni, O., Meslin, P. Y., Mangold, N., L'Haridon, J., et al. (2019). *Hematite Mineral Grains Observed by ChemCam Across the Vera Rubin Ridge Sedimentary Rocks at Gale Crater, Mars.* Presented at the Ninth International Conference on Mars, LPI Contributions, Pasadena, CA.

Eberl, D., & Hower, J. (1976). Kinetics of illite formation. *Geological Society of America Bulletin*, *87*(9), 1326-1330. https://doi.org/10.1130/0016-7606(1976)87<1326:KOIF>2.0.CO;2

Edgar, L. A., Fraeman, A. A., Gupta, S., Fedo, C. M., Grotzinger, J. P., Stack, K. M., et al. (2018). *Sedimentology and Stratigraphy Observed at Vera Rubin Ridge by the Mars Science Laboratory Curiosity Rover.* Abstract number 1704. Presented at the 49th Lunar and Planetary Science Conference, Houston, TX.

Edgett, K. S., Yingst, R. A., Ravine, M. A., Caplinger, M. A., Maki, J. N., Ghaemi, F. T., et al.

(2012). Curiosity's Mars hand lens imager (MAHLI) investigation. *Space Science Reviews*, *170*(1-4), 259-317. https://doi.org/10.1007/s11214-012-9910-4

Ehlmann, B. L., Swayze, G. A., Milliken, R. E., Mustard, J. F., Clark, R. N., Murchie, S. L., et al. (2016). Discovery of alunite in Cross crater, Terra Sirenum, Mars: Evidence for acidic, sulfurous waters. *American Mineralogist*, *101*(7), 1527-1542. https://doi.org/10.2138/am-2016-5574

Eigenbrode, J. L., Summons, R. E., Steele, A., Freissinet, C., Millan, M., Navarro-González, R., et al. (2018). Organic matter preserved in 3-billion-year-old mudstones at Gale crater, Mars. *Science*, *360*(6393), 1096-1101. https://doi.org/10.1126/science.aas9185

Evans, C. M., & Sparks, D. L. (1983). On the chemistry and mineralogy of boron in pure and in mixed systems: A review. *Communications in Soil Science and Plant Analysis*, *14*(9), 827-846. https://doi.org/10.1080/00103628309367412

Fan, Q., Ma, Y., Cheng, H., Wei, H., Yuan, Q., Qin, Z., & Shan, F. (2015). Boron occurrence in halite and boron isotope geochemistry of halite in the Qarhan Salt Lake, western China. *Sedimentary Geology*, *322*, 34-42. https://doi.org/10.1016/j.sedgeo.2015.03.012

Fedo, C. M., Grotzinger, J. P., Gupta, S., Fraeman, A., Edgar, L., Edgett, K., et al. (2018). *Sedimentology and Stratigraphy of the Murray Formation, Gale Crater, Mars*. Abstract number 2078. Presented at the 49th Lunar and Planetary Science Conference, Houston, TX.

Fedo, C. M., Grotzinger, J. P., Gupta, S., Stein, N. T., Watkins, J., Banham, S., et al. (2017). *Facies analysis and basin architecture of the upper part of the Murray formation, Gale Crater, Mars*. Abstract number 1689. Presented at the 48th Lunar and Planetary Science Conference, Houston, TX.

Forni, O., Vaniman, D. T., Le Deit, L., Clegg, S. M., Lanza, N. L., Lasue, J., et al. (2015). *Fluorine and lithium at the Kimberley outcrop, Gale Crater*. Abstract number 1989. Presented at the 46th Lunar and Planetary Science Conference, Houston, TX.

Forni, O., Meslin, P. Y., Cousin, A., Clegg, S. M., Mangold, N., Le Deit, L., et al. (2019). *Fluorine on Mars: Seven Years of Detection with ChemCam On-Board MSL*. Abstract number 6095. Presented at the Ninth International Conference on Mars, LPI Contributions, Pasadena, CA.

Forni, O., Meslin, P. Y., L'Haridon, J., Rapin, W., Nachon, M., Newsom, H., et al. (2017). *Detection of Fluorine-Rich Phases, Phosphates, and Halite in the Stimson-Murray Units, Gale Crater, Mars*. Abstract number 1838. Presented at the 48th Lunar and Planetary Science Conference, Houston, TX.

Fraeman, A. A., Catalano, J. G., Edgar, L. A., Fischer, W. W., Grotzinger, J. P., L'Haridon, J., et al. (2019). *Vera Rubin Ridge and Iron Oxide Bearing Sedimentary Rocks on Mars: The Integrated View from Curiosity and Orbital Data.* Abstract number 6237. Presented at the Ninth International Conference on Mars, LPI Contributions, Pasadena, CA.

Fraeman, A. A., Arvidson, R. E., Catalano, J. G., Grotzinger, J. P., Morris, R. V., Murchie, S. L, et al. (2013). A Hematite-Bearing Layer in Gale Crater, Mars: Mapping and Implications for Past Aqueous Conditions. *Geology*, *41*(10), 1103-1106. https://doi.org/10.1130/G34613.1

Fraeman, A. A., Edgar, L. A., Grotzinger, J. P., Vasavada, A. R., Johnson, J. R., Wellington, D. F., et al. (2018). *Curiosity's Investigation at Vera Rubin Ridge.* Presented at the 49th Lunar and Planetary Science Conference, Houston, TX.

Frederickson, A. F., & Reynolds, R. C., Jr. (1960). Geochemical Method for Determining

Paleosalinity. *Clays and Clay Minerals* (pp. 203-213). Pergamon. https://doi.org/10.1016/B978-0-08-009351-2.50023-4

Frydenvang, J., Mangold, N., Wiens, R. C., Fraeman, A. A., Edgar, L. A., Fedo, C. M., et al. (2019). *The chemostratigraphy of the lacustrine Murray formation in Gale crater, Mars, and evidence for large-scale diagenesis in Vera Rubin ridge bedrock as implied by ChemCam observations.* Abstract number 6334. Presented at the Ninth International Conference on Mars, LPI Contributions, Pasadena, CA.

Furukawa, Y., Chikaraishi, Y., Ohkouchi, N., Ogawa, N. O., Glavin, D. P., Dworkin, J. P., et al. (2019). Extraterrestrial ribose and other sugars in primitive meteorites. *Proceedings of the National Academy of Sciences, 116(49),* 24440-24445. https://doi.org/10.1073/pnas.1907169116

Furukawa, Y., Horiuchi, M., & Kakegawa, T. (2013). Selective stabilization of ribose by borate. *Origins of Life and Evolution of Biospheres*, *43*(4-5), 353-361. https://doi.org/10.1007/s11084-013-9350-5

Furukawa, Y., & Kakegawa, T. (2017). Borate and the Origin of RNA: A Model for the Precursors to Life. *Elements*, *13*(4), 261-265. https://doi.org/10.2138/gselements.13.4.261

Garrett, D. E. (1998). *Borates: Handbook of deposits, processing, properties, and use*. Elsevier, 482-483.

Gasda, P. J., Haldeman, E. B., Wiens, R. C., Rapin, W., Bristow, T. F., Bridges, J. C., et al. (2017). In situ detection of boron by ChemCam on Mars. *Geophysical Research Letters*, *44*(17), 8739-8748. https://doi.org/10.1002/2017GL074480.

Gast, R. G., & Klobe, W. D. (1971). Sodium-lithium exchange equilibria on vermiculite at 25 and 50 C. *Clays and Clay Minerals*, *19*(5), 311-319.

Glotch, T. D., Bandfield, J. L., Tornabene, L. L., Jensen, H. B., & Seelos, F. P. (2010). Distribution and formation of chlorides and phyllosilicates in Terra Sirenum, Mars. *Geophysical Research Letters*, *37*(16). https://doi.org/10.1029/2010GL044557

Goldberg, S. (1997). Reactions of boron with soils. *Plant and Soil*, *193*(1-2), 35-48. https://doi.org/10.1023/A:1004203723343

Goldberg, S., Forster, H. S., & Heick, E. L. (1993). Temperature effects on boron adsorption by reference minerals and soils. *Soil Science*, *156*(5), 316-321. https://doi.org/10.1097/00010694-199311000-00004

Goldberg, S., Suarez, D. L., & Shouse, P. J. (2008). Influence of soil solution salinity on boron adsorption by soils. *Soil Science*, *173*(6), 368-374.

Goldstein, R. H., & Samson, I. (2003). Petrographic analysis of fluid inclusions. *Fluid Inclusions: Analysis and Interpretation*, *32*, 9-53.

Greene-Kelly, R. (1955). Lithium absorption by kaolin minerals. *The Journal of Physical Chemistry*, *59*(11), 1151-1152. https://doi.org/10.1021/j150533a009

Grew, E. S. (2017). Boron: from cosmic scarcity to 300 minerals. *Elements*, *13*(4), 225-229. https://doi.org/10.2138/gselements.13.4.225

Grew, E. S., Bada, J. L., & Hazen, R. M. (2011). Borate minerals and origin of the RNA world. *Origins of Life and Evolution of Biospheres*, *41*(4), 307-316. https://doi.org/10.1007/s11084-010-9233-y

Grotzinger, J. P., Sumner, D. Y., Kah, L. C., Stack, K., Gupta, S., Edgar, L., et al. (2014). A habitable fluvio-lacustrine environment at Yellowknife Bay, Gale Crater, Mars. *Science*, *343*(6169), 1242777. https://doi.org/10.1126/science.1242777

Grotzinger, J. P., Gupta, S., Malin, M. C., Rubin, D. M., Schieber, J., Siebach, K., et al. (2015). Deposition, exhumation, and paleoclimate of an ancient lake deposit, Gale crater, Mars. *Science*, *350*(6257), aac7575. https://doi.org/10.1126/science.aac7575

Grotzinger, J. P., & Milliken, R. E. (2012). The sedimentary rock record of Mars: Distribution, origins, and global stratigraphy. *Sedimentary Geology of Mars*, *102*, 1-48.

Gwizd, S., Fedo, C., Grotzinger, J., Edgett, K., Rivera-Hernandez, F., & Stein, N. (2018). *Depositional History of the Hartmann's Valley Member, Murray Formation, Gale Crater, Mars.* Abstract number 2150. Presented at the 49th Lunar and Planetary Science Conference, Houston, TX.

Haber, J. T., Horgan, B., Fraeman, A. A., Johnson, J. R., Wellington, D., Bell, J. F., et al. (2019). *Mineralogy of a Possible Ancient Lakeshore in Gale Crater, Mars, from Mastcam Multispectral Images*. Abstract number 6229. Presented at the Ninth International Conference on Mars, LPI Contributions, Pasadena, CA.

Haferburg, G., Gröning, J. A., Schmidt, N., Kummer, N. A., Erquicia, J. C., & Schlömann, M. (2017). Microbial diversity of the hypersaline and lithium-rich Salar de Uyuni, Bolivia. *Microbiological Research*, *199*, 19-28. https://doi.org/10.1016/j.micres.2017.02.007

Hall, B. E. (1977). *U.S. Patent No. 4,056,146*. Washington, DC: U.S. Patent and Trademark Office.

Hamzaoui, A. H., M'nif, A., Hammi, H., & Rokbani, R. (2003). Contribution to the lithium recovery from brine. *Desalination*, *158*(1-3), 221-224. https://doi.org/10.1016/S0011-9164(03)00455-7

Harder, H. A. (1970). Boron content of sediments as a tool in facies analysis. *Sedimentary Ggeology*, *4*(1-2), 153-175. https://doi.org/10.1016/0037-0738(70)90009-6

Hardie, L. A. (1967). The gypsum—anhydrite equilibrium at one atmosphere pressure. *American Mineralogist*, *52*(1-2), 171-200.

Helvaci, C. (1977). *Geology, mineralogy and geochemistry of the borate deposits and associated rocks at the Emet Valley, Turkey* (Doctoral dissertation, University of Nottingham).

Helvaci, C., & Alaca, O. (1991). Geology and Mineralogy of the Bigadiç Borate Deposıts and Vicinity. *Bulletin of the Mineral Research and Exploration*, 113(113), 31-63.

Helvacı, C., Stamatakis, M. G., Zagouroglou, C., & Kanaris, J. (1993). Borate minerals and related authigenic silicates in northeastern Mediterranean late Miocene continental basins. *Exploration and Mining Geology*, *2*(2), 171-178.

Helvaci, C., & Orti, F. (1998). Sedimentology and diagenesis of Miocene colemanite-ulexite deposits (western Anatolia, Turkey). *Journal of Sedimentary Research*, *68*(5), 1021-1033.

Helvaci, C., & Ortí, F. (2004). Zoning in the Kirka borate deposit, western Turkey: primary evaporitic fractionation or diagenetic modifications? *The Canadian Mineralogist*, *42*(4), 1179-1204. https://doi.org/10.2113/gscanmin.42.4.1179

Helvaci, C., & Palmer, M. R. (2017). Origin and Distribution of Evaporite Borates: The Primary Economic Sources of Boron. *Elements*, *13*(4), 249-254. https://doi.org/10.2138/gselements.13.4.249

Hemming, N. G., Reeder, R. J., & Hanson, G. N. (1995). Mineral-fluid partitioning and isotopic fractionation of boron in synthetic calcium carbonate. *Geochimica et Cosmochimica Acta*, *59*(2), 371-379. https://doi.org/10.1016/0016-7037(95)00288-B

Heydari, E., Parker, T. J., Calef III, F. J., Schroeder, J. F., Van Beek, J., Rowland, S. K., & Fairen, A. G. (2018). *Characteristics and the Origin of the Vera Rubin Ridge, Gale Crater, Mars.* Abstract number 1817. Presented at the 49th Lunar and Planetary Science Conference, Houston, TX.

Hilgers, C., & Urai, J. L. (2002). Microstructural observations on natural syntectonic fibrous veins: implications for the growth process. *Tectonophysics*, *352*(3-4), 257-274. https://doi.org/10.1016/S0040-1951(02)00185-3.

Hingston, F. J. (1964). Reactions between boron and clays. *Soil Research*, *2*(1), 83-95. https://doi.org/10.1071/SR9640083

Horgan, B., Fraeman, A., Johnson, J. R., Thompson, L., Jacob, S., Bell, J. F., & Grotzinger, J. (2019). *Redox Conditions During Diagenesis in the Vera Rubin Ridge, Gale Crater, Mars, from Mastcam Multispectral Images*. Abstract number 1424. Presented at the 50th Lunar and Planetary Science Conference, Houston, TX.

Huang, W. H., & Keller, W. D. (1971). Dissolution of clay minerals in dilute organic acids at room temperature. *American Mineralogist: Journal of Earth and Planetary Materials*, *56*(5-6), 1082-1095.

Hud, N. V., & Fialho, D. M. (2019). RNA nucleosides built in one prebiotic pot. *Science*, *366*(6461), 32-33. https://doi.org/10.1126/science.aaz1130

Hunt, C. B. (1966). *Hydrologic Basin, Death Valley, California* (No. 494). US Government Printing Office. https://doi.org/10.3133/pp494B

Hurowitz, J. A., Grotzinger, J. P., Fischer, W. W., McLennan, S. M., Milliken, R. E., Stein, N., et al (2017). Redox stratification of an ancient lake in Gale crater, Mars. *Science*, *356*(6341), eaah6849. https://doi.org/10.1126/science.aah6849

Inan, K. (1973). Mineralogy, Chemistry and Origin of Kirka Borate Deposit, Eskishehir Province, Turkey. *Serial Issue in Instit. Ming Metallurgy Bull.*, 82(801), 114-123

Johnson, J. R., Bell, J. F., Lemmon, M., & Pinet, P. (2019). *Mastcam Visible/Near-Infrared Spectrophotometric Observations of the Red Hills Region of Vera Rubin Ridge*. Abstract number 1313. Presented at the 50th Lunar and Planetary Science Conference.

Kah, L. C., Stack, K. M., Eigenbrode, J. L., Yingst, R. A., & Edgett, K. S. (2018). Syndepositional precipitation of calcium sulfate in Gale Crater, Mars. *Terra Nova*, *30*(6), 431-439. https://doi.org/10.1111/ter.12359

Karahan, S. *et al.* (2006) 'Removal of boron from aqueous solution by clays and modified clays', *Journal of Colloid and Interface Science*, 293(1), pp. 36–42. doi: 10.1016/j.jcis.2005.06.048.

ten Kate, I. L. (2018). Organic molecules on Mars. *Science*, *360*(6393), 1068-1069.

https://doi.org/10.1126/science.aat2662

Keren, R., & O'connor, G. A. (1982). Effect of exchangeable ions and ionic strength on boron adsorption by montmorillonite and illite. *Clays and Clay minerals*, *30*(5), 341-346. https://doi.org/10.1346/CCMN.1982.0300504

Keren, R., & Mezuman, U. (1981). Boron adsorption by clay minerals using a phenomenological equation. *Clays and Clay Minerals*, *29*(3), 198-204. https://doi.org/10.1346/CCMN.1981.0290305

Keren, R., Gast, R. G., & Bar-Yosef, B. (1981). pH-Dependent Boron Adsorption by Na-Montmorillonite 1. *Soil Science Society of America Journal*, *45*(1), 45-48. https://doi.org/10.2136/sssaj1981.03615995004500010010x

Kim, H. J., Ricardo, A., Illangkoon, H. I., Kim, M. J., Carrigan, M. A., Frye, F., & Benner, S. A. (2011). Synthesis of carbohydrates in mineral-guided prebiotic cycles. *Journal of the American Chemical Society*, *133*(24), 9457-9468. https://doi.org/10.1021/ja201769f

Kistler, R. B., & Helvaci, C. (1994). Boron and Borates. *Industrial minerals and rocks*, *Society of Mining Engineers*, *6(5)*, 171-186.

Kitano, Y., Okumura, M., & Idogaki, M. (1978). Coprecipitation of borate-boron with calcium carbonate. *Geochemical Journal*, *12*(3), 183-189. https://doi.org/10.2343/geochemj.12.183

Kronyak, R. E., Kah, L. C., Edgett, K. S., VanBommel, S. J., Thompson, L. M., Wiens, R. C., et al. (2019). Mineral-filled fractures as indicators of multigenerational fluid flow in the Pahrump Hills member of the Murray formation, Gale crater, Mars. *Earth and Space Science*, *6*(2), 238-265. https://doi.org/10.1029/2018EA000482

Krüger, Y., García-Ruiz, J. M., Canals, À., Marti, D., Frenz, M., & Van Driessche, A. E. (2013). Determining gypsum growth temperatures using monophase fluid inclusions—Application to the giant gypsum crystals of Naica, Mexico. *Geology*, *41*(2), 119-122. https://doi.org/10.1130/G33581.1

L'Haridon, J., Mangold, N., Meslin, P. Y., Johnson, J. R., Rapin, W., Forni, O., et al. (2018). Chemical variability in mineralized veins observed by ChemCam on the lower slopes of Mount Sharp in Gale crater, Mars. *Icarus*, *311*, 69-86. https://doi.org/10.1016/j.icarus.2018.01.028

L'Haridon, J., Mangold, N., Wiens, R. C., Cousin, A., David, G., Johnson, J. R., et al. (2019). *Iron-Rich Diagenetic Features Analysed In the Murray Formation at Gale Crater, Mars, Using Chemcam Onboard the Curiosity Rover.* Abstract number 6079. Presented at the Ninth International Conference on Mars, LPI Contributions, Pasadena, CA.

Lanza, N. L., Wiens, R. C., Arvidson, R. E., Clark, B. C., Fischer, W. W., Gellert, R., et al. (2016). Oxidation of manganese in an ancient aquifer, Kimberley formation, Gale crater, Mars. *Geophysical Research Letters*, *43*(14), 7398-7407. https://doi.org/10.1002/2016GL069109

Larralde, R., Robertson, M. P., & Miller, S. L. (1995). Rates of decomposition of ribose and other sugars: implications for chemical evolution. *Proceedings of the National Academy of Sciences*, *92*(18), 8158-8160. https://doi.org/10.1073/pnas.92.18.8158

Lerman, A. (1966). Boron in clays and estimation of paleosalinities. *Sedimentology*, *6*(4), 267-286. https://doi.org/10.1111/j.1365-3091.1966.tb01895.x

Li, Q., Fan, Q., Wang, J., Qin, Z., Zhang, X., Wei, H., & Shan, F. (2019). Hydrochemistry, Distribution and Formation of Lithium-Rich Brines in Salt Lakes on the Qinghai-Tibetan Plateau. *Minerals*, *9*(9), 528. https://doi.org/10.3390/min9090528

Lowenstein, T. K., Li, J., & Brown, C. B. (1998). Paleotemperatures from fluid inclusions in halite: method verification and a 100,000-year paleotemperature record, Death Valley, CA. *Chemical Geology*, *150*(3-4), 223-245. https://doi.org/10.1016/S0009-2541(98)00061-8

Malin, M. C., Caplinger, M. A., Edgett, K. S., Ghaemi, F. T., Ravine, M. A., Schaffner, J. A., et al. (2010). *The Mars Science Laboratory (MSL) mast-mounted cameras (Mastcams) flight instruments*. Abstract number 1123. Presented at the 41st Lunar and Planetary Science Conference, Houston, TX.

Mangold, N., Schmidt, M. E., Fisk, M. R., Forni, O., McLennan, S. M., Ming, D. W., et al. (2017). Classification scheme for sedimentary and igneous rocks in Gale crater, Mars. *Icarus*, *284*, 1-17. https://doi.org/10.1016/j.icarus.2016.11.005

Mangold, N., Dehouck, E., Fedo, C., Forni, O., Achilles, C., Bristow, T., et al. (2019). Chemical alteration of fine-grained sedimentary rocks at Gale crater. *Icarus*, *321*, 619-631. https://doi.org/10.1016/j.icarus.2018.11.004

Marion, G. M., Mikhail V. Mironenko, & Morien W. Roberts (2010). "FREZCHEM: A geochemical model for cold aqueous solutions." *Computers & Geosciences,* 36.1, 10-15. https://doi.org/10.1016/j.cageo.2009.06.004

Martin, P. E., Farley K. A., Baker, M. B., Malespin, C. A., Schwenzer, S. P., Cohen, B. A., et al. (2017) "A two-step K-Ar experiment on Mars: Dating the diagenetic formation of jarosite from Amazonian groundwaters." *Journal of Geophysical Research: Planets 122(1),* 2803-2818. https://doi.org/10.1002/2017JE005445

Maurice, S., Wiens, R. C., Saccoccio, M., Barraclough, B., Gasnault, O., Forni, O., et al. (2012). The ChemCam instrument suite on the Mars Science Laboratory (MSL) rover: Science objectives and mast unit description. *Space Science Reviews*, *170*(1-4), 95-166. https://doi.org/10.1007/s11214-012-9912-2

Mavromatis, V., Montouillout, V., Noireaux, J., Gaillardet, J., & Schott, J. (2015). Characterization of boron incorporation and speciation in calcite and aragonite from co-precipitation experiments under controlled pH, temperature and precipitation rate. *Geochimica et Cosmochimica Acta*, *150*, 299-313. https://doi.org/10.1016/j.gca.2014.10.024

McLennan, S. M., Anderson, R. B., Bell, J. F., Bridges, J. C., Calef, F., Campbell, J. L., et al. (2014). Elemental geochemistry of sedimentary rocks at Yellowknife Bay, Gale crater, Mars. *Science*, *343*(6169), 1244734. http://doi.org/10.1126/science.1244734

Mianping, Z., Zhao Y., & Liu J. (2000) "Palaeoclimatic indicators of China's Quaternary saline lake sediments and hydrochemistry." *Acta Geologica Sinica-English Edition 74(2)*: 259-265. https://doi.org/10.1111/j.1755-6724.2000.tb00459.x

Ming, D. W., Archer, P. D., Glavin, D. P., Eigenbrode, J. L., Franz, H. B., Sutter, B., et al. (2014). Volatile and organic compositions of sedimentary rocks in Yellowknife Bay, Gale Crater, Mars. *Science*, *343*(6169), 1245267. https://doi.org/10.1126/science.1245267

Miranda-Gasca, M. A., Gomez-Caballero, J. A., & Eastoe, C. J. (1998). Borate deposits of northern Sonora, Mexico; stratigraphy, tectonics, stable isotopes, and fluid inclusions. *Economic Geology*, *93*(4), 510-523. https://doi.org/10.2113/gsecongeo.93.4.510

Morris, R. V., Bristow, T. F., Rampe, E. B., Yen, A. S., Vaniman, D. T., Tu, V., et al. (2019). *Mineralogy and Formation Processes for the Vera Rubin Ridge at Gale Crater, Mars from CheMin XRD Analyses.* Abstract number 1127. Presented at the 50th *Lunar and Planetary Science Conference*, Houston, TX.

Munk, L. A., Boutt, D. F., Hynek, S. A., & Moran, B. J., (2018). Hydrogeochemical fluxes and processes contributing to the formation of lithium-enriched brines in a hyper-arid continental basin. *Chemical Geology*, *493*, 37-57. https://doi.org/10.1016/j.chemgeo.2018.05.013

Le Mouélic, S., Gasnault, O., Herkenhoff, K. E., Bridges, N. T., Langevin, Y., Mangold, N., et al. (2015). The ChemCam Remote Micro-Imager at Gale crater: Review of the first year of operations on Mars. *Icarus*, *249*, 93-107. https://doi.org/10.1016/j.icarus.2014.05.030

Nachon, M., Clegg, S. M., Mangold, N., Schröder, S., Kah, L. C., Dromart, G., et al. (2014). Calcium sulfate veins characterized by ChemCam/Curiosity at Gale crater, Mars. *Journal of Geophysical Research: Planets*, *119*(9), 1991-2016. https://doi.org/10.1002/2013JE004588

Nachon, M., Mangold, N., Forni, O., Kah, L. C., Cousin, A., Wiens, R. C., et al. (2017). Chemistry of diagenetic features analyzed by ChemCam at Pahrump Hills, Gale crater, Mars. *Icarus*, *281*, 121-136. https://doi.org/10.1016/j.icarus.2016.08.026

Nir, S., Hirsch, D., Navrot, J., & Banin. A., (1986) "Specific adsorption of lithium, sodium, potassium, and strontium to montmorillonite: observations and predictions." *Soil Science Society of America Journal* 50, no. 1, 40-45. https://doi.org/10.2136/sssaj1986.03615995005000010008x

Palmer, M. R., Spivack, A. J., & Edmond, J. M. (1987). Temperature and pH controls over isotopic fractionation during adsorption of boron on marine clay. *Geochimica et Cosmochimica Acta*, *51*(9), 2319-2323. https://doi.org/10.1016/0016-7037(87)90285-7

Palmer, M. R., & Helvaci, C. (1997). The boron isotope geochemistry of the Neogene borate deposits of western Turkey. *Geochimica et Cosmochimica Acta*, *61*(15), 3161-3169. https://doi.org/10.1016/S0016-7037(97)00135-X

Payré, V., Fabre, C., Cousin, A., Sautter, V., Wiens, R. C., Forni, O., et al. (2017). Alkali trace elements in Gale crater, Mars, with ChemCam: Calibration update and geological implications. *Journal of Geophysical Research: Planets*, *122*(3), 650-679. https://doi.org/10.1002/2016JE005201

Peretyazhko, T. S., Fox, A., Sutter, B., Niles, P. B., Adams, M., Morris, R. V., and Ming, D. W. (2016). Synthesis of akaganeite in the presence of sulfate: Implications for akaganeite formation in Yellowknife Bay, Gale crater, Mars. *Geochimica et Cosmochimica Acta*, *188*, 284-296, http://dx.doi.org/10.1016/j.gca.2016.06.002.

Peretyazhko, T. S., Ming, D. W., Rampe, E. B., Morris, R. V., and Agresti, D. G. (2018). Effect of solution pH and chloride concentration on akaganeite precipitation: Implications for akaganeite formation on Mars. *Journal of Geophysical Research: Planets*, *123*, 2211-2222, http://dx.doi.org/10.1029/2018JE005630.

Perry, E. A. (1972). Diagenesis and the validity of the boron paleosalinity technique. *American Journal of Science*, *272*(2), 150-160. https://doi.org/10.2475/ajs.272.2.150

Powner, M. W., Gerland, B., & Sutherland, J. D. (2009). Synthesis of activated pyrimidine ribonucleotides in prebiotically plausible conditions. *Nature*, *459*(7244), 239. https://doi.org/10.1038/nature08013

Rampe, E. B., Bristow, T. F., Blake, D. F., Morris, R. V., Ming, D. W., Achilles, C. N., et al. (2019). *The Mineralogical Record of Ancient Fluvio-Lacustrine Environments in Gale Crater as Measured by the MSL CheMin Instrument*. Abstract number 6054. Presented at the Ninth International Conference on Mars, LPI Contributions, Pasadena, CA.

Rapin, W., Ehlmann, B. L., Dromart, G., Schieber, J., Thomas, N. H., Fischer, W. W., et al.

(2019). An interval of high salinity in ancient Gale crater lake on Mars. *Nature Geoscience*, *12*(11), 889-895. https://doi.org/10.1038/s41561-019-0458-8

Rapin, W., Meslin, P. Y., Maurice, S., Vaniman, D., Nachon, M., Mangold, N., et al., (2016). Hydration state of calcium sulfates in Gale crater, Mars: Identification of bassanite veins. *Earth and Planetary Science Letters*, *452*, 197-205. https://doi.org/10.1016/j.epsl.2016.07.045

Refait, P., and Génin, J. -M. R. (1997). The mechanisms of oxidation of ferrous hydroxychloride β -$Fe_2(OH)_3Cl$ in aqueous solution: The formation of akaganeite vs. goethite. *Corrosion Science*, *39*(3), 539-553, http://dx.doi.org/10.1016/S0010-938X(97)86012-1

Rémazeilles, C., and Refait, P. (2007). On the formation of β -FeOOH (akaganeite) in chloride-containing environments. *Corrosion Science*, *49*(2), 844-857, http://dx.doi.org/10.1016/j.corsci.2006.06.003.

Risacher, F.& Fritz, B. (2009) "Origin of salts and brine evolution of Bolivian and Chilean salars." *Aquatic Geochemistry 15*(*1-2)*, 123-157. https://doi.org/10.1007/s10498-008-9056-x

Risacher, F., & Fritz, B. (1991). Quaternary geochemical evolution of the salars of Uyuni and Coipasa, Central Altiplano, Bolivia. *Chemical Geology*, *90*(3-4), 211-231.

Rivera-Hernández, F., Sumner, D. Y., Mangold, N., Stack, K. M., Forni, O., Newsom, H., et al. (2019). Using ChemCam LIBS data to constrain grain size in rocks on Mars: Proof of concept and application to rocks at Yellowknife Bay and Pahrump Hills, Gale crater. *Icarus*, *321*, 82-98. https://doi.org/10.1016/j.icarus.2018.10.023

Ruiz-Mirazo, K., Briones, C., & de la Escosura, A. (2013). Prebiotic systems chemistry: new perspectives for the origins of life. *Chemical Reviews*, *114*(1), 285-366. https://doi.org/10.1021/cr2004844

Sansonetti, J. E., & Martin, W. C. (2005). Handbook of basic atomic spectroscopic data. *Journal of Physical and Chemical Reference Data*, *34*(4), 1559-2259. https://doi.org/10.1063/1.1800011

Schwenzer, S. P., Abramov, O., Allen, C. C., Clifford, S. M., Cockell, C. S., Filiberto, J., Treiman, A. H., et al. (2012). Puncturing Mars: How impact craters interact with the Martian cryosphere. *Earth and Planetary Science Letters*, *335*, 9-17. https://doi.org/10.1016/j.epsl.2012.04.031

Schwenzer, S. P., Bridges, J. C., Wiens, R. C., Conrad, P. G., Kelley, S. P., Leveille, R., et al. (2016). Fluids during diagenesis and sulfate vein formation in sediments at Gale crater, Mars. *Meteoritics & Planetary Science*, *51*(11), 2175-2202. https://doi.org/10.1111/maps.12668

Seryotkin, Y. V., Sokol, E. V., Kokh, S. N., & Murashko, M. N. (2018). Natural Cr $3^{+}$-rich ettringite: occurrence, properties, and crystal structure. *Physics and Chemistry of Minerals*, *45*(3), 279-292. https://doi.org/10.1007/s00269-017-0917-y

Seyfried, W. E., Janecky, D. R., & Mottl, M. J. (1984) "Alteration of the oceanic crust: implications for geochemical cycles of lithium and boron." *Geochimica et Cosmochimica Acta* 48(3), 557-569. https://doi.org/10.1016/0016-7037(84)90284-9

Siebach, K. L., Fedo, C. M., Edgar, L. E., Edgett, K., Grotzinger, J. P., Fraeman, A. A., et al. (2019, March). *Overview of Gale Crater Stratigraphy and Sedimentology from 6 Years of Roving with Mars Science Laboratory.* Abstract number 1479. Presented at the 50th *Lunar and Planetary Science Conference*, Houston, TX.

Siefke, J. W. (1991). The Boron open pit mine at the Kramer borate deposit. *The Diversity of Mineral and Energy Resources of Southern California. Soc. Econ. Geol. Guidebook Ser*, *12*, 4-15.

Simon, D. E., & Anderson, M. S. (1990). Stability of clay minerals in acid. *SPE Formation Damage Control Symposium*. Society of Petroleum Engineers. https://doi.org/10.2118/19422-MS

Sirbescu, M. L. C., Krukowski, E. G., Schmidt, C., Thomas, R., Samson, I. M., & Bodnar, R. J. (2013). Analysis of boron in fluid inclusions by microthermometry, laser ablation ICP-MS, and Raman spectroscopy: Application to the Cryo-Genie Pegmatite, San Diego County, California, USA. *Chemical Geology*, *342*, 138-150. https://doi.org/10.1016/j.chemgeo.2013.01.014

Smith, G. L., Almond, H., & Sawyer, D. L. (1958). Sassolite from the Kramer borate district, California. *American Mineralogist: Journal of Earth and Planetary Materials*, *43*(11-12), 1068-1078.

Smith, G. I., & Stuiver, M. (1979). *Subsurface stratigraphy and geochemistry of late Quaternary evaporites, Searles Lake, California*, US Geological Survey, Professional Paper, 1043, 130.

Stack, K. M., Grotzinger, J. P., Lamb, M. P., Gupta, S., Rubin, D. M., Kah, L. C., et al. (2018). Evidence for plunging river plume deposits in the Pahrump Hills member of the Murray formation, Gale crater, Mars. *Sedimentology*. https://doi.org/10.1111/sed.12558

Stanley, C. J., Jones, G. C., Rumsey, M. S., Blake, C., Roberts, A. C., Stirling, J. A., et al. (2007). Jadarite, $LiNaSiB_3O_7$ (OH), a new mineral species from the Jadar Basin, Serbia. *European Journal of Mineralogy 19(4)*, 575-580. https://doi.org/10.1127/0935-1221/2007/0019-1741

Starkey, H. C. (1982). *The role of clays in fixing lithium* (No. 1278). US Government Printing Office. https://doi.org/10.3133/b1278F

Stein, N., Grotzinger, J. P., Schieber, J., Mangold, N., Hallet, B., Newsom, H., et al. (2018). Desiccation cracks provide evidence of lake drying on Mars, Sutton Island member, Murray formation, Gale Crater. *Geology*, *46*(6), 515-518. https://doi.org/10.1130/G40005.1

Steinmetz, R. L. (2017). Lithium-and boron-bearing brines in the Central Andes: exploring hydrofacies on the eastern Puna plateau between 23 and 23 30′ S. *Mineralium Deposita*, *52*(1), 35-50. https://doi.org/10.1007/s00126-016-0656-x

Stephenson, J. D., Hallis, L. J., Nagashima, K., & Freeland, S. J. (2013). Boron enrichment in martian clay. *PloS One*, *8*(6), e64624. https://doi.org/10.1371/journal.pone.0064624

Stubican, V., & Roy, R. (1962). Boron substitution in synthetic micas and clays. *American Mineralogist: Journal of Earth and Planetary Materials*, *47*(9-10), 1166-1173.

Sun, V. Z., Stack, K. M., Kah, L. C., Thompson, L., Fischer, W., Williams, A. J., et al. (2019). Late-stage diagenetic concretions in the Murray formation, Gale crater, Mars. *Icarus*, *321*, 866-890. https://doi.org/10.1016/j.icarus.2018.12.030

Sun, V. Z., Stack, K. M., Nachon, M., Johnson, S. S., Kronyak, R. E., Wiens, R. C., et al. (2018). *Late-Stage Diagenesis in the Murray Formation, Gale Crater, Mars: Evidence from Diverse Concretion Morphologies*. Abstract number 1587. Presented at the 49th Lunar and Planetary Science Conference, Houston, TX.

Tanner, L. H. (2002). Borate formation in a perennial lacustrine setting: Miocene–Pliocene furnace creek formation, Death Valley, California, USA. *Sedimentary Geology*, *148*(1-2), 259-273. https://doi.org/10.1016/S0037-0738(01)00221-4

Thomas, N. H., Ehlmann, B. L., Meslin, P. Y., Rapin, W., Anderson, D. E., Rivera-Hernández, F., et al. (2019). Mars Science Laboratory Observations of Chloride Salts in Gale Crater, Mars. *Geophysical Research Letters*. https://doi.org/10.1029/2019GL082764

Thomas, N. H., Ehlmann, B. L., Meslin, P. Y., Cousin, A., Forni, O., Rapin, W., et al. (2018). *MSL ChemCam Observations of Chloride Salts in Gale Crater, Mars.* Abstract number 2876. Presented at the 49th Lunar and Planetary Science Conference.

Thompson, L. M., Fraeman, A. A., Berger, J. A., Rampe, E. B., Boyd, N. I., Gellert, R., et al. (2019). Compositional Characteristics and Trends Within the Vera Rubin Ridge, Gale Crater, Mars as Determined by APXS: Sedimentary, Diagenetic and Alteration History. Abstract number 3269. Presented at the 50th Lunar and Planetary Science Conference.

Tivey, M. K., Mills, R. A., & Teagle, D. A. (1998). Temperature and salinity of fluid inclusions in anhydrite as indicators of seawater entrainment and heating in the TAG active mound. Presented at the *Proceedings-ocean drilling program scientific results* 158(179-192). National science foundation, Alexandria, VA.

You, C. F., Spivack, A. J., Gieskes, J. M., Martin, J. B., & Davisson, M. L. (1996). Boron contents and isotopic compositions in pore waters: a new approach to determine temperature induced artifacts—geochemical implications. *Marine Geology*, *129*(3-4), 351-361. https://doi.org/10.1016/0025-3227(96)83353-6

Vaniman, D. T., Martínez, G. M., Rampe, E. B., Bristow, T. F., Blake, D. F., Yen, A. S., et al. (2018). Gypsum, bassanite, and anhydrite at Gale crater, Mars. *American Mineralogist: Journal of Earth and Planetary Materials*, *103*(7), 1011-1020. https://doi.org/10.2138/am-2018-6346

Vaniman, D. T., Bish, D. L., Ming, D. W., Bristow, T. F., Morris, R. V., Blake, D. F., et al. (2014). Mineralogy of a mudstone at Yellowknife Bay, Gale crater, Mars. *Science*, *343*(6169), 1243480. https://doi.org/10.1126/science.1243480

Vasavada, A. R., Grotzinger, J. P., Arvidson, R. E., Calef, F. J., Crisp, J. A., Gupta, S., et al. (2014). Overview of the Mars Science Laboratory mission: Bradbury landing to Yellowknife Bay and beyond. *Journal of Geophysical Research: Planets*, *119*(6), 1134-1161. https://doi.org/10.1002/2014JE004622

Vine, J. D., & Dooley J. R. (1980). *Where on Earth is all the lithium? with a section on uranium isotope studies*. No. 80-1234. US Geological Survey. Open-File Report. Series number 80-1234. https://doi.org/10.3133/ofr801234

Wiens, R. C., Maurice, S., Barraclough, B., Saccoccio, M., Barkley, W. C., Bell, J. F., et al. (2012). The ChemCam instrument suite on the Mars Science Laboratory (MSL) rover: Body unit and combined system tests. *Space Science reviews*, *170*(1-4), 167-227. https://doi.org/10.1007/s11214-012-9902-4

Wiens, R. C., Maurice, S., Lasue, J., Forni, O., Anderson, R. B., Clegg, S., et al. (2013). Pre-flight calibration and initial data processing for the ChemCam laser-induced breakdown spectroscopy instrument on the Mars Science Laboratory rover. *Spectrochimica Acta Part B: Atomic Spectroscopy*, *82*, 1-27. https://doi.org/10.1016/j.sab.2013.02.003

Wiens, R. C., Maurice, S., & MSL Science Team. (2015). ChemCam: Chemostratigraphy by the first Mars microprobe. *Elements*, *11*(1), 33-38. https://doi.org/10.2113/gselements.11.1.33

Williams, L. B., Hervig, R. L., Holloway, J. R., & Hutcheon, I. (2001). Boron isotope geochemistry during diagenesis. Part I. Experimental determination of fractionation during illitization of smectite. *Geochimica et Cosmochimica Acta*, *65*(11), 1769-1782. https://doi.org/10.1016/S0016-7037(01)00557-9

Williams, A. E., & Taylor, M. C. (1996). Mass spectrometric identification of boric acid in fluid inclusions in pegmatite minerals. *Geochimica et Cosmochimica Acta*, *60*(18), 3435-3443. https://doi.org/10.1016/0016-7037%2896%2900151-2

You, C. F., Spivack, A. J., Gieskes, J. M., Martin, J. B., & Davisson, M. L. (1996). Boron contents and isotopic compositions in pore waters: a new approach to determine temperature induced artifacts—geochemical implications. *Marine Geology*, *129*(3-4), 351-361.

Zhao, J., Lin, W., Chang, Q., Li, W., and Lai, Y. (2012). Adsorptive characteristics of akaganeite and its environmental applications: a review. *Environmental Technology Reviews*, *1*(1), 114-126, http://dx.doi.org/10.1080.09593330.2012.701239.

Zolensky, M. E. (2010). Liquid water in asteroids: Evidence from fluid inclusions in meteorites. In *Astrobiology Science Conference 2010: Evolution and Life: Surviving Catastrophes and Extremes on Earth and Beyond* (Vol. 1538, p. 5278).

Zolensky, M. E., Bodnar, R. J., Gibson, E. K., Nyquist, L. E., Reese, Y., Shih, C. Y., & Wiesmann, H. (1999). Asteroidal water within fluid inclusion-bearing halite in an H5 chondrite, Monahans (1998). *Science*, *285*(5432), 1377-1379. http://doi.org/10.1126/science.285.5432.1377

# Link to Chapter Two

In Chapter 1 we investigate the B and Li abundance in Ca-sulfate veins up to Vera Rubin ridge in Gale crater (results also summarized in Das et al., 2020). Vera Rubin ridge is an initially clay-rich formation which is inferred to have undergone later diagenetic alteration by acidic and saline groundwater (Rampe et al., 2020). Based on our findings summarized in Chapter 1, we hypothesized that Gale crater likely has two reservoirs of B and Li, primary borates of the lake acting as sources of B, and clay minerals that adsorbed B and Li onto their surface. We also hypothesize that primary evaporites were remobilized during multiple wet-dry events in Gale crater's aqueous history to be closely emplaced with the secondary Ca-sulfate veins. We observe a negative correlation between B and Li abundances in the Ca-sulfate veins and infer that that the sequential precipitation caused due to varying solubilities of B and Li and that this correlation is broadly preserved in the secondary Ca-sulfate veins in Gale crater.

In Chapter 2, we aim to understand the formation of primary evaporites in an ancient Gale crater playa/lake setting using thermochemical modeling techniques in order to determine constraints on formation of borates and Ca sulfates. We test the hypothesis established during the work on the first chapter that primary borates and Ca-sulfates formed over multiple wet-dry cycles, akin to how evaporite assemblages form on Earth, using thermochemical modeling while monitoring the concentration of Li in the evolving fluid. Li-salts are uncommon in terrestrial settings due to their hygroscopic nature and deliquescence in Earth's atmosphere (Gibbard and Scatchard, 1973); hence we monitor the Li concentration in the fluid to determine if any Li-salts could form in a drier Gale environment.  We combined the use of the tool CHIM-XPT with an updated database to include thermochemical parameters of borates with our observations from the analog site (chapter 3). We test the updated database by simulating evaporation on a known terrestrial dry lake fluid from Searles Lake, California and establish that the model successfully precipitated minerals, including borates, that are observed in Searles Lake. In order to model a Gale-relevant scenario, we start by modifying a widely accepted global Mars fluid (Gale Portage Water: Bridges et al., 2015) by adding B and Li in concentrations taken from stream waters from basaltic regions in Iceland. Water soluble elements readily remobilize during aqueous weathering and Gale crater is inferred to have experienced limited aqueous alteration (Rampe et al., 2020; Fraeman et al., 2020). For this work we assume that the aqueous alteration inferred for Gale crater drew out most of water-soluble elements from the basaltic rocks and that the abundance of water-soluble elements in the sedimentary rocks of Gale crater would be in the same order of magnitude as measured terrestrial analog basaltic rocks and measured igneous Martian meteorites.

After setting up a global Mars fluid with B and Li abundances, we simulate titration of this fluid with a representative Gale rock composition with added B and Li concentrations based on measured values from Martian meteorites to establish a Gale-relevant fluid. We then simulate cyclic evaporation and dilution in order to establish the minimum number of wet-dry cycles required to form primary evaporites that consist of borates and Ca-sulfates. We determine that a minimum of 250 wet-dry cycles are required to start forming primary evaporites that consist of borates and Ca-sulfates together from a Gale-relevant starting fluid and rock composition. We establish a relative time constraint for the 250 wet-dry cycles by using terrestrial lake systems as a reference and extend this time constraint to Gale crater by estimating lake levels based on the observed sedimentological facies in Gale crater. We estimate that a minimum of ~14,250 annual cycles (~7.5 k Earth years) of wet and dry periods would be required for the formation of the primary borates and Ca-sulfates that could later be remobilized to form veins and other deposits. No Li-salts form in 250 cycles modeled for the Gale-relevant scenario.

We compare the minerals formed as a result of the thermochemical modeling with the minerals observed and inferred plausible in Gale crater (Chapter 1) in order to test whether the modeling results are applicable to Gale crater. We report that the minerals formed as a result of modeling are generally consistent with ones observed in Gale crater. In the next chapter (Chapter 3), we investigate a terrestrial analog area in Southern California and use the results to test the hypothesis we present in Chapter 1 (based on observations made in Gale crater) and Chapter 2 (thermochemical modeling of a Gale relevant scenario).

## References

Bridges, J.C., Schwenzer, S.P., Leveille, R., Westall, F., Wiens, R.C., Mangold, N., Bristow, T., Edwards, P. and Berger, G., (2015). Diagenesis and clay mineral formation at Gale Crater, Mars. *Journal of Geophysical Research: Planets*, *120*(1), pp.1-19

Das, D., Gasda, P. J., Wiens, R. C., Berlo, K., Leveille, R. J., Frydenvang, J., Mangold, M., et al. "Boron and lithium in calcium sulfate veins: Tracking precipitation of diagenetic materials in Vera Rubin Ridge, Gale crater." *Journal of Geophysical Research: Planets* 125, no. 8 (2020): e2019JE006301.

Felmy, A.R. and Weare, J.H., 1986. The prediction of borate mineral equilibria in natural waters: Application to Searles Lake, California. *Geochimica et Cosmochimica Acta*, *50*(12), pp.2771-2783.

Fraeman, A.A., Edgar, L.A., Rampe, E.B., Thompson, L.M., Frydenvang, J., Fedo, C.M., Catalano, J.G., Dietrich, W.E., Gabriel, T.S., Vasavada, A.R. and Grotzinger, J.P., 2020. Evidence for a diagenetic origin of Vera Rubin ridge, Gale crater, Mars: Summary and synthesis of Curiosity's exploration campaign. *Journal of Geophysical Research: Planets*, *125*(12), p.e2020JE006527.

Gibbard Jr, H.F. and Scatchard, G., 1973. Liquid-vapor equilibrium of aqueous lithium chloride, from 25 to 100. deg. and from 1.0 to 18.5 molal, and related properties. *Journal of Chemical and Engineering Data*, *18*(3), pp.293-298.

Rampe, E.B., Bristow, T.F., Morris, R.V., Morrison, S.M., Achilles, C.N., Ming, D.W., Vaniman, D.T., Blake, D.F., Tu, V.M., Chipera, S.J. and Yen, A.S., 2020. Mineralogy of Vera Rubin ridge from the Mars science laboratory CheMin instrument. *Journal of Geophysical Research: Planets*, *125*(9), p.e2019JE006306.

# Chapter Two

## Simulating evaporative wet and dry cycles in Gale crater, Mars using thermochemical modeling techniques.

D. Das[1], S.M.R. Turner[2], S.P Schwenzer[2], P J. Gasda[3], J Palandri[4], M.H. Reed[4], K. Berlo[1], R. J. Leveille[1], L. Crossey[3], N. L. Lanza[3]

[1]Department of Earth and Planetary Sciences, McGill University, Quebec, Canada H3A 0E8.

[2]AstrobiologyOU, School of Environment, Earth and Ecosystem Sciences, The Open University, Milton Keynes, United Kingdom

[3] Los Alamos National Laboratory, Los Alamos, NM, USA 87545.

[4]Department of Earth Sciences, University of Oregon, Eugene, USA 97403

[5]Department of Earth and Planetary Sciences, University of New Mexico, NM, USA 87131

### Abstract

The aim of this work is to understand the formation of evaporites in Gale crater using thermochemical modeling to determine constraints on formation of borates and Ca-sulfates in a Gale-relevant environment. We test the hypothesis that borates and Ca-sulfates required multiple wet-dry cycles, akin to how evaporite assemblages form on Earth. On Earth similar dry-lake environments are also enriched in lithium, though Li-salts are uncommon. Hence, we also monitor the concentration of Li in the evolving fluid during the modeling. For this research the database of CHIM-XPT was updated to include thermochemical parameters of borates in order to model a Gale-relevant scenario. Starting with a global Mars fluid B and Li were added in concentrations taken from natural stream waters from basaltic regions in Iceland. This fluid was titrated with a representative Gale rock composition with added B and Li concentrations to establish a Gale-relevant fluid. Cyclic evaporation and dilution were simulated to establish the minimum number of wet-dry cycles required to form primary evaporites that consist of borates and Ca-sulfates. We determine that a minimum of 250 wet-dry cycles are required to start forming evaporites that consist of borates and Ca-sulfates together from a Gale-relevant starting fluid and rock composition. We estimate that a minimum of ~14,250 annual cycles (~7.5 k Earth years) of wet and dry periods would be required for the formation of the primary borates and Ca-sulfates that could later be remobilized to form the veins that we see today in Gale. No Li-salts form in 250 cycles modeled for the Gale-relevant scenario. The minerals precipitated in the model match those observed or inferred in Gale crater. Therefore, wet-dry cycles were likely important in the formation of the borates and Ca-sulfates in Gale crater, confirming the starting hypothesis.

## 1 Introduction

The rock record within Gale crater consists of a dominantly lacustrine sequence that shows extensive evidence for aqueous activities that are inferred to consist of fluvial and lacustrine sedimentary deposition and ground-water circulation that took place over multiple generations (L'Haridon et al., 2020; Kronyak et al., 2019; Rapin et al.,2019; 2021). One of the important markers of aqueous activities in Gale crater are evaporites. Evaporites form as a result of fluid evaporation, and their chemical and physical characteristics are representative of their parent fluid compositions and surrounding environment (Bąbel and Schreiber, 2014; Smykatz-Kloss et al., 2010; Eugster, 1980). In Gale crater, calcium sulfate, magnesium sulfate, and halite have been observed (e.g., Nachon et al., 2014, 2017; Vaniman et al., 2018; Rapin et al., 2019; Thomas et al., 2019). The Ca-sulfate found in veins also contains highly water-soluble elements boron and lithium (Gasda et al., 2017; Das et al., 2020). In this work we use thermochemical modeling techniques to understand the enrichment of B and Li in close association with Ca-sulfates of Gale crater.

The presence of boron in close association with Ca-sulfate veins of Gale crater is hypothesized to be due to remobilization of preexisting borates (Gasda et al., 2017; Das et al., 2020). Clay minerals have been hypothesized to be reservoirs of Li in acidic fluids conditions (Das et al., 2020)

In terrestrial settings, boron commonly intergrows with Ca-sulfates as aggregates of extremely fine crystalline borates consisting of micron-sized crystals (as shown in micrographs in Hunt, 1996) in dry-lake environments that have experienced multiple wet-dry cycles (Orti et al., 1998; Lowenstein et al., 1999; Swihart et al., 2014). B-rich fluid or mineral inclusions in Ca-sulfates in terrestrial settings are rarely reported (Karmanocky., 2014; Orti et al., 2016; 1998).

Lithium is commonly observed as either adsorbed to the surfaces of clay minerals in the same vicinity as Ca-sulfates (Warren., 2016., Karahan et al., 2006; Nellessen et al., 2019; Rohmah et al., 2020; Li and Liu., 2020) or as lithium chloride in solution of dry lake brines (Song et al., 2017; Xiang et al., 2016) in terrestrial dry lake environments.  LiCl is highly hygroscopic in terrestrial atmospheric conditions and forms a self-solution through its property of deliquescence (Gibbard and Scatchard, 1973). Li-rich fluid inclusions associated with Ca-sulfates are also not commonly reported even in Li-rich brine environments (Ericksen et al., 1978; Yu et al., 2022). A review of the literature on emplacement of Li in terrestrial dry lake settings by Warren (2016) reports that most lithium salts are highly soluble and tend to stay in solution or can be adsorbed to playa clays.

Based on established hypotheses for enrichment of B and Li in Ca-sulfate veins of Gale crater and based on reports of B and Li reservoirs juxtapositioned in close proximity with terrestrial Ca-sulfates in dry lake environments, for this work, we start with the assumption that one of the reservoirs for B found in Ca-sulfate veins is borates. We also assume that clay minerals can be reservoirs for B and Li. For this work we investigate the formation conditions of evaporative borates and Ca-sulfates (as these two salts are found commonly together in terrestrial dry lakes) using thermochemical modeling techniques. We also investigate the Li in the modeled fluids as Li is commonly found either as LiCl in solution in dry lake brines or as adsorbed as $Li^+$ ions to clay minerals.

In this work, evaporites are referred to as either primary or secondary. In terrestrial settings, evaporites commonly form crusts or crystal accumulates on the brine pool floor (Warren, 2000; 2006). Freshly precipitated evaporites that have not undergone any burial, replacement, dehydration, or dissolution are referred to as “primary.” With time and processes such as dissolution with new fluids, and re-precipitation, evaporites can experience diagenesis. Evaporites that have undergone any diagenetic processes are referred to as “secondary” (Warren, 2000; 2006). All evaporites observed in Gale crater are inferred to be representatives of secondary diagenetic processes that consisted of multiple generations of remobilization of primary evaporites by groundwater (Nachon et al. 2014, Gasda et al., 2017; Kronyak et al., 2019).

We simulate the conditions required to form primary borates and Ca-sulfates using a Gale-relevant fluid while reporting the corresponding Li concentration of the modeled fluid. We do not cover the secondary diagenetic remobilization processes that are inferred to have affected the primary evaporites or the Li adsorption process to clay minerals inferred for Gale crater (Frydenvang et al., 2020) under the simulation performed in this work and provide a base-level thermochemically stable scenario required for the formation of primary borates and Ca-sulfates from a Gale-relevant fluid with corresponding Li abundances possible for this fluid.

Brines precipitate evaporites in a sequence based on the relative availability and solubility of elements that compose the brine (Sarg, 2001). In a brine solution, the most soluble combination of elements will form an evaporitic phase once the relative concentration of the soluble elements is considerably higher than that of the relatively less soluble elements (Dalton et al., 2016). Similarly, when an assemblage of evaporites is in contact with a fluid, the first evaporites to dissolve are the ones that are made of elements with higher relative solubilities. Evaporitic phases will dissolve up to a certain amount depending on the amount of fluid in contact. Hence, in an assemblage of multiple evaporites, the composition of the evaporites is representative of specific fluid composition and extent of evaporation. A specific evaporitic assemblage can constrain the relative amount of time required to form the evaporites if the composition of the starting fluid is known. One of the terrestrial environments where evaporitic assemblages consisting of Ca-sulfates and borates are common is dry lakes that have experienced seasonal wet (with input of water by rain) and dry (dehydration during elevated summer temperatures) cycles (Orti et al., 1998; Lowenstein et al., 1999; Swihart et al., 2014). Evaporites vary in solubilities and precipitate in a sequence based on their relative saturation points in their parent fluid (Ochsenius, 1888; Scruton, 1953). The close association of specific types of evaporites can be representative of the precipitation sequence, the temporal range of their formation (Sarg, 2001), and the environmental conditions under which they have formed (Lowenstein et al., 1999).

In this study we focus on establishing a minimum time constraint to form borates and Ca-sulfates starting with a Gale relevant fluid. We hypothesize that multiple wet and dry cycles consisting of evaporation-assisted sequential precipitation and remobilization caused by dilution is required to form a part of the evaporitic assemblage we observe in Gale crater. We use thermochemical modeling to test this hypothesis as a continuation of previous thermochemical models established for Gale aqueous fluids (Bridges et al., 2015; Schwenzer et al., 2016; Turner et al., 2021). Determining this minimum number of wet and dry cycles and placing it in the context of the broader timeline established using sedimentological observations made by the Curiosity rover, enables a better understanding of the window of habitability at unprecedented temporal resolution.

## 2 Geologic context of Gale crater

Gale crater is a ~155 km wide crater with a central sedimentary mound (Aeolis Mons, informally known as "Mount Sharp") located between the Southern Highlands and Northern Lowlands division in the northwestern part of the Aeolis quadrangle (Milliken et al., 2010; Grotzinger and Milliken, 2012; Fraeman et al., 2016). NASA's Mars Science Laboratory (MSL) Curiosity rover landed in Gale crater on Aeolis Palus in 2012 and has since then traversed over 28 km towards Mount Sharp across outcrops interpreted as eolian, fluvial deltaic, and lacustrine deposits (e.g., Milliken et al., 2010; Grotzinger et al., 2014; 2015; Banham et al., 2018; Stack et al., 2019; Edgar et al., 2020, Vasavada et al., 2014; Vasavada 2022).

The geochemistry and sedimentology of rocks in Gale crater points to the presence of an ancient stratified habitable lake with possible varying lake levels (e.g., Grotzinger et al., 2015; Hurowitz et al., 2017; Rapin et al. 2020) and a long-standing extensive groundwater system (e.g., Siebach and Grotzinger, 2014; Frydenvang et al., 2017, Gasda et al., 2017). The varying lake levels in Gale are inferred from observations of features consistent with lake margin and evaporitic environments (e.g., Kah et al., 2018; Stein et al., 2018; Rapin et al., 2019; Gwizd et al., 2022).

In the lithological unit named the Mount Sharp group in Gale crater, evidence of desiccation and evaporation are observed in the Hartmann's Valley though Sutton Island lithologic members and are interpreted as fluctuating lake margins or a braided river deltaic environment (Stein et al, 2018; Fedo et al., 2018; Gwizd et al., 2022). The evidence includes presence of evaporites (Gasda et al., 2017; Thomas et al., 2019; Rapin et al., 2019, Das et al., 2020), desiccation cracks (Stein et al, 2018), altered clay minerals (Bristow et al., 2018), and lithologic facies that are interpreted as lake margin depositional settings (Fedo et al., 2018, Edgar et al., 2020; Gwizd et al., 2022).

In addition to varying lake levels, evidence for multiple stages of aqueous activity throughout much of its history are also observed in Gale crater. The inference of multiple stages of aqueous activity is based on the observation of textures of cross-cutting diagenetic features such as veins. Vein morphology is heterogeneous: they are observed to be massive, nodular, bowl-shaped, boxwork, resistant to erosion, and/or sub-horizontal. Thicker veins display toothy, fibrous, or nodular textures which are interpreted to indicate multiple generations of evaporitic deposition and remobilization within fractures (Siebach et al., 2014; Nachon et al., 2014; 2017; Schwenzer et al., 2016; Gasda et al., 2017; 2022; Kronyak et al., 2019; Das et al., 2020). Multiple generations of wet periods which may be cyclic in nature resulting in sequential precipitation are also inferred based on the relationship between the relative abundance of B and Li (which differ in solubilities) in diagenetic Ca-sulfate veins (Gasda et al., 2017; Das et al., 2020).

## 3 Hypothesis and objective

In this work, we aim to understand the formation of primary evaporites in Gale crater. We test the hypothesis that formation of primary borates and Ca-sulfates requires multiple wet-dry cycles, akin to how evaporite assemblages form on the Earth. Li salts are not common in terrestrial dry lake settings so although we include Li in our model, we focus on the minimum time constraint for the formation of borates and Ca-sulfates and use the results to verify if the precipitation of Li salts is feasible in a Gale-like environment.

The hypothesis of wet and dry cycles is based on textural, mineralogical, and sedimentological observations in Gale crater that also point towards multiple generations of wet-dry cycles in Gale crater as described in section 2. We also base this hypothesis on the terrestrial observation of B enrichment observed in close association with Ca-sulfates in analogue dry-lake environments that have experienced multiple generations of evaporation and dilution (Guo et al., 2021; Orti et al., 2016; 1998; Tanner, 2002).

Although primary evaporites are yet to be observed directly in Gale, for this work, we also start from the hypothesis that primary borate and Ca-sulfate minerals were present in Gale crater's aqueous history and later remobilized by groundwater (Gasda et al., 2017; Das et al., 2020). The objective of this work is therefore to simulate the conditions required to form primary borates and Ca-sulfates using a Gale-relevant fluid while monitoring the Li concentrations in the modeled fluids.

Through this work, we also aim to estimate a temporal constraint for the minimum number of cycles required to form primary Ca-sulfates and borates in a Gale-like environment based on comparison with terrestrial lake systems. For the purpose of this model, we assume that one annual cycle on Mars consists of one dry and one wet period and that the relative amount of time for the number of cycles can be constrained based on comparison with terrestrial closed lake systems. All assumptions made in this work are listed in section 4.2. The processes that are hypothesized to contribute to the geochemistry of the evaporites are water-rock reactions between Gale rocks and groundwater, evaporation of lake water, and groundwater-lake water mixing, taking place in cyclic intervals as shown in Figure 1. Each step shown in Figure 1 is explained in detail in the Methodology section.

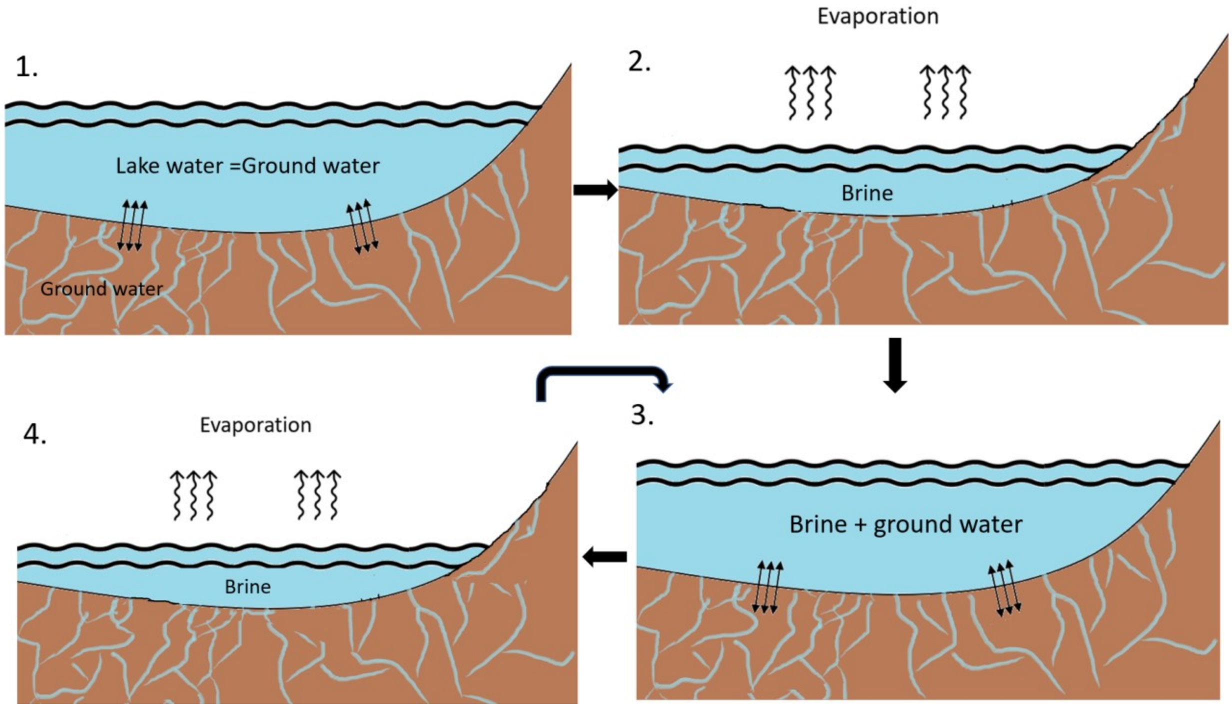

**Figure 1**. Illustration of the hypothesized sequence of events occurring in Gale crater and tested herein. The sequence involves equilibration of lake water with ground water, cyclic dissolution and evaporation loops. Each component is described in detail in the methodology section.

## 4 Methodology

In this work, we use a Gale-relevant fluid and a representative Gale rock composition to simulate cyclic dissolution and evaporation of lake water using CHIM-XPT and starting assumptions regarding the system (details in section 4.1 and 4.2). Prior to executing the simulation steps, we have updated the thermochemical database of CHIM-XPT to include phases that are relevant for this work (i.e., borates) and tested the updated database using a terrestrial analog fluid composition (details in 4.3). Following the data update and testing, we used CHIM-XPT to simulate fluid-rock titration, fluid-fluid mixing, and evaporation (details in section 4.4). We simulated four cycles of wet and dry periods using CHIM-XPT, and based on the composition of the resultant phases, we extrapolated brine compositions for up to 250 wet and dry cycles to test the minimum number of cycles required to form Ca-sulfates and borates (details in section 4.4). Following this step, we used time constraints established for terrestrial closed lakes to estimate a minimum time constraint for the number of wet and dry cycles required to form Ca-sulfates and borates for a Gale-relevant scenario (details in section 5).

### 4.1 Assumptions

For this work, we start from the hypothesis that the primary host of B associated with Ca-sulfate is borate minerals and the primary host of Li is clay minerals. In terrestrial dry lake settings, Li salt minerals are not common (as described in section 1 and 3).

We start by establishing a relevant fluid composition. First, we take the global Mars-relevant fluid i.e., Gale Portage Water (Bridges et al., 2015) and modify it to incorporate B and Li by adding B and Li in abundances observed in Icelandic stream waters (described in detail in section 4.4). This is the best available estimate for a global Mars-relevant fluid, and titration between this fluid and a Gale-relevant rock composition will equilibrate the fluids with local host rock chemistry and can thus be used to simulate a Gale-relevant groundwater composition (details in section 4.4.1).We assume that the average unweathered bedrock composition from the Hartmann's Valley member in Gale crater (Frydenvang et al., 2020) can be used as a representative of the bedrock hosting an early Gale lake for establishing a Gale-relevant groundwater for this model (explained in section 4.4.2).

We also assume, on the basis of the sedimentological observations (see section 2) that the wet-dry cycling process takes place in a relatively low-temperature range (25°C) and exclude high-temperature phases such as garnet, amphiboles, pyroxenes and high-temperature mica minerals that are known to form in igneous and metamorphic environments. We assume all silica forming as a resultant phase in this system is quartz and assume that no high-temperature silica polymorphs form in this system. This assumption does not change the results of the modeling steps as model inputs silica as $H_4SiO_4$ and other low temperature silica phases such as opal are very similar in their thermochemical properties and hence would form at the same point in the model and in the same quantities.

In order to determine a specific constraint on the number of cycles required to form Ca-sulfates and borates in a Gale-like environment, we have minimized the number of processes that participate in this system to include only water-rock interaction (between established Gale-relevant fluid and Gale-relevant rock composition), evaporation (that results in the formation of brine) and water-water mixing (between established Gale relevant fluid and the modeled brine). We also extrapolate the number of cycles required to form observed evaporites such as Mg sulfate and halite based on the results from this model and assuming a linear relationship.

For this reason, the results of this work are a minimum constraint and act as a baseline requirement for the start of formation of Ca-sulfates and borates. The results represent a part of a geologically complex system (i.e., formation of Ca-sulfates and borates through cyclic dissolution and evaporation) and cannot be used as a stand-alone representative of all aqueous processes in Gale crater. For this modeling, we assume that in a period when Gale crater hosted lakes, the ambient pressure and temperature was similar to that of the Earth's, and we set the ambient pressure to 1 bar and ambient temperature is 25°C. We assume that the system is closed to reaction with the martian atmosphere or fluids other than groundwater. We assume that one annual cycle on Mars consists of one dry and wet period and that the relative amount of time for the number of cycles can be constrained based on comparison with terrestrial closed lake systems.

We also assume that in case of evaporation, the lake does not evaporate to dryness as the majority of liquid water on Mars is inferred to have been underground longer than the surface water (Scheller et al., 2021). Hence, we assume that the presence of groundwater prevented Gale crater being fully dry in its early aqueous history and stop the model at 10 moles of $H_2O$ in the system. This point was chosen as sulfate precipitation is in equilibrium at this stage, but no salt more soluble than Ca-sulfate precipitates. We also assume linearity for the wet-dry cycle extrapolation as we assume it is a representative of an overall average for the specific scenario being modeled in this work where a Gale-relevant system is open to a local Gale fluid mixing with a brine. We also assume for the purpose of this modeling that there is a constant supply of the fluids involved.

## 4.2 Thermochemical modeling tool

CHIM-XPT (Reed et al., 2010) is a non-commercial and free of cost program for computing multicomponent heterogeneous chemical equilibria in aqueous–mineral–gas systems and was chosen because it has been specifically developed (and the database adjusted) for Mars-relevant basaltic systems (Reed and Spycher, 2006; Reed et al.,2010) and therefore been used extensively in modeling aqueous activities on Mars (Bridges et al., 2015; Filiberto & Schwenzer, 2013; Melwani-Daswani et al., 2016; Schwenzer & Kring, 2009; Schwenzer et al., 2012; 2014; 2016; 2020). The modeling calculations take place in steps where each step calculates the minimum Gibbs free energy of the system to attain equilibrium for fluids and their potential precipitates in case of evaporation or fluid-fluid mixing and to attain equilibrium between fluid, precipitates, and dissolved rock in case of fluid-rock rock mixing. The calculations are done based on a database consisting of thermochemical properties of minerals and molecular species. Step sizes are determined based on the requirement of the calculation and are independent of the amount of water in the system as weight ratios (with a base unit of moles) are used for the calculations. The calculations are based on 1 kg (55.5 mol) of water and the water-to-rock ratio (W/R) is the ratio of fluid to reacted host rock. Precipitates are not fractionated out of the system unless stated otherwise. No external gas phases are included or replenished in this model. We assume that the system is closed to reacting with the martian atmosphere and assume an ambient temperature of 25°C and atmospheric temperature of 1 bar. However, during the modeling gas phases were allowed to form unless stated otherwise. More details regarding the code, database and input files, can be found in the handbook for CHIM-XPT (Reed et al., 2010).

## 4.3 Thermochemical database update and testing

The version of CHIM-XPT thermochemical database available during the start of this work did not include thermochemical parameters for any borate minerals. The CHIM-XPT thermochemical database includes LiCl (which can be found in solution in terrestrial dry lake brines), however it does not include thermochemical parameters for Li-carbonates or other Li salts. As Li salts are not commonly formed in terrestrial dry lake settings, for this work we only focus on the formation conditions of primary borates and Ca-sulfates and report the abundance of Li in the modeled fluids.

To model the behavior of boron in a Gale-relevant evaporative environment using CHIM-XPT, thermochemical parameters of three borates (kernite, borax, and tincalconite) were added to the existing database before performing the modeling steps. The database was updated with heat capacity coefficients of kernite, borax, and tincalconite based on the values experimentally determined by Ruhl (2008).

The updated database was tested by simulating evaporation using a fluid composition from Searles Lake, in Southern California, as analyzed by Felmy and Weare (1986). This area was chosen due to the presence of borates in a dry lake environment and due to the availability of brine composition that is known to form borates in the corresponding dry lake system. This test confirmed that borates formed as products of the updated modeling database if an evaporation was simulated. Table 1 indicates the composition of the fluid used for testing the updated database. Evaporation was simulated for 1 kg of fluid at 25°C at 1 bar pressure by incrementally removing $H_2O$ from the system. The resultant minerals formed during this test included calcite, borax, kernite, halite, sylvite, and anhydrite and are comparable to the minerals observed by

Felmy and Weare (1986) in Searles Lake. Based on this test it was established that the updated database was functioning as expected and could be used to model a system involving borates.

**Table 1**. Fluid composition from Searles Lake (Felmy and Weare, 1986) used for testing the updated CHIM-XPT database

| **Ions** | **Moles/Kg** |
|---|---|
| $Cl^-$ | 5.41 |
| $SO_4^-$ | 0.75 |
| $HCO_3^-$ | 1.04 |
| $Ca_2^+$ | 0.141 |
| $Mg_2^+$ | 0.127 E-05 |
| $K^+$ | 1.01 |
| $Na^+$ | 7.45 |
| $Mn_2^+$ | 0.436 E-07 |
| $Li^+$ | 0.46 |
| $B_3O_3(OH)_4^-$ | 2.60 |

### 4.4 Establishing a Gale relevant scenario to model an evaporative environment

In order to model evaporative cycling in Gale-crater, a Gale relevant fluid was established by first modifying Gale Portage Water (Bridges et al., 2015a, 2015b; Schwenzer et al., 2016; Turner et al., 2019) to include B and Li and then titrating the modified Gale Portage Water (mGPW) composition with a Gale-relevant rock composition. In the following sub sections (4.4.1 and 4.4.2), the details about mGPW and the Gale-relevant rock composition is described. In section 4.4.3, details about titrating mGPW with a Gale-relevant host rock to establish a Gale-relevant fluid is described. Cyclic evaporation and dilution have been modeled using this Gale-relevant fluid, and the modeling methodologies for evaporation and dilution are described in sections 4.4.4 and 4.4.5. All the resultant minerals and fluid compositions formed during the simulations are summarized in section 5 (Results).

### 4.4.1 Global Mars-relevant fluid: Modified Gale Portage Water

The starting fluid used for the modeling is Gale Portage Water (Schwenzer and Kring, 2019; Bridges et al., 2015a, 2015b; Schwenzer et al., 2016; Turner et al., 2019). GPW was derived from a Deccan Trap fluid and adjusted to Mars-relevant element ratios to represent a global Mars-relevant groundwater. GPW is one of the widely used global Mars relevant fluids by the Mars fluid modeling community (Turner et al.,2020; Bedford et al., 2016), however the GPW does not contain B and Li. Using an established fluid allows us to compare our results directly with the literature.

Therefore, we modified the composition of GPW to include B and Li. The amount of B and Li added to the GPW composition is an average of Icelandic stream water from Reykjanes as summarized by Olaffson and Riley (1978). The value for B used is 11 ppm and for Li is 8ppm which are average concentrations from two natural spring water compositions (Spring 1967 and Spring 1918) reported by Olaffson and Riley (1978). For the modeling purposes, the B abundance value of 11 ppm was converted to a corresponding number of moles of $H_3BO_3$ in solution (i.e., 8.39E-04 moles in one kg of water as shown in Table 2) and the Li abundance value of 8 ppm was converted to corresponding number of moles of Li+ in solution (i.e., 1.15E-04 moles in one kg of water as shown in Table 2). Average concentrations of B and Li of Icelandic natural waters were used because Icelandic rocks are a widely used terrestrial analog for martian water-rock interaction (e.g., Ehlmann et al., 2012; Schwenzer et al., 2016; Thorpe et al., 2022) and the natural water compositions provide a geologically realistic abundance ratio of B and Li for a Gale-relevant terrain.

When compared to Icelandic fluids, GPW is lower in abundance of $SiO_2$, $Ca^{2+}$, $Mg^{2+}$, $K^+$, $Na^+$, and $Mn^{2+}$. This is due to the extent of weathering in Gale crater based on the observation of minerals such as clinopyroxene and plagioclase (e.g., Bridges et al., 2015; Rampe et al., 2020) and the inference that Ca-containing minerals clinopyroxene and plagioclase were only partially altered (Mangold et al., 2019). The presence of these minerals in the Gale crater bedrock indicates that Gale experienced enough weathering to produce smectite clays from olivine, but the rocks did not fully weather all the igneous minerals in the sediment (e.g., Morrison et al., 2018, Bridges et al., 2015; Thorpe et al., 2022).

The composition of GPW is based on observations made in Gale crater and measurements of martian meteorites and is different from Icelandic fluids, which are derived from a higher extent of aqueous alteration. Table 2 indicates that GPW is lower in $Cl^-$ compared to Icelandic fluids. The abundance of the water-soluble species in GPW, such as $Cl^-$ and $SO_4^{2-}$, are comparable to Nakhlites (a class of martian meteorite). $Cl^-$ abundance in Icelandic basalts range from $2.1 \times 10^{-3}$ to $1.9 \times 10^{-2}$ moles/kg (Arnórsson and Andrésdóttir, 1995), whereas the martian meteorite that is considered a close precursor of Gale contains $2.25 \times 10^{-3}$ moles/kg of $Cl^-$. The relative amount of $Cl^-$ of a Gale-relevant martian meteorite is on the lower end of the range of $Cl^-$ abundances measured for Icelandic basalts. GPW has comparable abundances (within an order of magnitude) of water-soluble species $Cl^-$ and $SO_4^{2-}$ as these species readily dissolve in the fluid unlike $SiO_2$, $Ca^{2+}$, $Mg^{2+}$, $K^+$, $Na^+$, and $Mn^{2+}$ which are major rock-forming elements and are bound in the crystal structure of igneous minerals that require higher rates of alteration to dissolve. For these reasons, the relative concentration of $SiO_2$, $Ca^{2+}$, $Mg^{2+}$, $K^+$, $Na^+$, $Mn^{2+}$ in GPW is expected to be lower than that of Icelandic fluids, which have undergone more weathering.

B and Li are not major rock-forming elements in most igneous minerals and are mobile, i.e., they can diffuse out of minerals due to their small size. These elements will quickly go into solution during aqueous alteration. Hence, the relative concentrations of these elements in Icelandic waters will likely be similar to Gale, regardless of the difference of degree of alteration between Iceland and Gale crater. The B and Li abundances chosen for modifying GPW are from a thermal brine that is associated with geothermal activity and are comparatively higher than B concentration range reported for non-thermal and low-temperature fluids which range between 0.01-3 moles $H_3BO_3$ (Arnórsson and Andrésdóttir, 1995). However, we use these values because these are measured B and Li concentrations in a natural system that is used as an analog for Gale crater's basaltic terrain (Thorpe et al., 2021) and note that these values are an upper estimate of what could be possible for a Gale-relevant fluid. We also note that the B and Li values selected for modifying GPW are overall comparable to the abundances of B and Li observed in Nakhlites.

Hence in order to establish a Mars-relevant fluid with best estimates for B and Li, we use fluid composition values from a natural terrestrial Gale crater analog while considering measured martian meteorite compositions and observations made in Gale crater. GPW is a global Mars-relevant fluid (Bridges et al., 2015). Modified GPW (mGPW) with updated B and Li is also representative of a global Mars fluid as it does not take into consideration the local geochemical variations in the rocks of Gale crater. So, the next step is to take this into account by equilibrating mGPW with a Gale crater rock.

**Table 2:** Fluid composition of Gale Portage Water and modification made using Icelandic natural lakes and groundwater. Compositions of fluid are indicated in molar concentration (moles/kg of water or rock).

| | Original GPW | Modified GPW | Reykjanes Spring water Olaffson and Riley (1978) | Nakhlite meteorite Lodders et al. (1998) |
|---|---|---|---|---|
| $Cl^-$ | 5.76 E-03 | 5.76 E-03 | 7.8 E-01 | 2.25 E-03 |
| $SO^{4-}$ | 3.97 E-03 | 3.97 E-03 | 1.7 E-03 | 5.41 E-03 |
| $HCO^{3-}$ | 1.68 E-04 | 1.68 E-04 | - | - |
| $SiO_2$ | 3.49 E-05 | 3.49 E-05 | 9.3 E-03 | 8.9 E-00 |
| $Ca^{2+}$ | 1.401 E-05 | 1.401 E-05 | 5.9 E-02 | 2.6 E-00 |
| $Mg^{2+}$ | 1.27 E-08 | 1.27 E-08 | 2.2 E-03 | 2.9 E-00 |
| $K^+$ | 5.02 E-04 | 5.02 E-04 | 5.3 E-02 | 1.2 E-02 |
| $Na^+$ | 9.20 E-03 | 9.20 E-03 | 6.1 E-01 | 7.3 E-02 |
| $Mn^{2+}$ | 4.36 E-08 | 4.36 E-08 | 6.8 E-05 | 6.7 E-02 |
| $Li^+$ | - | 1.15 E-04 | 1.15 E-04 | 4.62 E-04 |
| $H_3BO_3$ | - | 8.39 E-04 | 8.39 E-04 | 5.76 E-04 |

We select the Hartmann's Valley (HV) region for this work as it shows evidence of dehydration in an environment that is inferred to be that of a lake margin (Gwizd et al., 2018; Gwizd et al., 2022). We selected the average bedrock composition of HV, obtained by the ChemCam instrument, that is calculated from a dataset where points with obvious diagenetic materials, soils, and out of focus points, have been removed (Frydenvang et al., 2020). This contrasts with APXS data, which is representative of the bulk chemistry of the rock and includes a Ca sulfate component and other diagenetic materials in the rock. The small spot size (100-500 microns) of

ChemCam compared to 4 cm for APXS, enables this type of measurement (Wiens et al., 2012; Maurice et al., 2012; Gellert et al., 2013). For comparison, the average CaO composition of HV without diagenetic points is 1.6 wt% CaO (Table 3) and the APXS measurements of bulk rock (drill tailings) of Oudam on at the base of HV is 4.03 wt% CaO and 3.54 wt% $SO_3$ and Marimba just above HV is 5.27 wt% CaO and 6.78 wt% $SO_3$. ChemCam does not have a quantification for $SO_3$, but the average composition of HV sums to ~97 wt% (Table 3), indicating that there can be no more than 3 wt% of elements not quantified by ChemCam in Table 3 (e.g., S, P, Cl, H etc.), and we assume based on the clay content that the majority of the missing composition in HV is water (Thomas et al., 2020). Having data from areas in Hartmann's Valley which are not contaminated by Ca sulfate from late-stage diagenesis enables estimation of conditions that are relevant for the formation of primary evaporites. In the next section, we describe the steps taken for simulating a Gale-relevant fluid pertaining to an area that shows evidence of having experienced wet and dry cycles.

### 4.4.2 Gale-relevant host rock: Modified average Hartmann's Valley

We use a modified average Hartmann's Valley bedrock composition as a Gale-relevant host rock to simulate a Gale-relevant fluid. Although we have a ChemCam data of the Hartmann's Valley area with minimal Ca sulfate presence, we do not have a quantification of B, Li, or S in the targets of Hartmann's Valley area ChemCam data. For this reason, we estimate the B, Li, and S values of Hartmann's Valley area rocks based on measured martian meteorite Nakhlite. We use the major oxide compositions from the Hartmann's Valley target area determined using the ChemCam instrument and modify this composition by extrapolating S, B and Li concentrations based on concentrations observed in the Nakhlite meteorites (Lodders, 1998). B, Li, and S of a basaltic rock relevant to Gale crater helps us set a preliminary estimate on abundance of B, Li, and S in the early sedimentary rocks of Gale crater. The Hartmann's Valley modified rock composition based on ChemCam data reported by Frydenvang et al., 2020 and measured martian meteorite Nakhlite used for this modeling run are shown in Table 3.

**Table 3.** Average bedrock composition of the Hartmann's Valley target area modified with S, Li, and B concentrations measured in Nakhlite meteorites.

| **Oxide** | **Wt%** |
|---|---|
| $SiO_2$ | 53.6 |
| $TiO_2$ | 0.94 |
| $Al_2O_3$ | 11.9 |
| $FeO_T$ | 18.7 |
| MgO | 6.5 |
| CaO | 1.6 |
| $Na_2O$ | 2.58 |
| $K_2O$ | 1.16 |
| MnO | 0.05 |
| S | 0.02 |
| Li | 0.0004 |
| B | 0.0005 |

### 4.4.3. Establishing a local Gale-relevant fluid: Titrating modified GPW with modified Hartmann's Valley rock composition

In this section, we describe the process of simulating a Gale-relevant lake fluid from a modified Mars-relevant groundwater fluid (i.e., mGPW). As mentioned in the previous section, we are simulating wet and dry cycles for a specific region in Gale crater. Hence, in this modeling step we use a global Mars-relevant fluid which is an estimate for possible incoming martian ground water composition (mGPW) to simulate a local lake fluid which we estimate formed due to interaction between the global Mars groundwater and local Gale crater rocks. In order to estimate a composition of a Gale lake fluid, we start by simulating the interaction between early (unaffected by diagenesis) Gale rock composition from Hartmann's Valley (with an estimated value for B, Li, and S) and the modified global Mars groundwater (mGPW). We do this by equilibrating a range of water volumes (with a maximum of 1 liter of mGPW) with 1 kg of rock with the modified composition of Hartmann's Valley by using the titration function in CHIM-XPT.

For this work, titration was modeled at 25°C and 1 bar pressure in incremental water: rock steps with a minimum step size of 0.0001 and a minimum step limit of 0.001. The amount of resultant minerals for the various water-rock ratios are plotted in Figure 2. This enabled comparison between the modeled resultant minerals and their abundances with the mineral observations made in Gale crater.

Below the 1:50000 water rock ratio, the relative amount of chlorite forming due to the reaction between the local Gale lake water and the Hartmann's Valley rock is higher than what is expected for Gale crater as chlorite is observed in Gale crater only in minor amounts (<1 wt%) (Treiman et al., 2016; Vaniman et al., 2014). Abundant chlorite is not characteristic of rocks in Gale crater (Vaniman et al., 2014) and this minor amount is consistent for the local area surrounding Hartmann's Valley (Fraeman et al., 2020). Hence, we do not select a water: rock ratio below 1:50000. Above the 1:50000 water rock ratio, the relative amount of nontronite is lower with a relative increase in the amount of kaolinite which is not reported for Gale crater (Milliken et al., Rampe et al., 2020). Hence the selection of a water: rock ratio of 1:50000 is based on the comparison of the relative abundances of minerals formed during the lake water-rock reaction with the observations made in Gale crater. This comparison helps us estimate the most likely water-rock ratio present when a martian groundwater fluid interacted with the Hartmann's Valley rocks.

Therefore, for this work, we choose the water: rock ratio of 1:50000 as at this ratio, the resultant minerals in the reacted fraction are clay minerals (~98 wt%), sulfides (~1.5 wt%) and trace amounts of chlorite (~ 0.5 wt%). We note that these clay minerals, and sulfides would have formed in addition to the bulk rock from Hartmann's Valley. The weight percentages are representative of the fractions formed during the simulated reaction between 1 kg of the local Gale fluid and 1 kg of Hartmann's Valley water-rock ratio and are representative of the alteration assemblage fraction in Gale.

In the 1:50000 water-rock ratio we observe the alteration assemblage of ~60 wt% nontronite and ~30 wt% kaolinite. Nontronites are frequently observed in Gale crater including the area surrounding the Hartmann's Valley region (McAdam et al., 2020; Rampe et al., 2020) hence a relatively high abundance of nontronite in the simulated water-rock reaction points towards the plausibility of a water: rock ratio of 1:50000. Minor amounts of both kaolinite and chlorite are identified in Gale crater (Treiman et al., 2016; Vaniman et al., 2014) hence ~30 wt% of kaolinite and ~0.5 wt% chlorite in a 1 kg water: rock reaction is considered plausible for forming relative amounts of kaolinite and chlorite for a Gale-relevant scenario.

Resultant minerals and comparison to terrestrial and Martian observations are described in section 5 (Results). The selected water-to-rock ration is shown in Figure 2. The selected fluid composition is shown in Table 4 in the results section. This fluid composition at a water rock ratio of 1:50000 is the established local Gale lake fluid. We simulate evaporation of this fluid in the next steps to establish a brine composition and also use this local Gale lake fluid to dilute the brine for a fluid-mixing scenario simulation.

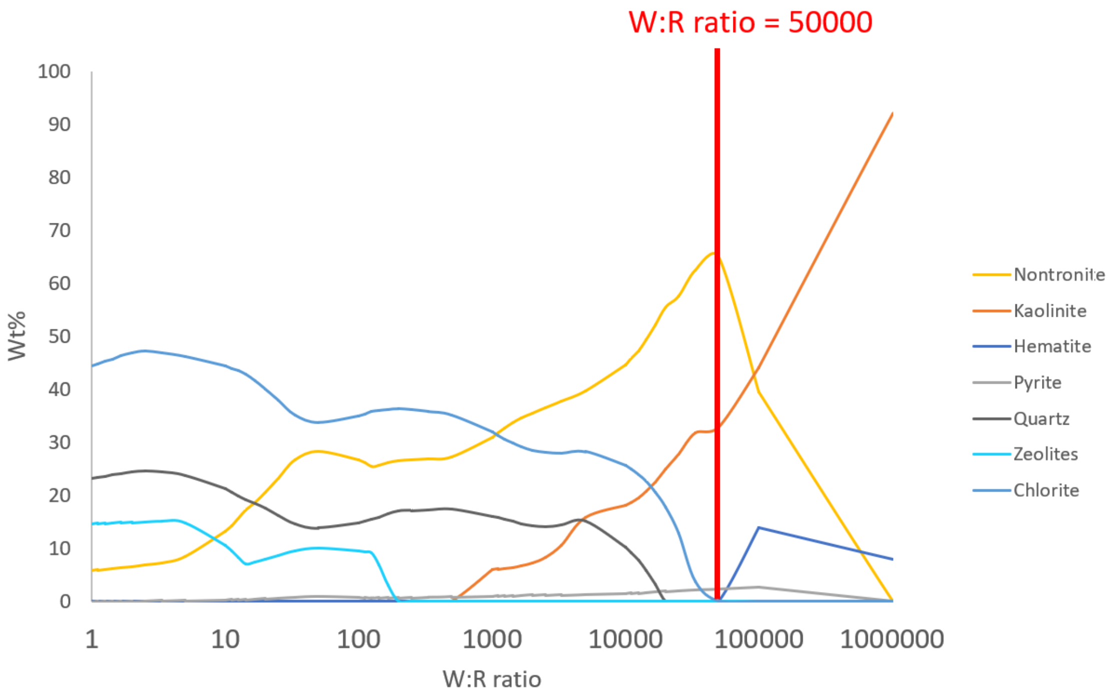

**Figure 2**. A plot indicating the relative abundances of minerals formed in varying water: rock ratio during the titration of a local Gale lake fluid and Hartmann's Valley rock. A fluid at a water: rock ratio of 1: 50000 was selected to forward the modeling steps based on mineralogical observations made in Gale crater as described in section 4.4.3.

### 4.4.4 Setting evaporation and dissolution cycles

After establishing the Gale lake fluid, we used modeling techniques to simulate evaporation and dissolution cycles that are assumed to represent dry and wet cycles. In this work, we model a total of 4 cycles (cycle 0-cycle 3) consisting of four evaporation runs and four dissolution runs. The fluid composition at each of these steps is shown in Tables 4 and 5, and the results are summarized in section 5. The next sections describe the methodology for simulating evaporation (section 4.4.4.1) and dissolution (section 4.4.4.2).

### 4.4.4.1 Evaporation

Evaporation of the Gale lake fluid was simulated by incrementally removing $H_2O$ from the system at 1 bar pressure and at 25°C down to 10 moles of water remaining in the system. As mentioned in section 4.1, we assume that in the case of evaporation, the lake does not evaporate to complete dryness, hence we stop the model at 10 moles of $H_2O$ in the system. The resulting brine composition is shown in Table 5. The resultant minerals formed throughout simulated evaporation are shown in Figure 3 and listed in Table 7. At 10 moles of $H_2O$, predominantly $SiO_2$ is formed, however, for a dilute lake water the resultant phases forming are expected to be proportionately low in quantity and thus only observed occasionally or below detection limit of the rover instrumentation entirely. Limited observations of low-temperature, hydrated silica have been made in Gale crater (Rapin et al., 2018, Morris et al., 2016) including observations made in the Hartmann's Valley region (Achilles et al., 2020) which points towards the plausibility of this modeled evaporative scenario in the Hartmann's Valley area of Gale crater. The evaporation process was repeated after every fluid mixing step for 3 cycles to simulate cyclicity. In every evaporation step the $H_2O$ was reduced to 10 moles to determine the brine composition for the subsequent fluid mixing step.

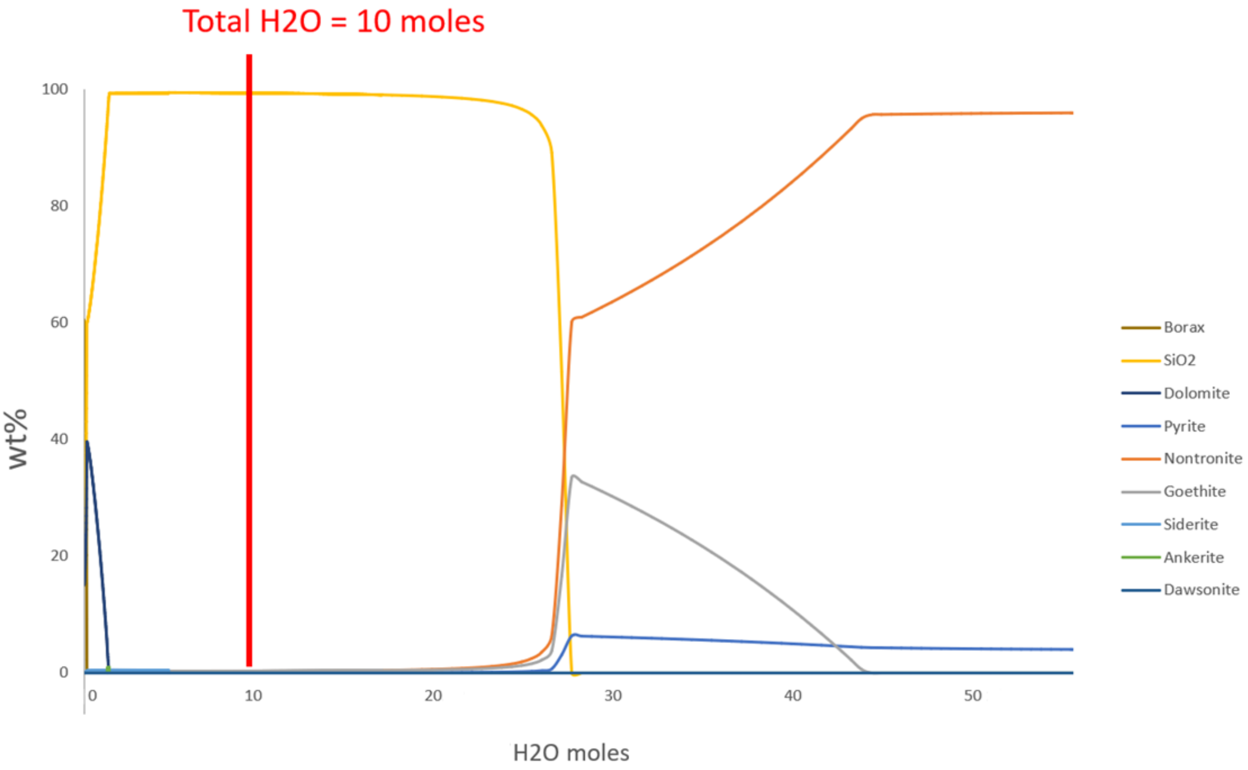

**Figure 3.** Resultant minerals after evaporating the fluid down to 10 moles $H_2O$. Weight percent of resultant minerals (y-axis) plotted against total water content (x-axis). Amount of water reduces from right to left.

### 4.4.4.2 Dilution

Following the simulation of evaporation, fluid mixing, or dilution, was simulated by iteratively mixing the local Gale lake water (described in section 4.3.3) with 1 kg of the brine composition described in the previous section (and shown in Table 5). In this step, a fluid-fluid mixing between brine and groundwater was simulated by incrementally titrating the two fluids in a range of mixing fractions between 0:1 and 1:1. We choose to feed forward the fluid composition for next steps of the model at a 1:1 mixing ration because we assume complete mixing between the brine composition and the local Gale lake fluid.

For the purpose of the model, we use 1 kg of starting fluids, however in a geologically realistic scenario, the amount of fluid left may not be 1 kg and would be similar to water levels in a terrestrial dry lake, especially for Hartmann's Valley where a lake margin environment is inferred. As we want to simulate complete mixing, we use a proportionate amount of local Gale lake fluid. Figure 4 indicates that at a mixing fraction of 1:1, predominantly kaolinite would form. The amount of kaolinite precipitated is less than a microgram per kilogram of water and therefore consistent with the occasional small amount observed in Gale. We assume that there is equal parts of brine and local Gale fluid mixing as in the Hesperian we are dealing with progressively drier climate. This is within the realistic parameter space. Because in the Hesperian, the climate is getting progressively drier (Rapin et al., 2021), we assume that the overall lake is shrinking and assume that the lake is not fully replenished but instead work with a 1:1 ratio of evaporated fluid to incoming fresh local Gale fluid.

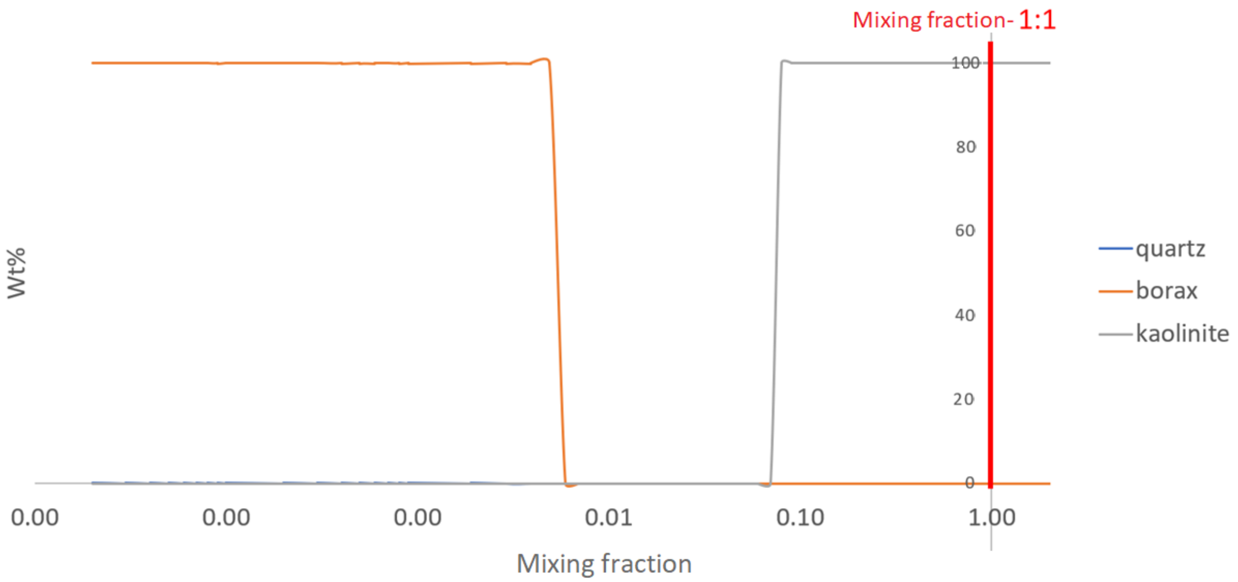

**Figure 4.** Resultant minerals after mixing early brine with ground water. Weight percent of resultant minerals (y-axis) plotted against mixing fraction of early brine and groundwater.

## 5 Results

We hypothesized that we require multiple wet and dry cycles to form an evaporitic assemblage that consists of Ca-sulfate and borates. In this work we model four sets of wet-dry cycles (cycle 0-3) and extrapolate up to 250 cycles based on the trends determined using the modeled cycle results. In this section, we summarize the cycling and extrapolation results in addition to comparing these results to observations made in Gale crater and terrestrial dry lake settings.

### 5.1 Cycling

A wet-dry cycle was simulated by repeating dilution and evaporation using the starting fluid composition of a local Gale lake fluid (see section 4.4.3) followed by evaporation (see section 4.4.4.1) and fluid mixing (see section 4.4.4.2) repeated for four sets. Table 4 lists all the fluid compositions used for simulating four wet-dry cycles (Cycle 0 to Cycle 3) using CHIM-XPT in addition to the established local Gale lake fluid and the evaporated local Gale lake fluid. In Table 5, the abundance of dissolved species in the fluid increases in a stepwise manner. In each cycle during the evaporation phase the relative concentration of water-soluble elements is higher compared to the fluid-mixing phase.

**Table 4.** Molar concentration (M) of fluid composition used in each step of the four cycles simulating a Gale relevant wet-dry scenario:

|  | Gale GW W: R 50000 | Evaporated Gale lake water | Cycle 0 Dilution | Cycle 0 Evaporation | Cycle 1 Dilution | Cycle 1 Evaporation | Cycle 2 Dilution | Cycle 2 Evaporation | Cycle 3 Dilution | Cycle 3 Evaporation |
|---|---|---|---|---|---|---|---|---|---|---|
| **$Cl^-$** | 1.69E-03 | 8.58E-03 | 1.97E-01 | 1.97E+00 | 2.02E-01 | 2.02E+00 | 2.02E-01 | 1.85E+00 | 2.07E-01 | 1.34E+00 |
| **$SO_4^{2-}$** | 3.96E-03 | 2.02E-02 | 4.44E-01 | 4.44E+00 | 4.49E-01 | 4.49E+00 | 4.49E-01 | 4.12E+00 | 4.49E-01 | 2.91E+00 |
| **$HCO_3^-$** | 1.69E-04 | 8.58E-04 | 1.46E-02 | 9.59E-03 | 1.06E-03 | 1.06E-02 | 1.11E-03 | 1.02E-02 | 1.21E-03 | 7.84E-03 |
| **$HS^-$** | 2.78E-09 | 2.47E-09 | 1.46E-09 | 6.06E-10 | 1.46E-09 | 5.55E-10 | 1.46E-09 | 5.09E-10 | 1.46E-09 | 8.82E-10 |
| **$H_4SiO_4$** | 8.72E-05 | 1.77E-04 | 1.56E-04 | 1.41E-05 | 4.59E-05 | 1.87E-05 | 4.64E-05 | 2.27E-05 | 4.69E-05 | 6.53E-05 |
| **$Al^{3+}$** | 6.84E-09 | 5.05E-13 | 2.57E-09 | 1.26E-08 | 9.59E-10 | 6.06E-09 | 1.01E-09 | 2.68E-09 | 1.06E-09 | 3.59E-10 |
| **$Ca^{2+}$** | 1.98E-05 | 1.01E-04 | 1.06E-04 | 1.06E-03 | 1.16E-04 | 1.16E-03 | 1.26E-04 | 1.16E-03 | 1.36E-04 | 8.82E-04 |
| **$Mg^{2+}$** | 3.17E-05 | 1.61E-04 | 1.51E-03 | 1.51E-02 | 1.51E-03 | 1.51E-02 | 1.56E-03 | 1.43E-02 | 1.56E-03 | 1.01E-02 |
| **$Fe^{2+}$** | 2.78E-07 | 5.05E-07 | 3.28E-07 | 3.28E-06 | 4.74E-07 | 4.69E-06 | 6.06E-07 | 5.55E-06 | 7.57E-07 | 4.90E-06 |
| **$K^+$** | 5.06E-04 | 2.57E-03 | 6.06E-02 | 6.06E-01 | 6.06E-02 | 6.06E-01 | 6.56E-02 | 6.01E-01 | 6.56E-02 | 4.24E-01 |
| **$Na^+$** | 9.12E-03 | 4.64E-02 | 1.03E+0 | 1.01E+01 | 1.02E+00 | 1.02E+01 | 1.02E+00 | 9.37E+00 | 1.03E+00 | 6.65E+00 |
| **$Mn^{2+}$** | 1.78E-07 | 9.08E-07 | 2.07E-05 | 2.07E-04 | 2.07E-05 | 2.07E-04 | 2.07E-05 | 1.90E-04 | 2.12E-05 | 1.37E-04 |
| **$Li^+$** | 9.91E-05 | 1.29E-01 | 1.29E-02 | 1.29E-01 | 1.30E-02 | 1.30E-01 | 1.30E-02 | 1.19E-01 | 1.31E-02 | 8.49E-02 |
| **$H_3BO_3$** | 7.93E-04 | 9.39E-01 | 9.43E-02 | 5.26E-01 | 5.31E-02 | 5.30E-01 | 5.34E-02 | 4.90E-01 | 5.38E-02 | 3.48E-01 |

Figure 5 shows the step-like and gradual increase in concentration of $Li^+$ with increasing cycle numbers i.e., step-like increments caused by the relative increase of $Li^+$ during an evaporation part of the cycle and a relative decrease during a dissolution part of the cycle, with an overall gradual increase due to fluid mixing. This gradual increase is assumed to continue linearly for the purpose of extrapolation in this work. In reality, evaporation will likely vary from year to year, however, we use a linear trend for the extrapolation because we assume that a linear trend represents an average of the evaporation over multiple cycles. The paleoclimate of Mars eventually reached a global drying stage with no large-scale events that would have replenished the surface water to its early lake levels, the inference of which is supported by both the sedimentological record and atmospheric deuterium-to-hydrogen isotope ratios (Milliken et al., 2010; Rapin et al. 2021, Scheller et al., 2021). Hence, we assume that although there may have been local variation in the ratios of fluid mixing, on a broad scale, the overall water availability declined, hence the relative abundances of soluble species in Gale fluids gradually increased without any major aqueous events diluting the Gale fluids (as also described in section 4.1: Assumptions).

An enrichment trend is determined by fitting an average composition line through the step-like increasing composition curve. The slope of this line is used for extrapolating the average fluid composition at higher cycle numbers. The following section describes the extrapolation methodology.

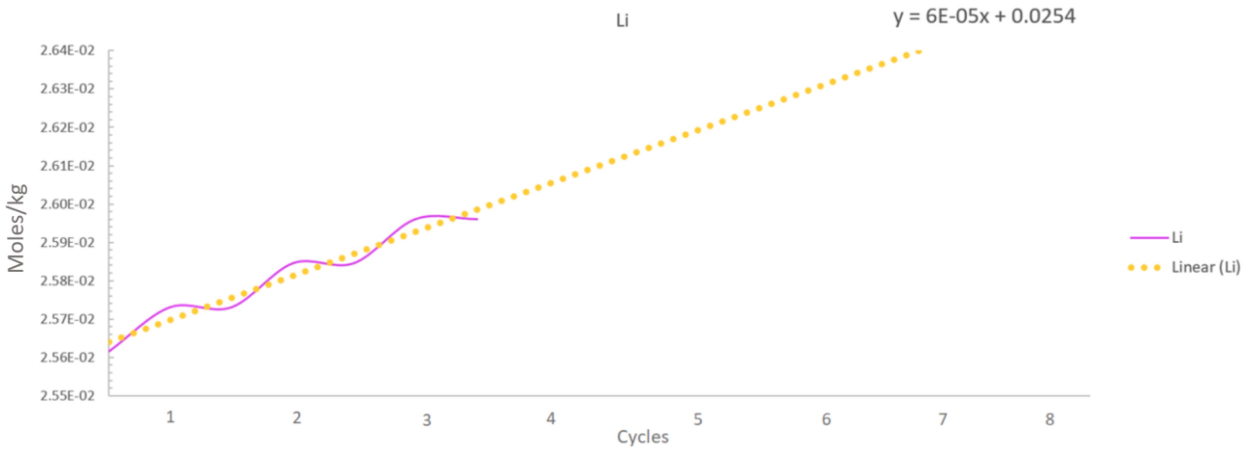

**Figure 5.** Step-like and gradual increase in concentration of $Li^+$ with increasing number of cycles. Cycle numbers are shown on x-axis and moles of Li in the fluid is shown on y-axis. A trend line is fitted through the step-like curve with equation for the trend line shown on the top right.

### 5.2 Extrapolation

Based on the evolution of the fluid through evaporation and mixing with groundwater in four cycles, the trend was extrapolated for 250 cycles. This was done by fitting a linear regression line through the step-like concentration curve for each aqueous species with increasing cycle numbers to determine the slope of the trend line (as shown in Figure 5 for $Li^+$ as an example) using Microsoft Excel. The slope of this line was then used for establishing the concentration of each aqueous species for a given cycle number. For example, the equation of the trend line established for $Li^+$ (in Figure 5) is

y = 6E-05x + 0.0254……………………………………………………………… (Equation 1)

where “x” is the number of cycles and “y” is the concentration in moles. Using the trend line equations, fluid compositions were established for a range of 5 to 250 cycles. The extrapolated fluid compositions are shown in Table 5 and are assumed to represent the average fluid composition for the corresponding cycle number.

**Table 5.** Extrapolated fluid composition for cycles 5-250. Fluid composition in molar concentration (moles/kg).

| | Cycles: | 5 | 25 | 50 | 75 | 100 | 125 | 150 | 250 |
|---|---|---|---|---|---|---|---|---|---|
| | Slope | | | | | | | | |
| Cl- | 3.80E-01 | 1.37E+00 | 1.80E+00 | 2.30E+00 | 2.83E+00 | 3.33E+00 | 4.00E+00 | 4.33E+00 | 6.33E+00 |
| $SO_4^{2-}$ | 8.75E-01 | 2.97E+00 | 3.23E+00 | 3.67E+00 | 4.00E+00 | 4.33E+00 | 4.67E+00 | 5.00E+00 | 6.33E+00 |
| $HCO_3^-$ | 1.60E-03 | 8.00E-03 | 1.87E-02 | 3.20E-02 | 4.67E-02 | 6.00E-02 | 7.33E-02 | 8.67E-02 | 1.40E-01 |
| $HS^-$ | 1.00E-09 | 4.00E-09 | 6.67E-09 | 1.00E-08 | 1.33E-08 | 1.67E-08 | 2.00E-08 | 2.33E-08 | 3.67E-08 |
| $H_4SiO_4$ | 3.00E-05 | 1.67E-04 | 4.33E-04 | 7.67E-04 | 1.10E-03 | 1.43E-03 | 1.77E-03 | 2.10E-03 | 3.33E-03 |
| $Al^{3+}$ | 3.00E-09 | 0.00E+00 | 0.00E+00 | 0.00E+00 | 0.00E+00 | 0.00E+00 | 0.00E+00 | 0.00E+00 | 0.00E+00 |
| $Ca^{2+}$ | 2.00E-04 | 1.00E-03 | 2.33E-03 | 4.00E-03 | 5.67E-03 | 7.33E-03 | 9.00E-03 | 1.07E-02 | 1.73E-02 |
| $Mg^{2+}$ | 2.90E-03 | 1.03E-02 | 1.30E-02 | 1.63E-02 | 1.97E-02 | 2.30E-02 | 2.63E-02 | 2.97E-02 | 4.33E-02 |
| $Fe^{2+}$ | 2.00E-07 | 4.00E-06 | 1.73E-05 | 3.33E-05 | 5.00E-05 | 6.67E-05 | 8.33E-05 | 1.00E-04 | 1.67E-04 |
| $K^+$ | 1.08E-01 | 4.33E-01 | 7.67E-01 | 1.20E+00 | 1.60E+00 | 2.03E+00 | 2.43E+00 | 2.87E+00 | 4.67E+00 |
| $Na^+$ | 1.99E+00 | 6.67E+00 | 7.33E+00 | 8.33E+00 | 9.00E+00 | 9.67E+00 | 1.03E+01 | 1.13E+01 | 1.43E+01 |
| $H_3BO_3$ | 1.03E-01 | 3.67E-01 | 4.00E-01 | 4.67E-01 | 5.33E-01 | 6.00E-01 | 6.67E-01 | 7.33E-01 | 1.00E+00 |
| $Li^+$ | 2.54E-02 | 8.67E-02 | 9.33E-02 | 1.03E-01 | 1.13E-01 | 1.23E-01 | 1.33E-01 | 1.43E-01 | 1.83E-01 |

Evaporation is simulated on these fluid compositions systematically by iteratively removing $H_2O$ from the system to determine the minimum number of cycles required to start precipitating primary Ca-sulfate and borates from a Gale-relevant fluid. Table 6 shows the resultant minerals formed at every modeled and extrapolated dissolution and evaporation stage with corresponding abundance of $Li^+$ ion in the fluid. We identify that it takes a minimum of 250 cycles to start forming Ca-sulfates and borates. In order to evaporate an extrapolated fluid that has undergone 250 wet-dry cycles, we iteratively reduce the $H_2O$ in the fluid as shown in Figure 6.

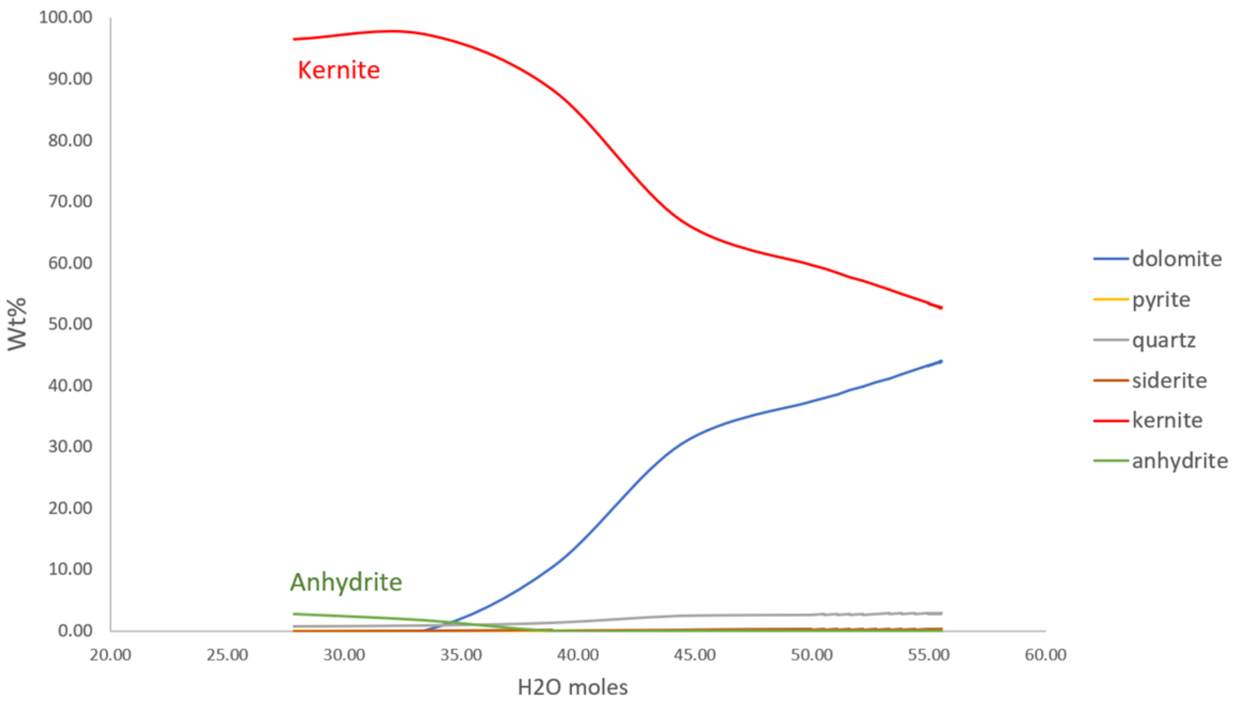

**Figure 6.** Resultant minerals obtained after evaporating the extrapolated fluid composition that has undergone 250 wet-dry cycles.

**Table 6.** Minerals formed throughout the modeled steps (titration, evaporation, and fluid-mixing) with corresponding molar concentration (moles/kg) of $Li^+$ ions in the fluid:

| Cycle | Process | Phases | $Li^+$ |
|---|---|---|---|
| Gale lake fluid | Titration (modeled) | Nontronite, Kaolinite, Hematite, Pyrite, Quartz, Zeolites, Chlorite | 9.91E-05 |
| Gale lake evap | Evaporation (modeled) | Quartz, Borax, Dolomite, Pyrite, Nontronite, Goethite, Siderite, Ankerite, Dawsonite | 1.29E-01 |
| 0 | Fluid mixing (modeled) | Borax, Quartz, Kaolinite | 1.29E-02 |
| 0 | Evaporation (modeled) | Kernite, Quartz, Kaolinite, Dolomite, Dawsonite, Siderite, Pyrite | 1.29E-01 |
| 1 | Fluid mixing (modeled) | Kaolinite | 1.30E-02 |
| 1 | Evaporation (modeled) | Kernite, Quartz, Kaolinite, Dawsonite, Pyrite | 1.30E-01 |

| | | | |
|---|---|---|---|
| 2 | Fluid mixing (modeled) | Kaolinite | 1.30E-02 |
| 2 | Evaporation (modeled) | Kernite, Quartz, Kaolinite, Dawsonite, Pyrite | 1.19E-01 |
| 3 | Fluid mixing (modeled) | Kaolinite | 1.31E-02 |
| 3 | Evaporation (modeled) | Kernite, Quartz, Kaolinite, Pyrite | 8.49E-02 |
| 5 | Evaporation (extrapolated) | Kernite, Quartz, Pyrite | 8.67E-02 |
| 25 | Evaporation (extrapolated) | Kernite, Quartz, Pyrite, Siderite | 9.33E-02 |
| 50 | Evaporation (extrapolated) | Kernite, Quartz, Pyrite, Siderite | 1.03E-01 |
| 75 | Evaporation (extrapolated) | Kernite, Quartz, Pyrite, Siderite | 1.13E-01 |
| 100 | Evaporation (extrapolated) | Kernite, Quartz, Pyrite, Siderite | 1.23E-01 |
| 125 | Evaporation (extrapolated) | Kernite, Quartz, Pyrite, Siderite | 1.33E-01 |
| 150 | Evaporation (extrapolated) | Kernite, Dolomite, Quartz, Pyrite, Siderite | 1.43E-01 |
| 250 | Evaporation (extrapolated) | Kernite, Anhydrite, Dolomite, Quartz, Pyrite, Siderite | 1.83E-01 |

### 5.3 Comparing the simulated mineral assemblage to terrestrial and martian observations

The minerals that form in this system are clay minerals (nontronite, kaolinite, chlorite), evaporites (borates: borax and kernite; sulfate: anhydrite, carbonates: dolomite, ankerite, dawsonite, siderite), Fe-oxide/oxyhydroxide (hematite, goethite), sulfide (pyrite), zeolites, and quartz. Precipitates vary based on the water-rock titration, evaporation, or fluid-mixing process as shown in Table 6. Clay minerals, evaporites, Fe-oxides, sulfide, chlorites, zeolites and quartz are observed as resultant minerals for the early steps of the modeling that consist of water-rock reactions, fluid mixing and evaporation. The extrapolated evaporation stages (cycle 5 to 250) resultant minerals consist of evaporites, sulfides, and quartz. We also note the relative sequence of evaporite formation through the progressive wet-dry cycles and establish that anhydrite (Ca-sulfate) forms in the later stages of the wet-dry cycle compared to borate. This result is tied to the relatively low abundance of Ca in the starting Gale lake fluid which is established based on the observations of low abundance of Ca-containing pyroxenes and plagioclase in soils of Gale crater as compared to terrestrial equivalents and the inferred limited extent of aqueous alteration in Gale crater (as explained in section 4.4.1). The abundance of B and Li estimated for the starting fluid is based on measured B and Li values in fluids from a terrestrial analog area and are comparable to values measured in a Martian meteorite, Nahklite (as explained in section 4.4.1). The composition of the starting fluids is tied to observations made in Gale crater, a Gale-relevant terrestrial analog area, and Martian meteorite measurements to determine estimates for a baseline model for the formation of primary evaporites in Gale crater.

In order to ground truth and assess the applicability of the modeling results, the resultant minerals have been compared with assemblages observed in a dry lake terrestrial analog, Death Valley, CA (Sarrazin et al., 2005; Baldridge et al., 2004), and with assemblages observed in Gale crater. In the case of the terrestrial analog, all the minerals resulting from the simulated wet-dry cycles, except dawsonite, have been observed in Death Valley. In the case of Gale crater, all the minerals forming in this model have either been observed or are suspected. A detailed comparison of these phases to terrestrial and Gale crater observations is provided in Table 7.

**Table 7.** Comparison of minerals resulting from this work to minerals reported in Death Valley and minerals observed or reported plausible in Gale crater:

| Minerals | Death Valley | Gale crater |
|---|---|---|
| **Clay:** | | |
| Nontronite | Observed (El-Maarry et al., 2015; Thomas and Coleman, 1964) | Observed (Rampe et al., 2020; He et al., 2022; Bristow et al., 2017b;) |
| Kaolinite | Observed (Duke, 2021; Kruse et al., 1993) | Plausible (Treiman et al., 2016; Vaniman et al., 2014) |
| **Evaporites:** | | |
| Borates | | |
| Borax | Observed (Muessig et al., 2019; Crowley et al., 1993) | Plausible (Gasda et al., 2017; Das et al., 2020) |
| Kernite | Observed (Crowley et al., 1996; Woods, 1994) | Plausible (Gasda et al., 2017; Das et al., 2020) |
| Carbonates | | |
| Dolomite | Observed (Duke, 2021; Corsetti and Grotzinger; 2005) | Observed (Sutter et al., 2017) |
| Ankerite | Observed (Petterson et al., 2011; Bouton 1984) | Observed (Rampe et al., 2022) |
| Dawsonite | Not predominantly reported in Death Valley | Plausible (Bridges et al., 2015; Schwenzer et al., 2016; 2020) |
| Siderite | Observed (Klee et al., 2021; Yang et al., 2005) | Observed (Archer et al., 2020) |
| Sulfate | | |
| Anhydrite | Observed (Crowley et al., 1993; Knott et al., 2018 Roberts and Spenser, 2020) | Observed (Vaniman et al., 2018; Nachon et al, 2014; Rapin et al., 2016) |
| **Fe-oxides:** | | |
| Hematite | Observed (Baldridge et al., 2004; Kruse et al., 1993) | Observed (L'Haridon et al., 2020; Fraeman et al., 2013) |
| Goethite | Observed (Minguez et al., 2012; Kruse et al., 1993) | Plausible (Fraeman et al., 2013; Bridges et al., 2015) |
| **Sulfide:** | | |
| Pyrite | Observed (Kaufman et al., 2007) | Observed (Morris et al., 2018; McAdam et al, 2014) |
| **Chlorites** | Observed (Ericksen et al., 1978) | Detected (Borlina et al., 2015; Ehlmann et al., 2011) |
| **Zeolites** | Observed (Kruse et al., 1993; Eriksen et al., 1988) | Plausible (Buz et al., 2017; Schwenzer et al., 2012) |
| **Quartz** | Observed (Crowley et al., 1996;) | Observed (Frydenvang et al., 2017; Rampe et al., 2020) |

In Gale crater we also observe the presence of Mg-sulfate (Rapin et al., 2019) and halite (e.g.,Thomas et al., 2019). We use the saturation points of Mg and Na at 1 bar pressure and 25°C for the Gale relevant fluid required to extrapolate the minimum number of wet-dry cycles to form Mg sulfate and halite. We establish that a minimum of 85 cycles are required to form Mg sulfate and a minimum of 200 cycles are required to form halite if there were no competing minerals in the system, for example, Ca-sulfate (competing with Mg-sulfate for the sulfate anion) and nontronite (competing with halite for the Na cation (as shown in Figures 7 and 8.) It is likely that Mg-sulfate and halite required a higher number of wet-dry cycles for all the relevant ionic components to saturate because of this competition. Hence the number of wet-dry cycles we have established are a minimum constraint for the number of wet-dry cycles possible in Gale crater and the observation of Mg-sulfate and halite in Gale crater points towards the likelihood of a higher number of wet-dry cycles that Gale crater experienced.

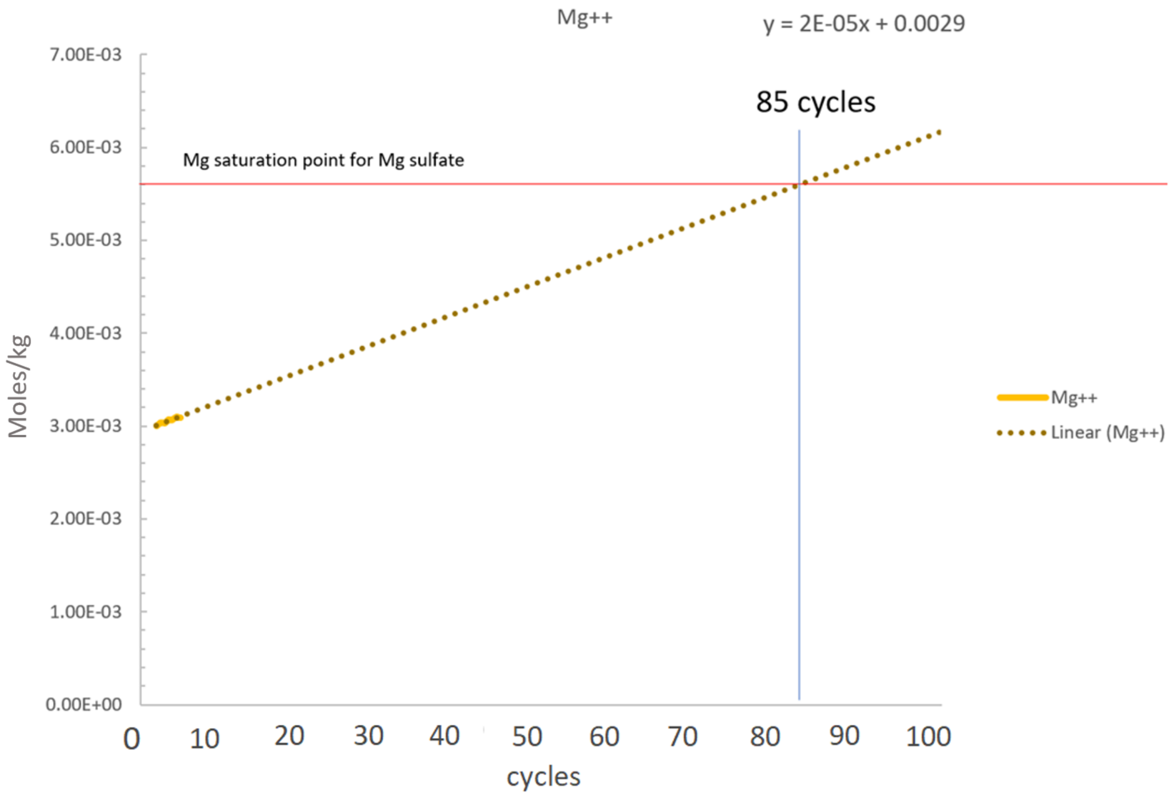

**Figure 7**. Number of moles/kg of $Mg^{2+}$ for a corresponding amount of $SO_4^{2-}$ to start precipitating Mg-sulfate using the Gale relevant fluid at 1 bar pressure and 25°C. Number of cycles shown on x-axis and number of moles of $Mg^{2+}$ shown on y-axis.

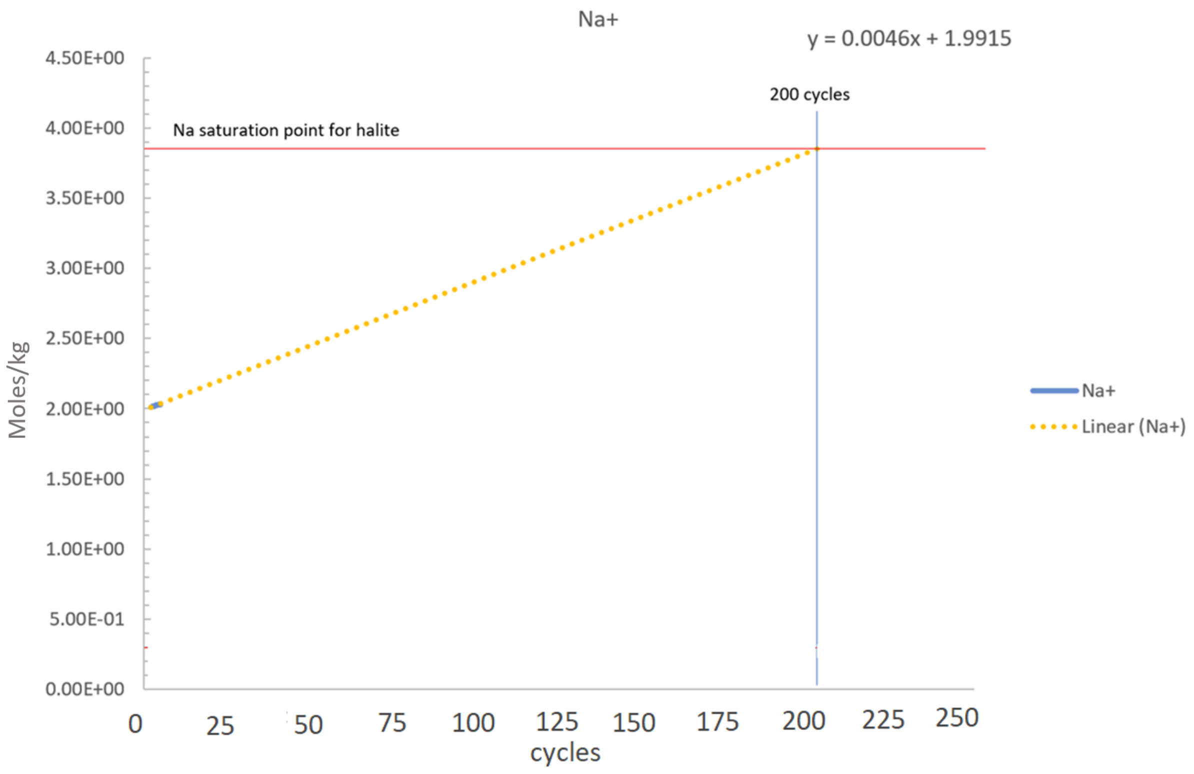

**Figure 8.** Number of moles/kg of $Na^+$ for a corresponding amount of $Cl^-$ to start precipitating halite using the Gale relevant fluid at 1 bar pressure and 25°C. Number of cycles shown on x-axis and number of moles of $Na^+$ shown on y-axis.

Table 7 shows that the concentration of $Li^+$ in the fluid ranges from 9.91E-05 to 1.83E-01 moles/kg (0.7 to 1270 ppm) with 0.7 ppm being the $Li^+$ concentration of the local Gale lake fluid and 1270 ppm being the $Li^+$ concentration of the resultant brine after 250 wet-dry cycles. The concentration of $Li^+$ in the Gale brine is comparable to $Li^+$ concentration of terrestrial dry lakes that have experienced multiple wet dry seasonal cycles (e.g., an annual average of 1400 ppm in Salar de Atacama and 1062 ppm in Salar de Pastos Grandes: Munk et al., 2016). The saturation point of $Li^+$ to start forming LiCl at 25°C and 1 bar pressure in 1 kg of water is $1.36 \times 10^7$ ppm (Rumble, 2017). Compared to this value, the concentration of $Li^+$ in the Gale brine of is $10^7$ times lower than required to start forming LiCl.

## 6 Discussion

### 6.1 Constraining time for simulated wet-dry cycles using terrestrial analogs

In this work we established that a minimum of 250 wet and dry cycles are required to form Ca-sulfates and borates. Ca-sulfates are the key mineral precipitating in close association with borate after 250 cycles. In this section we establish a time constraint for the 250 cycles based on terrestrial lake systems that can be applied to Gale crater.

Lakes in terrestrial settings vary in their characteristics based on climatic variations. There are broadly three types of lakes based on the ratio of lake inflow and discharge (Van der Meeren and Verschuren, 2021; Moknatian and Piasecki, 2019; Langbein, 1961): perennial lakes (high water content: water never fully evaporates even in drought periods and the system takes a relatively long time to form evaporites), ephemeral lakes (lower water content compared to perennial lakes with significantly low water levels during water periods enabling evaporite formation faster than in perennial lakes), and dry lakes (predominantly dry with sporadic water content which enables fastest evaporite formation compared to other closed lake systems).

The time required to complete a wet-dry cycle in lakes with high water content is longer than a system that has lower water content as the time required to evaporate large amounts of water is higher. In order to form a significant amount of primary evaporites (i.e., more than one thin crust of evaporite on the surface of a dry lakebed), long standing wet and dry cycles are required. In terrestrial settings the average wet-dry cycling time (i.e., the amount of time required for a closed lake system to complete a cycle comprising of highest water content in a wet period to lowest water content in a dry period) is approximately 1.5 years for dry lakes with sporadic water presence, 9 years for ephemeral lakes, and 65 years for perennial lakes. Figure 9 shows an illustration of relative water amounts varying over time with the average cycling time for dry lakes with sporadic water presence, ephemeral lakes, and perennial lakes (compiled from Van der Meeren and Verschuren, 2021. Moknatian and Piasecki, 2019; Langbain, 1961).

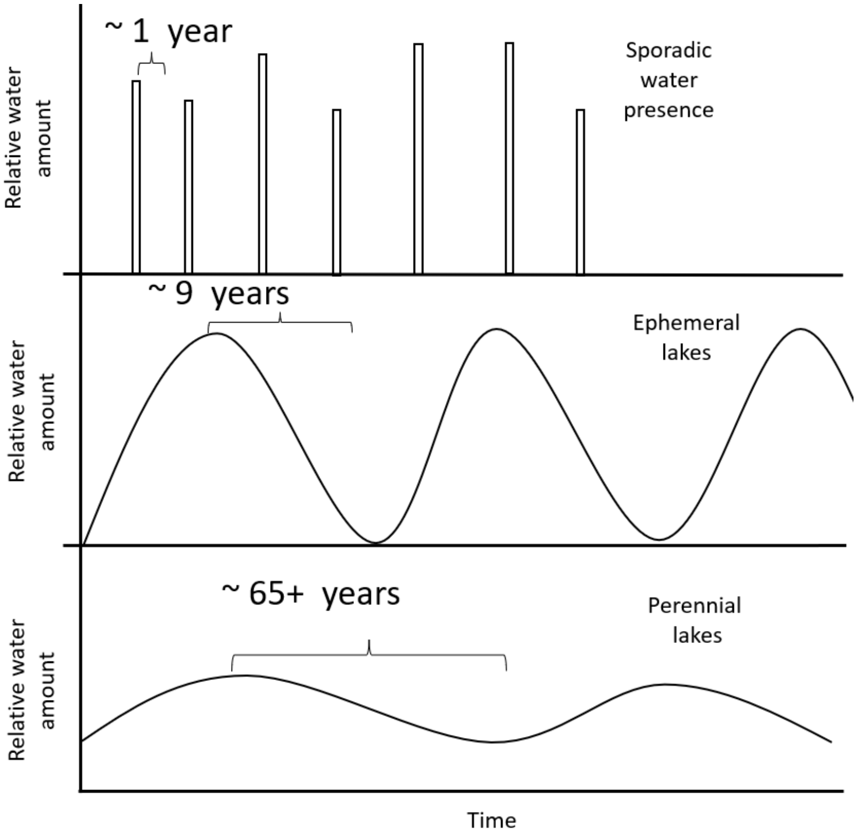

**Figure 9**. Average wet-dry cycling times for three types of terrestrial closed lakes. The x-axis indicates relative time, and the y-axis indicates relative water amount in the closed lake system (compiled from Van der Meeren and Verschuren, 2021. Moknatian and Piasecki, 2019; Langbain, 1961).

In the following section, we apply the knowledge from terrestrial analogues to estimate relative water levels and lake stages of Gale crater based on the sedimentological observations made by the Curiosity rover and discuss the possible time constraint of wet-dry cycles in Gale crater based on the modeling results and comparison to terrestrial closed lake systems.

### 6.2 Estimating time constraint for Gale crater

Three lake levels are inferred for Gale crater based on HiRISE (High Resolution Imaging Science Experiment) topographic data collected by the Mars Reconnaissance Orbiter (Palucis et al., 2016). The highest lake level is inferred to have a mean lake depth of 700 m (for the elevation range -3200 m to -3400 m close to the central mound Mount Sharp area) and is associated with deltaic deposits. The next lake level is inferred to have a mean lake depth of 400 m (for the elevation range -3800 m to -4000 m topographically above the highest elevation sampled by the Curiosity rover to date). The next lake level is inferred to have a mean lake depth of 300 m (for elevation range -4000 m to -4200 m, which is the current elevation range the Curiosity rover is measuring) associated with locally sourced water and periods of drying and rewetting. Based on the HiRISE data it is also inferred that Gale experienced a transition from relatively wet regional conditions to drier environments with local runoffs (Palucis et al., 2016)

The mean lake level inferred for the topographic area that has been traversed to date by the Curiosity rover based on HiRISE data is 300 m with intermittent lake level fluctuations (Palucis et al., 2016). The inference of fluctuating lake levels is also consistent with the inferences made based on observations of sedimentological facies made by the Curiosity rover in Gale crater (Hurowitz et al., 2017, Rapin et al., 2019, Rapin et al., 2021). The fluctuating lake levels in Gale crater are inferred based on the observations of both fine-grained deposits that indicate relatively deep lake environments (Fedo et al., 2018; Siebach et al., 2019) and the observations of desiccation cracks, altered clay minerals, and presence of evaporites which indicate lake margin with evaporative environments (Stein et al., 2018; Bristow et al., 2021 Thomas et al, 2019; Nachon et al., 2016; Gasda et al., 2017). These observations indicate that topography measured to date in Gale crater could have had deep lake levels (up to 300 m) which dropped down to levels that caused the formation of features observed in dry lake environments in terrestrial setting. Based on these observations that are inferred to represent relatively shallow lake levels dropping down to conditions that can form desiccation cracks in the lakebed, we assume possible terrestrial lake analogs of either ephemeral or lakes with sporadic water presence for Gale crater.

In this section, a number of annual wet-dry cycles are estimated for Gale crater after a lake type is assigned for the different stratigraphic units based on the sedimentological facies observed in these units. The number of wet-dry cycles are determined by comparing the assigned lake types for Gale crater to common cycling times for terrestrial ephemeral and dry lakes. Figure 10 summarizes the assigned lake types for Gale crater and the minimum annual wet-dry cycles estimated to form Ca-sulfates and borates from a Gale-relevant fluid for this model.

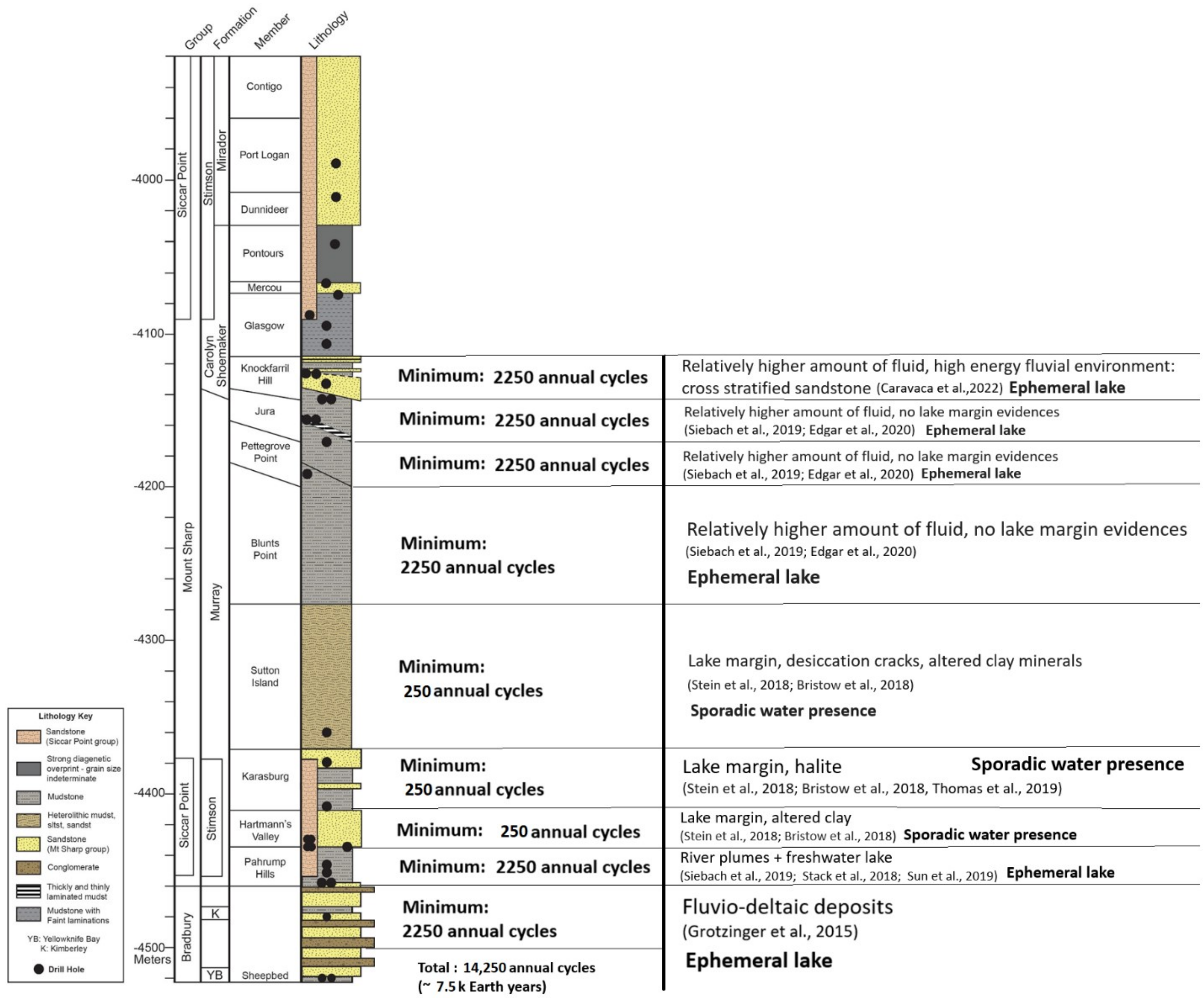

**Figure 10.** Gale stratigraphic record (Mars Science Laboratory Sedimentology and Stratigraphy Working Group) with minimum annual cycles estimated for forming Ca-sulfates and borates (middle column) based on water levels inferred using observed sedimentological facies (right hand side column).

The Pahrump Hills member is interpreted to represent fluvio-deltaic deposits which is associated with deeper lake levels compared to lake-margin environments (Siebach et al., 2019; Stack et al., 2018; Sun et al., 2019). Hence, we assign an ephemeral lake level for the stratigraphic unit in this elevation range. In terrestrial ephemeral lakes, the average amount of time required for one wet-dry cycle is approximately 9 years (as explained in section 6.1). We estimate that 250 wet-dry cycles in an ephemeral lake would take 2250 (250 times 9) martian years.

A lake-margin environment with episodic lake drying caused by fluctuating lake levels is inferred for the Hartmann's Valley through the Sutton Island members based on the observation of desiccation cracks, altered clay minerals, and the presence of halite (Fedo et al., 2018; Gwizd et al., 2018; Siebach et al., 2019, Bristow et al., 2018, Haber et al., 2019; Siebach et al., 2019; Stein et al., 2018; Sun et al., 2018, Achilles, 2018; Thomas et al., 2019). Based on the inference of lake-margin environment for the members Hartmann's Valley, Karasburg, and Sutton Island, we assign the status of sporadic water presence for these members. Based on comparison with cycling times for terrestrial lakes with sporadic water presence (i.e., approximately 1 year), we estimate that 250 wet-dry cycles in a lake with sporadic water presence would take 250 annual cycles on Mars.

The Blunts Point, Pettegrove point, and Jura members were deposited in a low-energy lacustrine environment which is inferred based on the presence of fine-grained mudstones which is associated with deeper lake levels compares to lake-margin environments (Siebach et al., 2019; Edgar et al., 2020; Caravaca et al., 2022) We assign ephemeral lake levels for these members and estimate that 250 wet-dry cycles would take 2250 annual cycles per stratigraphic unit.

Based on the relative water levels in Gale estimated using the observed sedimentological facies, the total minimum number of annual cycles required to precipitate sulfates and borates by a Gale relevant fluid using this modeling technique is 14,250. One annual cycle on Mars would include a wet and a dry period and a terrestrial equivalent of this time constraint is approximately 7.5 k years. This finding is in accordance with a wet-dry depositional environment inferred by Rapin et al., (2019 and 2021) and lake level fluctuations inferred by Hurowitz et al., (2017). Comparing the minerals predicted to form in our modelling work to observations made in a terrestrial dry lake system and to minerals observed and reported plausible for Gale crater, we find that the minerals in the model are broadly similar to observations made in Death Valley and Gale crater (as shown in Table 7 with references therein).

The $Li^+$ concentration in the modeled fluids through cycle 0-250 ranges from 0.7 ppm (local Gale lake fluid) to 1270 ppm (after 250 wet-dry cycles) (as explained in section 5.3). Although this range of $Li^+$ concentration for the Gale-relevant fluids is comparable to the range of $Li^+$ concentrations observed in terrestrial dry lake brines (Munk et al., 2016) the $Li^+$ concentration after 250 wet-dry cycles is still $10^7$ times lower than required to start forming LiCl at the modeled conditions. The concentration of $Li^+$ in the resultant Gale brine after 250 wet dry cycles is too low to form LiCl, however the concentration is sufficient to form Li-rich clay minerals that form by adsorption of $Li^+$ on the surface of the clay minerals similar to Li-rich clay minerals observed in terrestrial dry lakes (Yu et al., 2022; Warren, 2016). Based on this we infer that the reservoir of Li in close association with Ca-sulfates of Gale crater are likely clay minerals.

In summary, we established that formation of primary Ca-sulfates and borates, which are inferred to be precursors of Ca-sulfate veins in Gale crater, requires multiple wet-dry cycles are required. For the specific Gale-relevant scenario we modeled a minimum of 250 wet-dry cycles are required to precipitate primary Ca-sulfates and borates (see section 5). We note that this is important for the assessment of habitability at Gale, as wet-dry cycles have been invoked to be key in the origin of life on Earth (Hud and Fialho.,2019; Becker et al., 2019; Marsh, 2022). Thus, the presence of mineral assemblages in Gale crater that require multiple wet-dry cycles and the estimated duration of over 14k years of those wet-dry cycles, emphasize the habitability potential during the early stages of Gale crater's aqueous history. Through this work, we present a theoretical geochemical fluid composition and mineral assemblage and duration of the wet-dry cycling environment relevant for Gale crater's early aqueous history which could have resulted in the primary evaporites that are inferred to be precursors of the evaporitic veins observed in Gale crater today.

## 7 Conclusions

In this work, we model fluid and precipitate compositions in wet and dry cycles in Gale crater lakes. The formation of the observed Ca-sulfates and borates in Gale crater requires multiple generations of evaporation and dissolution as indeed evidenced by the sedimentary record. The water-to-rock ratios selected throughout the model are a best estimate based on observations of minerals made using the Curiosity rover. The result of this work shows that a minimum of 250 wet-dry cycles are required to start forming Ca sulfates and borates from a Gale-relevant fluid at a pressure of 1 bar and at 25°C. Comparing this result to terrestrial closed lake systems and placing the established time constraint in a broader context of Gale's timeline for aqueous activity, a minimum of 14,250 Mars annual cycles (~7.5k Earth years) is established for the start of formation of primary Ca-sulfates and borates. The result also shows that the concentration of Li in the resultant brine after 250 wet dry cycles is not enough to start forming LiCl, however it is sufficient to enable Li-adsorption on clay minerals. Based on this we infer that clay minerals in close association with Ca-sulfates are likely reservoirs of Li.

The results of this work are applicable for understanding the evaporative sequence in Gale crater and indicate that in this specific Gale-relevant model, borates form before Ca-sulfates with the formation of Ca-sulfate being the key mineral setting the minimum number of cycles. This work is the first theoretical constraint on fluid composition and mineral assemblages for Gale crater's early aqueous history. Through the results of this work, we estimate the fluid composition and minimum time required to start forming primary evaporites Ca-sulfate and borate (which are inferred to be precursors for Ca-sulfate veins observed in Gale crater today) for the specific Gale-relevant scenario that we chose to model. The results of this work are in accordance with sedimentological observations that also point towards multiple generations of wet-dry cycles. The results are a lower-limit time estimate for wet-dry cycles and the lifetime of aqueous activity is likely longer when late-stage ground water activity is considered.

## 8 References

Achilles, C., 2018. Analyses of crystalline and X-ray amorphous materials in Gale crater rocks and soils.

Achilles, C.N., Rampe, E.B., Downs, R.T., Bristow, T.F., Ming, D.W., Morris, R.V., Vaniman, D.T., Blake, D.F., Yen, A.S., McAdam, A.C. and Sutter, B., 2020. Evidence for multiple diagenetic episodes in ancient fluvial-lacustrine sedimentary rocks in Gale crater, Mars. *Journal of Geophysical Research: Planets*, *125*(8), p.e2019JE006295.

Arnórsson, S. and Andrésdóttir, A., 1995. Processes controlling the distribution of boron and chlorine in natural waters in Iceland. *Geochimica et Cosmochimica Acta*, *59*(20), pp.4125-4146.

Archer, P.D., Rampe, E.B., Clark, J.V., Tu, V., Sutter, B., Vaniman, D., Ming, D.W., Franz, H.B., McAdam, A.C., Bristow, T.F. and Achilles, C.N., 2020, March. Detection of siderite (FeCO3) in glen torridon samples by the Mars science laboratory rover. In *Lunar and Planetary Science Conference* (No. JSC-E-DAA-TN78281).

Bąbel, M., and B. C. Schreiber. "Geochemistry of Evaporites and Evolution of Seawater. Treatise on Geochemistry. Ed. by Heinrich D. Holland and Karl K. Turekian." (2014): 483-560.

Baldridge, A.M., Farmer, J.D. and Moersch, J.E., 2004. Mars remote-sensing analog studies in the Badwater Basin, Death Valley, California. *Journal of Geophysical Research: Planets*, *109*(E12).

Becker, S., Feldmann, J., Wiedemann, S., Okamura, H., Schneider, C., Iwan, K., Crisp, A., Rossa, M., Amatov, T. and Carell, T., 2019. Unified prebiotically plausible synthesis of pyrimidine and purine RNA ribonucleotides. *Science*, *366*(6461), pp.76-82.

Bedford, C.C., Schwenzer, S.P. and Bridges, J.C., 2016. An Investigation into Fluorine within Gale Crater and its Implications for Martian Geology.

Borlina, C.S., Ehlmann, B.L. and Kite, E.S., 2015. Modeling the thermal and physical evolution of Mount Sharp's sedimentary rocks, Gale crater, Mars: Implications for diagenesis on the MSL Curiosity rover traverse. *Journal of Geophysical Research: Planets*, *120*(8), pp.1396-1414.

Bouton, K.A., 1984. *A spectral reflectance study of the sedimentary paleozoic rocks around Racetrack Valley in Death Valley National Monument* (Master's thesis, California State University, Northridge).

Bridges, J.C., Schwenzer, S.P., Leveille, R., Westall, F., Wiens, R.C., Mangold, N., Bristow, T., Edwards, P. and Berger, G., 2015. Diagenesis and clay mineral formation at Gale Crater, Mars. *Journal of Geophysical Research: Planets*, *120*(1), pp.1-19.

Bristow, T.F., Blake, D.F., Vaniman, D.T., Chipera, S.J., Rampe, E.B., Grotzinger, J.P., McAdam, A.C., Ming, D.W., Morrison, S.M., Yen, A.S. and Morris, R.V., 2017b, March. Surveying clay mineral diversity in the Murray formation, Gale Crater, Mars. In *Lunar and Planetary Science Conference* (No. JSC-CN-38734).

Bristow, T.F., Grotzinger, J.P., Rampe, E.B., Cuadros, J., Chipera, S.J., Downs, G.W., Fedo, C.M., Frydenvang, J., McAdam, A.C., Morris, R.V. and Achilles, C.N., 2021. Brine-driven destruction of clay minerals in Gale crater, Mars. *Science*, *373*(6551), pp.198-204.

Buz, J., Ehlmann, B.L., Pan, L. and Grotzinger, J.P., 2017. Mineralogy and stratigraphy of the Gale crater rim, wall, and floor units. *Journal of Geophysical Research: Planets*, *122*(5), pp.1090-1118.

Caravaca, G., Mangold, N., Dehouck, E., Schieber, J., Zaugg, L., Bryk, A.B., Fedo, C.M., Le Mouélic, S., Le Deit, L., Banham, S.G. and Gupta, S., 2022. From Lake to River: Documenting an Environmental Transition across the Jura/Knockfarril Hill Members Boundary in the Glen Torridon Region of Gale crater (Mars). *Journal of Geophysical Research: Planets*, p.e2021JE007093.

Corsetti, F.A. and Grotzinger, J.P., 2005. Origin and significance of tube structures in Neoproterozoic post-glacial cap carbonates: example from Noonday Dolomite, Death Valley, United States. *Palaios*, *20*(4), pp.348-362.

Crowley, J.K., 1993. Mapping playa evaporite minerals with AVIRIS data: A first report from Death Valley, California. *Remote Sensing of Environment*, *44*(2-3), pp.337-356.

Crowley, J.K., 1996. Mg-and K-bearing borates and associated evaporites at Eagle Borax Spring, Death Valley, California; a spectroscopic exploration. *Economic Geology*, *91*(3), pp.622-635.

Dalton, G. R., Lee, A. Y., & Young, S. L. (2016). IUPAC/NIST Solubility Database (No. IUPAC/NIST Solubility Database).

Das, D., Gasda, P. J., Wiens, R. C., Berlo, K., Leveille, R. J., Frydenvang, J., Mangold, M., et al. "Boron and lithium in calcium sulfate veins: Tracking precipitation of diagenetic materials in Vera Rubin Ridge, Gale crater." *Journal of Geophysical Research: Planets* 125, no. 8 (2020): e2019JE006301.

Duke, E.F., 2021. Mapping metamorphic hydration fronts with field-based near-infrared spectroscopy: Teakettle Junction contact aureole, Death Valley National Park (California, USA). *Geosphere*, *17*(1), pp.306-321.

Edgar, L.A., Fedo, C.M., Gupta, S., Banham, S.G., Fraeman, A.A., Grotzinger, J.P., Stack, K.M., Stein, N.T., Bennett, K.A., Rivera-Hernández, F. and Sun, V.Z., 2020. A lacustrine paleoenvironment recorded at Vera RubinRidge, Gale crater: Overview of the sedimentology and stratigraphy observed by the Mars ScienceLaboratory Curiosity Rover. *Journal of Geophysical Research: Planets*, *125*(3), p.e2019JE006307.

Ehlmann, B.L., Mustard, J.F., Murchie, S.L., Bibring, J.P., Meunier, A., Fraeman, A.A. and Langevin, Y., 2011. Subsurface water and clay mineral formation during the early history of Mars. *Nature*, *479*(7371), pp.53-60.

Ehlmann, B.L., Bish, D.L., Ruff, S.W. and Mustard, J.F., 2012. Mineralogy and chemistry of altered Icelandic basalts: Application to clay mineral detection and understanding aqueous environments on Mars. *Journal of Geophysical Research: Planets*, *117*(E11).

El-Maarry, M.R., Watters, W.A., Yoldi, Z., Pommerol, A., Fischer, D., Eggenberger, U. and Thomas, N., 2015. Field investigation of dried lakes in western United States as an analogue to desiccation fractures on Mars. *Journal of Geophysical Research: Planets*, *120*(12), pp.2241-2257.

Ericksen, G.E., Vine, J.D. and Ballon, R., 1978. Chemical composition and distribution of lithium-rich brines in Salar de Uyuni and nearby salars in southwestern Bolivia. In *Lithium Needs and Resources* (pp. 355-363). Pergamon.

Ericksen, G.E., Hosterman, J.W. and Amand, P.S., 1988. Chemistry, mineralogy and origin of the clay-hill nitrate deposits, Amargosa River valley, Death Valley region, California, USA. *Chemical geology*, *67*(1-2), pp.85-102.

Eugster, Hans P. "Geochemistry of evaporitic lacustrine deposits." *Annual Review of Earth and Planetary Sciences* 8, no. 1 (1980): 35-63.

Fedo, C.M., Grotzinger, J.P., Gupta, S., Fraeman, A., Edgar, L., Edgett, K., Stein, N., Rivera-Hernandez, F., Lewis, K., Stack, K.M. and House, C., 2018, March. Sedimentology and stratigraphy of the Murray formation, Gale crater, Mars. In *49th Lunar and Planetary Science Conference, The Woodlands, TX* (p. 2083).

Felmy, A.R. and Weare, J.H., 1986. The prediction of borate mineral equilibria in natural waters: Application to Searles Lake, California. *Geochimica et Cosmochimica Acta*, *50*(12), pp.2771-2783.

Filiberto, J., and S. P. Schwenzer (2013), Alteration mineralogy of the Home Plate and Columbia Hills—Formation conditions in context to impact, volcanism and fluvial activity, Meteorit. Planet. Sci.

Fraeman, A.A., Arvidson, R.E., Catalano, J.G., Grotzinger, J.P., Morris, R.V., Murchie, S.L., Stack, K.M., Humm, D.C., McGovern, J.A., Seelos, F.P. and Seelos, K.D., 2013. A hematite-bearing layer in Gale Crater, Mars: Mapping and implications for past aqueous conditions. *Geology*, *41*(10), pp.1103-1106.

Fraeman, A.A., Edgar, L.A., Rampe, E.B., Thompson, L.M., Frydenvang, J., Fedo, C.M., Catalano, J.G., Dietrich, W.E., Gabriel, T.S., Vasavada, A.R. and Grotzinger, J.P., 2020. Evidence for a diagenetic origin of Vera Rubin ridge, Gale crater, Mars: Summary and synthesis of Curiosity's exploration campaign. *Journal of Geophysical Research: Planets*, *125*(12), p.e2020JE006527.

Frydenvang, J., Gasda, P.J., Hurowitz, J.A., Grotzinger, J.P., Wiens, R.C., Newsom, H.E., Edgett, K.S., Watkins, J., Bridges, J.C., Maurice, S. and Fisk, M.R., 2017. Diagenetic silica enrichment and late-stage groundwater activity in Gale crater, Mars. *Geophysical Research Letters*, *44*(10), pp.4716-4724.

Frydenvang, J., Mangold, N., Wiens, R.C., Fraeman, A.A., Edgar, L.A., Fedo, C.M., L'Haridon, J., Bedford, C.C., Gupta, S., Grotzinger, J.P. and Bridges, J.C., 2020. The chemostratigraphy of the Murray formation and role of diagenesis at Vera Rubin ridge in Gale crater, Mars, as observed by the ChemCam instrument. *Journal of Geophysical Research: Planets*, *125*(9), p.e2019JE006320.

Gasda, P. J., Haldeman, E. B., Wiens, R. C., Rapin, W., Bristow, T. F., Bridges, J. C., et al. (2017). In situ detection of boron by ChemCam on Mars. Geophysical Research Letters, 44(17), 8739-8748. 795

Gasda, P.J., Comellas, J., Essunfeld, A., Das, D., Bryk, A.B., Dehouck, E., Schwenzer, S.P., Crossey, L., Herkenhoff, K., Johnson, J.R. and Newsom, H., 2022. Overview of the Morphology and Chemistry of Diagenetic Features in the Clay-Rich Glen Torridon Unit of Gale Crater, Mars. *Journal of Geophysical Research: Planets*, p.e2021JE007097.

Gellert, R & Berger, Jeff & Boyd, Neat & Brunet, C & Campbell, J & Curry, M & Elliott, B & Fulford, P & Grotzinger, J & Hipkin, V & A., Hurowitz & King, P & A., Leshin & Limonadi, Daniel & Pavri, B & Pradler, Irina & Marchand, G & Perrett, Glynis & Scodary, A & Yen, A. (2013). Initial MSL APXS Activities and Observations at Gale Crater, Mars. 44th LPSC, Abstract 1432

Gibbard Jr, H.F. and Scatchard, G., 1973. Liquid-vapor equilibrium of aqueous lithium chloride, from 25 to 100. deg. and from 1.0 to 18.5 molal, and related properties. *Journal of Chemical and Engineering Data*, *18*(3), pp.293-298.

Guo, P., Wen, H., Li, C., Jin, J. and Lei, H., 2021. Origin and enrichment of borates in a Late Paleozoic alkaline lake-playa deposit, Junggar Basin, NW China. *Ore Geology Reviews*, *138*, p.104389.

Gwizd, S., Fedo, C., Grotzinger, J., Edgett, K., Rivera-Hernandez, F., & Stein, N. (2018). Depositional history of the Hartmann's valley member, Murray formation, Gale crater, Mars. Paper presented at Lunar and Planetary Science Conference XLIV, Houston, TX.

Gwizd, S., Fedo, C., Grotzinger, J., Banham, S., Rivera-Hernández, F., Stack, K. M. (2022) Sedimentological and geochemical perspectives on a marginal lake environment recorded in the Hartmann’s Valley and Karasburg members of the Murray formation, Gale crater, Mars, *Journal of Geophysical Research: Planets*, in press.

Haber, J. T., Horgan, B., Fraeman, A. A., Johnson, J. R., Wellington, D., Bell, J. F., Starr, M. S., Rice, M. S., & Mangold, N. (2019). Mineralogy of a possible ancient lakeshore in Gale crater, Mars, from Mastcam multispectral images. Abstract number 6229. Presented at the Ninth International Conference on Mars, LPI Contributions, Pasadena, CA.

He, L., Arvidson, R.E., O'Sullivan, J.A., Morris, R.V., Condus, T., Hughes, M.N. and Powell, K.E., 2022. Surface Kinetic Temperatures and Nontronite Single Scattering Albedo Spectra from Mars Reconnaissance Orbiter CRISM Hyperspectral Imaging Data Over Glen Torridon, Gale Crater, Mars. *Journal of Geophysical Research: Planets*, p.e2021JE007092.

Hurowitz, J.A., Grotzinger, J.P., Fischer, W.W., McLennan, S.M., Milliken, R.E., Stein, N., Vasavada, A.R., Blake, D.F., Dehouck, E., Eigenbrode, J.L. and Fairen, A.G., 2017. Redox stratification of an ancient lake in Gale crater, Mars. *Science*, *356*(6341), p.eaah6849.

Hud, N.V. and Fialho, D.M., 2019. RNA nucleosides built in one prebiotic pot. *Science*, *366*(6461), pp.32-33.

Hunt CB, Robinson TW, Bowles WA, and Washburn AL (1966) Hydrologic basin, Death Valley, California. U.S. Geological Survey Professional Paper 494-B: 1–138.

Karmanocky, F.J., 2014. *Fluid inclusion study of gypsum precipitated in acid saline waters: Salar Ignorado, northern Chile*. West Virginia University.

Karahan, S., Yurdakoç, M., Seki, Y. and Yurdakoç, K., 2006. Removal of boron from aqueous solution by clays and modified clays. *Journal of Colloid and Interface Science*, *293*(1), pp.36-42.

Kaufman, A.J., Corsetti, F.A. and Varni, M.A., 2007. The effect of rising atmospheric oxygen on carbon and sulfur isotope anomalies in the Neoproterozoic Johnnie Formation, Death Valley, USA. *Chemical Geology*, *237*(1-2), pp.47-63.

Klee, J., Chabani, A., Ledésert, B.A., Potel, S., Hébert, R.L. and Trullenque, G., 2021. Fluid-rock interactions in a paleo-geothermal reservoir (Noble hills granite, California, USA). part 2:

The influence of fracturing on granite alteration processes and fluid circulation at low to moderate regional strain. *Geosciences*, *11*(11), p.433.

Knott, J.R., Machette, M.N., Wan, E., Klinger, R.E., Liddicoat, J.C., Sarna-Wojcicki, A.M., Fleck, R.J., Deino, A.L., Geissman, J.W., Slate, J.L. and Wahl, D.B., 2018. Late Neogene–Quaternary tephrochronology, stratigraphy, and paleoclimate of Death Valley, California, USA. *Bulletin*, *130*(7-8), pp.1231-1255.

Kronyak, R.E., Kah, L.C., Edgett, K.S., VanBommel, S.J., Thompson, L.M., Wiens, R.C., Sun, V.Z. and Nachon, M., 2019. Mineral-filled fractures as indicators of multigenerational fluid flow in the Pahrump Hills member of the Murray formation, Gale crater, Mars. *Earth and Space Science*, *6*(2), pp.238-265.

Kruse, F.A., Lefkoff, A.B. and Dietz, J.B., 1993. Expert system-based mineral mapping in northern Death Valley, California/Nevada, using the airborne visible/infrared imaging spectrometer (AVIRIS). *Remote Sensing of Environment*, *44*(2-3), pp.309-336.

Langbein, W.B., 1961. *Salinity and hydrology of closed lakes: A study of the long-term balance between input and loss of salts in closed lakes* (Vol. 412). US Government Printing Office.

L'Haridon, J., Mangold, N., Fraeman, A.A., Johnson, J.R., Cousin, A., Rapin, W., David, G., Dehouck, E., Sun, V., Frydenvang, J. and Gasnault, O., 2020. Iron mobility during diagenesis at Vera Rubin ridge, Gale crater, Mars. *Journal of Geophysical Research: Planets*, *125*(11), p.e2019JE006299.

Li, W. and Liu, X.M., 2020. Experimental investigation of lithium isotope fractionation during kaolinite adsorption: Implications for chemical weathering. *Geochimica et cosmochimica acta*, *284*, pp.156-172.

Lodders, K., 1998. A survey of shergottite, nakhlite and chassigny meteorites whole-rock compositions. *Meteoritics & Planetary Science*, *33*(S4), pp.A183-A190.

Lowenstein, Tim K., Jianren Li, Christopher Brown, Sheila M. Roberts, Teh-Lung Ku, Shangde Luo, and Wenbo Yang. "200 ky paleoclimate record from Death Valley salt core." *Geology* 27, no. 1 (1999): 3-6.

Mangold, N., Dehouck, E., Fedo, C., Forni, O., Achilles, C., Bristow, T., Downs, R.T., Frydenvang, J., Gasnault, O., l'Haridon, J. and Le Deit, L., 2019. Chemical alteration of fine-grained sedimentary rocks at Gale crater. *Icarus*, *321*, pp.619-631.

Marsh, G.E., 2022. Thermodynamics and the Origin of Life. *Canadian Journal of Physics*, (ja).

Maurice, S., et al. (2012), The ChemCam instrument suite on the Mars science laboratory (MSL) rover: Science objectives and mast unit description, Space Sci. Rev., 170(1–4), 95–166

McAdam, A.C., Franz, H.B., Sutter, B., Archer Jr, P.D., Freissinet, C., Eigenbrode, J.L., Ming, D.W., Atreya, S.K., Bish, D.L., Blake, D.F. and Bower, H.E., 2014. Sulfur-bearing phases detected by evolved gas analysis of the Rocknest aeolian deposit, Gale Crater, Mars. *Journal of Geophysical Research: Planets*, *119*(2), pp.373-393.

McAdam, A.C., Sutter, B., Archer, P.D., Franz, H.B., Wong, G.M., Lewis, J.M., Eigenbrode, J.L., Stern, J.C., Knudson, C.A., Clark, J.V. and Andrejkovičová, S., 2020. Constraints on the mineralogy and geochemistry of Vera Rubin ridge, Gale crater, Mars, from Mars Science Laboratory Sample Analysis at Mars evolved gas analyses. *Journal of Geophysical Research: Planets*, *125*(11), p.e2019JE006309.

Melwani Daswani, M., Schwenzer, S.P., Reed, M.H., Wright, I.P. and Grady, M.M., 2016. Alteration minerals, fluids, and gases on early Mars: Predictions from 1-D flow geochemical modeling of mineral assemblages in meteorite ALH 84001. *Meteoritics & Planetary Science*, *51*(11), pp.2154-2174.

Milliken, R.E., Grotzinger, J.P. and Thomson, B.J., 2010. Paleoclimate of Mars as captured by the stratigraphic record in Gale Crater. *Geophysical Research Letters*, *37*(4).

Moknatian, M. and Piasecki, M., 2019. Lake volume data analyses: A deep look into the shrinking and expansion patterns of Lakes Azuei and Enriquillo, Hispaniola. *Hydrology*, *7*(1), p.1.

Morris, R.V., Ming, D.W., Gellert, R., Vaniman, D.T., Bish, D.L., Blake, D.F., Chipera, S.J., Morrison, S.M., Downs, R.T., Rampe, E.B. and Treiman, A.H., 2015, March. Update on the chemical composition of crystalline, smectite, and amorphous components for Rocknest soil and John Klein and Cumberland mudstone drill fines at Gale crater, Mars. In *Lunar and Planetary Science Conference* (No. JSC-CN-32822).

Morris, R.V., Vaniman, D.T., Blake, D.F., Gellert, R., Chipera, S.J., Rampe, E.B., Ming, D.W., Morrison, S.M., Downs, R.T., Treiman, A.H. and Yen, A.S., 2016. Silicic volcanism on Mars evidenced by tridymite in high-SiO2 sedimentary rock at Gale crater. *Proceedings of the National Academy of Sciences*, *113*(26), pp.7071-7076.

Morrison, S.M., Downs, R.T., Blake, D.F., Vaniman, D.T., Ming, D.W., Hazen, R.M., Treiman, A.H., Achilles, C.N., Yen, A.S., Morris, R.V. and Rampe, E.B., 2018. Crystal chemistry of martian minerals from Bradbury Landing through Naukluft Plateau, Gale crater, Mars. *American Mineralogist: Journal of Earth and Planetary Materials*, *103*(6), pp.857-871.

Muessig, S.J., Pennell, W.M., Knott, J.R. and Calzia, J.P., 2019. *Geology of the Monte Blanco borate deposits, Furnace Creek Wash, Death Valley, California* (No. 2019-1111). US Geological Survey.

Munk, L.A., Hynek, S.A., Bradley, D., Boutt, D., Labay, K. and Jochens, H., 2016. Lithium brines: A global perspective. *Reviews in Economic Geology*, *18*, pp.339-365.

Nachon, M., Clegg, S.M., Mangold, N., Schröder, S., Kah, L.C., Dromart, G., Ollila, A., Johnson, J.R., Oehler, D.Z., Bridges, J.C. and Le Mouélic, S., 2014. Calcium sulfate veins characterized by ChemCam/Curiosity at Gale crater, Mars. *Journal of Geophysical Research: Planets*, *119*(9), pp.1991-2016.

Nellessen, M.A., Crossey, L., Peterson, E., Gasda, P.J., Lanza, N., Yeager, C., Parsons, B., Labouriau, A., Wiens, R.C., Clegg, S. and Das, D., 2019, July. Boron Adsorption in Clay Minerals: Implications for Martian Groundwater Chemistry and Prebiotic Processes. In *Ninth International Conference on Mars* (Vol. 2089, p. 6353).

Ochsenius, C., 1888. On the formation of rock-salt beds and mother-liquor salts. *Proceedings of the Academy of Natural Sciences of Philadelphia*, pp.181-187.

Ólafsson, J. and Riley, J.P., 1978. Geochemical studies on the thermal brine from Reykjanes (Iceland). *Chemical Geology*, *21*(3-4), pp.219-237.

Orti, F., Helvaci, C., Rosell, L. and Gündoğan, İ., 1998. Sulphate–borate relations in an evaporitic lacustrine environment: the Sultancayir gypsum (Miocene, western Anatolia). *Sedimentology*, *45*(4), pp.697-710.

Ortí, F., Rosell, L., García-Veigas, J. and Helvaci, C., 2016. Sulfate–Borate Association (Glauberite–Probertite) In the Emet Basin: Implications For Evaporite Sedimentology (Middle Miocene, Turkey). *Journal of Sedimentary Research*, *86*(5), pp.448-475.

Palucis, M.C., Dietrich, W.E., Williams, R.M., Hayes, A.G., Parker, T., Sumner, D.Y., Mangold, N., Lewis, K. and Newsom, H., 2016. Sequence and relative timing of large lakes in Gale crater (Mars) after the formation of Mount Sharp. *Journal of Geophysical Research: Planets*, *121*(3), pp.472-496.

Petterson, R., Prave, A.R., Wernicke, B.P. and Fallick, A.E., 2011. The Neoproterozoic Noonday Formation, Death Valley region, California. *Bulletin*, *123*(7-8), pp.1317-1336.

Rampe, E.B., Blake, D.F., Bristow, T.F., Ming, D.W., Vaniman, D.T., Morris, R.V., Achilles, C.N., Chipera, S.J., Morrison, S.M., Tu, V.M. and Yen, A.S., 2020. Mineralogy and geochemistry of sedimentary rocks and eolian sediments in Gale crater, Mars: A review after six Earth years of exploration with Curiosity. *Geochemistry*, *80*(2), p.125605.

Rampe, E.B., Bristow, T.F., Blake, D.F., Vaniman, D.T., Chipera, S.J., Downs, R.T., Ming, D.W., Morris, R.V., Tu, V.M., Thorpe, M.T. and Yen, A.S., 2022, March. Mineralogical Trends Over the Clay-Sulfate Transition in Gale Crater from the Mars Science Laboratory CheMin Instrument. In *53rd Lunar and Planetary Science Conference*.

Rapin, W., Chauviré, B., Gabriel, T.S.J., McAdam, A.C., Ehlmann, B.L., Hardgrove, C., Meslin, P.Y., Rondeau, B., Dehouck, E., Franz, H.B. and Mangold, N., 2018. In situ analysis of opal in Gale Crater, Mars. *Journal of Geophysical Research: Planets*, *123*(8), pp.1955-1972.

Rapin, W., Ehlmann, B.L., Dromart, G., Schieber, J., Thomas, N.H., Fischer, W.W., Fox, V.K., Stein, N.T., Nachon, M., Clark, B.C. and Kah, L.C., 2019. An interval of high salinity in ancient Gale crater lake on Mars. *Nature Geoscience*, *12*(11), pp.889-895.

Rapin, W., Dromart, G., Rubin, D., Deit, L.L., Mangold, N., Edgar, L.A., Gasnault, O., Herkenhoff, K., Le Mouélic, S., Anderson, R.B. and Maurice, S., 2021. Alternating wet and dry depositional environments recorded in the stratigraphy of Mount Sharp at Gale crater, Mars. *Geology*, *49*(7), pp.842-846.

Reed, M.H. and Spycher, N.F., 2006. User's guide for CHILLER: A program for computing water-rock reactions, boiling, mixing and other reaction processes in aqueous-mineralgas systems and minplot guide. *Eugene, OR: University of Oregon*.

Reed, M. H., N. F. Spycher, and J. Palandri (2010), User Guide for CHIM-XPT: A Program for Computing Reaction Processes in Aqueous-Mineral-Gas Systems and Minplot Guide, Univ. of Oregon, Eugene

Roberts, S.M. and Spencer, R.J., 2020. A desert responds to Pleistocene climate change: Saline lacustrine sediments, Death Valley, California, USA. In *Quaternary deserts and climatic change* (pp. 357-370). CRC Press.

Rohmah, M., Lalasari, L.H., Natasha, N.C., Sulistiyono, E., Firdiyono, F. and Soedarsono, J.W., 2020. Adsorption Behavior of Alkali Metal (Na+, Li+, and K+) from Bledug Kuwu brine by Resin Adsorbent for Purification: pH and Flow Rate Parameter. *Orient. J. Chem*, *36*(2), pp.273-279.

Ruhl, L.S., 2008. *Thermodynamics of 1: 2 Sodium Borate Minerals* (Doctoral dissertation, University of Florida).

Rumble, J. ed., 2017. CRC handbook of chemistry and physics.

Sarrazin, P., Blake, D., Feldman, S., Chipera, S., Vaniman, D. and Bish, D., 2005. Field deployment of a portable X-ray diffraction/X-ray flourescence instrument on Mars analog terrain. *Powder Diffraction*, *20*(2), pp.128-133.

Sarg, J.F., 2001. The sequence stratigraphy, sedimentology, and economic importance of evaporite–carbonate transitions: a review. *Sedimentary Geology*, *140*(1-2), pp.9-34.

Scheller, E.L., Ehlmann, B.L., Hu, R., Adams, D.J. and Yung, Y.L., 2021. Long-term drying of Mars by sequestration of ocean-scale volumes of water in the crust. *Science*, *372*(6537), pp.56-62.

Schwenzer, S.P., Abramov, O., Allen, C.C., Bridges, J.C., Clifford, S.M., Filiberto, J., Kring, D.A., Lasue, J., McGovern, P.J., Newsom, H.E. and Treiman, A.H., 2012. Gale Crater: Formation and post-impact hydrous environments. *Planetary and Space Science*, *70*(1), pp.84-95.

Schwenzer, S.P., Bridges, J., Leveille, R.J., Westall, F., Wiens, R.C., Mangold, N., McAdam, A., Conrad, P.G., Martín-Torres, J. and Zorzano, M.P., 2014, December. Fluids and Sulfate Vein Formation in Gale Crater, Mars. In *AGU Fall Meeting Abstracts* (Vol. 2014, pp. P42C-08).

Schwenzer, S.P., Bridges, J.C., Wiens, R.C., Conrad, P.G., Kelley, S.P., Leveille, R., Mangold, N., Martín-Torres, J., McAdam, A., Newsom, H. and Zorzano, M.P., 2016. Fluids during diagenesis and sulfate vein formation in sediments at Gale crater, Mars. *Meteoritics & Planetary Science*, *51*(11), pp.2175-2202.

Schwenzer, S., Bridges, J., Turner, S., Ramkissoon, N., Cogliati, S., Seidel, R., Reed, M., Filiberto, J., Vaniman, D. and Olsson-Francis, K., 2020. Martian fluids and their evaporation products–an overview using thermochemical modelling.

Scruton, P.C., 1953. Deposition of evaporites. *AAPG Bulletin*, *37*(11), pp.2498-2512.

Siebach, K.L., Fedo, C.M., Edgar, L.E., Edgett, K., Grotzinger, J.P., Fraeman, A.A., Thompson, L.M., Gupta, S., House, C.H. and O'Connell-Cooper, C., 2019, March. Overview of Gale crater stratigraphy and sedimentology from 6 years of roving with Mars Science Laboratory. In *50th Annual Lunar and Planetary Science Conference* (No. 2132, p. 1479).

Smykatz-Kloss, Werner, and Priyadarsi D. Roy. "Evaporite mineralogy and major element geochemistry as tools for palaeoclimatic investigations in arid regions: A synthesis." *Boletín de la Sociedad Geológica Mexicana* 62, no. 3 (2010): 379-390.

Song, J.F., Nghiem, L.D., Li, X.M. and He, T., 2017. Lithium extraction from Chinese salt-lake brines: opportunities, challenges, and future outlook. *Environmental Science: Water Research & Technology*, *3*(4), pp.593-597.

Stack, K.M., Grotzinger, J.P., Lamb, M.P., Gupta, S., Rubin, D.M., Kah, L.C., Edgar, L.A., Fey, D.M., Hurowitz, J.A., McBride, M. and Rivera-Hernández, F., 2018. Evidence for plunging river plume deposits in the Pahrump Hills member of the Murray formation, Gale crater, Mars. *Sedimentology*, *66*(5), pp.1768-1802.

Stein, N., J. P. Grotzinger, J. Schieber, Nicolas Mangold, B. Hallet, H. Newsom, K. M. Stack et al. "Desiccation cracks provide evidence of lake drying on Mars, Sutton Island member, Murray formation, Gale Crater." *Geology* 46, no. 6 (2018): 515-518.

Sun, V.Z., Stack, K.M., Kah, L.C., Thompson, L., Fischer, W., Williams, A.J., Johnson, S.S., Wiens, R.C., Kronyak, R.E., Nachon, M. and House, C.H., 2019. Late-stage diagenetic concretions in the Murray formation, Gale crater, Mars. *Icarus*, *321*, pp.866-890.

Sutter, B., Amy C. Mcadam, Paul R. Mahaffy, Doug W. Ming, Ken S. Edgett, Elizabeth B. Rampe, Jennifer L. Eigenbrode et al. "Evolved gas analyses of sedimentary rocks and eolian sediment in Gale Crater, Mars: Results of the Curiosity rover's sample analysis at Mars instrument from Yellowknife Bay to the Namib Dune." *Journal of Geophysical Research: Planets* 122, no. 12 (2017): 2574-2609.

Swihart, George H., Steven B. Carpenter, Yun Xiao, Eddie H. McBay, David H. Smith, and Yingkai Xiao. "A Boron Isotope Study of the Furnace Creek, California, Borate District." *Economic Geology* 109, no. 3 (2014): 567-580.

Thomas, N.H., Ehlmann, B.L., Meslin, P.Y., Rapin, W., Anderson, D.E., Rivera-Hernández, F., Forni, O., Schröder, S., Cousin, A., Mangold, N. and Gellert, R., 2019. Mars Science Laboratory observations of chloride salts in Gale crater, Mars. *Geophysical Research Letters*, *46*(19), pp.10754-10763.

Thomas, N. H., Ehlmann, B. L., Rapin, W., Rivera-Hernández, F., Stein, N. T., Frydenvang, J., et al. (2020). Hydrogen Variability in the Murray Formation, Gale Crater, Mars. *Journal of Geophysical Research: Planets*.

Tanner, L. H. "Borate formation in a perennial lacustrine setting: Miocene–Pliocene furnace creek formation, Death Valley, California, USA." *Sedimentary Geology* 148, no. 1-2 (2002): 259-273.

Thomas, G. and Coleman, N.T., 1964. The fate of exchangeable iron in acid clay systems. *Soil Science*, *97*(4), pp.229-232.

Thorpe, M.T., Rampe, E.B., Tamborski, J.J., Siebach, K.L., Putnam, A., Kovtun, R., Lynch, K.L., Leeb, D., Gundjonsson, G., Tu, V.M. and Ewing, R.C., 2022, March. Overview and Initial Results of DIGMARS: Digging Iceland Geology for Mars Analog Research Science. In 53rd Lunar and Planetary Science Conference (LPSC).

Treiman, A.H., 2005. The nakhlite meteorites: Augite-rich igneous rocks from Mars. *Geochemistry*, *65*(3), pp.203-270.

Treiman, A.H., Bish, D.L., Vaniman, D.T., Chipera, S.J., Blake, D.F., Ming, D.W., Morris, R.V., Bristow, T.F., Morrison, S.M., Baker, M.B. and Rampe, E.B., 2016. Mineralogy, provenance, and diagenesis of a potassic basaltic sandstone on Mars: CheMin X-ray diffraction of the Windjana sample (Kimberley area, Gale Crater). *Journal of Geophysical Research: Planets*, *121*(1), pp.75-106.

Turner, S.M.R., Schwenzer, S.P., Bridges, J.C., Rampe, E.B., Bedford, C.C., Achilles, C.N., McAdam, A.C., Mangold, N., Hicks, L.J., Parnell, J. and Fraeman, A.A., 2021. Early diagenesis at and below Vera Rubin ridge, Gale crater, Mars. *Meteoritics & Planetary Science*, *56*(10), pp.1905-1932.

Van der Meeren, T. and Verschuren, D., 2021. Zoobenthos community turnover in a 1650-yr lake-sediment record of climate-driven hydrological change. *Ecosphere*, *12*(1), p.e03333.

Vaniman, D.T., Bish, D.L., Ming, D.W., Bristow, T.F., Morris, R.V., Blake, D.F., Chipera, S.J., Morrison, S.M., Treiman, A.H., Rampe, E.B. and Rice, M., 2014. Mineralogy of a mudstone at Yellowknife Bay, Gale crater, Mars. *science*, *343*(6169), p.1243480.

Vaniman, D.T., Martínez, G.M., Rampe, E.B., Bristow, T.F., Blake, D.F., Yen, A.S., Ming, D.W., Rapin, W., Meslin, P.Y., Morookian, J.M. and Downs, R.T., 2018. Gypsum, bassanite, and anhydrite at Gale crater, Mars. *American Mineralogist: Journal of Earth and Planetary Materials*, *103*(7), pp.1011-1020.

Vasavada, A. R. (2022). Mission Overview and Scientific Contributions from the Mars Science Laboratory Curiosity Rover After Eight Years of Surface Operations. *Space Science Reviews*, *218*(3), 14.

Warren, J.K., 2000. Evaporites, brines and base metals: low-temperature ore emplacement controlled by evaporite diagenesis. *Australian Journal of Earth Sciences*, *47*(2), pp.179-208.

Warren, J.K., 2006. *Evaporites: Sediments, Resources and Hydrocarbons*. Springer Science & Business Media.

Warren, J.K., 2016. Non-potash salts: Borates, Na-sulphates, Na-carbonate, lithium salts, gypsum, halite and zolites. In *Evaporites* (pp. 1187-1302). Springer, Cham.

Wiens, R. C., et al. (2012), The ChemCam instrument suite on the Mars science laboratory (MSL) rover: Body unit and combined system tests, Space Sci. Rev., 170(1–4)

Xiang, W., Liang, S., Zhou, Z., Qin, W. and Fei, W., 2016. Extraction of lithium from salt lake brine containing borate anion and high concentration of magnesium. *Hydrometallurgy*, *166*, pp.9-15.

Yang, W., Lowenstein, T.K., Krouse, H.R., Spencer, R.J. and Ku, T.L., 2005. A 200,000-year δ18O record of closed-basin lacustrine calcite, Death Valley, California. *Chemical Geology*, *216*(1-2), pp.99-111.

Yen, A.S., Morris, R.V., Ming, D.W., Schwenzer, S.P., Sutter, B., Vaniman, D.T., Treiman, A.H., Gellert, R., Achilles, C.N., Berger, J.A. and Blake, D.F., 2021. Formation of tridymite and evidence for a hydrothermal history at gale crater, Mars. *Journal of Geophysical Research: Planets*, *126*(3), p.e2020JE006569.

Yu, X., Liu, C., Wang, C., Wang, J., Li, Q. and Meng, L., 2022. Origin of Li brine-type deposits in the Cretaceous gypsum-bearing formation of the Jitai Basin, South China: Constraints from geochemistry and H, O, Li, B, and Sr isotopes. *Applied Geochemistry*, *139*, p.105257.

# Link to Chapter Three

In Chapter 1 we found that B and Li abundance in Ca-sulfate veins of Gale crater show an inverse correlation. We hypothesized that B enrichment in secondary Ca-sulfates of Gale crater is likely due to pre-existing primary borate deposits that were remobilized and precipitated with Ca-sulfates, and B and Li were likely drawn out of clay minerals during aqueous events with varying pH conditions over multiple wet-dry cycles.

In Chapter 2 we established using thermochemical modeling that wet-dry cycles (with a minimum requirement of 250 annual cycles for Gale crater) are required to form primary evaporites that consist of borates and Ca-sulfates in close association with each other. In Chapter 1 and 2, we also note that the reservoir for B and Li associated with Ca-sulfates in Gale crater are still unknown as we have not detected crystalline borates or Li-salts in Gale crater to this day.

In this chapter we investigate the distribution of B and Li in various phases within samples collected from a terrestrial analog area in Southern California. The environments in the selected areas are similar to that inferred for Gale crater (i.e., multiple wet-dry events with variable aqueous pH conditions) in addition to the presence of evaporites (borates, Ca-sulfates, halite, and carbonates) and sedimentary rocks.

Observations in Gale crater show mixing between evaporites and surrounding sedimentary rocks (e.g., L'Haridon et al., 2018; Hurowitz et al., 2017; Gasda et al., 2022). This mixing is inferred to be due to presence of cements or simultaneously sampling an evaporite vein and bedrock at the same time during Curiosity rover analytical techniques (Gasda et al., 2022). Hence, we chose a terrestrial analog area which enabled the determination of the distribution and abundance trends of B and Li in a sample set with physical mixing between evaporites and sedimentary rocks, and end member representatives (i.e., predominantly borate or Ca-sulfate, or basaltic) as a representative of early primary evaporitic setting in Gale crater.

We investigate whether B enrichment in terrestrial analog samples is linked with evaporite formation while Li enrichment is linked with clay minerals through adsorption. We also observe a consistent negative relationship between B and Li in the terrestrial analog samples as observed for Ca-sulfate veins in Gale crater (as shown in Chapter 1).

We extend our inference to Gale crater through comparative analogy and suggest that Li and B adsorption took place in clay minerals during alkaline aqueous conditions while primary borates, Ca-sulfates and halite formed in low-pH high evaporation conditions over multiple wet-dry cycles with varying fluid pH conditions.

The inferences of pH-controlled emplacement of B in borates and B and Li in clay minerals for the terrestrial analog samples are consistent with previous analytical studies of fluid pH, evaporites and sedimentary rock in the same area (Tanner, 2002; Swihart et al., 2014, 1996; Lowenstein et al., 1999). The physical mixing trends between evaporites and sedimentary rocks in the terrestrial analog samples are broadly consistent with mixing trends observed in Gale crater. The phases identified in the terrestrial samples are also broadly consistent with phases reported in Gale crater and phases formed in a thermochemical simulation of wet-dry cycles in a Gale-relevant environment as summarized in Chapter 2. Hence the inferences made for the terrestrial analog samples are broadly applicable to Gale crater and provide a ground truthing for data obtained using the Curiosity rover and using thermochemical modeling technique in Chapter 1 and Chapter 2, respectively.

## References

Gasda, P.J., Comellas, J., Essunfeld, A., Das, D., Bryk, A.B., Dehouck, E., Schwenzer, S.P., Crossey, L., Herkenhoff, K., Johnson, J.R. and Newsom, H., 2022. Overview of the Morphology and Chemistry of Diagenetic Features in the Clay-Rich Glen Torridon Unit of Gale Crater, Mars. *Journal of Geophysical Research: Planets*, p.e2021JE007097.

Hurowitz, J.A., Grotzinger, J.P., Fischer, W.W., McLennan, S.M., Milliken, R.E., Stein, N., Vasavada, A.R., Blake, D.F., Dehouck, E., Eigenbrode, J.L. and Fairen, A.G., 2017. Redox stratification of an ancient lake in Gale crater, Mars. *Science*, *356*(6341), p. eaah6849.

L'Haridon, J., Mangold, N., Meslin, P.Y., Johnson, J.R., Rapin, W., Forni, O., Cousin, A., Payré, V., Dehouck, E., Nachon, M. and Le Deit, L., 2018. Chemical variability in mineralized veins observed by ChemCam on the lower slopes of Mount Sharp in Gale crater, Mars. *Icarus*, *311*, pp.69-86.

Swihart, G.H., McBay, E.H., Smith, D.H. and Siefke, J.W., 1996. A boron isotopic study of a mineralogically zoned lacustrine borate deposit: the Kramer deposit, California, USA. *Chemical geology*, *127*(1-3), pp.241-250.

Swihart, George H., Steven B. Carpenter, Yun Xiao, Eddie H. McBay, David H. Smith, and Yingkai Xiao. "A Boron Isotope Study of the Furnace Creek, California, Borate District." *Economic Geology* 109, no. 3 (2014): 567-580.

Tanner, L. H. "Borate formation in a perennial lacustrine setting: Miocene–Pliocene furnace creek formation, Death Valley, California, USA." *Sedimentary Geology* 148, no. 1-2 (2002): 259-273.

Lowenstein, Tim K., Jianren Li, Christopher Brown, Sheila M. Roberts, Teh-Lung Ku, Shangde Luo, and Wenbo Yang. "200 ky paleoclimate record from Death Valley salt core." *Geology* 27, no. 1 (1999): 3-6.

# Chapter 3

## Estimating Past Fluid pH and Evaporative Conditions in Gale Crater Using Terrestrial Analog Evaporites and Clay Minerals

D. Das[1], P. J. Gasda[2], K. Berlo[1], R. J. Leveille[1], M. A. Nellessen[3], L. Crossey[3], E. Peterson[3], R. Beal[3], A. L. Reyes-Newell[2], S. M. Clegg[2], A. M. Ollila[2], N. L. Lanza[2]

[1]Department of Earth and Planetary Sciences, McGill University, Quebec, Canada H3A 0E8.

[2]Los Alamos National Laboratory, Los Alamos, NM, USA 87545.

[3]Department of Earth and Planetary Sciences, University of New Mexico, NM, USA 87131

### Abstract

Boron and lithium have been observed in Ca-sulfate veins of Gale crater. These elements are highly water mobile and can tell us about the aqueous history in Gale crater; however the analysis of B in Gale crater is limited to low-Fe rocks and minerals due to spectral interference of Fe with B in the Laser Induced Breakdown Spectroscopy instrument onboard the Curiosity rover. This limitation prevents the determination of B and Li relationship in sedimentary rocks of Gale crater that contain up to 19 wt% Fe.

In this work, we investigate the distribution of B and Li in various phases within samples collected from a terrestrial analog area in Southern California where presence of an environment that is similar to that estimated for Gale crater (i.e., multiple wet-dry events with variable aqueous pH conditions) is reported in addition to the presence of evaporites (borates, Ca-sulfates, halite, and carbonates) and sedimentary rocks. We chose a terrestrial analog area which enabled the determination of the distribution and relation of B and Li in a sample set with physical mixing between evaporites and sedimentary rocks, and end member representatives (i.e., predominantly borate or Ca-sulfate, or basaltic) as a representative of early primary evaporitic settings in Gale crater.

In the terrestrial analog samples, the B concentration is associated with evaporites requiring acidic pH conditions and high evaporation whereas Li concentration is linked with clay minerals presence, suggesting $Li^+$ adsorption requires high pH. We also observe a negative relationship between B and Li in the terrestrial analog samples as observed for Ca-sulfate veins in Gale crater. We extend our inference to Gale crater through comparative analogy and suggest that Li and B adsorption took place in clay minerals during alkaline aqueous conditions, whereas primary borates, Ca-sulfates and halite formed in low-pH high evaporation conditions over multiple wet-dry cycles with varying fluid pH conditions.

## 1 Introduction

Boron and lithium are water-soluble elements that, in terrestrial aqueous settings, commonly are either incorporated as evaporites or adsorbed on clay minerals (Warren, 2000, 2006). Evaporite precipitation and adsorption to clay minerals are pH-sensitive processes (Rohman et al., 2020; Li and Liu, 2020; Karahan et al., 2006; Nellessen et al., 2019) that also depend on extent of fluid evaporation (Warren, 2000, 2006). Adsorption of B and Li onto clay minerals requires high pH aqueous conditions (Rohman et al., 2020; Li and Liu, 2020; Karahan et al., 2006; Nellessen et al., 2019) while incorporation of boron in borate minerals and in other evaporites such as Ca-sulfates (anhydrite, gypsum, bassanite) and halite requires relatively high concentration of borate ions in the fluid followed by a dry period that enables the precipitation of the evaporites (Kistler and Helvaci, 1994; Birsoy and Ozbas, 2012; Felmy and Weare, 1986; Li et al., 2010; Bixler and Sawyer, 1957).

As borate precipitation and B and Li adsorption are pH-sensitive processes that require different sets of pH conditions, in an environment, where both evaporites and clay minerals are present, the distribution of B and Li between evaporites and clay minerals can indicate the changing fluid pH and evaporative conditions.

B and Li have been observed in Ca-sulfate veins of Gale crater on Mars using the ChemCam instrument onboard the Curiosity rover (Gasda et al 2017; Das et al., 2020). No crystalline borates or Li salts have been identified in Gale crater, and the detection of B in Gale crater by ChemCam is limited to low-Fe Ca-sulfate targets (i.e., Ca-sulfate veins). However, Li has been detected in diverse sedimentary rocks of Gale crater (Frydenvang et al., 2020). Gypsum-fluid partition coefficients for B and Li are low, because Ca-sulfate minerals do not structurally accommodate large concentrations of boron or lithium ions in their crystal lattices (Hawthorne et al., 2000; Follner et al., 2002, Ma et al., 2017; Türker and Türker, 2019). Due to the lack of observation of crystalline borates or B measurements in clay-rich sedimentary rocks using the Curiosity rover (the presence of Fe spectrally interferes with B detection; Gasda et al., 2017), and due to the lack of detection of Li-containing minerals in close association with Ca-sulfates, the reservoirs of B and Li associated with Ca-sulfate veins in Gale crater are still unknown.

We hypothesized in Chapter 1 (Das et al., 2020), based on models from Gasda et al. (2017) and Schwenzer et al., (2016), that B enrichments in Ca-sulfates of Gale crater may have been due to pre-existing borate deposits that were remobilized and precipitated in close association with Ca-sulfates veins. In areas where evaporative environments were unlikely, we hypothesized that B and Li are drawn out of clay minerals during acidic aqueous events (Gasda et al., 2017; Das et al, 2020).

In this work, we test the above hypothesis using samples from a terrestrial analog area which were formed in a similar environment as that is inferred for Gale crater for the formation of B and Li-containing Ca-sulfate veins. We chose four sites in Southern California (Furnace Creek and Ryan in Death Valley, Searles Lake, and Kramer borate deposit) as to sample analog materials. This general area is known to have undergone multiple wet-dry cycles (Lowenstein et al., 1999) and multiple periods of fluid influx with varying pH (Swihart et al., 2014). The diverse geology, consisting of volcanics and playa-lacustrine deposits, enabled the sampling of a range of rock types and minerals that include evaporites, clay-rich sedimentary rocks, and igneous rocks from an environment that is similar to the inferred ancient Gale crater environment. We use analytical techniques that consist of Laser Induced Breakdown Spectroscopy (LIBS), Fusion X-Ray Fluorescence (Fus-XRF), Fusion Laser Ablation Inductively Coupled Plasma Mass Spectrometry (Fus-LAICPMS), X-Ray Diffraction (XRD) and Prompt Gamma Neutron Activation Analysis (PGNAA) to characterize the phases in the terrestrial analog samples and determine the distribution of B and Li and estimate fluid pH and evaporative conditions. We apply our findings from terrestrial analog samples to infer fluid pH and evaporative extent on Gale crater based on broad consistency in physical mixing trends between phases and based on broad consistency of mineral assemblages identified in both the terrestrial analog area and in Gale crater.

The comparison of terrestrial analogs with Gale observations enables constraining bounds on the relative pH, and the evaporation stages of fluids possible in Gale crater; this is important for determining the range of habitable conditions possible in Gale crater during an evolving aqueous history.

## 2 Geologic context of Gale crater

### 2.1 Fluvio-lacustrine deposits of Gale crater

The NASA Mars Science Laboratory (MSL) Curiosity rover landed in Gale crater on Aeolis Palus in 2012 and has since then traversed ~28.7 km across outcrops interpreted as eolian, fluvial deltaic, and lacustrine deposits towards Mount Sharp (e.g., Milliken et al., 2010; Grotzinger et al., 2014; 2015; Banham et al., 2018; Stack et al., 2019a; Edgar et al., 2020, Vasavada et al., 2014;2022). Gale crater is a ~155 km wide crater with a central sedimentary mound (Aeolis Mons, informally known as “Mt. Sharp”) located between the Southern Highlands and Northern Lowlands division in the northwestern part of the Aeolis quadrangle (Milliken et al., 2010; Grotzinger and Milliken, 2012; Fraeman et al., 2016). Figure 1 indicates the rover traverse, topographic features, and lithologic formations, members and units described in this section with a corresponding stratigraphic column prepared by the Mars Science Laboratory Sedimentology and Stratigraphy Working Group.

Gale crater is interpreted to have housed an ancient habitable lake (Grotzinger et al., 2015; Hurowitz et al., 2017) with a long-standing extensive groundwater system (e.g., Siebach and Grotzinger, 2014; Frydenvang et al., 2017; 2020, Gasda et al., 2017; 2022). The Bradbury group is a fluvio-deltaic environment which is interfingered with the Mount Sharp group (Grotzinger et al., 2015; Stack et al., 2019a, Bedford et al., 2019; Mangold et al., 2016). The Mount Sharp group deposits are interpreted as primarily lacustrine with lake margin and evaporitic environments (Kah et al., 2018; Stein et al., 2018; Rapin et al., 2019, Edgar et al., 2020). The

Siccar Point group, comprising the Stimson formation, is interpreted as a younger mafic eolian deposit that overlies the Mount Sharp group (Banham et al., 2018; Bedford et al., 2019).

In the Mount Sharp group, evidence of desiccation and evaporation are observed in the Hartmann's Valley though Sutton Island members, and these are interpreted as fluctuating lake margins or a braided river deltaic environment (Stein et al, 2018; Fedo et al., 2018). The evidence includes presence of evaporites (Gasda et al., 2017; Thomas et al., 2019; Rapin et al., 2019, Das et al., 2020), desiccation cracks (Stein et al, 2018), altered clay mineralogy that is inferred to have been formed due to interaction with brines (Bristow et al., 2021), and lake margin lithological facies (Fedo et al., 2018, Edgar et al., 2020). The Blunts Point, Pettegrove Point, and Jura members lie above the Sutton Island member and represent a lacustrine setting (Fraeman et al., 2016; 2020). The Pettegrove Point and Jura members make up the Vera Rubin ridge topographic feature which is interpreted to have formed due to late-stage diagenetic cementation after the lithification of the bedrocks in this area (Rivera-Hernandez et al., 2020; Edgar et al., 2020; Fraeman et al., 2020; Thompson et al., 2020; Frydenvang et al., 2020; Rampe et al., 2020; Turner et al. 2021). The late-stage diagenetic events likely took place over multiple episodes with variable fluid pH, salinity and temperatures based on the presence of minerals such as hematite, akageneite, jarosite, and Ca-sulfates (Rampe et al., 2020).

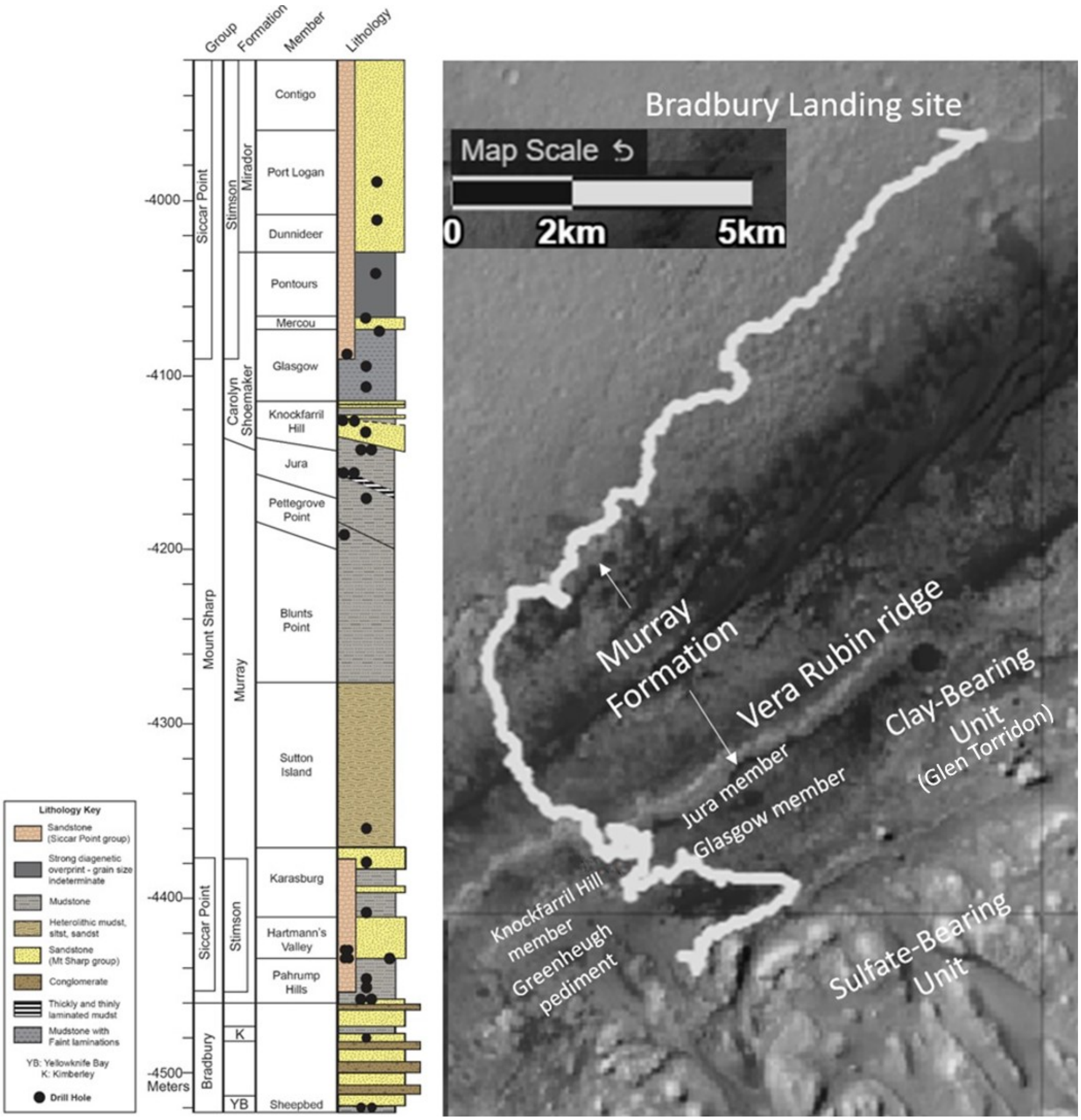

**Figure 1**. Stratigraphic column (left) and rover path indicating topographic features, lithologic formations, members and units as described in section 2. Sstratigraphic column prepared by the Mars Science Laboratory Sedimentology and Stratigraphy Working Group.

The clay-bearing unit (informally named as Glen Torridon) lies on the south of Vera Rubin Ridge as shown in Figure 1 and shows strong clay mineral spectral signatures in orbital remote sensing data (Bennett et al., 2021; Hughes and Arvidson, 2020; Milliken et al., 2010; Fraeman et al., 2016). Following the Jura member, Glen Torridon consists of the Knockfarril Hill member and the Glasgow member (transitioning into the Carolyn Shoemaker formation from the Murray formation as shown in Figure 1) (Caravaca et al., 2021a). The lower Glen Torridon region is characterized by presence of periodic ridges in the bedrock (Stack et al., 2019b), and the Knockfarril Hill member, which consists of cross-laminated sandstone is observed to form resistant caps on some of the bedrock ridges (Fox et al., 2020). The Knockfarril Hill member is interpreted to represent a high-energy lacustrine deposit (Fox et al., 2020). The Glasgow member consists of laminated mudstones and exhibits a variety of textures that are interpreted to be resultant of late-stage diagenesis (Bennett et al., 2022). The "Greenheugh pediment" unconformably overlies the Glasgow member and is composed of eolian Stimson sandstone similar to those previously encountered in sections of the Mount Sharp group (Bedford et al., 2022).

The Glen Torridon region shows the highest abundance of clay-rich minerals observed to date (up to 34 wt%) and consists of five major chemical rock types that indicate multiple stages of fluid activity and diagenesis (Dehouck et al., 2021; Gasda et al., 2022; Thorpe et al., 2022). The sulfate-bearing unit overlies the clay-bearing unit and shows predominantly Mg-sulfate mineral spectral signatures in the orbital remote sensing data (Milliken et al., 2010; Fraeman et al., 2016). The sulfate-bearing unit is not yet investigated for B and Li as the Curiosity rover is currently transitioning from the clay-rich region during the time of writing this manuscript. The results of this study are relevant for understanding the geochemistry of sulfates as the rover traverses towards the sulfate-bearing unit and provide a base for comparison with terrestrial settings to gain a nuanced perspective of behavior of B and Li in close association with sulfates. This transition region from clay-rich to sulfate-rich starts at Mercou member (Figure 1) and as of this writing, the rover is at approximately -3800 m elevation in the Mirador formation and has not definitely entered the sulfate unit based on its observations.

## 2.2 Evaporites in Gale crater

In this work, evaporites are referred to as either primary or secondary. In terrestrial settings, freshly precipitated evaporites which have not undergone any burial, replacement, dehydration, or dissolution are referred to as “primary”. Primary evaporites usually form crusts or crystal cumulates on the brine pool floor (Warren, 2000, 2006). With time and processes such as burial, dehydration, dissolution and remobilization, remixing with new fluids, and re-precipitation, evaporites can experience multiple degrees of diagenesis which is reflected in their mineralogy and textures. Evaporites that have undergone any diagenetic processes are referred to as “secondary” (Warren, 2000; 2006).

In Gale crater, evaporites have been observed using multiple instruments on the Curiosity rover; in addition to orbital spectral instruments (e.g., Vaniman et al., 2018; McAdam et al., 2014; Rapin et al., 2019; 2019; Dromart et al 2021; Caravaca et al., 2021; Hughes and Arvidson 2020). The evaporitic Ca-sulfate veins are interpreted to be predominantly representative of secondary diagenetic processes which consisted of multiple generations of dissolution and reprecipitation of primary evaporites into rock fractures (Thomas et al., 2019; Nachon et al., 2017; Kah et al., 2018; Schwenzer et al., 2016; Gasda et al., 2017; Dietrich et al., 2022; Rapin et al., 2021). The presence of secondary evaporite veins in Gale crater is accepted to be indirect evidence of pre-existing primary evaporites (Thomas et al., 2019; Gasda et al., 2017) which are interpreted to have formed after weathering of igneous rocks (Hurowitz and McLennan., 2007). It is inferred that prolonged interaction of fluids with martian igneous rocks likely caused the water-soluble elements (e.g., Ca, Na, K, Cl, B, Li, etc.) to be dissolved in the fluids and be removed from the rocks, leaving weathered products residually enriched in fluid-immobile components like $Al_2O_3$, FeO, and MgO (often forming clay minerals) (Hurowitz and McLennan., 2007).

Data collected using the instruments onboard the Curiosity rover in Gale crater indicate that the sites contain mixtures between secondary evaporites and surrounding sedimentary rocks (L'Haridon et al., 2018; Gasda et al., 2022). This mixing is inferred to be due to presence of cements or simultaneously sampling an evaporite vein and bedrock at the same time by the Curiosity rover (Gasda et al., 2022).

### 2.3 B and Li in Gale crater

Boron and Li have been frequently detected within secondary Ca-sulfate veins of Gale crater, Mars, using the Laser Induced Breakdown Spectroscopy (LIBS) instrument on board the ChemCam suite of the NASA Curiosity rover (Gasda et al., 2017; Das et al., 2020). The B and Li in the Ca-secondary sulfate veins show a broad negative correlation; this is interpreted to reflect a combination of dehydration, sequential precipitation, multiple generations of dilution and remobilization during wet and dry periods. We hypothesized that the B in the secondary Ca-sulfate were drawn out of primary borates in evaporative environments (e.g., Hartmann's Valley where an evaporative environment is inferred based on presence of desiccation cracks and altered clay minerals in the bed rock). On Vera Rubin ridge we hypothesized that both B and Li were leached out of clay minerals in areas that do not show evidence of evaporative environments but show evidence that are interpreted as acidic diagenesis. On Vera Rubin ridge, little evidence of evaporative environment has been discovered, and acidic diagenesis is inferred based on the presence of hematite, akageneite, and jarosite (Das et al., 2020; Gasda et al., 2017; Bristow et al., 2021; Rampe et al., 2020).

In terrestrial settings, primary pure Ca-sulfates do not accommodate large proportions of borate ions in their crystal lattice due to the low Ca-sulfate-fluid partition coefficient (Hawthorne et al., 2000; Follner et al., 2002, Ma et al., 2017; Türker and Türker, 2019) resulting in up to ~0.8 ppm of B in observed natural Ca-sulfate samples (Ma et al., 2017). In Gale crater, secondary Ca-sulfates veins contain up to 150 ppm B (Das et al., 2020) which is two orders of magnitude higher than the amount of boron in natural pure Ca-sulfate. Similarly, natural pure Ca-sulfate samples from Li-brine deposits in terrestrial settings contain less than 0.01 ppm of Li (Yu et al., 2022). However, secondary Ca-sulfate veins from Gale crater contain up to 65 ppm of Li (Das et al., 2020) which is also two orders of magnitude higher than the amount of Li measured in pure Ca-sulfate crystals in terrestrial brine lakes. In terrestrial settings, Li enrichment in Ca-sulfate containing deposits is attributed to the presence of clay minerals that adsorb Li onto their surface (Warren, 2006).

Hence it is hypothesized here that the most geologically plausible way secondary Ca-sulfate veins in Gale crater contain boron is if they are intergrown with phases that either structurally contain B (e.g., borates) or clay minerals that can adsorb B and Li (Das et al., 2020).

To this day, no crystalline borates or Li salts have been identified in Gale crater that are above the detection limit of instruments onboard the Curiosity rover or using orbital data. Clay-rich rocks in Gale crater contain Li (up to 56 ppm) which is inferred to be adsorbed to the surface of the clay minerals (Payre et al., 2017; Cousin et al., 2021; Gasda et al., 2022). Clay minerals that are commonly found on Mars (e.g., nontronite and saponite) are also known to adsorb up to 900 ppm of B on Earth (Nellessen et al., 2019). Although we expect clay minerals to contain B, the detection of B in Gale crater is limited to low-Fe Ca-sulfate targets (e.g., Ca-sulfate veins) as the

Fe in relatively Fe-rich targets interferes with the measurement of B using the ChemCam instrument (Gasda et al., 2017; Das et al., 2020). Therefore, it is not known how much B is found in rocks on Gale crater apart from low Fe-sites. Due to the lack of observation of crystalline borates or B measurements in clay-rich rocks using the Curiosity rover, the reservoirs of B and Li associated with Ca-sulfate veins in Gale crater are still unknown.

## 3 Terrestrial analog study sites

Southern California (Furnace Creek and Ryan areas in Death Valley, the Searles Lake area, and the Kramer borate deposit area) is an ideal terrestrial analog for understanding the enrichment and reservoir phases of water-soluble elements in a Gale-like system that includes evaporites, clay-rich rocks, and igneous rocks. In the Furnace Creek area of Death Valley, the presence of Ca-sulfates is reported in close association with borates (Tanner, 2002; Swihart et al., 1992; 1996; 2014; Li et al., 1996; Crowley, 1993). Seasonal influx of fluids with varying pH is also reported for Furnace Creek (Swihart et al., 2014; Li et al, 1996; 1997), in addition to the presence of wet-dry seasonal cycles with a predominantly arid environment (Lowenstein et al., 1999). The multiple wet-dry seasonal cycles in the Furnace Creek area are interpreted to have remobilized primary evaporites and to have reprecipitated them as secondary diagenetic evaporites (Hunt et al., 1966; Lowenstein and Hardie, 1985; Crowley, 1996; Lowenstein and Risacher, 2009).

In both Furnace Creek area and Ryan area the presence of clay-rich sedimentary and aqueously altered basaltic rocks are reported. The clay-rich rocks in these regions are reported to be closely associated with borates (Gates, 1959) with a concentration of up to 967 ppm of B (Nellessen et al., 2019) and up to 110 ppm of Li adsorbed to the surface of clay minerals (determined by analyzing clay minerals isolated from the bulk samples through centrifugation and rinsing). In the Searles Lake area, halite, borates, and clay-rich sedimentary rocks are reported (Felmy et al., 1986) and the Kramer borate deposit area reports the presence of borates that include borax, kernite, ulexite, probertite, colemanite, and howlite (Swihart et al., 1996; 1992; Birsoy and Ozbas, 2012). The presence of Ca-sulfates in close association with borates and clay-rich rocks that are known to contain both B and Li is ideal for gaining perspective on potential reservoirs of B and Li in Ca-sulfates in both terrestrial settings and, by analogy, Gale crater.

## 4 Hypotheses and objective

Based on observations in Gale crater the following hypotheses have been made by Gasda et al., (2017) and Das et al., (2020) that are also described in Chapter 1:

1) The secondary Ca-sulfate veins in Gale crater contain B and Li because they are likely intergrown with primary borates and/or cemented by clay minerals.
2) Primary borates are a source of B for the secondary Ca-sulfate veins that likely formed in high evaporative environment.
3) Clay minerals acted as temporary reservoirs of B and Li through adsorption that likely released B and Li in acidic pH conditions for the formation of secondary B and Li-containing Ca-sulfate veins.

In this work we test the above hypotheses using terrestrial analog samples with the objective of identifying the phases in the samples and determining the distribution of B and Li within them to estimate fluid pH and evaporative conditions in the terrestrial analog area, and by analogy, in an early primary evaporative Gale crater environment.

# 5 Methods

## 5.1 Terrestrial analog sample collection

Twenty-two samples were collected in total from the four sites: the Gower Gulch area in the Furnace Creek (17 samples) and the Ryan regions (1 sample) in Death Valley, from the Searles Lake region (1 sample), and from the Kramer borate deposit region (2 samples).

The specific sampling areas were selected in order to collect representative end member rocks (i.e., evaporites, clay-rich sedimentary rocks, and altered igneous rocks) and areas that show the presence of mixtures between the end members. In Gale crater, Ca-sulfate veins are targeted for analysis based on its visual identification and are not predictably tied to the lithologic succession (Nachon et al., 2014; Kronyak et al., 2019). The presence of evaporite veins is challenging to predict on both Mars and Earth because the veins are emplaced due to multiple periods of fluid activity, the extent and directional spread of which is not consistent. Although the broader sampling sites were selected based on the previously reported presence of evaporites, clay-rich rocks and altered igneous rocks, the specific sampling in the analog site was done based on the availability of the features that visually resemble Ca-sulfate veins in Gale crater. The Furnace Creek area presented the maximum number of sites with juxtapositions that are visually similar to Ca-sulfate veins and its immediate surroundings and enabled sampling of evaporite veins and surrounding clay-rich sedimentary rocks. The identification of the minerals within the veins was estimated based on the texture, habit, and hardness of the mineral in addition to testing its reaction with dilute hydrochloric acid.

This region was also used for sampling altered basaltic rocks. Although basalts are not observed by the Curiosity rover compared to clay-rich sedimentary rocks in Gale crater, it is inferred that primary Ca-sulfates form on Mars due to weathering of basaltic rocks in its early history (Hurowitz and McLennan., 2007). We therefore collected altered basaltic samples from the Furnace Creek area in order to measure the B and Li values and compare the relative concentrations with borates and clay minerals in order to assess whether altered basaltic samples can be reservoirs of B and Li for Ca-sulfate veins.

One site in Searles Lake was selected in order to sample a halite-containing playa lake evaporite crust. This area showed the presence of a crust-like layer on the dry lakebed consisting of evaporite crystals that were visually identified as halite. The crust-like material in addition to the clay-rich sedimentary material supporting the crust were carefully collected in order to determine the B and Li distribution in the presence of halite. In Gale crater, the presence of halite is inferred based on the presence Na and Cl in the targets measured using the Curiosity rover. The presence of halite is also inferred to be in the form of scattered grains or cements that could be present in vein margins, in nodular and altered textures as a resultant of late-stage diagenetic events (Thomas et al., 2019; Meslin et al., 2022). We collected only one sample from this area due to restricted access to the Searles lake.

One site in Ryan was selected for sampling a silicious igneous ash deposit. The sample identification was based on its appearance and based on previous reports of igneous ash deposits in the vicinity of this region (Cemen et al., 1985). This sampling site was chosen as ash is inferred in Gale crater (Morris et al., 2016; Weitz et al., 2022) and we wanted to measure the abundance of B and Li in ash order to determine whether ash can be a potential reservoir for B and Li that is relevant to Gale crater. We only encountered one region that showed the presence of ash within the perimeters of the area permitted for sampling by the Death Valley National Park authorities that coincided with our sampling plan.

In addition to the abovementioned sampling areas, we also selected the Kramer borate deposit region (Rio Tinto borate mine) in order to collect samples of borates. Although crystalline borate minerals are not reported in Gale crater as of this work, borates are inferred based on the presence of boron in Ca-sulfate veins (Das et al., 2020; Gasda et al., 2017). Hence, we collected samples of borates and their surrounding sedimentary rocks in order to characterize possible reservoirs for B that could be responsible for enrichment of B in Ca-sulfates. Borate samples were collected from within the mine along excavated mine walls under the supervision of the Rio Tinto borate mine geologist and identified based on their crystal textures and habits.

The locations of the Furnace Creek and Ryan region, the Searles Lake region and the Kramer borate deposit region in the southern California area are shown in Figure 2 a. Most samples were collected from the Furnace Creek region; Figure 2 b. shows the geologic units and the sampling sites in the Gower Gulch area. The Gower Gulch was chosen for detailed sampling because this area presented the most lithological diversity and provided the opportunity to sample Ca-sulfates from the gypsiferous member (shown in green in Figure 2 b) which is interbedded with clay-rich rocks from the laminated mudstone member (shown in magenta in Figure 2 b) and the borate rich mudstone unit (yellow), and igneous samples from the altered basalts with borate veins unit (shown in orange in Figure 2 b). Representative field context images for the five categories (borates, sulfates, halite, clay-rich sedimentary rocks, and igneous rocks) of samples collected are shown in Figure 3 a-f. with close-up images of the representative samples shown in Figure 4 a-f.

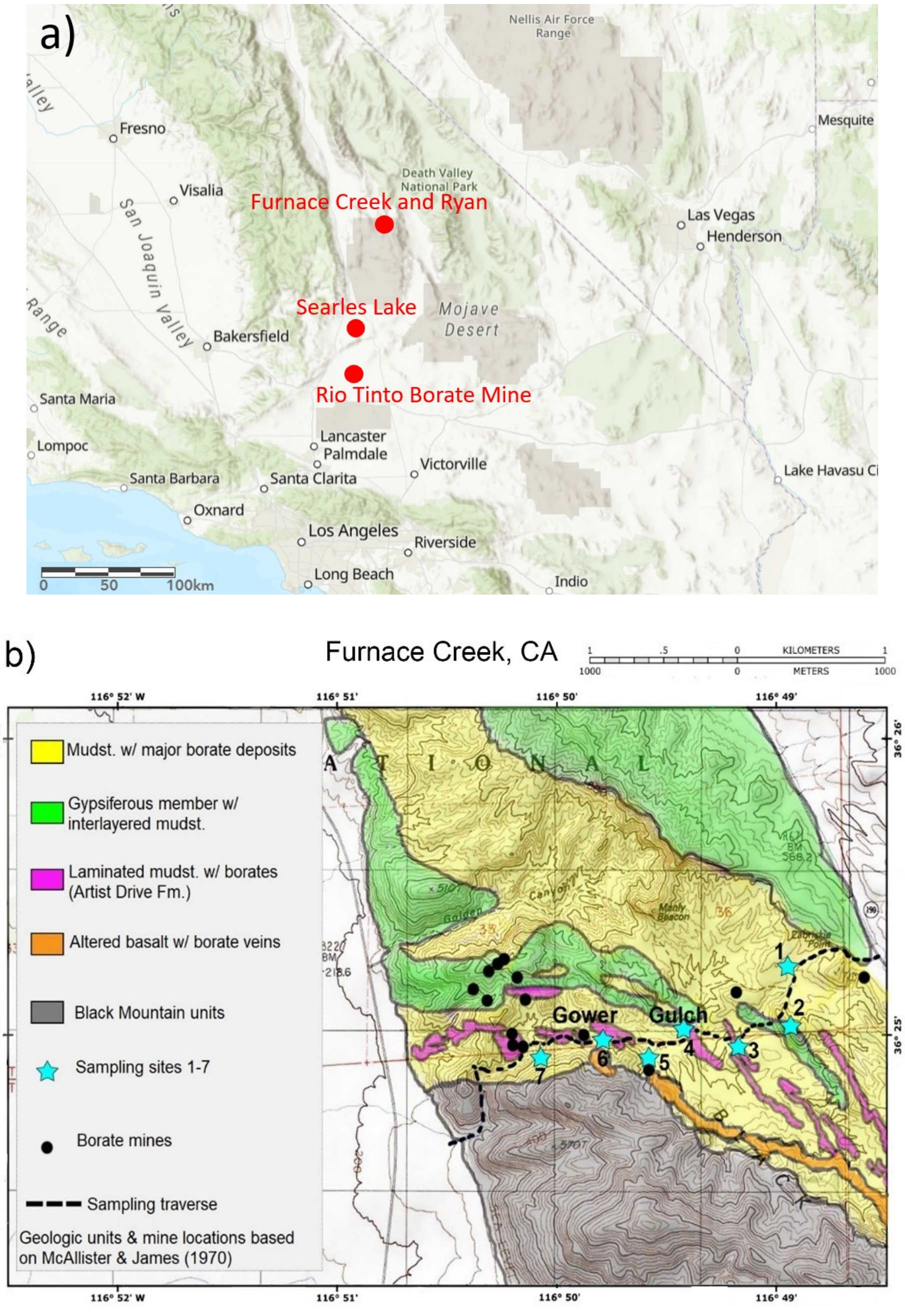

**Figure 2.** a) Sampling areas in Furnace Creek, Ryan, Searles Lake, and Rio Tinto borate mine indicated in b) Geologic map of Furnace Creek, CA, indicating the geologic units and sampling sites in the Gower Gulch area (USGS topographic base map, Furnace Creek Quadrangle, 2011). Geologic units, mine locations and elevations based on maps compiled by USGS (McAllister, 1970; U.S. Geological Survey, 1952).

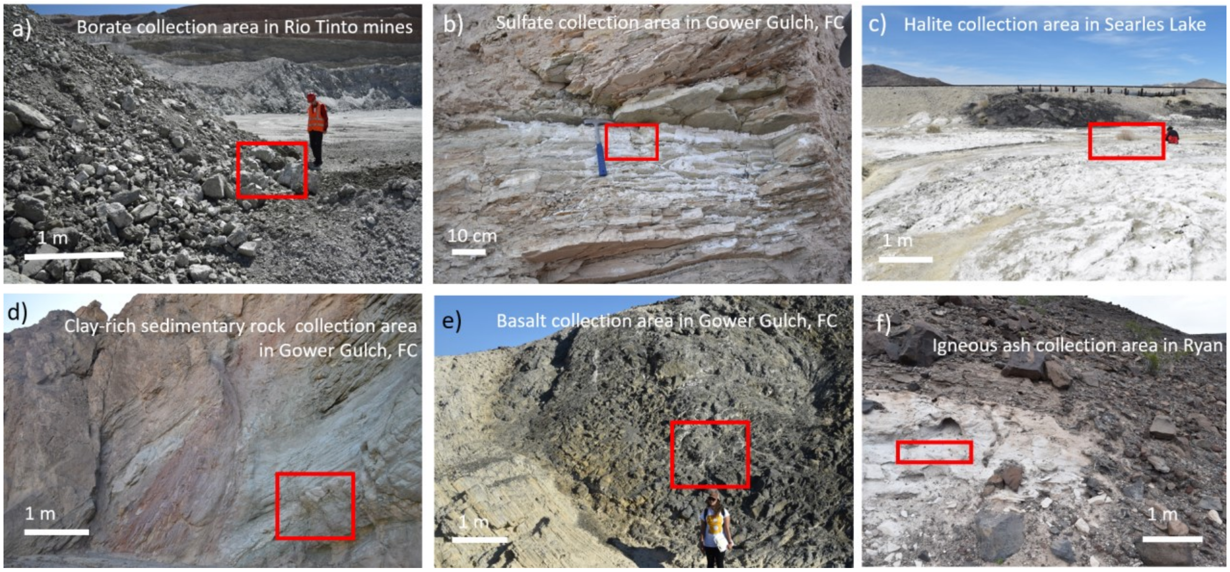

**Figure 3.** Field context images for sampling locations of: borates (a), sulfate (b), halite (c), clay-rich sedimentary rocks (d), basalt (e), and ash (f) collected from borate mine, Searles Lake and Gower Gulch.

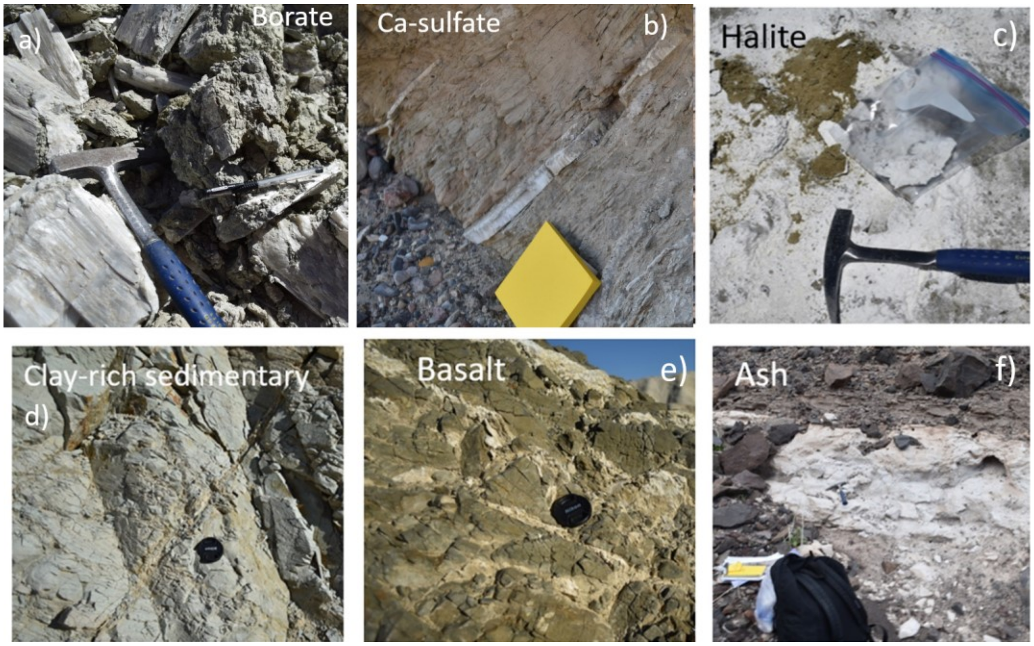

**Figure 4.** Close-up images of the samples including borates(a), Ca-sulfate(b), halite (c), clay-rich sedimentary rocks (d), basalt (e), and ash (f) collected from borate mine, Searles Lake and Gower Gulch.

### 5.2 Sample analysis and data processing

Twenty-two samples (all samples listed in Table 1) were analyzed by Activation Laboratory Ltd. (ActLabs). Twenty-one samples (all samples listed in Table 1 excluding sample 34 e- which was not analyzed due to funding limitations) were analyzed at Los Alamos National Laboratory (LANL) using the ChemCam engineering model mast unit LIBS instrument, and at the University of New Mexico (UNM) using an XRD instrument. The techniques used for the sample analyses consisted of flux fusion XRF method, and PGNAA. Major oxides of the twenty-two samples were determined using the Fus-XRF technique and the abundances for the major oxides $SiO_2$, $Al_2O_3$, $Fe_2O_{3(Total)}$, MnO, MgO, CaO, $Na_2O$, $K_2O$, $TiO_2$, and the major oxide totals, in addition to the detection limits are shown in Table 1 *(in weight percent)*. Loss on Ignition (LOI) was measured using gravimetry and is also shown in Table 1. Li abundance was determined using Fus-LAICPMS technique with sodium peroxide as a flux. B abundance was determined using the PGNAA technique. B and Li abundances of the samples are listed in ppm in Table 1. For the Fus-XRF technique analytical error at 10 times the concentration of detection limit is +/- 30% while at 100 times detection limit is +/- 5%. For the PGNAA technique, the analytical error at 10 times detection limit is +/- 30% while at 100 times detection limit is +/- 5%. For the LAICPMS technique, the analytical error at 10 times detection limit is +/- 30% while at 100 times detection limit is +/- 10%. The certified and measured values of the standard reference materials analyzed are also listed in Table 1 (labeled as "Cert" for certified values and "Meas" below the terrestrial analog sample data).

In order to make powder pellets for the ChemCam LIBS instrument, 3 grams of each sample were powdered using an agate mortar and pestle. For the XRD analysis, 1 gram of each sample was analyzed. For the fusion XRF, fusion LAICPM, and PGNAA analysis, 0.75 grams of each sample were analyzed per technique.

### 5.2.1 X-Ray Diffraction

X-Ray Diffraction was performed at the University of New Mexico to determine sample mineralogy. A Rigaku SmartLab Diffractometer with a 5° source and detector Soller slits was used. Data were collected at 6°/min with a 0.02° step size and a collection range of 3-150° 2θ. Copper was used for the X-ray source. The limit of quantification of crystalline phases is approximately 1 wt%.

The relative crystalline portions of the multicomponent mixed samples were estimated using the measured XRD patterns and Rietveld refinement full-pattern fitting method (Rietveld, 1969). Rietveld refinements of XRD patterns were performed using the Materials Data, Inc. (MDI) Jade analytical software. The backgrounds were fitted with a 6th or 7th order polynomial curve and crystalline phases were modeled using a Pseudo Voigt peak shape function. When peak broadening was apparent, a crystallite size coefficient was refined for individual phases. This method enabled the relative quantification of the identified crystalline phases in the samples.

After the relative crystalline proportions were estimated using the full-pattern fitting method, the amorphous component of the samples was calculated. This was done by calculating the stoichiometric major oxide composition of the crystalline abundances determined using the full pattern fitting method and subtracting it from the major oxide abundances determined using the ActLabs XRF method. The remnant after subtracting the major oxides calculated for the crystalline fraction from the bulk major oxide composition is considered as the amorphous fraction for this study and includes all the trace phases that are present at < 1 wt%. The phases identified using the XRD technique are shown in Table 2.

### 5.2.2 Laser Induced Breakdown Spectroscopy (LIBS)

Powder pellets were used for LIBS analyses using the ChemCam engineering unit at LANL. Samples were powdered using an agate mortar and pestle at McGill University and sent to LANL and pressed into pellets. 3 grams of sample powder was used to make 3 mm diameter pellets with no binding material. The powders used for all the analytical techniques reported in this work belong to the same subset of samples selected for powdering.

The LANL ChemCam setup consists of the ChemCam engineering model mast unit, the Laser Induced Breakdown Spectroscope (LIBS), telescope, a Remote Micro Imager, associated electronics with the optical demultiplexer, a trio of crossed Czerny-Turner spectrometers, and data processing unit (Clegg et al., 2017). The ChemCam testbed and the laser is placed in an enclosure and cooled to 4 °C in order to achieve the maximum 14 mJ/pulse laser energy and to avoid condensation in the setup. The setup has a 12 cm opening, through which the laser is fired, and the LIBS signal is collected. This instrument produces optical spectra that are similar to the ChemCam instrument on Mars in a simulated Mars surface pressure and atmosphere (933 Pa $CO_2$). Optical differences between the ChemCam setup at LANL and the ChemCam instrument on Mars are quantified by Clegg et al. (2017). Based on this quantified difference, an Earth-to-Mars correction factor was applied in order to compensate for the differences between the LANL ChemCam set up and the Mars ChemCam instrument (Clegg et al., 2017). Each sample pellet was shot in 5 spots using 30 laser shots per spot and the first five shots were discarded to remain consistent with the methodology used for the ChemCam instrument. To obtain a spectrum per shot for a sample, the intensities of the 25 shots were averaged.

The instrument response function in the laboratory unit is less efficient than in the Mars ChemCam instrument in all regions except the 850–900 nm region (Clegg et al., 2017). The spectral-range edges in the laboratory model's gain curves increase more sharply compared with Mars ChemCam instrument leading to increased noise. These regions were masked out of the Death Valley sample spectra to eliminate noise. These regions do not include any unique major element diagnostic peaks. The spectral ranges masked out of the analysis are 240.811–246.635, 338.457–340.797, 382.138–387.859, 473.184–492.427, and 849–905.574 nm regions. An Earth-to-Mars correction was applied in order to compensate for the differences between the LANL ChemCam set up and the Mars ChemCam instrument (Clegg et al., 2017). The spectral data were normalized to total wavelength emission intensity for all three spectral ranges measured by the ChemCam instrument (ultraviolet, visible, and infrared). Major and minor element composition quantifications were obtained using the calibration models developed by the ChemCam team (Wiens et al., 2013; Clegg et al., 2017; Gasda et al., 2021; Payre et al., 2017). The data obtained by the ChemCam set up at LANL were used for comparing mixing trends observed in Gale crater and mixing trends between samples obtained from Southern California and in explained in detail in section 6.2.

# 6 Results

## 6.1 Sample characterization (major oxide compositions; crystalline and amorphous fractions; B and Li abundances)

The twenty-two samples collected from Southern California are multicomponent mixtures between multiple crystalline and amorphous phases. The major element data (measured using Fus-XRF technique) with B (measured using PGNAA technique) and Li (measured using Fus-LAICPMS technique) concentrations are shown in Table 1. All samples except sample 34e have been measured via XRF in order to determine the sample mineral phases. Sample 34e is estimated to be predominantly altered basalt based on its major element composition, and textural appearance, however we do not have an XRD-backed phase identification for this sample and only use the B and Li concentrations for the discussion of B and Li distribution in a multimineralic system in section 7 (Discussion).

**Table 1.** Major oxide composition with B and Li concentrations for the twenty-two samples collected from Southern California. Standard reference material measured, and certified values shown below the sample data.

| Samples | $SiO_2$ wt% | $Al_2O_3$ wt% | $Fe_2O_{3(T)}$ wt% | MnO wt% | MgO wt% | CaO wt% | $Na_2O$ wt% | $K_2O$ wt% | $TiO_2$ wt% | Li (ppm) | B (ppm) | Total wt% | LOI wt% |
|---|---|---|---|---|---|---|---|---|---|---|---|---|---|
| Analysis method | Fus-XRF | Fus-XRF | Fus-XRF | Fus-XRF | Fus-XRF | Fus-XRF | Fus-XRF | Fus-XRF | Fus-XRF | FusLA-ICPMS | PGNAA | Fus-XRF | Grav |
| Det. Limit | 0.01 | 0.01 | 0.01 | 0.01 | 0.01 | 0.01 | 0.01 | 0.01 | 0.01 | 15 | 2 | 0.01 | |
| 26 dark | 10.49 | 2.03 | 0.89 | 0.017 | 1.7 | 12.22 | 7.8 | 0.96 | 0.11 | 506 | 10000+ | 76.69 | 40.45 |
| 26 white | 1 | 0.44 | 0.2 | 0.008 | 0.32 | 0.18 | 20.86 | 0.03 | 0.03 | 84 | 10000+ | 52.04 | 28.96 |
| 28 | 34 | 8.45 | 2.73 | 0.064 | 2.94 | 13.27 | 7.59 | 0.91 | 0.35 | 294 | 1010 | 95.61 | 25.15 |
| 29 | 71.66 | 11.69 | 1.31 | 0.079 | 0.64 | 0.73 | 3.13 | 5.18 | 0.1 | 89 | 317 | 99.83 | 5.25 |
| 31 | 3.61 | 1.04 | 0.49 | 0.026 | 0.59 | 31.16 | 6.47 | 0.71 | 0.05 | 199 | 1340 | 50.88 | 6.72 |
| 32 | 30.14 | 6.86 | 3.33 | 0.104 | 3.54 | 26.7 | 1.06 | 2.42 | 0.37 | 363 | 579 | 99.93 | 25.24 |
| 33 | 1.2 | 0.39 | 0.1 | 0.008 | 0.14 | 34.65 | 0.05 | 0.01 | 0.02 | 23 | 165 | 53.06 | 16.46 |
| 34a | 17.18 | 3.08 | 5.11 | 0.122 | 9.34 | 20.68 | 0.24 | 0.05 | 0.09 | 390 | 92 | 80.15 | 24.13 |

| | | | | | | | | | | | | |
|---|---|---|---|---|---|---|---|---|---|---|---|---|
| 34b | 0.54 | 0.27 | 0.08 | 0.007 | 0.06 | 32.53 | 0.02 | 0.01 | 0.01 | 0 | 23 | 54.82 | 21.27 |
| 34c | 9.23 | 2.35 | 1.33 | 0.046 | 1.94 | 28.91 | 0.26 | 0.76 | 0.1 | 116 | 111 | 66.38 | 21.39 |
| 34d | 26.98 | 6.02 | 2.21 | 0.226 | 3.01 | 30.64 | 0.59 | 2.96 | 0.22 | 250 | 446 | 99.28 | 26.34 |
| 34e | 45.92 | 17.08 | 9.98 | 0.132 | 6.62 | 8.02 | 3.33 | 0.78 | 1.81 | 328 | 93 | 99.07 | 4.95 |
| 34f | 15.66 | 3.65 | 3.84 | 0.272 | 6.72 | 25.33 | 0.74 | 0.18 | 0.18 | 247 | 106 | 81.08 | 24.44 |
| 35 | 9.88 | 0.82 | 0.4 | 0.038 | 0.74 | 31.57 | 0.13 | 0.1 | 0.04 | 80 | 134 | 62 | 18.25 |
| 36 congl | 36.38 | 8.04 | 2.23 | 0.055 | 2.7 | 18.71 | 1.4 | 3.24 | 0.3 | 351 | 3410 | 90.06 | 16.87 |
| 36 vein | 14.43 | 0.15 | 0.1 | 0.004 | 0.01 | 27.92 | 0.06 | 0.05 | 0.02 | 15 | 10000+ | 55.11 | 12.37 |
| 37a | 7.65 | 0.48 | 0.17 | 0.015 | 2.94 | 13.19 | 6.69 | 0.16 | 0.03 | 618 | 10000+ | 63.3 | 31.95 |
| 37b | 4.93 | 0.37 | 0.16 | 0.015 | 1.76 | 24.86 | 0.14 | 0.1 | 0.02 | 409 | 10000+ | 54.86 | 22.5 |
| 37c | 39.65 | 8.16 | 2.75 | 0.076 | 5.3 | 16.76 | 1.69 | 2.28 | 0.39 | 804 | 10000+ | 94.93 | 17.72 |
| 37c vein | 3.85 | 0.44 | 0.15 | 0.012 | 1.35 | 24.58 | 0.21 | 0.1 | 0.02 | 305 | 10000+ | 52.97 | 22.24 |
| 38a | 61.37 | 12.95 | 2.31 | 0.028 | 1.73 | 3.65 | 3.6 | 2.07 | 0.34 | 129 | 625 | 99.24 | 11.09 |
| 38b int | 56.46 | 11.9 | 2.51 | 0.038 | 2.77 | 6.44 | 2.91 | 2.41 | 0.38 | 238 | 376 | 98.26 | 12.32 |
| Standards: | | | | | | | | | | | | | |
| BE-N Meas | 38.26 | 10.11 | 13.02 | 0.2 | 13.1 | 14.12 | 3.22 | 1.37 | 2.66 | - | - | - | - |
| BE-N Cert | 38.2 | 10.1 | 12.8 | 0.2 | 13.1 | 13.9 | 3.18 | 1.39 | 2.61 | - | - | - | - |
| AC-E Meas | 71.08 | 14.76 | 2.59 | 0.063 | 0.02 | 0.36 | 6.7 | 4.54 | 0.11 | - | - | - | - |
| AC-E Cert | 70.35 | 14.7 | 2.56 | 0.058 | 0.03 | 0.34 | 6.54 | 4.49 | 0.11 | - | - | - | - |
| DR-N Meas | 52.75 | 17.44 | 9.8 | 0.227 | 4.31 | 7.04 | 3 | 1.71 | 1.07 | - | - | - | - |
| DR-N Cert | 52.85 | 17.52 | 9.7 | 0.22 | 4.4 | 7.05 | 2.99 | 1.7 | 1.09 | - | - | - | - |
| SY-2 Meas | - | - | - | - | - | - | - | - | - | - | 89 | - | - |
| SY-2 Cert | - | - | - | - | - | - | - | - | - | - | 88 | - | - |
| SY-3 Meas | - | - | - | - | - | - | - | - | - | - | 112 | - | - |
| SY-3 Cert | - | - | - | - | - | - | - | - | - | - | 107 | - | - |
| OREAS 148 Meas | - | - | - | - | - | - | - | - | - | 4760 | - | - | - |
| OREAS 148 Cert | - | - | - | - | - | - | - | - | - | 4760 | - | - | - |
| OREAS 193 Meas | - | - | - | - | - | - | - | - | - | 41 | - | - | - |
| OREAS 193 Cert | - | - | - | - | - | - | - | - | - | 40.4 | - | - | - |

The minerals determined using XRD, the calculated amorphous fraction, and B and Li concentrations are summarized in Table 2. Ca-sulfates, borates (probertite, tincalconite, ulexite, howlite, and colemanite), halite, calcite, minor Fe, Mn, and Mg carbonates, clay-minerals (muscovite, vermiculite, and illite), zeolite (heulandite), quartz, feldspars and feldspathoids, Na-sulfate, and sulfide, were identified.

**Table 2.** Crystalline and amorphous phase quantifications for twenty-one samples estimated using XRD and quantifications done using full-pattern analysis with corresponding B and Li concentrations measured using PGNAA and Fus-LAICPMS techniques, respectively.

| **Samples** | **Total oxide wt%** | **Crystalline mineral fraction % (XRD)** | **Amorphous fraction %** | **B (ppm) PGNAA** | **Li (ppm) LAICPMS** |
|---|---|---|---|---|---|
| 26 dark | 76.69 | Probertite (83%), Calcite (1%) | 16% | 10000+ | 506 |
| 26 white | 52.04 | Tincalconite (99%) | 1% | 10000+ | 84 |
| 28 | 95.61 | Halite (22%), Calcite (25%), Albite (14%), Quartz (6%), Thenardite (Na-sulfate) (4%), Wurtzite (Zn, Fe) S (1%), Sphalerite (Zn,Fe)S (1%) | 27% | 1010 | 294 |
| 29 | 99.83 | 0% | 100% | 317 | 89 |
| 31 | 50.88 | Anhydrite (78%), Gypsum (10%), Zinc Sulfide (2%), Magnesite ($MgCO_3$) (4%) | 6% | 1340 | 199 |
| 32 | 99.93 | Calcite (17%), Quartz (12%), Muscovite (13%), Albite (14%), Orthoclase (16%), Ankerite $Ca(Fe,Mg,Mn)(CO_3)_2$ (10%) | 18% | 579 | 363 |
| 33 | 53.06 | Gypsum (74%), Anhydrite (25%) | 1% | 165 | 23 |
| 34a | 80.15 | Gypsum (78%), Anhydrite (1%) Vermiculite (13%) | 8% | 92 | 390 |
| 34b | 54.82 | Gypsum (99%) | 1% | 23 | 0 |
| 34c | 66.38 | Gypsum (76%), Calcite (11%), Anhydrite (2%) | 11% | 111 | 116 |
| 34d | 99.28 | Calcite (56%), Quartz (11%) Orthoclase (27%) | 6% | 446 | 250 |
| 34f | 81.08 | Gypsum (53%), Calcite (34%), Analcime (2%), dolomite $CaMg(CO_3)_2$ (7%), Lansfordite ($MgCO_3 \cdot 5H_2O$) (2%) | 2% | 106 | 247 |
| 35 | 62 | Gypsum (51%), Anhydrite (19%), Quartz (7%), Calcite (17%), Lansfordite (5%) | 1% | 134 | 80 |
| 36 congl | 90.06 | Gypsum (28%) Calcite (27%) Quartz (15%) Orthoclase (18%) Albite (9%) | 3% | 3410 | 351 |
| 36 vein | 55.11 | Howlite (98%), Calcite (1%) | 1% | 10000+ | 0 |
| 37a | 63.3 | Ulexite (92%) | 8% | 10000+ | 618 |
| 37b | 54.86 | Colemanite (90%), Gypsum (1%), Calcite (5%) | 4% | 10000+ | 409 |

|  |  |  |  |  |  |
|---|---|---|---|---|---|
| 37c | 94.93 | Albite (20%), Calcite (28%), Quartz (13%), Illite (2%), Halite (4%), Suanite ($Mg_2B_2O_5$) (8%) | 25% | 10000+ | 804 |
| 37c vein | 52.97 | Ulexite (65%), Suanite (17%), Calcite (4%) | 14% | 10000+ | 305 |
| 38a | 99.24 | Heulandite (28%), Quartz (1%), Anorthite (6%), Calcite (2%) | 63% | 625 | 129 |
| 38b int | 98.26 | Quartz (3%), Calcite (2%), Heulandite (28%), Gypsum (2%), Anorthite (7%) | 58% | 376 | 238 |

In Figure 5, the crystalline and amorphous fractions in twenty-one samples (normalized to measured oxide totals) are plotted as stacked bars with the legend indicating the crystalline phase identification obtained using XRD and the calculated amorphous phase. Samples containing borates are grouped in the left side of the plot (first seven bars). The samples containing Ca-sulfates are grouped in the middle of the plot (bars 8-15). The samples that do not predominantly contain borates or Ca-sulfates are grouped on the right-hand side of the plot (bars 16-21). The top two panels in Figure 5 indicate the corresponding Li and B concentrations in ppm. The x and y axis for the Li panel are shown in linear scale while the y axis for the B panel is shown in logarithmic scale (in order to show both borates and non-borates, which differ in concentration of B by orders of magnitude, in the same panel) with a linear x axis.

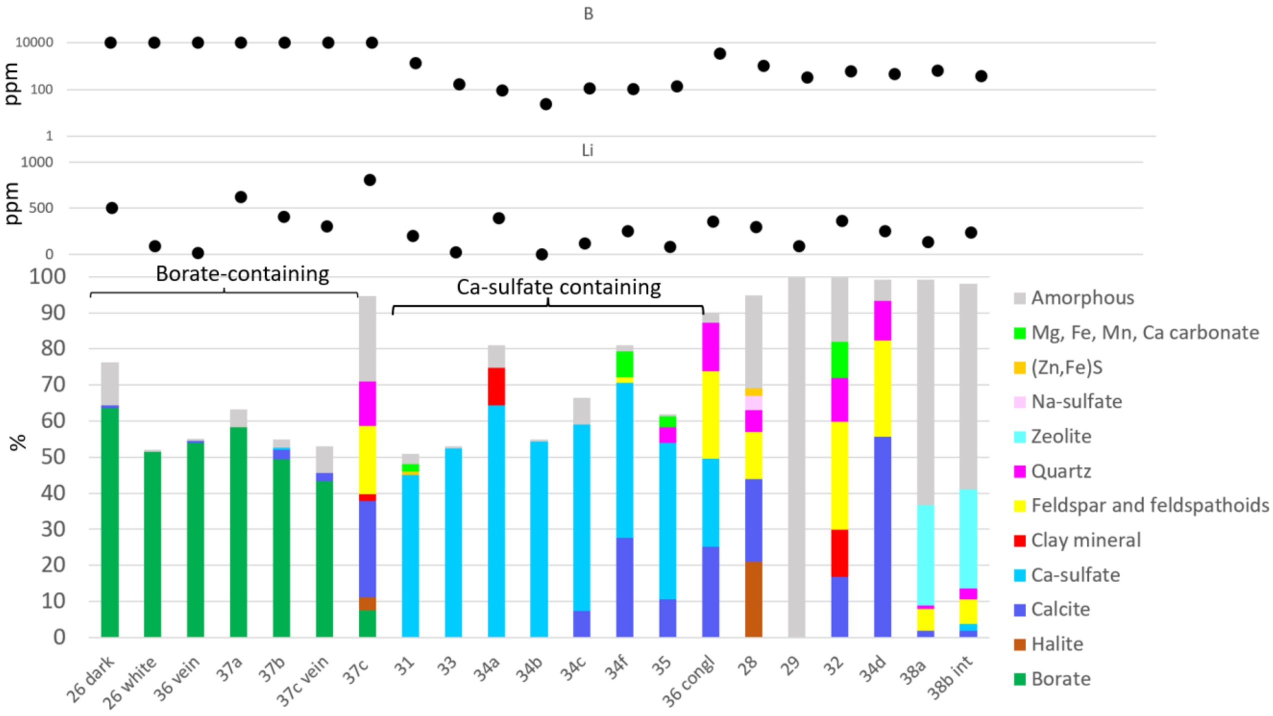

**Figure 5**. Relative crystalline and amorphous proportions in twenty-one samples determined using XRD and full-pattern analysis techniques. Corresponding B and Li concentrations are shown in top panels.

### 6.1.1 Borate-containing samples

Table 2 shows that seven samples (26 dark, 26 white, 36 vein, 37a, 37b, 37c vein, and 37c) out of the twenty-two samples contain crystalline borates above the XRD detection limit (with borate abundance varying from 8% to 99%). The B concentration of these seven samples exceed 10000 ppm (as shown in both Table 2 and Figure 5 B panel). Six of the seven borate-containing samples contain 83-99% borates with one sample containing 8% borate. The majority of the borate-containing samples are predominantly borate rich with minor presence of amorphous material (1-16%), calcite (1-4%), and Ca-sulfate (1-4%). The one sample (37c) with 5% borate consists of 20% feldspar, 28% calcite, 13% quartz, 4% halite, 2% clay and 25% amorphous material. The Li abundance for these borate containing samples range from 0 to 804 ppm. The highest abundance of Li in the borate-containing samples corresponds to the sample that contains clay minerals.

Figure 6 shows a plot of Li abundance in the seven borate-containing samples plotted with the abundance of all the phases identified in these samples using XRD in order to determine whether Li enrichment is dependent on a specific phase. In Figure 6, Li abundance is plotted in ppm on x-axis on a linear scale and phase abundance is plotted on the y axis on a logarithmic scale. This figure shows that the highest amount of Li corresponds to the sample that also contains clay minerals (at 804 ppm). A linear regression is plotted for the amorphous phase to check whether there is a relationship between Li abundance and amorphous phase abundance. The $R^2$ value of 0.64 for the linear regression of the amorphous phase abundances is considered too low to represent a strong correlation between Li abundance and amorphous phase abundance. There are no visual correlation trends between Li abundance and other phase abundances either.

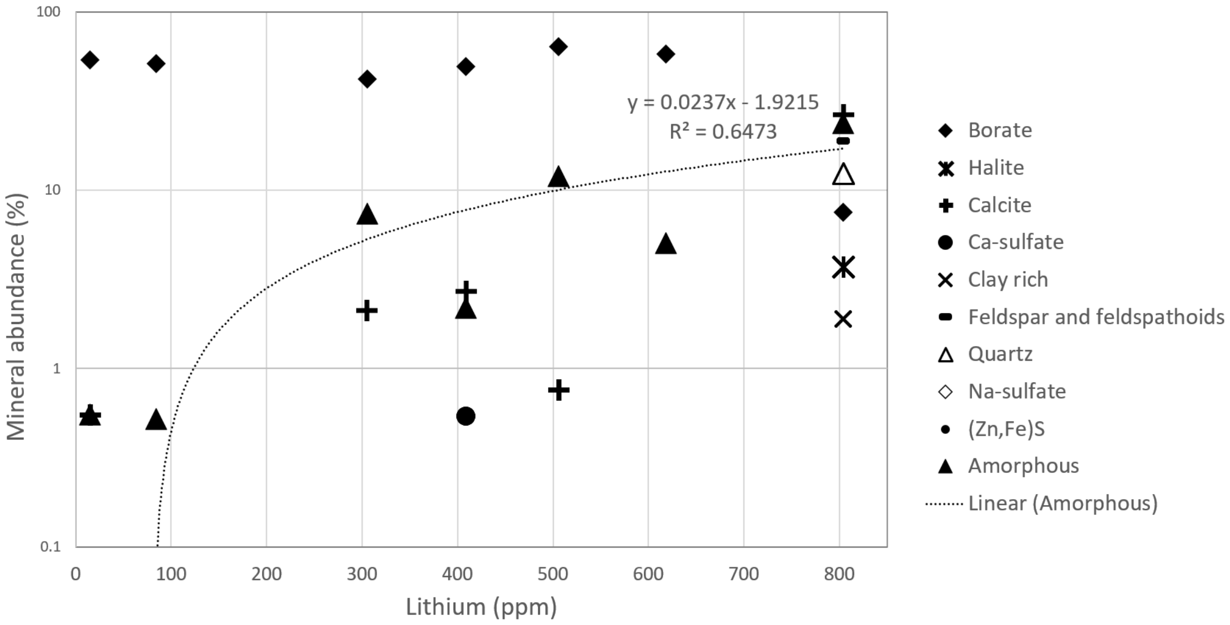

**Figure 6**. Lithium concentration in seven borate-containing samples plotted with abundances of phases identified using XRD.

### 6.1.2 Ca-sulfate-containing samples

Table 2 shows that eight samples (31, 33, 34a, 34b, 34c, 34f, 35, and 36 congl) out of the twenty-one samples contain more than 20% Ca-sulfate with abundance of Ca-sulfate in the sample varying from 28% to 99%. These eight samples are labeled "Ca-sulfate containing" in Figure 5. The B concentration of these eight samples range between 23 ppm to 3410 ppm (as shown in both Table 2 and Figure 5 B panel). Six out of the eight Ca-sulfate containing samples have a B abundance that range between 23-446 ppm B. The majority of the Ca-sulfate-containing samples contain up to 446 ppm of B. Two Ca-sulfate-containing samples show the presence of 1340 ppm and 3410 ppm of B. Hence majority of the Ca-sulfate containing samples have a B abundance up to 445 ppm with two exceptions which contain more than a 1000 ppm of B. The Li abundance of the eight Ca-sulfate samples vary from 0 To 390 ppm and the highest amount of Li is present in the sample that contains clay minerals.

Figure 7 shows a plot of B and Li abundance in the eight Ca-sulfate-containing samples plotted with the abundance of all the phases identified in these samples using XRD in order to determine whether B and Li enrichments are dependent on specific phases. In Figure 7a, B abundance is plotted in ppm on x-axis on a logarithmic scale and phase abundance is plotted on the y axis on a logarithmic scale. This figure shows that the majority of the Ca-sulfate containing samples have a B abundance in the 100-ppm order of magnitude with two exceptions. There is no correlation between B abundance and amorphous abundance as the linear regression $R^2$ value is low (0.0001). In Figure 7b, Li abundance is plotted in ppm on the x-axis on a linear scale and phase abundance is plotted on the y axis on a logarithmic scale. This figure shows the highest amount of Li corresponds to the sample that also contains clay minerals (at 390 ppm). The $R^2$ value for the linear regression across the amorphous phase abundances is 0.24 which is too low to represent a strong correlation. There are no visual correlation trends between Li abundance and other phase abundances either.

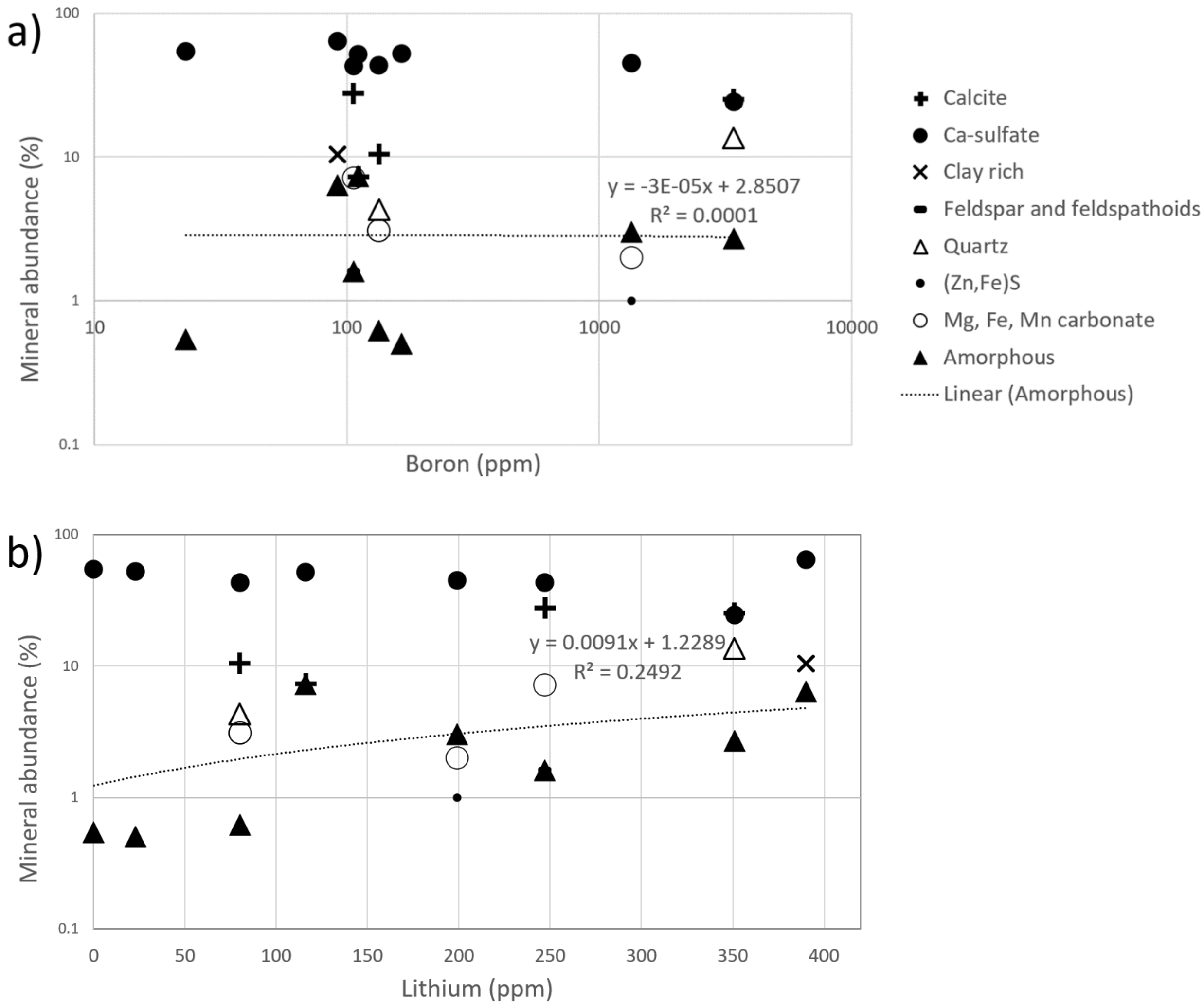

**Figure 7.** B (a) and Li (b) concentration in eight Ca-sulfate-containing samples plotted with abundances of phases identified using XRD and a linear regression to indicate the relationship between amorphous phase abundance and B and Li abundance. The phases identifications using XRD are represented using different symbols and shown in the legend on the top right side.

### 6.1.3 Samples with no predominant borates or Ca-sulfates

Table 2 and Figure 5 shows that the sample set consists of six samples that are neither borate-containing nor predominantly Ca-sulfate containing (28, 29, 32, 34d, 38a, 38b int). These samples are characterized by the presence of 22% halite (sample 28), 100% amorphous phase (sample 29), 13 % clay mineral content without borates or Ca-sulfate (sample 32), 56% calcite (sample 34 d), and presence of zeolite (samples 38a and 38b int). These samples are shown on the right-hand side of the Ca-sulfate containing samples in Figure 5. Sample 29 is 100% amorphous, and based on its major oxide composition, we estimate a possible igneous ash composition.

The B concentration of these eight samples range between 111 ppm to 1010 ppm (as shown in both Table 2 and Figure 5 B panel). The Li abundance of the eight Ca-sulfate samples vary from 89 to 363 ppm. Figure 8 shows a plot of B and Li abundance in these six samples plotted with the abundance of all the phases identified using XRD in order to determine whether B and Li enrichments are dependent on specific phases.

In Figure 8a, B abundance is plotted in ppm on x-axis on a logarithmic scale and phase abundance is plotted on the y axis on a logarithmic scale. This figure shows that the highest amount of B in these samples corresponds to a sample that contains halite (1010 ppm B). There is no correlation between B abundance and amorphous abundance as the linear regression $R^2$ value is low (0.19). There are no visual correlation trends between B abundance and other phase abundances either. In Figure 8b, Li abundance is plotted in ppm on x-axis on a linear scale and phase abundance is plotted on the y axis on a logarithmic scale. This figure shows the highest amount of Li corresponds to the sample that also contains clay minerals (at 363 ppm). Table 1 also indicates that the sample that contains clay minerals also contains 579 ppm B. The $R^2$ value for the linear regression across the amorphous phase abundances is 0.70 which is too low to represent a strong correlation. There are no visual correlation trends between Li abundance and other phase abundances either.

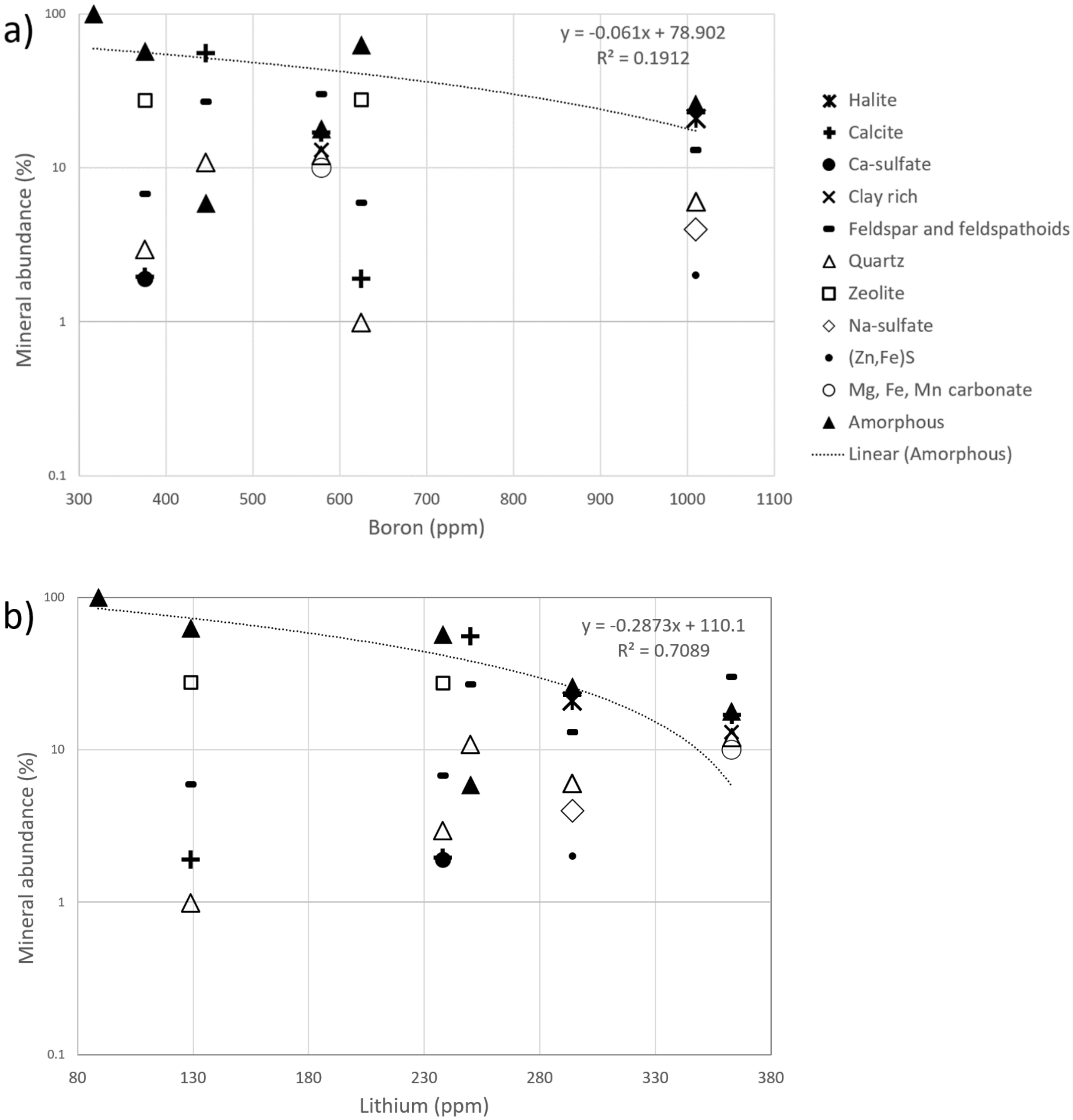

**Figure 8.** B (a) and Li (b) concentration in the six samples that do not predominantly contain borates or Ca-sulfates plotted with abundances of phases identified using XRD and a linear regression to indicate the relationship between amorphous phase abundance and B and Li abundance. The phase identifications using XRD are represented using different symbols and shown in the legend on the top right side.

To summarize, the twenty-one samples measured using Fus-XRF, Fus-LAICPMS, PGNAA, and XRD techniques consist of seven samples that are predominantly borate-containing, eight samples that are predominantly Ca-sulfate containing, and seven samples that do not predominantly contain borates or sulfates.

All the borate-containing samples show B abundances that exceed 10000 ppm even at low abundance. The borate-containing samples also contain varying proportions of other minor phases consisting of halite, calcite, Ca-sulfate, clay minerals, feldspar and feldspathoids, quartz, Na-sulfate, sulfides, and amorphous materials. The borate containing samples contain 0-618 ppm Li with no strong correlation trend between Li abundance and abundance of phases identified using the XRD technique. The highest amount of Li in the predominantly borate containing samples corresponds to the sample that also contains clay minerals.

The eight samples that are predominantly Ca-sulfate, also contain varying proportions of other minor phases consisting of calcite, clay minerals, feldspars and feldspathoids, quartz, sulfides, Mg, Fe, Mn -carbonates, and amorphous materials. The majority of the predominantly Ca-sulfate-containing samples show B abundances that fall between 0-500 with two exceptions where B abundance exceeds 1000 ppm. The Li abundance in these samples vary between 0 to 390 ppm with the highest amount of Li corresponding to the sample that also contains clay minerals. There is no strong correlation trend between B or Li abundance with any of the phase abundances.

The six samples that do not predominantly contain borates or Ca-sulfates consist of varying proportions of halite, calcite, amorphous materials, clay minerals, zeolite, quartz, feldspars and feldspathoids, Na-sulfate, sulfides, and Mg, Fe, Mn-carbonates. The B abundance in these samples varies between 111-1010 ppm with the highest abundance of B corresponding to the sample that contains halite. The Li abundance in these samples vary between 89-363 ppm with the highest abundance of Li corresponding to the sample that contains clay minerals. The clay containing sample also shows the presence of 567 ppm B. There is no strong correlation trend between B or Li abundance with any of the phase abundances.

### 6.2 Determining elemental distribution in the samples using Principal Component Analysis

Principal Component Analysis (PCA) was performed on the spectral data collected using the ChemCam set up at LANL for twenty-one samples. The PCA models were constructed using a commercial software *The Unscrambler* on mean centered data, calibrated using non-linear iterative partial least squares (NIPALS) algorithm (Lever et al., 2017; Esbensen et al., 2002). For this study, PCA was run for the Earth-to-Mars corrected, masked, and normalized spectral data of the samples (spectral correction, masking, and normalization described in section 5.2.2). PCA recasts the data into a new coordinate system based on directions of maximum variance in the data. As a result, the variables are clustered and can be interpreted in terms of processes that have acted on the data to create the variance.

PCA was used in order to identify the distribution of B and Li among the samples and is especially helpful to visualize how samples that exceed 10000 ppm B group with other samples. In Figure 10a the samples analyzed using the LANL ChemCam LIBS instrument are plotted in the coordinate space of PC1 and 2 which capture 63 % and 13 % of the total variance in the dataset respectively. Samples shown in the PC1 vs PC2 plot in Figure 9a are named based on the predominant phases identified by XRD and are grouped as “Borate containing”, “Ca-sulfate containing”, and “Non-borate/Ca-sulfate containing”, similar to previous sections. Figure 9b and c show the loading of the original variables on the principal components and indicate the loadings plot for PC1 and PC2 respectively. The peaks in the loadings plots can be interpreted as a process that separates the samples that score highly along that PC. Figure 9b indicates that PC1 is associated with Al, Fe, Li, Mg, Na and K and Si, which anti-correlate with Ca. Figure 10c indicates that along PC2 the elements Ca, Mg, K and Li anti-correlate with B, and Na. The loadings plot of PC2 indicates that B and Li are anticorrelated in these samples.

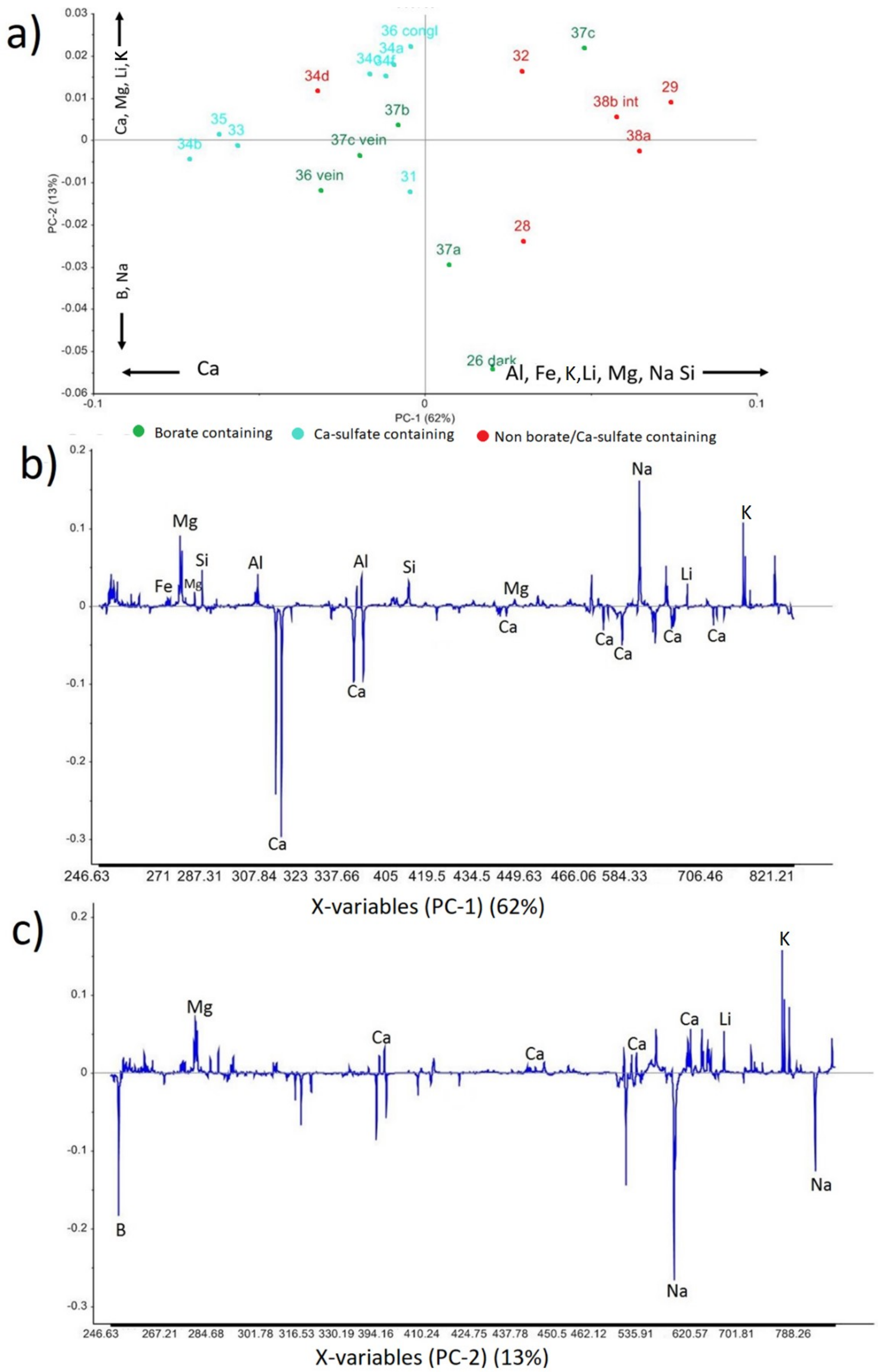

**Figure 9** a) Principal components PC 1 (62% of variance) and PC 2 (13% of variance) for terrestrial analog samples, b) loadings plot for PC1with Al, Fe, Li, Mg, Na, K and Si positive and

Ca negative c) loadings plot for PC2 with the elements Mg, Al, Ca, Li and K positive and B and Na negative.

### 6.3 Comparison of terrestrial and Gale crater observations

As explained in section 6.1, the samples collected from Southern California are multi-mineralic and include amorphous phases. In this section we compare the physical mixing trends between the terrestrial samples and the physical mixing trend observed in Gale crater. We also compare the phases identified in the terrestrial samples with phases observed or reported plausible in Gale crater and with phases that formed as a result of thermochemical modeling of a Gale-relevant scenario in Chapter 2 in this thesis.

#### 6.3.1 Comparing physical mixing trends between terrestrial samples and Gale crater

The average major oxide composition of the twenty-one samples determined using the LANL ChemCam engineering unit LIBS are shown in Table 3. Five spots were measured for each sample and Table 3 shows the average major oxide composition of the five spots and the standard deviation at 1σ level for a sample size of five.

**Table 3.** Major oxides measured using the LANL ChemCam unit. (Average of 5 spots with 1σ standard deviations)

| Sample | $SiO_2$ | $TiO_2$ | $Al_2O_3$ | $FeO_T$ | MgO | CaO | $Na_2O$ | $K_2O$ |
|---|---|---|---|---|---|---|---|---|
| 26-white | 13.0 | 0.1 | 4.5 | 0.7 | 0.1 | 1.5 | 10.5 | 0.1 |
| Stddev | 3.7 | 0.1 | 0.3 | 0.3 | 0.4 | 0.1 | 0.6 | 0.0 |
| 26-dark | 1.9 | 0.3 | 5.6 | 5.8 | 0.8 | 0.8 | 19.1 | 0.6 |
| stddev | 1.0 | 0.1 | 1.7 | 0.9 | 0.1 | 0.1 | 0.2 | 0.2 |
| 28 | 31.7 | 0.4 | 7.7 | 3.0 | 3.8 | 14.0 | 6.4 | 0.6 |
| stddev | 8.6 | 0.1 | 0.8 | 1.9 | 0.7 | 4.1 | 2.4 | 0.3 |
| 29 | 71.1 | 0.4 | 10.6 | 1.4 | 0.5 | 1.0 | 2.2 | 4.2 |
| stddev | 0.4 | 0.0 | 0.2 | 0.8 | 0.8 | 0.5 | 0.2 | 0.2 |
| 31 | 5.9 | 0.2 | 1.6 | 1.0 | 0.8 | 32.1 | 4.4 | 0.3 |
| stddev | 1.8 | 0.0 | 0.8 | 0.4 | 0.2 | 3.2 | 0.2 | 0.1 |

| | | | | | | | | |
|---|---|---|---|---|---|---|---|---|
| 32 | 31.1 | 0.3 | 8.0 | 3.2 | 4.0 | 24.1 | 1.0 | 2.0 |
| stddev | 4.0 | 0.0 | 0.2 | 0.5 | 0.1 | 1.0 | 0.1 | 0.1 |
| 33 | 1.1 | 0.1 | 0.1 | 0.0 | 0.8 | 35.1 | 0.0 | 0.0 |
| stddev | 0.1 | 0.0 | 0.6 | 0.0 | 0.3 | 0.9 | 0.0 | 0.0 |
| 34a | 16.4 | 0.2 | 3.5 | 4.9 | 8.2 | 21.8 | 0.1 | 0.0 |
| stddev | 2.0 | 0.0 | 0.3 | 0.8 | 0.9 | 3.2 | 0.0 | 0.0 |
| 34b | 0.0 | 0.0 | 1.0 | 0.0 | 0.4 | 33.1 | 0.0 | 0.0 |
| stddev | 0.0 | 0.0 | 0.3 | 0.0 | 0.1 | 1.5 | 0.0 | 0.0 |
| 34c | 9.4 | 0.2 | 3.5 | 1.8 | 1.4 | 30.0 | 0.1 | 0.4 |
| stddev | 5.3 | 0.0 | 1.2 | 1.5 | 0.9 | 5.8 | 0.1 | 0.2 |
| 34d | 20.2 | 0.2 | 5.5 | 1.9 | 3.8 | 31.5 | 0.1 | 2.1 |
| stddev | 9.0 | 0.1 | 0.7 | 1.2 | 0.9 | 4.4 | 0.0 | 0.4 |
| 34f | 14.2 | 0.2 | 4.4 | 4.0 | 7.1 | 29.0 | 0.2 | 0.1 |
| stddev | 7.1 | 0.0 | 1.1 | 1.3 | 1.4 | 5.6 | 0.3 | 0.0 |
| 35 | 8.7 | 0.0 | 1.0 | 0.0 | 1.2 | 31.5 | 0.0 | 0.1 |
| stddev | 5.5 | 0.1 | 0.6 | 0.1 | 0.5 | 3.7 | 0.0 | 0.0 |
| 36-Congl | 34.9 | 0.3 | 6.8 | 2.4 | 2.3 | 20.6 | 1.3 | 2.4 |
| stddev | 9.5 | 0.1 | 2.0 | 1.4 | 1.0 | 9.8 | 0.3 | 1.1 |
| 36-Vein | 14.9 | 0.2 | 0.8 | 1.0 | 0.3 | 29.6 | 0.0 | 0.0 |
| stddev | 1.4 | 0.1 | 0.6 | 0.8 | 0.3 | 1.0 | 0.0 | 0.0 |
| 37a | 8.2 | 0.2 | 0.6 | 0.8 | 2.6 | 13.6 | 5.2 | 0.1 |
| stddev | 4.5 | 0.0 | 1.0 | 0.3 | 1.4 | 6.6 | 0.5 | 0.0 |
| 37b | 3.0 | 0.0 | 0.4 | 0.1 | 0.2 | 24.3 | 0.0 | 0.0 |
| stddev | 0.9 | 0.0 | 0.6 | 0.9 | 0.1 | 2.2 | 0.0 | 0.0 |
| 37c | 38.9 | 0.4 | 8.8 | 3.9 | 5.9 | 15.4 | 1.3 | 1.7 |
| stddev | 6.7 | 0.1 | 2.5 | 0.5 | 1.5 | 4.4 | 1.0 | 0.5 |
| 37c-vein | 2.9 | 0.2 | 0.8 | 0.3 | 1.7 | 23.2 | 0.1 | 0.0 |
| stddev | 1.3 | 0.0 | 0.6 | 0.2 | 0.6 | 1.6 | 0.0 | 0.0 |
| 38a | 60.7 | 0.7 | 12.0 | 4.5 | 1.6 | 4.2 | 3.2 | 1.2 |
| stddev | 3.9 | 0.3 | 0.9 | 1.6 | 1.0 | 1.1 | 0.2 | 0.3 |
| 38-int | 59.2 | 0.5 | 10.0 | 3.7 | 1.5 | 6.0 | 2.0 | 1.9 |
| stddev | 4.2 | 0.0 | 1.0 | 1.5 | 1.0 | 1.8 | 0.3 | 0.9 |

In order to visualize and compare physical mixing trends for the terrestrial samples and Gale crater, molecular major oxide proportions of the samples from Southern California are plotted on a ternary $Al_2O_3$, ($CaO + Na_2O + K_2O$), ($FeO_T + MgO$) (AFM-CNK) in Figure 10 which also shows a physical mixing trend reported for Gale crater by Comellas et al., 2022. Figure 10 indicates the molecular major oxide proportions of the samples and are characterized by whether they are predominantly borate containing, predominantly Ca-sulfate containing or if they do not predominantly contain borates or Ca-sulfates (similar grouping used in previous sections). In addition to the samples collected for this work, the ternary diagram also shows reference endmember igneous samples (Death Valley plutonic and basaltic rocks measured by Ramo et al., 2002) and clay mineral data (illite measured by Srodon et al., 2009 and Awwiller, 1993). These are plotted in order to compare the mixed samples with relatively unmixed reference igneous and clay mineral end members. Reference igneous samples plot close to the feldspar line, while illite plots above the feldspar line, closer to the $Al_2O_3$ apex. The multicomponent terrestrial samples indicate this combination of evaporites and sedimentary rocks plot closer towards the CNK corner compared to the reference end member igneous and illite samples.

A line that represents a physical mixture of clay containing rocks and evaporites as observed in Gale crater is shown in this tri-plot in red extending from a Gale crater nontronite composition (plotted based on "possible mixing line" reported by Comellas et al., 2022 and made by extending a line between a Gale crater nontronite composition reported in Comellas et al., 2022 towards $CaO + Na_2O + K_2O$ corner). The physical mixture of sedimentary rocks and evaporites observed in Gale crater is explained in section 2 (Geologic context of Gale crater) and expanded in the section 7.3. This Gale-relevant mixing line is plotted in order to compare the terrestrial physical mixing trend between evaporites and clay-containing rocks with that observed in Gale crater.

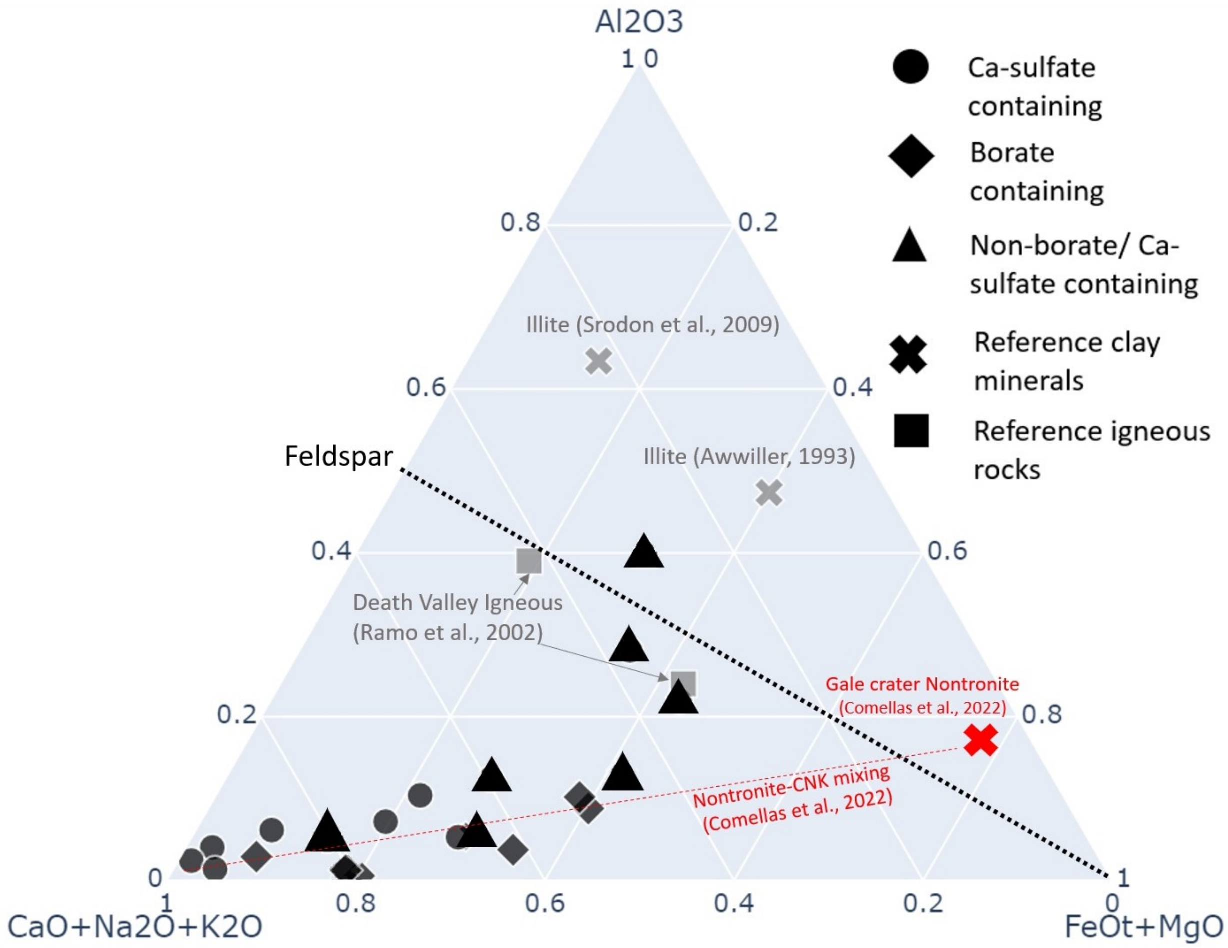

**Figure 10.** Ternary diagram indicating molar proportions of $Al_2O_3$, ($CaO$+$Na_2O$+$K_2O$), and ($FeO_T$+$MgO$) for terrestrial samples collected for this work, reference pure igneous and clay mineral data, and reference Gale crater nontronite data plotted in mole percent. Black dotted line indicates the feldspar line (Hurowitz and McLennan, 2007), and red dotted line indicates the Nontronite-CNK physical mixing line for Gale crater (Comellas et al., 2022).

### 6.3.2 Comparing phases between terrestrial samples and Gale crater

Table 4 shows a comparison of the phases identified in the twenty- one samples with phases observed or plausible in Gale crater and phases formed as a resultant of thermochemical modeling of a Gale-relevant scenario as summarized in Chapter 2. This table shows that all the phase groups identified in Southern California are reported in Gale crater. This table also shows that all phase groups other than feldspars and feldspathoids have formed or are plausible as a result of thermochemical modeling of a Gale-relevant scenario (as described in Chapter 2).

**Table 4**: Comparison of phases identified in the samples from Southern California to minerals observed or reported plausible in Gale crater and to minerals formed as a result of thermochemical modeling of a Gale-relevant scenario.

| Southern California | Gale crater | Gale-relevant model |
|---|---|---|
| **Evaporites:** | | |
| Borates<br>Probertite, Tincalconite, Suanite, Howlite, Ulexite, Colemanite | Plausible (Gasda et al., 2017; Das et al., 2020) | Borax, Kernite |
| Sulfate<br>Gypsum, Anhydrite<br>Thenardite (Na-sulfate) | Gypsum and Anhydrite: Observed (Vaniman et al., 2018; Nachon et al, 2014; Rapin et al., 2019; Gasda et al., 2022); Na-sulfate : Plausible (Schwenzer et al, 2016) | Anhydrite |
| Carbonates<br>Calcite, Dolomite, Ankerite, Lansfordite, Magnesite (Mg-carbonate), Fe, Mg, Mn-carbonate | Calcite : Plausible (Turner et al., 2021), Dolomite: Observed (Sutter et al., 2017), Ankerite: Observed (Rampe et al., 2022)<br>Mn-carbonate: Plausible (Gasda et al., 2022), Fe-Carbonate: Observed (Gasda et al., 2022)<br>Lansfordite and Mg carbonate: Not reported | Dolomite, Ankerite, Dawsonite, Siderite |
| **Clay minerals:**<br>Illite, Vermiculite, Muscovite | Illite : Plausible (Dehouck et al., 2022), Vermiculite : Plausible (Sheppard et al., 2021) | Nontronite, Kaolinite |
| **Feldspar and feldspathoids:**<br>Plagioclase (Albite, Anorthite) Orthoclase, Analcime | Plagioclase: Observed (Achilles, 2018; Wu et al., 2021), Orthoclase: Observed (Wu et al., 2021), Analcime: Plausible (Wernicke et al., 2021), Sanidine: Observed (Treiman et al., 2016) | - |

| | | |
|---|---|---|
| **Sulfide:**<br>Sphalerite, Wurtzite | Sphalerite: Plausible (Peretyazhko et al., 2021)<br>Wurtzite: Not reported | Pyrite |
| **Zeolites:**<br>Heulandite | Plausible (Buz et al., 2017; Schwenzer et al., 2012) | Stilbite |
| **Quartz** | Observed (Payre et al., 2022; Wu et al., 2021; Frydenvang et al., 2017; Rampe et al., 2020) | Silica |
| **Amorphous material** | Observed (Smith et al., 2021) | Plausible |

## 7 Discussion

### 7.1 B and Li distribution in phases of multi-mineralic analog samples

In Gale crater the Ca-sulfates that are measured using the Curiosity rover are physically mixed with sedimentary rocks (e.g., Comellas et al., 2022). These Ca-sulfates also show the presence of B and Li without crystalline borates or Li salts (Das et al., 2020). The sedimentary rocks contain Li (Frydenvang et al., 2020). B and Li are distributed in both evaporitic phases and Li within phases that constitute the sedimentary rocks in Gale crater. However, we are limited to measuring B only in low-Fe targets using the ChemCam instrument and no other instrument onboard the Curiosity rover has been used for a focused in-situ measurement of the Ca-sulfate veins. This makes it challenging to determine the distribution and the abundance trends of B and Li in the rocks and minerals of Gale crater. As B and Li are highly water soluble, pH-sensitive elements with varying solubilities, their distribution and abundance trends and indicative of fluid pH and extent of evaporation (as described in the introduction section and expanded further in this section). With the measurement of B limited to only low-Fe areas in Gale crater, we only have a part of the data that can help us estimate fluid pH and evaporative state during an early aqueous history of Gale crater. Hence, we chose a terrestrial analog area which enabled the determination of the distribution and abundance trends of B and Li in a sample set with physical mixing between evaporites and sedimentary rocks, and end member representatives (i.e., predominantly borate or Ca-sulfate, or basaltic) as a representative of early primary evaporitic setting in Gale crater.

The samples analyzed for this work are multimineralic physical mixtures with seven samples predominantly containing borates, eight samples predominantly containing Ca-sulfate, and six samples that are neither predominantly borate or Ca-sulfate containing but contain halite and clay minerals, feldspars and feldspathoids, zeolites, carbonates, and quartz. The measurement of the samples using both Fus-XRF and XRD technique also indicates that there are phases that contribute to the major oxide, and possibly B and Li abundances, however, as they are below the detection limit of the XRD technique as crystalline phases (i.e., below 1 wt%) hence we were unable to characterize them with the analytical techniques used in this work. We name the fraction which is below the detection limit of the XRD instrument “amorphous” for the purpose of this work. We also note that the major element abundances of the samples measured using Fus-XRF technique do not add up to a 100 (as shown in Table 1) which is likely due to loss of volatile components, hence we are limited to assessing B and Li distribution in the non-volatile fractions of the samples.

In the twenty-one samples the seven predominantly borate samples show a B abundance that consistently exceeds 10000 ppm. These samples also contain 0-618 ppm Li with the highest amount of Li corresponding to the predominantly borate sample that also contains clay. The range of Li abundance in these samples is not dependent on the abundance of any other phases that are present or estimates in the samples. The eight predominantly Ca-sulfate samples contain both B and Li. The B abundance of these samples fall between 0-500 with two exceptions where B abundance exceeds 1000 ppm. No crystalline borates are detected in these predominantly Ca-sulfate samples. The Li abundance of these samples varies between 0-390 ppm with the highest amount of Li corresponding to the sample that also contains clay. In the predominantly Ca-sulfate samples the abundances of neither B nor Li are dependent on the abundance of any other phases in these samples. In the six samples that are neither predominantly borate or Ca-sulfate containing show a B abundance range of 111-1010 ppm and Li abundance range of 89-363 ppm. The highest B abundance in these samples corresponds to the one that also contains halite, and the highest Li abundance corresponds to the sample that contains clay. The clay containing sample also contains ~600 ppm B. There is no correlation between B and Li abundances with any other phases present or estimated in these samples.

The above observations indicate that high Li abundance is consistently correlated with the presence of clay minerals in all three sample groups. However, clay minerals containing samples that do not contain any crystalline borates also show up to ~600 ppm B. Borates are associated with high B abundance and the predominantly Ca-sulfate samples show B abundance up to ~3000 ppm (with majority of the Ca-sulfate samples containing up to ~500 ppm B). The sample group with no predominant borates or Ca-sulfates shows up to ~1000 ppm B which is associated with the presence of halite. Based on these observations, we infer that Li enrichment is specifically associated with the presence of clay minerals while B enrichment is associated with the presence of evaporites. Although Li is enrichment is specifically associated with clay minerals, clay mineral containing samples also show the presence of ~600 ppm B in samples that are not predominantly borate containing or Ca-sulfate containing.

The distribution of B and Li in at least two different phases is likely indicative of fluid pH and evaporative state. In terrestrial settings, Li is associated with clay minerals due to adsorption of Li on their surface (Rohman et al., 2020; Li and Liu, 2020). Clay minerals are also known to adsorb B on to their surface (Karahan et al., 2006; Nellessen et al., 2019). Clay minerals are adsorptive due their surface forces in operation in order to neutralize the mineral surface charge (Nagy and Konya, 2009). Li and B adsorption to clay minerals in only possible in high pH aqueous conditions. In low pH conditions, Li and B will be released into the fluid (Karahan 2006; Rohman et al., 2020). We note that the samples containing high Li also contain other phases (such as crystalline calcite, halite, and quartz) however, we do not attribute the enrichment of Li to these phases as these phases have neutral surface charge and they are not known to characteristically adsorb ions on their crystal surfaces as clay minerals do (Aquilano et al., 2016; Yutkin et al., 2018).

Borates form when the concentration of borate ions in the fluid reaches the saturation level at specific temperature and pH conditions (Birsoy and Ozbas, 2012). Common borates found in terrestrial dry-lake settings are borax, ulexite, tincalconite, howlite, probertite, and colemanite (Kistler and Helvaci, 1994; Birsoy and Ozbas, 2012). For a fluid to reach the saturation level of these common terrestrial borates, approximately 1000 - 2000 ppm of boron is required to be present in the fluid at 25°C at 1 bar pressure (Dalton et al., 2016; Rumble, 2017). This concentration of B in brines is common in highly evaporative environments (Felmy and Weare, 1986; Li et al., 2010; Bixler and Sawyer, 1957) where fluids interact with rocks over multiple periods (Gaillardet and Lemarchand, 2018; Warren, 2006; Li, 2006). In an area where there are both clay minerals with Li and borates are present in close association with each other, as is observed for the terrestrial analog area selected for this work, the following set of events are possible:

1) Adsorption of B and Li on to the surface of clay minerals during interaction with alkaline fluid containing B and Li.

2) Release of B and Li into fluid during a relatively acidic aqueous event increasing B and Li concentration in the fluid.
3) Evaporation of fluid causing borate precipitation in close association with other evaporites such as Ca-sulfates and halite, while Li remains in the fluid due to its higher solubility compared to boron (Dalton et al., 2006). Boron may precipitate as large crystalline aggregates that are identifiable by XRD or as micro crystalline powders co-precipitating with other evaporites such as Ca-sulfates and halite: Hunt, 1966 that may be below the detection limit of XRD).
4) Adsorption of Li and remaining B partially dissolved B from a borate on the clay minerals back on the clay minerals in a following separate alkaline fluid event causing B-rich evaporites and B and Li clay minerals to coexist in close association.

We note that the above series of events may not be the only pathway to form B-rich evaporites and B and Li containing clay minerals in close association with each other. However, in the area where the terrestrial analog samples were collected from, both multiple fluid events with varying pH conditions and presence of wet-dry cycles have been reported in previous studies (Swihart et al., 2014; Lowenstein et al., 1999). Hence, we emphasize on the requirement of multiple aqueous events with varying pH conditions and wet-dry cycling for formation of B-rich evaporites and Li and B containing clay minerals. Li-adsorption requires an alkaline environment while borate formation requires high boron concentration in fluid which can be enabled due to low pH conditions and release of B from clay minerals (Palmer and Helvaci, 1995 report that ulexite requires low pH for their precipitation) and fluid evaporation. In order to form B-containing evaporites and Li-containing clay minerals in close association with each other, multiple wet-dry cycles with varying pH conditions are required.

In the next section, we discuss the distribution of B in evaporites and Li in clay minerals based on elemental association using Principal Component Analysis technique.

### 7.2 B and Li distribution in phases determined using Principal Component Analysis

In Figure 9, we plot the samples analyzed using the LANL ChemCam LIBS instrument in the coordinate space of two principal components (PC1 and PC2). PCA successively identifies axes of maximum variance in the highly dimensional spectroscopic data. The first PC is a combination of Al, Fe, Li, Mg, Na, Si, K and Ca and explain 63% of the variance in the dataset. The second PC is a combination of Ca, Mg, Li, B, and Na and explains 13% of the total variance. The association of these elements indicate the process that caused the maximum variance in this dataset, which we interpret as following.

PC1 shows a positive correlation with respect to Al, Fe, Li, Mg, Na, Si, and K and a negative correlation with Ca. The positive PC1 space (on the right size of the zero line on the PC1 axis) is representative of samples that contain Al, Fe, Li, Mg, Na, Si, and K. Clay minerals are predominantly composed of the elements Al, Fe, Mg, Si, and K and are known to adsorb Li on their surface, whereas halite is characteristically high in Na. Hence, we interpret that the positive PC1 space is representative of clay minerals and halite. The negative PC1 space (on the left-hand side of the PC1 axis) is representative of samples that contain Ca. Ca-sulfates, calcite, and borates contain Ca, hence we interpret that the negative PC1 space is representative of Ca-rich evaporitic samples.

PC2 shows a positive correlation with Ca, Mg, K and Li and a negative correlation with B, and Na. The positive PC2 space (above the zero line on the PC2 axis) is representative of Ca-containing samples. The majority of the Ca-sulfate containing samples plot positive PC2 space except sample 31. Although sample 31 is predominantly Ca-sulfate, it also contains >1000 ppm of B (Table 1 and Table2) which is why it plots in the negative PC2 space. The negative PC2 space (below the zero line on the PC2 axis) is representative of samples that contain Ca, B, and Na. Majority of the borate-containing samples in the negative PC2 space except samples 37b and 37c. Sample 37b which is a borate containing sample, however it also contains 5% calcite which is why it plots in the positive PC2 space. Sample 37c is also a borate containing sample however it consists of 8% borate and 20% albite, 28% calcite, 13% quartz, 2% illite, and 4% halite hence it falls on the positive PC1 and positive PC2 space. The non-borate and non-Ca sulfate samples fall on the positive PC1 space except sample 34d. Sample 34 d is composed of 56% of calcite, 11% of quartz, and 27 % of albite (Table 1) and plots on the negative PC1 space.

The positive PC1 and positive PC2 quadrant is predominantly representative of clay minerals and Li enrichment. The negative PC2 space is representative of borates, Ca-sulfate and halite and B enrichments. Hence, we observe a negative correlation between B and Li on PC2 with an association of B enrichment with borates, Ca-sulfate, and halite and an association of Li enrichment with clay minerals on PC1 and PC2.

This association inferred using PCA is consistent with the B and Li association with evaporites, and clay minerals respectively as inferred using the results of Fus-XRF, XRD, PGNAA and LAICPMS techniques (described in the previous section 7.1). The observation of negative correlation between B and Li is consistent with what we observe in Gale crater. In the case of Gale crater Ca-sulfate veins, we hypothesized that B and Li anti-correlation reflects sequential precipitation due to higher solubility and mobility of Li compared to B leading to faster emplacement of B as borates (as described in Chapter 1 and published by Das et al., 2020). The observation of negative correlation between B and Li in the terrestrial analog samples provides a terrestrial ground truthing of this hypothesis presented for Gale crater.

### 7.3 Comparing terrestrial analog samples and Gale crater rocks

Figure 10 indicates the distribution of samples in an A-FM-CNK diagram (i.e. $Al_2O_3$, $(CaO + Na_2O + K_2O)$, $(FeO_T + MgO)$ diagram) to visualize the extent of physical mixing between the various sample types (characterized as predominantly borate containing, Ca-sulfate containing, and samples with no predominant borates or Ca-sulfates and described in previous sections) and to compare the physical mixing trend with the trend observed in Gale crater. The ternary representation and uses molar proportions of $Al_2O_3$, $(CaO + Na_2O + K_2O)$, and $(FeO_T + MgO)$ to understand the distribution of soluble and insoluble elements in the samples. In the ternary diagram, the $Al_2O_3$ apex represents the insoluble remnants after igneous rocks undergo aqueous weathering in circumneutral conditions (e.g., Hurowitz et al., 2006). Most terrestrial igneous rock compositions fall along the feldspar line. The $CaO + Na_2O + K_2O$ corner represents the soluble materials drawn out of igneous rocks as a result of aqueous weathering (Hurowitz and McLennan, 2007). Mars igneous rocks are inferred to have undergone aqueous weathering which drew out soluble elements and left behind of clay-rich sedimentary rocks which consist of Fe-rich clay minerals including nontronite as a result of the weathering (Hurowitz and McLennan., 2007; Bibring et al., 2005). Notably, Al is a fluid-mobile element in acidic ($Al^{3+}$) or alkaline conditions ($Al(OH)_4^-$) (Hurowitz et al., 2006). Weathering under these conditions drives weathering towards the FM apex, producing Fe and Mg rich clays (Hurowitz et al., 2006). Nontronite is also reported as one of the clay minerals detected in Gale crater (He et al., 2022) and the Fe-rich clay minerals found in Gale crater are inferred to be a resultant of aqueous weathering driven by fluctuating lake levels (Bristow et al., 2018). Ferrian saponite was likely detected in the Yellowknife Bay samples in Gale crater (Treiman et al., 2014).

In terrestrial dry lake settings, primary evaporites and clay-rich sedimentary rocks are frequently intermixed at micron-scale levels (Hunt, 1966; Tanner, 2002). The multicomponent terrestrial samples analyzed for this work also indicate this physical mixture of evaporites and sedimentary rocks in the AFM-CNK diagram where both evaporites and clay-containing samples plot close to each other towards the CNK corner in Figure 10. The tri-plot also shows reference endmember igneous samples (Death Valley plutonic and basaltic rocks measured by Ramo et al., 2002) and clay mineral (Illite measured by Srodon et al., 2009 and Awwiller, 1993) data. Endmember igneous samples plot close to the feldspar line, while endmember clay mineral falls above the feldspar line, closer to the $Al_2O_3$ apex. The samples analyzed for this work show a broad linear trend, and the clay-containing samples fall below the feldspar line and significantly closer to the $CaO + Na_2O + K_2O$ corner compared to pure illite references indicating mixing with evaporites that are predominantly rich in CaO, $Na_2O$, and $K_2O$.

Observations in Gale crater also show a mixing between evaporites and surrounding sedimentary rocks (L'Haridon et al., 2018; Hurowitz et al., 2017; Gasda et al., 2022). This mixing is inferred to be due to presence of cements or simultaneously sampling an evaporite vein and bedrock at the same time during Curiosity rover analytical techniques (Gasda et al., 2022) within the 200–500 micron spot size of ChemCam (Wiens et al., 2012; Maurice et al., 2012). Similarly, Comellas et al., (2022) use nontronite to represent all Fe/Mg clays in altered bedrock in Yellowknife Bay sediments. They plot a possible mixing trend between evaporites (veins in and around Yellowknife Bay) and a nontronite clay mineral measured in Gale crater on an AFM-CNK diagram using ChemCam data collected from the Yellowknife Bay formation. This possible mixing trend is shown in red extending from the nontronite composition towards the $CaO + Na_2O + K_2O$ corner. The physical mixing trend in the terrestrial samples is broadly consistent with the trend observed in Gale crater.

In Table 4 we compare the phases identified and estimated for the samples from the terrestrial analog area with phases observed and plausible for Gale crater and also with phases formed as a resultant of Gale-relevant thermochemical modeling (as described in Chapter 2 of this thesis). All the phase groups identified in Southern California are reported in Gale crater and are consistent with phases that have formed or are plausible as a result of thermochemical modeling of a Gale-relevant scenario (except feldspars and feldspathoids- these are inferred to be representative of Gale crater's unaltered igneous fraction: Rampe et al., 2017).

The mixing between evaporites and clay minerals enables the study of B and Li distribution between evaporative phases and clay minerals, both of which can be a source (borates as a source of B) or temporary storage phases (clay minerals as a temporary source of both B and Li through adsorption) of B and Li. Borate formation and B and Li adsorption to clay minerals require different fluid pH and evaporative conditions. The preferential distribution of B and Li between borates and clay minerals when both phases are physically mixed enables the estimation of fluid pH conditions and evaporative extent. A broad consistency between the physical mixing trend in the terrestrial analog samples and Gale crater, and between the phases observed in the terrestrial analog area, Gale crater, and a Gale-relevant enables estimation of possible fluid conditions in Gale crater's aqueous history especially for pH and evaporative conditions through analogy.

### 7.4 Implications for Gale crater

In Gale crater we observed up to 300 ppm of B and up to 65 ppm of Li in secondary Ca-sulfate veins and hypothesize that B enrichments may be due to pre-existing primary borate deposits that were remobilized and precipitated in close association with Ca-sulfates or that B and Li were drawn out of clay minerals during acidic aqueous events (Gasda et al., 2017; Das et al. 2020). We also observe an inverse correlation between B and Li in the secondary Ca-sulfate veins in Gale crater and hypothesize that inverse correlation is due to sequential precipitation caused by higher solubility of Li compared to B. We have not observed crystalline borates or Li salts in Gale crater as of this work and the sources of B and Li in Ca-sulfates in Gale crater are unknown. However, we hypothesized that the source of B could be borates and clay minerals while the source of Li could be clay minerals. As described in the previous sections, borate formation and B and Li adsorption on clay minerals are pH sensitive processes that require two different pH and evaporative conditions. Hence studying B and Li in an area where evaporites and sedimentary rocks are mixed provides an opportunity to estimate fluid pH and evaporative conditions.

In this work, we identified two potential reservoirs for B (borates and clay minerals) and one reservoir for Li (clay minerals) in multimineralic terrestrial analog samples that we use as representatives of early primary evaporative environment in Gale crater. We show that B enrichment is closely linked with evaporites, while Li enrichment is linked with clay minerals, although clay containing samples also show the presence of B. We also observe an anticorrelation between B and Li in the terrestrial samples. Based on the on the observations made in this work, we infer that multiple aqueous events with varying pH conditions and presence of wet-dry periods are required for the formation of B-containing evaporites and B and

Li containing clay minerals in the terrestrial analog areas. Multiple aqueous events with varying pH conditions and seasonal wet-dry periods are both reported in the terrestrial analog sample collection area in previous studies which is consistent with the inferences made based on the results of this study (Swihart et al., 2014, Lowenstein et al., 1999)

We compare the physical mixing trends between evaporites and sedimentary rocks in the terrestrial analog samples with mixing trends observed in Gale crater in addition to comparing the phase groups identified in the terrestrial analog samples to the phases reported in Gale carter and phases a Gale-relevant thermochemical model. We find that the mixing trends in the terrestrial analog area are broadly consistent with ones reported in Gale crater and phases in terrestrial analog samples are also consisted with ones reported in Gale crater and phases formed during thermochemical modeling of a Gale-relevant system. We also find that the negative relationship between B and Li observed in secondary Ca-sulfate veins in Gale crater is consistent with the observation of B and Li anticorrelation in the terrestrial analog samples. Based on these consistencies between the terrestrial analog sample set, Gale crater observations, and results from a Gale-relevant model, we infer that observations from the terrestrial analog and corresponding inferences regarding fluid pH and evaporation can be broadly applicable to Gale crater.

In Gale crater we observe enrichment of B and Li in secondary Ca-sulfate veins without the observation of crystalline borates of Li-salts. Measurement of B is also limited to low-Fe targets due to spectral interferences of Fe from high Fe-sedimentary rocks with spectral signal of B. The objective of the terrestrial analog work was to determine the sources of B and Li in primary Ca-sulfates in an early Gale-like environment and estimate fluid pH and evaporative conditions possible in Gale crater's early aqueous history.

Based on results of terrestrial analog analysis we infer that B and Li enrichment in primary Ca-sulfates in Gale crater could have been due to close association of Ca-sulfates with borates and clay minerals. B may be likely stored in both borates and clay minerals while Li may be stored in clay minerals. We infer that during multiple late-stage diagenetic events with varying pH conditions (Rampe et al., 2020) in Gale crater, primary borates and B and Li-containing clay minerals may have been remobilized to be closely emplaced with the secondary Ca-sulfate veins. Borates may have been present as microcrystals within Ca-sulfates veins (as also inferred for the analog samples analyzed for this work and reported in other terrestrial dry lake environments: Hunt, 1966) while B and Li containing clay minerals may be present on the walls of the secondary evaporitic veins both of which are likely below the detection limit of the instruments onboard the Curiosity rover. We infer that the negative relationship between B and Li on both Earth and Mars are due to the varying solubilities between B and Li where B precipitates as primary borates earlier than Li. We also infer that the sequential precipitation trend between B and Li are broadly preserved in the secondary Ca-sulfate veins in Gale crater (as summarized in Chapter 1 and in Das et al., 2020).

The inference of multiple wet-dry cycles with varying pH conditions is consistent with inferences made using other Gale sedimentological and Gale-relevant experimental studies (wet dry cycles in Gale crater: Rapin et al., 2019; 2020; Kronyak et al., 2019; varying fluid pH conditions in Gale crater: Hurowitz et al., 2017; Turner et al., Hausrath et al., 2021). The inference of multiple wet dry cycles based on this work is also consistent with the results of thermochemical modeling of a Gale-relevant scenario in Chapter 2 where we establish that the formation of borates and Ca-sulfates in Gale crater in close association with each other likely takes at least 250 annual wet-dry cycles.

In Chapter 1 we hypothesized that B enrichment in Ca-sulfates of Gale crater may be due to pre-existing borate deposits that were remobilized and precipitated in close association with Ca-sulfates and in areas where evaporative environments were not inferred feasible based on observed lithologic facies, B and Li are inferred to be drawn out of clay minerals during acidic aqueous events. B and Li distribution in multi-mineralic terrestrial analog samples indicate that B and Li enrichment in close association with Ca-sulfate require multiple wet dry cycles with varying pH conditions. Hence this work provides a terrestrial ground truthing for the previous hypothesis presented for B and Li enrichment in Gale crater.

Estimates of pH are important of determining the range and extent of habitable environments. Extremely acidic environments denature proteins and hydrolyze cellular components while extremely alkaline environments limit hydrogen availability for crucial bioenergetic processes and therefore both highly acidic and alkaline are hazardous to majority of terrestrial organisms (Dartnell, 2011). However, life has been found on Earth that lives at pH -3.6, far beyond what has so far been predicted for Mars (e.g., Merino et al., 2019). The majority of terrestrial organisms can survive within moderately acidic to alkaline conditions showing optimal habitability conditions at neutral pH (Shock and Holland, 2007). This work shows that both acidic and alkaline aqueous conditions (with possible intermittent phases of neutral aqueous conditions) with multiple wet dry cycles were required for the formation of B and Li containing secondary Ca-sulfate veins in Gale crater. The relative constraints on fluid pH conditions possible in Gale crater improves our understanding of types of microbial communities feasible through Gale crater's evolving aqueous history. The presence of wet-dry cycles has also been inferred to play and important role in the origin of life on Earth (Hud and Fialho.,2019; Becker et al., 2019; Marsh, 2022). Thus, the study of B and Li in phases that can help us determine an estimate on Gale crater fluid pH and evaporative state, provide a higher resolution of understanding of habitability potential during the various stages of Gale crater's aqueous history.

## 8 Conclusions

In this work we use terrestrial analog samples to establish that B and Li enrichment in Ca-sulfate veins of Gale crater are due to presence of borates and clay minerals that are likely below the detection limit of instruments onboard the Curiosity rover. We establish that B enrichment is linked with evaporite formation likely supported by a relatively acidic pH condition and high evaporation that enabled precipitation of evaporites while Li enrichment is linked with clay minerals through adsorption which was likely supported by a relatively high pH aqueous condition. We infer that in Gale crater, Li and B adsorption took place in clay minerals during alkaline aqueous conditions while primary borates, Ca-sulfates and halite formed in low-pH high evaporation conditions over multiple wet-dry cycles with varying fluid pH conditions. We also infer that the B and Li enrichment in Ca-sulfate veins formed during secondary diagenetic events due to remobilization of primary evaporites and clay minerals while preserving the negative trend between B and Li caused on their relative solubilities. The inferences for variable fluid pH conditions and the presence of wet-dry cycles for the terrestrial analog samples are consistent with previous analytical studies of evaporites and sedimentary rock in the same area. The physical mixing trends between evaporites and sedimentary rocks are broadly consistent with mixing trends observed in Gale crater. The phases identified in the terrestrial samples are also broadly consistent with phases reported in Gale crater and phases formed in a thermochemical simulation of wet-dry cycles in a Gale-relevant environment. Hence the inferences made for the terrestrial analog samples are broadly applicable to Gale crater and provide a ground truthing for the observation made using the Curiosity rover. The results of this work provide a higher resolution understanding of fluid pH and evaporative states that are relevant for determining the range and extent of habitable conditions possible in Gale crater's evolving aqueous past.

## 9 References

Achilles, C., 2018. Analyses of crystalline and X-ray amorphous materials in Gale crater rocks and soils.

Awwiller, D.N., 1993. Illite/smectite formation and potassium mass transfer during burial diagenesis of mudrocks; a study from the Texas Gulf Coast Paleocene-Eocene. *Journal of Sedimentary Research*, *63*(3), pp.501-512.

Aquilano, D., Otálora, F., Pastero, L. and García-Ruiz, J.M., 2016. Three study cases of growth morphology in minerals: Halite, calcite and gypsum. *Progress in Crystal Growth and Characterization of Materials*, *62*(2), pp.227-251.

Banham, S. G., Gupta, S., Rubin, D. M., Watkins, J. A., Sumner, D. Y., Edgett, K. S., et al. (2018). Ancient Martian aeolian processes and palaeomorphology reconstructed from the Stimson formation on the lower slope of Aeolis Mons, Gale crater, Mars. Sedimentology, 65(4), 993–1042.

Becker, S., Feldmann, J., Wiedemann, S., Okamura, H., Schneider, C., Iwan, K., Crisp, A., Rossa, M., Amatov, T. and Carell, T., 2019. Unified prebiotically plausible synthesis of pyrimidine and purine RNA ribonucleotides. *Science*, *366*(6461), pp.76-82.

Bedford, C. C., Bridges, J. C., Schwenzer, S. P., Wiens, R. C., Rampe, E. B., Frydenvang, J., & Gasda, P. J. (2019). Alteration trends and geochemical source region characteristics preserved in the fluviolacustrine sedimentary record of Gale crater, Mars. Geochimica et Cosmochimica Acta, 246, 234–266.

Bedford, C. C., Banham, S. G., Bridges, J. C., Forni, O., Cousin, A., Bowden, D., et al. (2022). An insight into ancient aeolian processes and post-Noachian aqueous alteration in Gale crater, Mars, using ChemCam geochemical data from the Greenheugh capping unit. *Journal of Geophysical Research: Planets*.

Bennett, K., et al., (2021) An Overview of the Curiosity rover's Campaign in Glen Torridon, Gale Crater, Mars, Journal of Geophysical research: Planets (GT Special Issue Paper), in review.

Bennett, K.A., Fox, V.K., Bryk, A., Dietrich, W. and MSL Team, 2022. An Overview of Key Findings from the Curiosity Rover's Campaign in Glen Torridon, Gale Crater, Mars. *LPI Contributions*, *2678*, p.2223.

Bibring, J.-P., Langevin, Y., Gendrin, A., Gondet, B., Poulet, F., Berthe, M., Soufflot, A. Arvidson, R.E., Mangold N., Mustard, J.F., Drossart, P., 2005. OMEGA-Team, Mars surface diversity as revealed by the OMEGA/Mars Express observations. Science 307, 1576–1581.

Birsoy, R. and Özbaş, Ü., 2012. Activity diagrams of borates: implications on common deposits. *Carbonates and Evaporites*, *27*(1), pp.71-85.

Bixler, G.H. and Sawyer, D.L., 1957. Boron Chemicals from Searles Lake Brines. *Industrial & Engineering Chemistry*, *49*(3), pp.322-333.

Bristow, T.F., Grotzinger, J.P., Rampe, E.B., Cuadros, J., Chipera, S.J., Downs, G.W., Fedo, C.M., Frydenvang, J., McAdam, A.C., Morris, R.V. and Achilles, C.N., 2021. Brine-driven destruction of clay minerals in Gale crater, Mars. *Science*, *373*(6551), pp.198-204.

Buz, J., Ehlmann, B.L., Pan, L. and Grotzinger, J.P., 2017. Mineralogy and stratigraphy of the Gale crater rim, wall, and floor units. *Journal of Geophysical Research: Planets*, *122*(5), pp.1090-1118.

Caravaca, G., Mangold, N., Dehouck, E., Schieber, J., Zaugg, L., Bryk, A.B., Fedo, C.M., Le Mouélic, S., Le Deit, L., Banham, S.G. and Gupta, S., 2022. From Lake to River: Documenting an Environmental Transition across the Jura/Knockfarril Hill Members Boundary in the Glen Torridon Region of Gale crater (Mars). *Journal of Geophysical Research: Planets*, p.e2021JE007093.

Caravaca, G., Le Mouélic, S., Rapin, W., Dromart, G., Gasnault, O., Fau, A., et al. (2021b). Long-Distance 3D Reconstructions Using Photogrammetry with Curiosity's ChemCam Remote Micro-Imager in Gale Crater (Mars). Remote Sensing, 13(20), 4068.

Clegg, S. M., Wiens, R. C., Anderson, R., Forni, O., Frydenvang, J., Lasue, J., et al. (2017). Recalibration of the Mars Science Laboratory ChemCam instrument with an expanded geochemical database. Spectrochimica Acta Part B: Atomic Spectroscopy, 129, 64–85.

Comellas, J.M., Essunfeld, A., Morris, R., Lanza, N., Gasda, P.J., Delapp, D., Wiens, R.C., Gasnault, O., Clegg, S., Bedford, C.C. and Dehouck, E., 2022. Evidence of Multiple Fluid Events in Elevated-Mn ChemCam Targets in the Bradbury Rise, Gale Crater, Mars. *LPI Contributions*, *2678*, p.2445.

Cousin, A., Desjardins, M., Dehouck, E., Forni, O., David, G., Berger, G., Caravaca, G., Meslin, P.Y., Lasue, J., Ollila, A.M. and Rapin, W., 2021, March. K-rich rubbly bedrock at Glen Torridon, Gale crater, Mars: Investigating the possible presence of illite. In *52nd lunar and planetary science conference*.

Crowley, J.K., 1993. Mapping playa evaporite minerals with AVIRIS data: A first report from Death Valley, California. *Remote Sensing of Environment*, *44*(2-3), pp.337-356.

Dalton, G. R., Lee, A. Y., & Young, S. L. (2016). IUPAC/NIST Solubility Database (No. IUPAC/NIST Solubility Database).

Dartnell, L., 2011. Biological constraints on habitability. *Astronomy & Geophysics*, *52*(1), pp.1-25.

Das, D., Gasda, P. J., Wiens, R. C., Berlo, K., Leveille, R. J., Frydenvang, J., Mangold, M., et al. "Boron and lithium in calcium sulfate veins: Tracking precipitation of diagenetic materials in Vera Rubin Ridge, Gale crater." *Journal of Geophysical Research: Planets* 125, no. 8 (2020): e2019JE006301.

Dehouck, E., Cousin, A., Mangold, N., Frydenvang, J., Gasnault, O., Rapin, W., Forni, O., Gasda, P., David, G., Caravaca, G. and Lasue, J., 2021, March. Leaving Glen Torridon: Bedrock geochemistry measured by ChemCam en route to the sulfate unit of Gale crater. In 52nd lunar and planetary science conference.

Dehouck, E., Cousin, A., Mangold, N., Frydenvang, J., Gasnault, O., Forni, O., Rapin, W., Gasda, P.J., Caravaca, G., David, G. and Bedford, C.C., 2022. Bedrock geochemistry and alteration history of the clay-bearing Glen Torridon region of Gale crater, Mars. *Journal of Geophysical Research: Planets*, p.e2021JE007103.

Dietrich, W., Bryk, A., Banham, S., Rubin, D., Thompson, L., Caravaca, G. and Williams, R., 2022, March. Climate and Diagenetic Implications of Possible Soft Sediment Deformation of the Basal Aeolian Stimson Sediments in Gale Crater. In *53rd Lunar and Planetary Science Conference*.

Dromart, G., Le Deit, L., Rapin, W., Gasnault, O., Le Mouélic, S., Quantin-Nataf, C., et al. (2021). Deposition and erosion of a Light-Toned Yardang-forming unit of Mt Sharp, Gale crater, Mars. *Earth and Planetary Science Letters*, *554*, 116681.

Edgar, L. A., Fedo, C. M., Gupta, S., Banham, S. G., Fraeman, A. A., Grotzinger, J. P., et al. (2020). A Lacustrine Paleoenvironment Recorded at Vera Rubin Ridge, Gale Crater: Overview of the Sedimentology and Stratigraphy Observed by the Mars Science Laboratory Curiosity Rover. Journal of Geophysical Research: Planets, 125(3).

Esbensen, K.H., Guyot, D., Westad, F. and Houmoller, L.P., 2002. *Multivariate data analysis: in practice: an introduction to multivariate data analysis and experimental design*. Multivariate Data Analysis.

Fedo, C. M., Grotzinger, J. P., Gupta, S., Fraeman, A., Edgar, L., Edgett, K., et al. (2018). Sedimentology and Stratigraphy of the Murray Formation, Gale Crater, Mars. Abstract number 2078. Presented at the 49 th Lunar and Planetary Science Conference, Houston, TX.

Felmy, A.R. and Weare, J.H., 1986. The prediction of borate mineral equilibria in natural waters: Application to Searles Lake, California. *Geochimica et Cosmochimica Acta*, *50*(12), pp.2771-2783.

Follner, S., Wolter, A., Helming, K., Silber, C., Bartels, H. and Follner, H., 2002. On the real structure of gypsum crystals. *Crystal Research and Technology: Journal of Experimental and Industrial Crystallography*, *37*(2-3), pp.207-218.

Fox, V.K., Bennett, K.A., Bryk, A., Arvidson, R.E., Bristow, T., Dehouck, E., Dietrich, B., Ehlmann, B.L., Fedo, C., Mangold, N. and O'Connell, C., 2020, March. One year in Glen

Torridon: Key results from the Mars Science Laboratory curiosity rover exploration of clay-bearing units. In *Lunar and Planetary Science Conference* (No. 2326, p. 2833).

Fraeman, A. A., Ehlmann, B. L., Arvidson, R. E., Edwards, C. S., Grotzinger, J. P., Milliken, R. E., et al. (2016). The stratigraphy and evolution of lower Mount Sharp from spectral, morphological, and thermophysical orbital data sets: Stratigraphy and Evolution of Mount Sharp. Journal of Geophysical Research: Planets, 121(9), 1713–1736.

Fraeman, A.A., Edgar, L.A., Rampe, E.B., Thompson, L.M., Frydenvang, J., Fedo, C.M., Catalano, J.G., Dietrich, W.E., Gabriel, T.S., Vasavada, A.R. and Grotzinger, J.P., 2020. Evidence for a diagenetic origin of Vera Rubin ridge, Gale crater, Mars: Summary and synthesis of Curiosity's exploration campaign. *Journal of Geophysical Research: Planets*, *125*(12), p.e2020JE006527.

Frydenvang, J., Gasda, P. J., Hurowitz, J. A., Grotzinger, J. P., Wiens, R. C., Newsom, H. E., et al. (2017). Diagenetic silica enrichment and late-stage groundwater activity in Gale crater, Mars: Silica enriching diagenesis, Gale, Mars. Geophysical Research Letters.

Frydenvang, J., Mangold, N., Wiens, R. C., Fraeman, A. A., Edgar, L. A., Fedo, C., et al. (2020). The chemostratigraphy of the Murray formation and role of diagenesis at Vera Rubin ridge in Gale crater, Mars, as observed by the ChemCam instrument. Journal of Geophysical Research: Planets.

Gaillardet, J. and Lemarchand, D., 2018. Boron in the weathering environment. *Boron Isotopes*, pp.163-188.

Gasda, P. J., Haldeman, E. B., Wiens, R. C., Rapin, W., Bristow, T. F., Bridges, J. C., et al. (2017). In situ detection of boron by ChemCam on Mars. Geophysical Research Letters, 44(17), 8739-8748. 795

Gasda, P. J., Anderson, R. B., Cousin, A., Forni, O., Clegg, S. M., Ollila, A., et al. (2021). Quantification of manganese for ChemCam Mars and laboratory spectra using a multivariate model. *Spectrochimica Acta Part B: Atomic Spectroscopy*, *181*, 106223.

Gasda, P.J., Comellas, J., Essunfeld, A., Das, D., Bryk, A.B., Dehouck, E., Schwenzer, S.P., Crossey, L., Herkenhoff, K., Johnson, J.R. and Newsom, H., 2022. Overview of the Morphology and Chemistry of Diagenetic Features in the Clay‐Rich Glen Torridon Unit of Gale Crater, Mars. *Journal of Geophysical Research: Planets*, p.e2021JE007097.

Gates, G.R., 1959. Clay mineral composition of borate deposits and associated strata at Boron, California. *Science*, *130*(3367), pp.102-102.

Grotzinger, J. P., and Milliken, R. E. (2012). The sedimentary rock record of Mars: Distribution, origins, and global stratigraphy. Sedimentary Geology of Mars, 102, 1-48.

Grotzinger, J. P., Sumner, D. Y., Kah, L. C., Stack, K., Gupta, S., Edgar, L., et al. (2014). A habitable fluvio-lacustrine environment at Yellowknife Bay, Gale Crater, Mars. Science, 343(6169), 1242777.

Grotzinger, J. P., Gupta, S., Malin, M. C., Rubin, D. M., Schieber, J., Siebach, K., et al. (2015). Deposition, exhumation, and paleoclimate of an ancient lake deposit, Gale crater, Mars. Science, 350(6257), aac7575.

Hausrath, E.M., Ming, D.W., Rampe, E.B. and Peretyazhko, T.S., 2021. Reactive Transport Modeling of Aqueous Alteration in the Murray Formation, Gale Crater, Mars. *ACS Earth and Space Chemistry*, *5*(3), pp.424-435.

Hawthorne, F.C., Krivovichev, S.V. and Burns, P.C., 2000. The crystal chemistry of sulfate minerals.

He, L., Arvidson, R.E., O'Sullivan, J.A., Morris, R.V., Condus, T., Hughes, M.N. and Powell, K.E., 2022. Surface Kinetic Temperatures and Nontronite Single Scattering Albedo Spectra from Mars Reconnaissance Orbiter CRISM Hyperspectral Imaging Data Over Glen Torridon, Gale Crater, Mars. *Journal of Geophysical Research: Planets*, p.e2021JE007092.

Hud, N.V. and Fialho, D.M., 2019. RNA nucleosides built in one prebiotic pot. *Science*, *366* (6461), pp.32-33.

Hughes, M.N. and Arvidson, R.E., 2020, December. Identification and Characterizations of the Basal Sulfate-Bearing Stratum, Northern Mount Sharp, Mars. In *AGU Fall Meeting Abstracts* (Vol. 2020, pp. P069-0012).

Hunt CB, Robinson TW, Bowles WA, and Washburn AL (1966) Hydrologic basin, Death Valley, California. U.S. Geological Survey Professional Paper 494-B: 1–138.

Hurowitz, J. A., McLennan, S. M., Tosca, N. J., Arvidson, R. E., Michalski, J. R., Ming, D. W., et al. (2006). In situ and experimental evidence for acidic weathering of rocks and soils on Mars. *Journal of Geophysical Research*, *111*(E2).

Hurowitz, J.A. and McLennan, S.M., 2007. A∼ 3.5 Ga record of water-limited, acidic weathering conditions on Mars. *Earth and Planetary Science Letters*, *260*(3-4), pp.432-443.

Hurowitz, J.A., Grotzinger, J.P., Fischer, W.W., McLennan, S.M., Milliken, R.E., Stein, N., Vasavada, A.R., Blake, D.F., Dehouck, E., Eigenbrode, J.L. and Fairen, A.G., 2017. Redox stratification of an ancient lake in Gale crater, Mars. *Science*, *356*(6341), p.eaah6849.

Kah, L. C., Stack, K. M., Eigenbrode, J. L., Yingst, R. A., & Edgett, K. S. (2018). Syndepositional precipitation of calcium sulfate in Gale Crater, Mars. Terra Nova, 30(6), 431-439.

Karahan, S., Yurdakoç, M., Seki, Y. and Yurdakoç, K., 2006. Removal of boron from aqueous solution by clays and modified clays. *Journal of Colloid and Interface Science*, *293*(1), pp.36-42.

Kistler, R.B. and Helvaci, C., 1994. Boron and borates. *Industrial minerals and rocks*, *6*, pp.171-186.

Kronyak, R. E., Kah, L. C., Edgett, K. S., VanBommel, S. J., Thompson, L. M., Wiens, R. C., et al. (2019). Mineral-Filled Fractures as Indicators of Multigenerational Fluid Flow in the Pahrump Hills Member of the Murray Formation, Gale Crater, Mars. Earth and Space Science, 6(2), 238–265.

Lever, J., Krzywinski, M. and Altman, N., 2017. Points of significance: Principal component analysis. *Nature methods*, *14*(7), pp.641-643.

L'Haridon, J., Mangold, N., Meslin, P.Y., Johnson, J.R., Rapin, W., Forni, O., Cousin, A., Payré, V., Dehouck, E., Nachon, M. and Le Deit, L., 2018. Chemical variability in mineralized veins observed by ChemCam on the lower slopes of Mount Sharp in Gale crater, Mars. *Icarus*, *311*, pp.69-86.

Li, W. and Liu, X.M., 2020. Experimental investigation of lithium isotope fractionation during kaolinite adsorption: Implications for chemical weathering. *Geochimica et cosmochimica acta*, *284*, pp.156-172.

Li, J., Tim K. Lowenstein, Christopher B. Brown, Teh-Lung Ku, and Shangde Luo. "A 100 ka record of water tables and paleoclimates from salt cores, Death Valley, California." *Palaeogeography, Palaeoclimatology, Palaeoecology* 123, no. 1-4 (1996): 179-203.

Li, J., Lowenstein, T.K. and Blackburn, I.R., 1997. Responses of evaporite mineralogy to inflow water sources and climate during the past 100 ky in Death Valley, California. *Geological Society of America Bulletin*, *109*(10), pp.1361-1371.

Li, M., Kang, S., Ge, J., Yi, C. and Fang, X., 2010. Saline rhythm and climatic change since 20.6 kyr BP from the Qiulinanmu Playa Lake in Tibet. *Carbonates and Evaporites*, *25*(1), pp.5-14.

Lowenstein, T.K. and Hardie, L.A., 1985. Criteria for the recognition of salt-pan evaporites. *Sedimentology*, *32*(5), pp.627-644.

Lowenstein, Tim K., Jianren Li, Christopher Brown, Sheila M. Roberts, Teh-Lung Ku, Shangde Luo, and Wenbo Yang. "200 ky paleoclimate record from Death Valley salt core." *Geology* 27, no. 1 (1999): 3-6.

Lowenstein, T.K. and Risacher, F., 2009. Closed basin brine evolution and the influence of Ca–Cl inflow waters: Death Valley and Bristol Dry Lake California, Qaidam Basin, China, and Salar de Atacama, Chile. *Aquatic Geochemistry*, *15*(1), pp.71-94.

Ma, Y.Q., Peng, Z.K., Yang, J., Xiao, Y.K. and Zhang, Y.L., 2017. Determination of boron content and isotopic composition in gypsum by inductively coupled plasma optical emission spectroscopy and positive thermal ionization mass spectrometry using phase transformation. *Talanta*, *175*, pp.250-255.

Mangold, N., Thompson, L.M., Forni, O., Williams, A.J., Fabre, C., Le Deit, L., Wiens, R.C., Williams, R., Anderson, R.B., Blaney, D.L. and Calef, F., 2016. Composition of conglomerates analyzed by the Curiosity rover: Implications for Gale Crater crust and sediment sources. *Journal of Geophysical Research: Planets*, *121*(3), pp.353-387.

Marsh, G.E., 2022. Thermodynamics and the Origin of Life. *Canadian Journal of Physics*, (ja).

Maurice, S., Wiens, R.C., Saccoccio, M., Barraclough, B., Gasnault, O., Forni, O., Mangold, N., Baratoux, D., Bender, S., Berger, G. and Bernardin, J., 2012. The ChemCam instrument suite on the Mars Science Laboratory (MSL) rover: Science objectives and mast unit description. *Space science reviews*, *170*(1), pp.95-166.

McAdam, A.C., Franz, H.B., Sutter, B., Archer Jr, P.D., Freissinet, C., Eigenbrode, J.L., Ming, D.W., Atreya, S.K., Bish, D.L., Blake, D.F. and Bower, H.E., 2014. Sulfur-bearing phases detected by evolved gas analysis of the Rocknest aeolian deposit, Gale Crater, Mars. *Journal of Geophysical Research: Planets*, *119*(2), pp.373-393.

McAllister, J. F. "Geology of the Furnace Creek borate area." *Death Valley, Inyo County, California: California Division of Mines and Geology Map Sheet* 14, no. 9 (1970).

Merino, N., Aronson, H.S., Bojanova, D.P., Feyhl-Buska, J., Wong, M.L., Zhang, S. and Giovannelli, D., 2019. Living at the extremes: extremophiles and the limits of life in a planetary context. *Frontiers in microbiology*, *10*, p.780.

Meslin, P.Y., Rapin, W., Forni, O., Cousin, A., Gasnault, O., Loche, M., Dehouck, E., Mangold, N., Caravaca, G., Schröder, S. and Gasda, P., 2022, March. Significant Halite Enrichment in the Sulfate-Unit of Gale Crater, Mars. In *53rd Lunar and Planetary Science Conference*.

Michalski, J.R., Niles, P.B., Glotch, T.D. and Cuadros, J., 2021. Infrared Spectral Evidence for K-Metasomatism of Volcanic Rocks on Mars. *Geophysical Research Letters*, *48*(10), p.e2021GL093882.

Milliken, R. E., J. P. Grotzinger, and B. J. Thomson. "Paleoclimate of Mars as captured by the stratigraphic record in Gale Crater." *Geophysical Research Letters* 37, no. 4 (2010).

Morris, R.V., Vaniman, D.T., Blake, D.F., Gellert, R., Chipera, S.J., Rampe, E.B., Ming, D.W., Morrison, S.M., Downs, R.T., Treiman, A.H. and Yen, A.S., 2016. Silicic volcanism on Mars evidenced by tridymite in high-SiO2 sedimentary rock at Gale crater. *Proceedings of the National Academy of Sciences*, *113*(26), pp.7071-7076.

Nachon, M., Mangold, N., Forni, O., Kah, L. C., Cousin, A., Wiens, R. C., et al. (2017). Chemistry of diagenetic features analyzed by ChemCam at Pahrump Hills, Gale crater, Mars. Icarus, 281, 121-136.

Nagy, N.M. and Kónya, J., 2009. *Interfacial chemistry of rocks and soils*. CRC Press.

Nellessen, M.A., Crossey, L., Peterson, E., Gasda, P.J., Lanza, N., Yeager, C., Parsons, B., Labouriau, A., Wiens, R.C., Clegg, S. and Das, D., 2019, July. Boron Adsorption in Clay Minerals: Implications for Martian Groundwater Chemistry and Prebiotic Processes. In *Ninth International Conference on Mars* (Vol. 2089, p. 6353).

Palmer, M.R. and Helvaci, C., 1995. The boron isotope geochemistry of the Kirka borate deposit, western Turkey. *Geochimica et Cosmochimica Acta*, *59*(17), pp.3599-3605.

Payré, V., Fabre, C., Cousin, A., Sautter, V., Wiens, R. C., Forni, O., et al. (2017). Alkali trace elements in Gale crater, Mars, with ChemCam: Calibration update and geological implications. Journal of Geophysical Research: Planets, 122(3), 650–679.

Payré, V., Siebach, K.L., Thorpe, M.T., Antoshechkina, P. and Rampe, E.B., 2022. Tridymite in a lacustrine mudstone in Gale Crater, Mars: Evidence for an explosive silicic eruption during the Hesperian. *Earth and Planetary Science Letters*, *594*, p.117694.

Peretyazhko, T.S., Ming, D.W., Morris, R.V., Agresti, D.G. and Buckley, W.P., 2021. Formation of Fe (III)(Hydr) oxides from Fe (II) Sulfides: Implications for akaganeite detection on Mars. *ACS Earth and Space Chemistry*, *5*(8), pp.1934-1947.

Rämö, T.O., Calzia, J.P. and Kosunen, P.J., 2002. Geochemistry of Mesozoic plutons, southern Death Valley region, California: Insights into the origin of Cordilleran interior magmatism. *Contributions to Mineralogy and Petrology*, *143*(4), pp.416-437.

Rampe, E. B., Bristow, T. F., Morris, R. V., Morrison, S. M., Achilles, C. N., Ming, D. W., et al. (2020). Mineralogy of Vera Rubin Ridge from the Mars Science Laboratory CheMin Instrument. Journal of Geophysical Research: Planets.

Rampe, E.B., Bristow, T.F., Blake, D.F., Vaniman, D.T., Chipera, S.J., Downs, R.T., Ming, D.W., Morris, R.V., Tu, V.M., Thorpe, M.T. and Yen, A.S., 2022, March. Mineralogical Trends Over the Clay-Sulfate Transition in Gale Crater from the Mars Science Laboratory CheMin Instrument. In *53rd Lunar and Planetary Science Conference*.

Rapin, W., Ehlmann, B. L., Dromart, G., Schieber, J., Thomas, N. H., Fischer, W. W., et al. (2019). An interval of high salinity in ancient Gale crater lake on Mars. Nature Geoscience, 12(11), 889-895.

Rapin, W., Dromart, G., Rubin, D., Le Deit, L., Mangold, N., Edgar, L.A., Gasnault, O., Herkenhoff, K., Le Mouélic, S., Anderson, R.B. and Maurice, S., 2021. Alternating wet and dry depositional environments recorded in the stratigraphy of Mount Sharp at Gale crater, Mars. *Geology*, *49*(7), pp.842-846.

Rietveld, H.M., 1969. A profile refinement method for nuclear and magnetic structures. *Journal of applied Crystallography*, *2*(2), pp.65-71.

Rivera-Hernández, F., Sumner, D. Y., Mangold, N., Banham, S. G., Edgett, K. S., Fedo, C. M., et al. (2020). Grain Size Variations in the Murray Formation: Stratigraphic Evidence for Changing Depositional Environments in Gale Crater, Mars. Journal of Geophysical Research: Planets, 125(2).

Rohmah, M., Lalasari, L.H., Natasha, N.C., Sulistiyono, E., Firdiyono, F. and Soedarsono, J.W., 2020. Adsorption Behavior of Alkali Metal (Na+, Li+, and K+) from Bledug Kuwu brine by Resin Adsorbent for Purification: pH and Flow Rate Parameter. *Orient. J. Chem*, *36*(2), pp.273-279.

Rumble, J. ed., 2017. CRC handbook of chemistry and physics.

Schwenzer, S. P., Bridges J. C.,Wiens R. C., Pamela G. Conrad, S. P. Kelley, R. Leveille, Nicolas Mangold et al. "Fluids during diagenesis and sulfate vein formation in sediments at Gale crater, Mars." *Meteoritics & Planetary Science* 51, no. 11 (2016): 2175-2202.

Sheppard, R.Y., Thorpe, M.T., Fraeman, A.A., Fox, V.K. and Milliken, R.E., 2021. Merging Perspectives on Secondary Minerals on Mars: A Review of Ancient Water-Rock Interactions in Gale Crater Inferred from Orbital and In-Situ Observations. *Minerals*, *11*(9), p.986.

Shock, E.L. and Holland, M.E., 2007. Quantitative habitability. *Astrobiology*, *7*(6), pp.839-851.

Siebach, K.L. and Grotzinger, J.P., 2014. Volumetric estimates of ancient water on Mount Sharp based on boxwork deposits, Gale Crater, Mars. *Journal of Geophysical Research: Planets*, *119*(1), pp.189-198.

Smith, R.J., McLennan, S.M., Achilles, C.N., Dehouck, E., Horgan, B.H.N., Mangold, N., Rampe, E.B., Salvatore, M., Siebach, K.L. and Sun, V., 2021. X-Ray Amorphous Components in Sedimentary Rocks of Gale Crater, Mars: Evidence for Ancient Formation and Long-Lived Aqueous Activity. *Journal of Geophysical Research: Planets*, *126*(3), p.e2020JE006782.

Środoń, J., Zeelmaekers, E. and Derkowski, A., 2009. The charge of component layers of illite-smectite in bentonites and the nature of end-member illite. *Clays and Clay Minerals*, *57*(5), pp.649-671.

Stack, K. M., Grotzinger, J. P., Lamb, M. P., Gupta, S., Rubin, D. M., Kah, L. C., et al. (2019a). Evidence for plunging river plume deposits in the Pahrump Hills member of the Murray formation, Gale crater, Mars. Sedimentology, 66(5), 1768–1802.

Stack, K., Arvidson, R.E., Bennett, K.A., Bryk, A.B., Edgett, K.S., Fedo, C., Fox, V.K., Fraeman, A., House, C.H., Rabinovitch, J. and Sullivan Jr, R.J., (2019b), December. In-situ investigation of periodic bedrock ridges in the Glen Torridon area with the MSL Curiosity rover, Gale crater, Mars. In *AGU Fall Meeting Abstracts* (Vol. 2019, pp. P33B-02).

Stein, N., Grotzinger, J. P., Schieber, J., Mangold, N., Hallet, B., Newsom, H., et al. (2018). Desiccation cracks provide evidence of lake drying on Mars, Sutton Island member, Murray formation, Gale Crater. Geology, 46(6), 515-518.

Sutter, B., Amy C. Mcadam, Paul R. Mahaffy, Doug W. Ming, Ken S. Edgett, Elizabeth B. Rampe, Jennifer L. Eigenbrode et al. "Evolved gas analyses of sedimentary rocks and eolian sediment in Gale Crater, Mars: Results of the Curiosity rover's sample analysis at Mars instrument from Yellowknife Bay to the Namib Dune." *Journal of Geophysical Research: Planets* 122, no. 12 (2017): 2574-2609.

Swihart, G.H., McBay, E.H., Smith, D.H. and Siefke, J.W., 1992. The Kramer deposit of southern California--Preliminary insights on the origins of zoned lacustrine evaporite borate deposits. *Geological Society of America, Abstracts with Programs;(United States)*, *24*(CONF-921058-).

Swihart, G.H., McBay, E.H., Smith, D.H. and Siefke, J.W., 1996. A boron isotopic study of a mineralogically zoned lacustrine borate deposit: the Kramer deposit, California, USA. *Chemical geology*, *127*(1-3), pp.241-250.

Swihart, George H., Steven B. Carpenter, Yun Xiao, Eddie H. McBay, David H. Smith, and Yingkai Xiao. "A Boron Isotope Study of the Furnace Creek, California, Borate District." *Economic Geology* 109, no. 3 (2014): 567-580.

Tanner, L. H. "Borate formation in a perennial lacustrine setting: Miocene–Pliocene furnace creek formation, Death Valley, California, USA." *Sedimentary Geology* 148, no. 1-2 (2002): 259-273.

Thomas, N. H., Ehlmann, B. L., Meslin, P. -Y., Rapin, W., Anderson, D. E., Rivera-Hernández, F., et al. (2019). Mars Science Laboratory Observations of Chloride Salts in Gale Crater, Mars. Geophysical Research Letters, 46(19), 10754–10763.

Thompson, L. M., Berger, J. A., Spray, J. G., Fraeman, A. A., McCraig, M. A., O'Connell-Cooper, C. D., et al. (2020). APXS-Derived Compositional Characteristics of Vera Rubin Ridge and Murray Formation, Gale Crater, Mars: Geochemical Implications for the Origin of the Ridge. Journal of Geophysical Research: Planets, 125(10).

Thorpe, M.T., Bristow, T.F., Rampe, E.B., Tosca, N.J., Grotzinger, J.P., Bennett, K.A., Achilles, C.N., Blake, D.F., Chipera, S.J., Downs, G. and Downs, R.T., 2022. Mars Science Laboratory CheMin data from the Glen Torridon region and the significance of lake-groundwater interactions in interpreting mineralogy and sedimentary history. *Journal of Geophysical Research: Planets*, p.e2021JE007099.

Treiman, A. H., Morris, R. V., Agresti, D. G., Graff, T. G., Achilles, C. N., Rampe, E. B., et al. (2014). Ferrian saponite from the Santa Monica Mountains (California, U.S.A., Earth): Characterization as an analog for clay minerals on Mars with application to Yellowknife Bay in Gale Crater. *American Mineralogist*, *99*(11–12), 2234–2250.

Türker, A. and Türker, A.R., 2019. A critical review on the determination of boron in various matrices. *Journal of Boron*, *4*(1), pp.31-38.

Turner, S.M.R., Schwenzer, S.P., Bridges, J.C., Rampe, E.B., Bedford, C.C., Achilles, C.N., McAdam, A.C., Mangold, N., Hicks, L.J., Parnell, J. and Fraeman, A.A., (2021). Early diagenesis at and below Vera Rubin ridge, Gale crater, Mars. *Meteoritics & Planetary Science*, *56*(10), pp.1905-1932.

U.S. Geological Survey, 1952, USGS 1:62500-scale Quadrangle for Furnace Creek, CA 1952: U.S. Geological Survey.

Yu, X., Liu, C., Wang, C., Wang, J., Li, Q. and Meng, L., 2022. Origin of Li brine-type deposits in the Cretaceous gypsum-bearing formation of the Jitai Basin, South China: Constraints from geochemistry and H, O, Li, B, and Sr isotopes. *Applied Geochemistry*, *139*, p.105257.

Yutkin, M.P., Mishra, H., Patzek, T.W., Lee, J. and Radke, C.J., 2018. Bulk and surface aqueous speciation of calcite: implications for low salinity waterflooding of carbonate reservoirs. *SPE Journal*, *23*(01), pp.84-101.

Vaniman, D.T., Martínez, G.M., Rampe, E.B., Bristow, T.F., Blake, D.F., Yen, A.S., Ming, D.W., Rapin, W., Meslin, P.Y., Morookian, J.M. and Downs, R.T., 2018. Gypsum, bassanite, and anhydrite at Gale crater, Mars. *American Mineralogist: Journal of Earth and Planetary Materials*, *103*(7), pp.1011-1020.

Vasavada, A. R., Grotzinger, J. P., Arvidson, R. E., Calef, F. J., Crisp, J. A., Gupta, S., et al. (2014). Overview of the Mars Science Laboratory mission: Bradbury landing to Yellowknife Bay and beyond. Journal of Geophysical Research: Planets, 119(6), 1134-1161.

Vasavada, A. R. (2022). Mission Overview and Scientific Contributions from the Mars Science Laboratory Curiosity Rover After Eight Years of Surface Operations. *Space Science Reviews*, *218*(3), 14.

Warren, J.K., 2000. Evaporites, brines and base metals: low-temperature ore emplacement controlled by evaporite diagenesis. *Australian Journal of Earth Sciences*, *47*(2), pp.179-208.

Warren, J.K., 2006. *Evaporites: sediments, resources and hydrocarbons*. Springer Science & Business Media.

Weitz, C.M., Lewis, K.W., Bishop, J.L., Thomson, B.J., Arvidson, R.E., Grant, J.A., Seelos, K.D. and Ettenborough, I., 2022. Orbital Observations of a Marker Horizon at Gale Crater. *Journal of Geophysical Research: Planets*, *127*(4), p.e2022JE007211.

Wernicke, L.J. and Jakosky, B.M., 2021. Martian hydrated minerals: A significant water sink. *Journal of Geophysical Research: Planets*, *126*(3), p.e2019JE006351.

Wiens, R.C., Maurice, S., Barraclough, B., Saccoccio, M., Barkley, W.C., Bell, J.F., Bender, S., Bernardin, J., Blaney, D., Blank, J. and Bouyé, M., 2012. The ChemCam instrument suite on the Mars Science Laboratory (MSL) rover: Body unit and combined system tests. *Space science reviews*, *170*(1), pp.167-227.

Wiens, R. C., Maurice, S., Lasue, J., Forni, O., Anderson, R. B., Clegg, S., et al. (2013). Pre-flight calibration and initial data processing for the ChemCam laser-induced breakdown spectroscopy instrument on the Mars Science Laboratory rover. Spectrochimica Acta Part B: Atomic Spectroscopy, 82, 1–27.

Wu, P., Gazel, E., Udry, A., Setera, J.B. and Ostwald, A., 2021. Melt inclusions in chassignite NWA 2737: A link between processes recorded in Martian meteorites and rocks at Gale crater. *Meteoritics & Planetary Science*, *56*(7), pp.1328-1349.

# Final conclusions

## 1 Major findings

Through this work we expanded the investigation of the water-soluble elements, B and Li, in secondary Ca-sulfate veins observed using the Curiosity rover to gain a better perspective on the early aqueous history in Gale crater (Chapter 1). Based on the result of this study, we hypothesized that B and Li enrichment in secondary Ca-sulfates of Gale crater is likely due to remobilization of pre-existing primary borate deposits and B and Li containing clay minerals over multiple wet-dry cycles with variable fluid pH. We use thermochemical modeling techniques to estimate a minimum number of wet and dry cycles required in a Gale-relevant scenario to form primary borates and Ca-sulfate (Chapter 2). We test our hypothesis regarding B and Li enrichment in secondary Ca-sulfate veins of Gale crater by ground-truthing Curiosity rover data and thermochemical modeling results through detailed investigation of terrestrial analog samples collected from Southern California (Chapter 3). The following are the key findings and inferences of this work:

- B and Li concentration in Ca-sulfate veins of Gale crater are inversely correlated.
- We infer that the negative B and Li abundance correlation in Ca-sulfate veins of Gale indicates a combination of sequential precipitation (caused by varying solubilities of B and Li) and remobilization of early primary borates and Ca-sulfates over multiple wet-dry cycles.
- For areas in Gale crater with no evaporitic environment, we suggest that the reservoirs for B and Li are clay minerals which adsorbed B and Li during the relatively alkaline fluid

events (where the fluid is carrying B and Li due to weathering igneous rocks in Gale crater over multiple aqueous events).

- Based on thermochemical modeling of a Gale-relevant scenario, the minimum number of annual wet-dry cycles required to form an evaporitic assemblage consisting of primary borates and Ca-sulfates is 250 (~14k annual Martian cycles; ~7.5k annual Earth cycles).
- At a starting concentration of 4 x $10^{-4}$ ppm Li, Li-salts do not form in 250 cycles modeled for the Gale-relevant scenario. The modeled fluid composition indicates 0.18 moles/kg of $Li^+$ in the brine after 250 cycles which is within the same order of magnitude of $Li^+$ abundance reported for a terrestrial dry lake brine (Searles Lake: Felmy and Weare, 1986).
- The minerals formed in the thermochemical modeling are consistent with observed minerals and minerals inferred plausible in Gale crater. Therefore, we establish that wet-dry cycles are important for the formation of borates and Ca-sulfates in Gale crater.
- In the terrestrial analog samples, which consists of mixtures between evaporites and clay-rich sedimentary rocks, B enrichment is linked with evaporites (inferred to be supported by a relatively acidic pH condition and high evaporation that enabled precipitation of evaporites) while Li enrichment is linked with clay minerals (inferred to be through adsorption likely supported by a relatively high pH aqueous condition).
- B and Li in the terrestrial analog samples are negatively correlated which is consistent with the negative B and Li abundance correlation observed in Ca-sulfate veins of Gale crater.
- The phases identified in the terrestrial analog samples and the physical mixing trend between evaporites, and clay-rich sedimentary rocks is broadly consistent with the

reported phases and the physical mixing trend between evaporites and clay-rich sedimentary rocks in Gale crater. Therefore, we establish that, in Gale crater, similar to observation made in terrestrial samples, borates and clay minerals are the likely source and temporary reservoirs of B and Li in Ca-sulfates.

- The phases identified in the terrestrial analog samples are also broadly consistent with the phases formed as a resultant of thermochemical modeling of a Gale-relevant scenario summarize in Chapter 2 of this work. This shows that the presence of multiple wet-dry cycles (as established in Chapter 2), with varying pH conditions (as established in Chapter 3) is important for the formation of B and Li rich Ca-sulfate veins in Gale crater.

## 2 Conclusions and implications

We conclude that Gale crater experienced multiple generations of wet-dry cycles. This finding is consistent with inferences made based on sedimentological observations summarized in Gale-relevant studies other than this work (Hurowiz et al., 2017; Rapin et al., 2019; 2021) and on Earth where evaporite assemblages form over multiple wet-dry cycles (Tanner, 2002; Swihart et al., 2014, 1996; Lowenstein et al., 1999). This is the first work that applies the wet-dry cycle paradigm for Earth to Mars to estimate the temporal constraints on forming primary evaporites in Gale crater. We establish that the presence of wet-dry cycling is required to form an assemblage that consist of Ca-sulfates, borates, and clay minerals with adsorbed B and Li.

We infer that borates formed as primary precipitates, and clay minerals (either primary precipitates or as aqueous weathering products) adsorbed B and Li on their surfaces in addition to the precipitation of primary Ca-sulfates in Gale crater's early aqueous history. We also note that borate formation and B and Li adsorption are pH sensitive processes that require two different sets of pH and evaporative conditions where B enrichment dependent predominantly on the presence of an evaporative environment, relatively lower pH and linked with the presence of other evaporites such as Ca-sulfates and halite while B and Li enrichment through adsorption is linked with clay minerals and relatively high aqueous pH conditions. In Gale crater, both B and Li containing evaporites and Li-containing sedimentary rocks (with clay minerals in them) are present. Hence, we infer through analogy with terrestrial analog samples that the distribution of B and Li between evaporites and clay minerals indicates the changing fluid pH and evaporative conditions over multiple wet-dry cycles.

We also suggest that with multiple events of fluid activity, primary Ca-sulfates, borates, and B and Li containing clay minerals were remobilized and reprecipitated where Ca-sulfates and borates likely formed microcrystalline aggregates within secondary Ca-sulfate veins and clay minerals may be present on the walls of the secondary evaporitic veins.

This work shows that both acidic and alkaline aqueous conditions (with possible intermittent phases of neutral aqueous conditions) with multiple wet dry cycles were required for the formation B and Li containing evaporites in Gale crater. The relative constraints on fluid pH conditions possible in Gale crater also improves our understanding of types of microbial communities feasible through Gale crater's evolving aqueous history. Thus, the study of B and Li in phases can provide a higher resolution of understanding of fluid pH and habitability potential during the various stages of Gale crater's aqueous history. We conclude that aqueous pH and seasonal conditions required to support Earth-like life was possible during Gale crater's early aqueous history.

## 3 Topics for further research

During this work we identified areas of further investigation required with respect to study of the following topics that will be undertaken as postdoctoral projects at the Los Alamos National Laboratory:

- Continued investigation of evaporites and water-soluble elements in Gale crater as the Curiosity rover makes progress towards a lithologic unit that indicates a significantly high amount of evaporites in orbital data (i.e., the sulfate unit) in order to further expand our understanding of the aqueous processes in Gale crater.
- Detailed investigation of evaporites and water-soluble elements in Jezero crater similar to the investigations done in Gale crater in order to gain a global perspective of aqueous activities and climate on Mars.
- Determination of thermochemical parameters of evaporitic minerals forming in dry-lake environments to expand the database available for thermochemical modeling techniques in order to refine our understanding of the behavior of water-soluble elements and minerals in evaporative environments. This has applications in both Martian geology (as an updated modeling database is important for improving the robustness of model-based results) and for terrestrial investigations of brine-based reservoirs of Li that can be used as sustainable sources of Li, compared to a carbon-footprint heavy hard-rock mining during a period where the demand for Li-sourced batteries is on a rise.

## 4 References

Becker, S., Feldmann, J., Wiedemann, S., Okamura, H., Schneider, C., Iwan, K., Crisp, A., Rossa, M., Amatov, T. and Carell, T., 2019. Unified prebiotically plausible synthesis of pyrimidine and purine RNA ribonucleotides. *Science*, *366*(6461), pp.76-82.

Bristow, T.F., Grotzinger, J.P., Rampe, E.B., Cuadros, J., Chipera, S.J., Downs, G.W., Fedo, C.M., Frydenvang, J., McAdam, A.C., Morris, R.V. and Achilles, C.N., 2021. Brine-driven destruction of clay minerals in Gale crater, Mars. *Science*, *373*(6551), pp.198-204.

Dartnell, L., 2011. Biological constraints on habitability. *Astronomy & Geophysics*, *52*(1), pp.1-25.

Felmy, A.R. and Weare, J.H., 1986. The prediction of borate mineral equilibria in natural waters: Application to Searles Lake, California. *Geochimica et Cosmochimica Acta*, *50*(12), pp.2771-2783.

Hud, N.V. and Fialho, D.M., 2019. RNA nucleosides built in one prebiotic pot. *Science*, *366*(6461), pp.32-33.

Hurowitz, J.A., Grotzinger, J.P., Fischer, W.W., McLennan, S.M., Milliken, R.E., Stein, N., Vasavada, A.R., Blake, D.F., Dehouck, E., Eigenbrode, J.L. and Fairen, A.G., 2017. Redox stratification of an ancient lake in Gale crater, Mars. *Science*, *356*(6341), p.eaah6849.

Jarvinen, P., Oivanen, M. and Lonnberg, H., 1991. Interconversion and phosphoester hydrolysis of 2', 5'-and 3', 5'-dinucleoside monophosphates: kinetics and mechanisms. *The Journal of Organic Chemistry*, *56*(18), pp.5396-5401.

Küpfer, P.A. and Leumann, C.J., 2007. The chemical stability of abasic RNA compared to abasic DNA. *Nucleic acids research*, *35*(1), pp.58-68.

Lowenstein, Tim K., Jianren Li, Christopher Brown, Sheila M. Roberts, Teh-Lung Ku, Shangde Luo, and Wenbo Yang. "200 ky paleoclimate record from Death Valley salt core." *Geology* 27, no. 1 (1999): 3-6.

Marsh, G.E., 2022. Thermodynamics and the Origin of Life. *Canadian Journal of Physics*, (ja).

Shock, E.L. and Holland, M.E., 2007. Quantitative habitability. *Astrobiology*, *7*(6), pp.839-851.

Stein, N., Grotzinger, J. P., Schieber, J., Mangold, N., Hallet, B., Newsom, H., et al. (2018). Desiccation cracks provide evidence of lake drying on Mars, Sutton Island member, Murray formation, Gale Crater. Geology, 46(6), 515-518.

Swihart, G.H., McBay, E.H., Smith, D.H. and Siefke, J.W., 1996. A boron isotopic study of a mineralogically zoned lacustrine borate deposit: the Kramer deposit, California, USA. *Chemical geology*, *127*(1-3), pp.241-250.

Swihart, George H., Steven B. Carpenter, Yun Xiao, Eddie H. McBay, David H. Smith, and Yingkai Xiao. "A Boron Isotope Study of the Furnace Creek, California, Borate District." *Economic Geology* 109, no. 3 (2014): 567-580.

Tanner, L. H. "Borate formation in a perennial lacustrine setting: Miocene–Pliocene furnace creek formation, Death Valley, California, USA." *Sedimentary Geology* 148, no. 1-2 (2002): 259-273.

Roberts, R.W. and Crothers, D.M., 1992. Stability and properties of double and triple helices: dramatic effects of RNA or DNA backbone composition. *Science*, *258*(5087), pp.1463-1466.

Rapin, W., Ehlmann, B.L., Dromart, G., Schieber, J., Thomas, N.H., Fischer, W.W., Fox, V.K., Stein, N.T., Nachon, M., Clark, B.C. and Kah, L.C., 2019. An interval of high salinity in ancient Gale crater lake on Mars. *Nature Geoscience*, *12*(11), pp.889-895.

Rapin, W., Dromart, G., Rubin, D., Le Deit, L., Mangold, N., Edgar, L.A., Gasnault, O., Herkenhoff, K., Le Mouélic, S., Anderson, R.B. and Maurice, S., 2021. Alternating wet and dry depositional environments recorded in the stratigraphy of Mount Sharp at Gale crater, Mars. *Geology*, *49*(7), pp.842-846.